

MICROFABRICATED SENSORS FOR WATER QUALITY  
MONITORING

MICROFABRICATED PH, TEMPERATURE, AND FREE  
CHLORINE SENSORS FOR INTEGRATED DRINKING  
WATER QUALITY MONITORING SYSTEMS

By  
YIHENG QIN

B. ENG. SOUTHWEST JIAOTONG UNIVERSITY, 2009  
M. SC. CHALMERS UNIVERSITY OF TECHNOLOGY, 2011

A Thesis Submitted to the School of Graduate Studies in Partial Fulfilment of the  
Requirements for the Degree of Doctor of Philosophy

McMaster University © Copyright by Yiheng Qin, April 2017

McMaster University  
Hamilton, Ontario

Doctor of Philosophy (2017)  
(Electrical and Computer Engineering)

**TITLE:** Microfabricated pH, temperature, and free chlorine sensors  
for integrated drinking water quality monitoring systems

**AUTHOR:** Yiheng Qin,  
B. Eng. Southwest Jiaotong University, Chengdu, China  
M. Sc. Chalmers University of Technology, Göteborg,  
Sweden

**SUPERVISOR:** Dr. Matiar M. R. Howlader  
Dr. M. Jamal Deen (Co-supervisor)  
Dr. Yaser M. Haddara (Co-supervisor)

**NUMBER OF PAGES:** xxx, 224

# Lay Abstract

Sensitive, easy-to-use, and low-cost pH and free chlorine monitoring systems are important for drinking water safety and public health. In this thesis, we develop an inkjet printing technology to deposit palladium/palladium oxide films for potentiometric pH sensors and resistive temperature sensors. The different electrical and electrochemical properties of the palladium/palladium oxide films are realized by creating different film morphologies using different ink thermolysis atmospheres. The developed pH and temperature sensors are highly sensitive, fast in response, and stable. For free chlorine sensors, a hand drawing process is used to deposit poly(3,4-ethylenedioxythiophene):poly(styrenesulfonate), which is an indicator for the free chlorine concentration over a wide range. We also developed a calibration-free free chlorine sensors based on modified pencil leads. Such a free chlorine sensor is integrated with the pH and temperature sensors, and an electronic readout system for accurate on-site drinking water quality monitoring at low cost is demonstrated.

# Abstract

The monitoring of pH and free chlorine concentration in drinking water is important for water safety and public health. However, existing laboratory-based analytical methods are laborious, inefficient, and costly. This thesis focuses on the development of an easy-to-use, sensitive, and low-cost drinking water quality monitoring system for pH and free chlorine.

An inkjet printing technology with a two-step thermolysis process in air is developed to deposit palladium/palladium oxide (Pd/PdO) films as potentiometric pH sensing electrodes. The redox reaction between PdO and hydronium ions generates the sensor output voltage. A large PdO percentage in the film provides a high sensitivity of  $\sim 60$  mV/pH. A defect-free Pd/PdO film with small roughness contributes to a fast response and a high stability.

When the Pd ink is thermalized in low vacuum, the deposited Pd/PdO film shows a bilayer structure. The residual oxygen in the low vacuum environment assists the decomposition of organic ligands for Pd to form a thin and continuous layer beneath submicron Pd aggregates. The oxidized bilayer film behaves as a temperature sensor with a sensitivity of 0.19% resistance change per  $^{\circ}\text{C}$ , which can be used to compensate the sensed pH signals.

Poly(3,4-ethylenedioxythiophene):poly(styrenesulfonate) (PEDOT:PSS) is drawn by hand to form a free chlorine sensor. Free chlorine oxidises PEDOT:PSS, whose resistivity increment indicates the free chlorine concentration in the range of 0.5-500 ppm. Also, we simplified an amperometric free chlorine sensor based on amine-modified pencil leads. The simplified sensor is calibration-free, potentiostat-free, and easy-to-use.

The pH, temperature, and free chlorine sensors are fabricated on a common substrate and connected to a field-programmable gate array board for data processing and display. The sensing system is user-friendly, cheap, and can accurately monitor real water samples.

# Acknowledgements

I would like to express my gratitude to Dr. Matiar M. R. Howlader for providing me this opportunity to study as a Ph.D. student at McMaster University. As my supervisor, he built a good research team for me with talented researchers such as Arif U. Alam, Fangfang Zhang, and Rishad Arfin. I really appreciate his efforts in maintaining the equipment in the unique and advanced Micro and Nano Systems Laboratory, where my research work is carried out. Also, his door is always open for me for technical supports and valuable discussions. I am grateful for his continuous guidance and support on my research.

I would like to express my deep appreciation and thanks to my co-supervisor Dr. M. Jamal Deen for giving me this exciting and challenging project to work on, and also for his help, encouragement, guidance and insightful discussions throughout this research work. I would like to express my special appreciation to Dr. Deen for his efforts in arranging me to work at Xerox Research Centre of Canada (XRCC) as a visiting scientist, and maintaining the collaboration with XRCC. I would like to thank Dr. Deen for the training he provided to me in all aspects of research, including critical thinking, experiment planning, problem solving, data analysis, technical writing, and presentation to people with different education levels and backgrounds. In addition, I truly appreciate the extra opportunities Dr. Deen gave me to communicate and interact with top water researchers from Canada and India under the umbrella of RES'EAU WaterNET and IC-IMPACTS projects. It is also a great pleasure to work in Dr. Deen's water research team with Dr. Hyuck-Jin Kwon, Si Pan, and Pankaj Saini.

I would like to express my thanks to my cosupervisor, Dr. Yaser M. Haddara, for his valuable comments on my research over the past four years. I would also like to thank my other committee members Dr. Ravi Selvaganapathy and Dr. Aleksandar Jeremic for their advice on my research and for taking the time to review my thesis.

I would like to sincerely thank Dr. Yiliang Wu and Dr. Nan-Xing Hu from XRCC for their continuous interests in my project, for the helpful discussions, and for the valuable assistance offered during my research. Their experience and knowledge in chemistry and materials have greatly helped me. I am also thankful to Michelle Chrétien, Carolyn Moorlag, Biby Abraham, Chad Smithson, Darko Ljubic, Gail Song, Ping Liu, Sandra Gardner, Jonathan Lee, and Geoff Allen from XRCC for their assistance in my experiments.

It is also a memorable experience working with Dr. Zeng Cheng, Xiaoqing Zheng, Dr. Darek Palubiak, Dr. Zhiyun Li, Dr. Tianyi Guo, Hytham Afifi, Hani Alhems, Mrwan Alayed, Sumit Majumder, Mozghan Parsa, Javad Monshi Zadeh, Sasan Naseh in our group for their valuable suggestions and feedback on my research.

Last but not least, I am grateful for the support and help that I have received from my friends Rui Xu, Yifang Chen, Kuan Lin, and Xiaowei Deng. I sincerely thank my parents for their unconditional support and encouragement over all these years, and my dear wife, Lei Qin, for her endless love and for always being there for me and putting me first. This thesis is dedicated to them.

# Table of Contents

<b>Lay Abstract .....</b>	<b>iii</b>
<b>Abstract.....</b>	<b>iv</b>
<b>Acknowledgements .....</b>	<b>v</b>
<b>Table of Contents .....</b>	<b>vii</b>
<b>Lists of Figures .....</b>	<b>xi</b>
<b>List of Tables .....</b>	<b>xix</b>
<b>List of Appendices.....</b>	<b>xxi</b>
<b>List of Abbreviations .....</b>	<b>xxii</b>
<b>List of Symbols .....</b>	<b>xxvi</b>
<b>Declaration of Academic Achievement .....</b>	<b>xxx</b>
<b>Chapter 1 Introduction.....</b>	<b>1</b>
1.1. Research background .....	2
1.1.1. pH and free chlorine sensing for drinking water quality monitoring.....	2
1.1.2. Conventional ways of pH sensing.....	3
1.1.3. Conventional ways of free chlorine sensing .....	4
1.1.4. Conventional ways of temperature sensing .....	5
1.1.5. Future pH and free chlorine sensors .....	7
1.2. Microfabricated electrochemical pH sensors.....	8
1.2.1. Potentiometric sensor.....	9
1.2.2. ISFET .....	13
1.2.3. Chemoresistor and chemotransistor .....	19
1.2.4. Research challenges .....	26
1.3. Microfabricated electrochemical free chlorine sensors .....	30
1.3.1. Amperometric sensor configuration and sensing mechanism .....	30
1.3.2. Applicable materials and sensor performance .....	32
1.3.3. Research challenges .....	33

1.4.	Research motivation.....	35
1.5.	Research contributions.....	37
1.6.	Thesis organization .....	40
<b>Chapter 2 Solution-processed Pd/PdO: pH sensing mechanisms and properties.....</b>		<b>43</b>
2.1.	Background .....	44
2.2.	Experimental set-up .....	45
2.2.1.	Chemicals and reagents.....	45
2.2.2.	Methods for characterizing solutions and thin films.....	46
2.2.3.	Solution processing of Pd/PdO pH sensing electrodes .....	50
2.2.4.	Set-up for pH sensing tests .....	51
2.3.	Characterization of Pd/PdO thin films .....	52
2.3.1.	Chemical composition .....	52
2.3.2.	Surface morphology .....	54
2.3.3.	pH sensing mechanism .....	56
2.3.4.	pH sensitivity .....	61
2.3.5.	Response time .....	64
2.3.6.	Reversibility and drift .....	66
2.3.7.	Stability .....	67
2.3.8.	Reproducibility .....	69
2.4.	Conclusions.....	70
<b>Chapter 3 Inkjet-printed Pd/PdO for integrated pH sensors .....</b>		<b>71</b>
3.1.	Background .....	71
3.2.	Inkjet printing of Pd/PdO pH sensing electrodes.....	73
3.2.1.	Pd Ink formulation and properties .....	73
3.2.2.	Formation of Pd thin films .....	75
3.2.3.	Electrical resistivity of inkjet-printed Pd thin films.....	80
3.2.4.	Adhesion of inkjet-printed Pd thin films .....	82
3.2.5.	Modeling the response of the pH sensing electrodes.....	84
3.2.6.	Design of Pd/PdO pH sensing electrodes .....	89

3.3.	Integrated pH sensors.....	94
3.3.1.	Fabrication process .....	94
3.3.2.	Evaluation of pH sensing performance.....	96
3.3.3.	Test of real water samples.....	103
3.4.	Conclusions.....	104
<b>Chapter 4 Inkjet-printed Pd/PdO for temperature sensors .....</b>		<b>105</b>
4.1.	Background .....	106
4.2.	Thin film formation in air, low vacuum, and nitrogen .....	108
4.2.1.	Film morphologies .....	109
4.2.2.	Chemical compositions .....	111
4.2.3.	Thermogravimetric analysis.....	112
4.2.4.	Film formation mechanisms .....	115
4.3.	Electrical properties of inkjet-printed Pd/PdO films.....	116
4.3.1.	Effect of temperature .....	117
4.3.2.	Effect of relative humidity .....	119
4.3.3.	Electrical conduction mechanisms.....	123
4.4.	Conclusions.....	125
<b>Chapter 5 Paper-based, hand-drawn free chlorine sensor .....</b>		<b>127</b>
5.1.	Background .....	127
5.2.	Sensor design and operation .....	129
5.3.	Sensor fabrication and usage.....	132
5.4.	Sensor characterization .....	134
5.4.1.	Test in DI water .....	134
5.4.2.	Mechanical stability .....	134
5.4.3.	Reusability .....	135
5.4.4.	Sensitivity .....	137
5.4.5.	Stability .....	139
5.4.6.	Selectivity .....	140
5.4.7.	Test of real water samples.....	140

5.5.	Advantages of the hand-drawn free chlorine sensor .....	141
5.6.	Conclusions .....	142
<b>Chapter 6 FPGA-based, integrated drinking water quality monitoring system .....</b>		<b>143</b>
6.1.	Background .....	143
6.2.	Fabrication of integrated sensors .....	146
6.3.	System design .....	148
6.4.	Characterization of pH sensor .....	153
6.5.	Characterization of free chlorine sensor .....	154
6.5.1.	Sensitivity and response time .....	155
6.5.2.	Reversibility and drift .....	158
6.5.3.	Selectivity .....	158
6.5.4.	Stability .....	159
6.6.	Characterization of temperature sensor .....	159
6.6.1.	Sensitivity .....	160
6.6.2.	Reversibility and drift .....	162
6.7.	Measurement of real water samples .....	162
6.8.	Conclusions .....	163
<b>Chapter 7 Conclusions and recommendations .....</b>		<b>164</b>
7.1.	Conclusions .....	164
7.2.	Recommendations .....	168
<b>References .....</b>		<b>173</b>
<b>Appendix A Comparison table of microfabricated electrochemical pH sensors .....</b>		<b>194</b>
<b>Appendix B Comparison table of microfabricated electrochemical free chlorine sensors .....</b>		<b>200</b>
<b>Appendix C Digital masks for integrated pH, free chlorine, and temperature sensors .....</b>		<b>201</b>
<b>Appendix D Verilog/VHDL code for FPGA programming .....</b>		<b>203</b>
<b>Appendix E Copyright permissions .....</b>		<b>214</b>

# Lists of Figures

<b>Figure 1-1.</b> Distribution of hypochlorous acid and hypochlorite ion in water at different pH values at 25 °C. ....	5
<b>Figure 1-2.</b> Schematic of a potentiometric pH sensor and its possible sensing mechanisms. ....	10
<b>Figure 1-3.</b> Schematic of an ISFET-based pH sensor and its sensing mechanism. ....	14
<b>Figure 1-4.</b> Schematic of an ExGFET-based pH sensor and its sensing mechanism. ....	17
<b>Figure 1-5.</b> Schematic of a pH sensor in chemoresistor structure and its possible sensing mechanisms. ....	20
<b>Figure 1-6.</b> Schematic of an ECT-based pH sensor and its sensing mechanism. ....	22
<b>Figure 1-7.</b> Schematic of an EGFET-based pH sensor and its sensing mechanism. ....	24
<b>Figure 1-8.</b> Schematic of a pH sensor in FET structure and its possible sensing mechanisms. ....	25
<b>Figure 1-9.</b> Schematic of an amperometric free chlorine sensor and its sensing mechanism. ....	31
<b>Figure 2-1.</b> (a)-(c) Fabrication process of Pd/PdO-based pH sensing electrodes. (a) Glass substrate cleaning by rising with IPA and DI water. (b) Spin coating of Pd precursor solution. (c) Pd precursor conversion by baking and sample annealing at different conditions. (d) Characterization set-up for pH sensing behavior of fabricated electrodes. ....	50
<b>Figure 2-2.</b> (a-d) Pd 3d XPS spectra of the surface and bulk of sensing electrodes annealed at different temperatures for 4 min (solid lines), 24 h (dot-dash lines), and 48 h (dashed lines). (a) Surface, 200 °C. (b) Bulk, 200 °C. (c) Surface, 250 °C. (d) Bulk, 250 °C. (e) and (f) Curve fitting of XPS spectra for calculating atomic ratio between Pd <sup>0</sup> and Pd <sup>2+</sup> ; square boxes are original data, solid lines are fitted curves, dotted lines are fitted peaks for Pd <sup>0</sup> and Pd <sup>2+</sup> , and dashed lines are background lines. (e) Surface of a sample annealed at 200 °C for	

48 h (the intensity of 2 Pd <sup>0</sup> peaks is too low to be seen). (f) Bulk of the same sample annealed at 200 °C for 48 h.....	53
<b>Figure 2-3.</b> (a-b) AFM images over a 20 μm × 20 μm area of surfaces of pH sensing electrodes annealed at (a) 200 °C; (b) 250 °C for 48 h. (c) AFM image over a 1 μm × 1 μm area of surfaces of a pH sensing electrode annealed at 200 °C for 48 h.....	55
<b>Figure 2-4.</b> SEM images of surfaces of sensing electrodes annealed at (a) 200 °C for 4 min. (b) 200 °C for 24 h. (c) 200 °C for 48 h. (d) 250 °C for 4 min. (e) 250 °C for 24 h. (f) 250 °C for 48 h.....	56
<b>Figure 2-5.</b> Dissociative adsorption of water at the surface of PdO. (a) Pristine surface of PdO. (b) Water adsorption. (c) Proton displacement at the PdO surface.....	57
<b>Figure 2-6.</b> Open circuit potential versus pH values for an electrode annealed at (a) 200 °C for 4 min. (b) 200 °C for 24 h. (c) 200 °C for 48 h. (d) 250 °C for 4 min. (e) 250 °C for 24 h. (f) 250 °C for 48 h.....	62
<b>Figure 2-7.</b> (a) Real-time response of an electrode annealed at 200 °C for 48 h between pH of 2 and 12; full-scale view. (b) Enlarged view of the voltage transition between pH = 2 and 4, indicating how the response time was determined. (c-g) Real-time response of an electrode annealed at (c) 200 °C for 4 min. (d) 200 °C for 24 h. (e) 250 °C for 4 min. (f) 250 °C for 24 h. (g) 250 °C for 48 h. ....	65
<b>Figure 2-8.</b> Response time at different pH values for electrodes annealed at different conditions.....	66
<b>Figure 2-9.</b> Hysteresis at different pH values for electrodes annealed at different conditions.....	67
<b>Figure 2-10.</b> Operation stability of Pd/PdO pH sensing electrodes over a 60-day period.....	68
<b>Figure 3-1.</b> TGA test results of as-received Pd precursor solution, Pd-PhMe, and Pd-IBB using 1-step and 2-step thermolysis methods (inset: temperature profiles of 1-step and 2-step thermolysis).....	75
<b>Figure 3-2.</b> Voltage waveforms of the printhead for jetting different inks.....	76

<b>Figure 3-3.</b> Photographs showing wetting behaviors of inkjet-printed Pd-PhMe ink on different substrates. (a) On glass, 547 $\mu\text{m}$ -wide lines. (b) On PI treated by air plasma for 2 min, 547 $\mu\text{m}$ -wide lines. (Droplet pitch = 30 $\mu\text{m}$ , designed line width = 520 $\mu\text{m}$ in both cases.).....	76
<b>Figure 3-4.</b> (a-e) SEM images of surface morphologies of Pd films printed using Pd-PhMe ink. (a) 30 $\mu\text{m}$ droplet pitch, glass substrate, 1-step thermolysis; (b) 30 $\mu\text{m}$ droplet pitch, glass substrate, 2-step thermolysis; (c) 40 $\mu\text{m}$ droplet pitch, glass substrate, 2-step thermolysis; (d) 20 $\mu\text{m}$ droplet pitch, glass substrate, 2-step thermolysis; (e) 30 $\mu\text{m}$ droplet pitch, PI substrate, 2-step thermolysis; (f) Optical microscopy image of 2-step thermalized Pd lines printed using Pd-PhMe ink with 20 $\mu\text{m}$ droplet pitch on a glass substrate. (g) Thickness profiles of printed Pd lines shown in (f). (h) Thickness dependence of the resistivity of printed Pd. ....	78
<b>Figure 3-5.</b> SEM images of surface morphologies of a printed Pd layer using Pd-IBB as ink and 2-step thermolysis. (a) A typical inhomogeneous surface morphology. (b) Magnified view of (a). ....	79
<b>Figure 3-6.</b> Schematic of the physical dimensions of a printed Pd/PdO film. ....	80
<b>Figure 3-7.</b> (a) Depth-dependent chemical compositions of printed Pd films thermalizes at 200 $^{\circ}\text{C}$ for 4 min and 48 h obtained by XPS depth profiling. (b) Pd 3d XPS spectra and curve fitting of the surface and bulk of printed Pd thermalizes at 200 $^{\circ}\text{C}$ for 4 min. (c) Pd 3d XPS spectra and curve fitting of the surface and bulk of printed Pd annealed at 200 $^{\circ}\text{C}$ for 48h. ....	81
<b>Figure 3-8.</b> AFM images of different substrates. (a) PI treated by air plasma for 2 min. (b) Glass.....	84
<b>Figure 3-9.</b> Equivalent circuit model for determining the pH response at the Pd/PdO-electrolyte interface.....	85
<b>Figure 3-10.</b> Comparison between experimental data and modeling results (two time constant model) of the sensor response towards a pH step change. (a) Linear time scale. (b) Logarithm time scale.....	87

<b>Figure 3-11.</b> The linear approximation of the sensor response for the calculation of response time using the time constant extracted from the two time constant model.....	88
<b>Figure 3-12.</b> Comparison between the sensor response time and hysteresis obtained by experimental measurements and theoretical calculation using the two time constant model. ....	89
<b>Figure 3-13.</b> Effect of Pd/PdO electrode size on the pH sensitivity, response time, and hysteresis.....	91
<b>Figure 3-14.</b> Effect of Pd/PdO electrode thickness on the pH sensitivity, response time, and hysteresis. ....	93
<b>Figure 3-15.</b> Integration process of a pH sensor using printing techniques. (a1) Substrate cleaning. (a2) Air plasma treatment of PI substrate. (b) Inkjet printing of Pd ink. (c) Thermolysis and annealing of printed Pd to form Pd/PdO sensing electrode. (d) Inkjet printing of SU-8 ink as adhesion between Ag and the substrate. (e) Inkjet printing of AgNP ink for the reference electrode. (f) Pipette printing of NaOCl ink for the chlorination of the surface of Ag. (g) Pipette printing of PVC/KCl/AgCl ink to form the solid electrolyte of the reference electrode, and painting of Ag paste for electrical contacts. ....	94
<b>Figure 3-16.</b> (a) SEM image of the surface morphology of a printed Ag layer. (b) SEM image of the surface morphology of a printed AgCl layer. (c) XPS analysis of the surfaces of printed Ag and AgCl layers. ....	96
<b>Figure 3-17.</b> (a) Temporal response of an integrated sensor on glass when the pH of buffer solutions cycles between 4 and 10; inset: photograph of an integrated sensor on glass. (b) Temporal response of an integrated sensor on PI when the pH of buffer solutions cycles between 4 and 10; inset: photograph of an integrated sensor on PI. (c) Open circuit potential versus pH values for an integrated sensor on glass. (d) Open circuit potential versus pH values for an integrated sensor on PI. (e) Drift behavior an integrated sensor on glass. (f) Drift behavior an integrated sensor on PI. ....	97
<b>Figure 3-18.</b> The measured sensitivity of the pH sensor as a function of temperature.....	98
<b>Figure 3-19.</b> Stability of integrated sensors on glass and PI. ....	100

<b>Figure 3-20.</b> The electrical potential stability of a PRE in solutions with: (a) Different concentrations of Cl <sup>-</sup> ions. (b) Different pH values. ....	101
<b>Figure 3-21.</b> The response of a printed pH sensor in interfering solutions with different concentrations. ....	102
<b>Figure 3-22.</b> pH measurement results of real water samples using the integrated sensors on glass and on PI. ....	103
<b>Figure 4-1.</b> (a)-(c) Top-view optical images of Pd/PdO films for the thermolysis atmosphere of: (a) Air (ANOX). (b) Low vacuum (VNOX). (c) N <sub>2</sub> (N <sub>2</sub> NOX). (d)-(f) Top-view SEM images of Pd/PdO films for the thermolysis atmosphere of: (d) Air (ANOX). (e) Low vacuum (VNOX). (f) N <sub>2</sub> (N <sub>2</sub> NOX). (g)-(i) Cross-sectional SEM images of Pd/PdO films for the thermolysis atmosphere of: (g) Air (ANOX). (h) Low vacuum (VNOX). (i) N <sub>2</sub> (N <sub>2</sub> NOX). ....	110
<b>Figure 4-2.</b> XRD patterns of the Pd/PdO films with different precursor thermolysis atmospheres. ....	111
<b>Figure 4-3.</b> Raman spectra of Pd/PdO films with different precursor thermolysis atmospheres. ....	112
<b>Figure 4-4.</b> TG analysis of Pd/PdO mixture with different precursor thermolysis atmospheres. ....	113
<b>Figure 4-5.</b> TGA curves of Pd precursor and Pd/PdO mixture. ....	113
<b>Figure 4-6.</b> Proposed Pd/PdO film formation mechanisms in different precursor thermolysis atmospheres: (a) air, (b) low vacuum, and (c) N <sub>2</sub> . ....	115
<b>Figure 4-7.</b> Resistance drift in vacuum for the Pd/PdO films prepared: (a) In air before oxidation (ANOX). (b) In air after oxidation (AOX). (c) In low vacuum before oxidation (VNOX). (d) In low vacuum after oxidation (VOX). (e) Temperature dependence of resistance for the 4 samples for TCR calculations. ....	118
<b>Figure 4-8.</b> Resistance drift in humid air for the Pd/PdO films prepared: (a) In air before oxidation (ANOX). (b) In air after oxidation (AOX). (c) In low vacuum before oxidation (VNOX). (d) In low vacuum after oxidation (VOX). (e) RH dependence of resistance for the 4 samples. ....	120

<b>Figure 4-9.</b> FTIR spectra of Pd/PdO films with different precursor thermolysis atmospheres before and after testing in humid air. ....	121
<b>Figure 4-10.</b> Resistance change during temperature cycling tests of Pd/PdO films prepared: (a) In air before oxidation (ANOX). (b) In air after oxidation (AOX). (c) In low vacuum before oxidation (VNOX). (d) In low vacuum after oxidation (VOX). (e) Temperature dependence of resistance in humid air for the 4 samples for TCR calculation. ....	122
<b>Figure 4-11.</b> Proposed electrical conduction mechanisms of Pd/PdO films with different morphologies prepared: (a) In air before oxidation (ANOX). (b) In air after oxidation (AOX). (c) In low vacuum before oxidation (VNOX). (d) In low vacuum after oxidation (VOX). (e) In N <sub>2</sub> before oxidation (N <sub>2</sub> NOX). (f) Schematic illustrating the inter-grain charge transport mechanism. ....	124
<b>Figure 5-1.</b> (a) Oxidation of PEDOT in a free chlorine solution (adopted from reference 23). (b) Top view schematic and equivalent circuit of the drawn sensor. (c) Image of a drawn sensor after fabrication; (d-f) SEM images (scale bars represent 100 μm) of the surface of: (d) Paper substrate. (e) Drawn PEDOT:PSS film. (f) Drawn PEDOT:PSS after testing in 100 ppm NaOCl solution for 15 s. (g) Resistance variation of a 4 cm long drawn PEDOT:PSS chemoresistor during bending tests. ....	130
<b>Figure 5-2.</b> Fabrication process of a paper-based free chlorine sensor. (a) Drawing a PEDOT:PSS film as a chemoresistor. (b) Drawing Ag films for electrical contacts. (c) Coating waterproof Vaseline <sup>®</sup> Jelly. (d) Sensor conditioning in a NaOCl solution. ....	132
<b>Figure 5-3.</b> Resistance change during the drying period of the PEDOT:PSS film after free chlorine sensing. ....	133
<b>Figure 5-4.</b> Reusability of paper-based drawn PEDOT:PSS sensor stripes in solutions with different free chlorine (NaOCl) concentrations. (a) 0 ppm (DI water). (b) 0.5 ppm. (c) 1 ppm. (d) 2 ppm. (e) 5 ppm. (f) 10 ppm. (g) 20 ppm. (h) 50 ppm. (i) 100 ppm. (j) 200 ppm. (k) 500 ppm. Legend in each figure: time of each test. X axis: accumulated testing time. ....	136
<b>Figure 5-5.</b> Reusability of the free chlorine sensor after conditioning in a 10 ppm NaOCl solution for 5 min. ....	137

<b>Figure 5-6.</b> Sensor responses in different free chlorine solutions using different testing durations.....	138
<b>Figure 5-7.</b> Flow chart of the procedures to use the drawn sensor for practical free chlorine measurement. ....	139
<b>Figure 5-8.</b> Storage stability of the drawn free chlorine sensor. ....	139
<b>Figure 5-9.</b> Sensor responses in free chlorine solutions and 1000 ppm interference solutions (1: 100 ppm NaOCl (15 s); 2: 10 ppm NaOCl; 3: 1 ppm NaOCl; 4: DIW; 5: NaCl, 6: CaCl <sub>2</sub> ; 7: MgCl <sub>2</sub> ; 8: ZnCl <sub>2</sub> ; 9: K <sub>2</sub> SO <sub>4</sub> ; 10: CuSO <sub>4</sub> ; 11: (NH <sub>4</sub> ) <sub>2</sub> SO <sub>4</sub> ; 12: NaHCO <sub>3</sub> ; 13: Na <sub>2</sub> CO <sub>3</sub> ; 14: CH <sub>3</sub> COONa; 15: Na <sub>2</sub> HPO <sub>4</sub> ; 16: KNO <sub>3</sub> ; 17: Urea; 18: Ethylene glycol). Inset: sensor responses in logarithm scale. ....	140
<b>Figure 6-1.</b> Fabrication process of an integrated pH, free chlorine and temperature sensor. ....	148
<b>Figure 6-2.</b> (a) A portable integrated water quality monitoring system measuring the pH value of tap water. (b) An integrated water quality sensing probe with pH, temperature and free chlorine sensors. (c) A schematic diagram of the water quality monitoring system including signal conditioning (amplification and filtering for free chlorine sensor), data analysis (on the FPGA board), and results display (on the FPGA board). “T” represents “temperature” in the schematic diagram. ....	149
<b>Figure 6-3.</b> (a) Circuit diagram of a transimpedance amplifier with a low-pass filter for the signal conditioning for the free chlorine sensor. (b) Photo of the fabricated transimpedance amplifier with a low-pass filter. (c) Transfer characteristic curve of the transimpedance amplifier with a low-pass filter circuit. ....	151
<b>Figure 6-4.</b> Wheatstone bridge circuit of an inkjet-printed temperature sensor with 4 thermistors.....	152
<b>Figure 6-5.</b> Calibration curves for three inkjet-printed pH sensors. ....	154
<b>Figure 6-6.</b> (a) Temporal response of a free chlorine sensor for free chlorine concentrations between 0.2 and 8 ppm. (b) Calibration curves for five free chlorine sensors. (c) Drift behavior of a free chlorine sensor in 2 ppm NaOCl solution in dark. (d) The response of a free chlorine sensor to NaOCl solutions and 400 ppm interfering solutions. Each green	

arrow indicates the addition of 0.2 mL of 5% interfering solution to 25 mL NaOCl solution (1, KNO<sub>3</sub>; 2, K<sub>2</sub>SO<sub>4</sub>; 3, Na<sub>2</sub>CO<sub>3</sub>; 4, NaHCO<sub>3</sub>; 5, NaCl; 6, (NH<sub>4</sub>)<sub>2</sub>SO<sub>4</sub>; 7, NaHPO<sub>4</sub>; 8, NaOAc). ..... 156

**Figure 6-7.** (a) The measured sensitivity of the free chlorine sensor as a function of temperature (without considering the temperature dependence of the dissociation constant of HOCl). (b) Corrected sensitivity of the free chlorine sensor as a function of temperature (considering the temperature dependence of the dissociation constant of HOCl). ..... 156

**Figure 6-8.** Stability of the pencil-lead-based free chlorine sensor. .... 159

**Figure 6-9.** (a) Temporal response of a thermistor fabricated by an inkjet-printed Ag film when the temperature cycles between 0 °C and 50 °C. (b) Calibration curve of the inkjet-printed Ag thermistor. (c) Temporal response of a thermistor fabricated by an inkjet-printed Pd/PdO film when the temperature cycles between 0 °C and 50 °C. (d) Calibration curve of the inkjet-printed Pd/PdO thermistor. .... 160

**Figure 6-10.** (a) Temporal response of the temperature sensor for temperatures between 0 and 50 °C. (b) Calibration curve of the temperature sensor. (c) Drift of the temperature sensor at 25 °C in water in dark. .... 161

**Figure 7-1.** Proposed future water quality monitoring system. .... 169

**Figure A-1.** Digital mask for the inkjet printing pattern of rough Pd/PdO films for temperature sensors (2 cm in figure = 1 cm in real device). .... 201

**Figure A-2.** Digital mask for the inkjet printing pattern of smooth Pd/PdO films for pH sensors (2 cm in figure = 1 cm in real device). .... 201

**Figure A-3.** Digital mask for the inkjet printing pattern of SU-8 films (2 cm in figure = 1 cm in real device). .... 202

**Figure A-4.** Digital mask for the inkjet printing pattern of Ag films (2 cm in figure = 1 cm in real device). .... 202

# List of Tables

<b>Table 1-1.</b> Comparison of glass pH electrodes and different types of microfabricated electrochemical pH sensors.....	29
<b>Table 1-2.</b> Comparison of conventional and microfabricated electrochemical free chlorine sensors.....	34
<b>Table 1-3.</b> Proposed specifications for pH, free chlorine, and temperature sensors. ....	36
<b>Table 2-1.</b> Summary of preparation conditions, thickness, chemical composition, and performance parameters of pH sensing electrodes. ....	51
<b>Table 2-2.</b> Response time at different pH values for electrodes annealed at different conditions (unit: s). ....	65
<b>Table 2-3.</b> Hysteresis at different pH values for electrodes annealed at different conditions. ....	66
<b>Table 3-1.</b> Physical properties, key jetting parameters, and thermolysis parameters for the functional inks.....	74
<b>Table 3-2.</b> Adhesion test results of inkjet-printed thin films.....	83
<b>Table 3-3.</b> Extracted parameters for a two time constant model for the modeling of the pH step response. ....	88
<b>Table 3-4.</b> Extracted parameters for a two time constant model for the modeling of the pH step response of electrodes with different thicknesses.....	93
<b>Table 4-1.</b> Summary of the morphologies and electrical properties of the inkjet-printed Pd/PdO films. ....	108
<b>Table 5-1.</b> Comparison of 6 types of paper substrates and their adhesion to PEDOT:PSS films. ....	132
<b>Table 5-2.</b> Free chlorine measurement of real water samples (average results from n measurements). ....	141
<b>Table 6-1.</b> Monitoring of pH, free chlorine concentration and temperature of real water samples (average results from 5 measurements). ....	163

<b>Table A-1.</b> Summary of microfabricated electrochemical pH sensors. ....	194
<b>Table A-2.</b> Summary of microfabricated electrochemical free chlorine sensors. ....	200

# List of Appendices

**Appendix A Comparison table of microfabricated electrochemical pH sensors .....194**  
**Appendix B Comparison table of microfabricated electrochemical free chlorine sensors .....200**  
**Appendix C Digital masks for integrated pH, free chlorine, and temperature sensors .....201**  
**Appendix D Verilog/VHDL code for FPGA programming .....203**  
**Appendix E Copyright permissions .....214**

# List of Abbreviations

APTES	3-triethoxysilylpropylamine
DDFTTF	5,5-bis-(7-dodecyl-9H-fluoren-2-yl)-2,2-bithiophene
HOAc	Acetic acid
AC	Alternating current
Al <sub>2</sub> O <sub>3</sub>	Aluminum oxide
AlGaN	Aluminum-gallium-nitride
(NH <sub>4</sub> ) <sub>2</sub> IrCl <sub>6</sub>	Ammonium chloriridate
(NH <sub>4</sub> ) <sub>2</sub> SO <sub>4</sub>	Ammonium sulfate
ADC	Analogue-to-digital converter
Sb	Antimony
Ar	Argon
AFM	Atomic force microscopy
ALD	Atomic layer deposition
BJT	Bipolar junction transistor
BP	Boiling point
H <sub>3</sub> BO <sub>3</sub>	Boric acid
CaCl <sub>2</sub>	Calcium chloride
CNT	Carbon nanotube
-COOH	Carboxyl group
CVD	Chemical vapor deposition
Cl <sup>-</sup>	Chloride ion
Co <sub>3</sub> O <sub>4</sub>	Cobalt oxide
CRE	Commercial reference electrode
CMOS	Complementary metal-oxide-semiconductor
CP	Conductive polymer
CuS	Copper monosulfide
CuO	Copper oxide
CuSO <sub>4</sub> ·5H <sub>2</sub> O	Copper(II) sulfate pentahydrate
DRIE	Deep reactive-ion etching
DI	Deionized
EDL	Electrical double layer
ECT	Electrochemical transistor
EGFET	Electrolyte-gated field-effect transistor
EIS	Electrolyte-insulator-semiconductor

E-beam	Electron-beam
ExGFET	Extended-gate field-effect transistor
FET	Field-effect transistor
FPGA	Field-programmable gate array
FTIR	Fourier transform infrared
Gd <sub>2</sub> O <sub>3</sub>	Gadolinium oxide
GaN	Gallium nitride
Au	Gold
HfO <sub>2</sub>	Hafnium oxide
HL	Helmholtz layer
H <sub>3</sub> O <sup>+</sup>	Hydronium ion
OH <sup>-</sup>	Hydroxide ion
-OH	Hydroxyl group
OCl <sup>-</sup>	Hypochlorite ion
HOCl	Hypochlorous acid
InAs	Indium arsenide
In <sub>2</sub> O <sub>3</sub>	Indium(III) oxide
ISFET	Ion-sensitive field-effect transistor
Ir	Iridium
IrO <sub>2</sub>	Iridium(IV) oxide
Fe <sub>2</sub> O <sub>3</sub>	Iron(III) oxide
IBB	Isobutylbenzene
IPA	Isopropanol
LPCVD	Low-pressure chemical vapor deposition
MgCl <sub>2</sub>	Magnesium chloride
MOCVD	Metal-organic chemical vapor deposition
MOS	Metal-oxide-semiconductor
MWCNT	Multi-walled carbon nanotube
DPD	<i>N,N</i> -diethyl- <i>p</i> -phenylenediamine
NP	Nanoparticle
Ni	Nickel
Nb <sub>2</sub> O <sub>5</sub>	Niobium pentoxide
N <sub>2</sub>	Nitrogen
R-NH <sub>2</sub>	Organoamine
Ga <sub>x</sub> O <sub>y</sub>	Oxides of gallium
IrO <sub>x</sub>	Oxides of iridium
PbO <sub>x</sub>	Oxides of lead
PdO <sub>x</sub>	Oxides of palladium
O <sub>2</sub>	Oxygen

Pd	Palladium
PdO	Palladium(II) oxide
ppm	Parts per million
Pd-X	Pd salt
PBS	Phosphate buffered saline
H <sub>3</sub> PO <sub>4</sub>	Phosphoric acid
PECVD	Plasma-enhanced chemical vapor deposition
Pt	Platinum
PAA	Poly(1-aminoanthracene)
PEDOT:PSS	Poly(3,4-ethylenedioxythiophene) doped with poly(styrenesulfonate)
P3HT	Poly(3-hexylthiophene)
PMMA	Poly(methyl methacrylate)
PPI	Poly(propylenimine)
PVC	Poly(vinyl chloride)
PANI	Polyaniline
PEI	Polyethylenimine
PI	Polyimide
PPY	Polypyrrole
PTAA	Polytriarylamine
KCl	Potassium chloride
K <sup>+</sup>	Potassium ion
KNO <sub>3</sub>	Potassium nitrate
K <sub>2</sub> SO <sub>4</sub>	Potassium sulfate
PRE	Printed reference electrode
PSE	Printed sensing electrode
PGMEA	Propylene glycol monomethyl ether acetate
RF	Radio frequency
RTA	Rapid thermal annealing
RH	Relative humidity
RTD	Resistance temperature detector
RMS	Root-mean-square
RuO <sub>2</sub>	Ruthenium oxide
SEM	Scanning electron microscopy
Si	Silicon
SiO <sub>2</sub>	Silicon dioxide
Si <sub>3</sub> N <sub>4</sub>	Silicon nitride
Ag	Silver
AgCl	Silver chloride
SWCNT	Single-walled carbon nanotube

NaOAc	Sodium acetate
NaHCO <sub>3</sub>	Sodium bicarbonate
Na <sub>2</sub> CO <sub>3</sub>	Sodium carbonate
NaCl	Sodium chloride
NaOH	Sodium hydroxide
NaOCl	Sodium hypochlorite
Na <sub>2</sub> HPO <sub>4</sub>	Sodium phosphate dibasic
SD	Standard deviation
Ta <sub>2</sub> O <sub>5</sub>	Tantalum pentoxide
TCR	Temperature coefficient of resistance
TEOS	Tetraethyl orthosilicate
CF <sub>4</sub>	Tetrafluoromethane
TG	Thermogravimetric
TGA	Thermogravimetric analysis
SnO <sub>2</sub>	Tin dioxide
Ti	Titanium
TiN	Titanium nitride
TiO <sub>2</sub>	Titanium oxide
PhMe	Toluene
WO <sub>3</sub>	Tungsten oxide
UV	Ultraviolet
V <sub>2</sub> O <sub>5</sub>	Vanadium(V) oxide
WHO	World Health Organization
XRD	X-ray diffraction
XPS	X-ray photoelectron spectroscopy
Yb <sub>2</sub> O <sub>3</sub>	Ytterbium(III) oxide
ZnCl <sub>2</sub>	Zinc chloride
ZnO	Zinc oxide
α6T	α-sexithiophene

# List of Symbols

$\Delta V_{90}$	90% change of voltage from initial to final values
$T$	Absolute temperature
$Q_{SS}$	Accumulated charge per unit area at the dielectric-semiconductor interface
$Q_{OX}$	Accumulated charge per unit area in the dielectric
$\beta$	Acidic and basic equilibrium constants of surface reactions
$E_a$	Activation energy
$\gamma_I$	Activity coefficient for species $I$
$a_I$	Activity of species $I$
$I_{out}$	Amplitude of the output current of the free chlorine sensor
$k$	Boltzmann's constant
$\phi_b$	Boundary potential
$R_e$	Bulk electrode resistance
$C_{DL}$	Capacitance of the electrical double layer
$E$	Cell potential
$\mu$	Charge carrier mobility
$z_I$	Charge number of species $I$
$R_F$	Charge transfer resistance
$\mu_I$	Chemical potential of species $I$
$\mu_I^0$	Chemical potential of species $I$ in a standard state
$I$	Chemical species $I$
$C_I$	Concentration of a species $I$
$C_{OCl^-}$	Concentration of hypochlorite ion
$C_{HOCl}$	Concentration of hypochlorous acid
$C_{NaOCl}$	Concentration of NaOCl in a water sample
$C_I^{ele}$	Concentration of species $I$ in the electrode phase
$C_I^{sol}$	Concentration of species $I$ in the solution phase
$C_{free\ chlorine}$	Concentration of the free chlorine in water
$L_{crystallite}$	Crystallite size
$\rho_{PdO}$	Density of palladium oxide
$Q_B$	Depletion charge per unit area in the semiconductor
$\Delta G$	Difference in Gibbs free energy
$C_D$	Diffusion layer capacitance
$Z_c$	Dimensionless cracking parameter
$K_a$	Dissociation constant of acid

$K_b$	Dissociation constant of base
$C_{DL}$	Double-layer capacitance
$I_D$	Drain current
$\phi$	Electrical potential
$\phi_{HD}$	Electrical potential at the Helmholtz layer-diffusion layer interface
$\phi^{ele}$	Electrical potential of the electrode phase
$\phi^{sol}$	Electrical potential of the solution phase
$R_{ele}$	Electrical resistance
$R_{0B}$	Electrical resistance of the film without energy barriers
$\rho$	Electrical resistivity
$\tilde{\mu}$	Electrochemical potential
$\tilde{\mu}_I^{ele}$	Electrochemical potential of species $I$ in the electrode phase
$\tilde{\mu}_I^{sol}$	Electrochemical potential of species $I$ in the solution phase
$\phi_{Ag/AgCl/KCl}$	Electrode potential of a commercial reference electrode
$\phi_{Pd/PdO}$	Electrode potential of a Pd/PdO electrode
$q$	Elementary charge
$S^0$	Entropy of a system in a standard state
$F$	Faraday's constant
$\phi_f$	Fermi voltage
$R$	Gas constant
$C_{OX}$	Gate dielectric capacitance per unit area
$G$	Gibbs free energy
$G^0$	Gibbs free energy in a standard state
$W_{hyst}$	Hysteresis of a pH sensor
$C_c$	Input capacitance of a readout circuit
$R_c$	Input resistance of a readout circuit
$U^0$	Internal energy of a system in a standard state
$\alpha$	Ion concentration in the bulk solution
$L$	Length of a film
$pK_a$	Logarithmic dissociation constant of hypochlorous acid
$C_m$	Lumped capacitance of an electrode
$R_m$	Lumped resistance of an electrode
$m_e$	Mass of the pH sensing electrode
$R_0$	Measured initial resistance
$E_{meas}$	Measured output voltage of a pH sensor
$\Delta R$	Measured resistance difference
$T_{meas}$	Measured temperature of a water sample
$E_f$	Modulus of elasticity
$n_I$	Number of moles of species $I$

$\varepsilon_i$	Normalized amplitude for the time constant of the exponential term $i$
$O(t)$	Normalized sensor output as a function of time
$V$	Output voltage of the signal conditioning circuit for a free chlorine sensor
$V_{out}$	Output voltage of the temperature sensor
$C_e$	Parasitic capacitance of electrical connection of pH sensing electrode
$G_I$	Partial Gibbs free energy of species $I$
$G_I^0$	Partial Gibbs free energy of species $I$ in a standard state
$p_I$	Partial pressure of species $I$
$\theta$	Peak position in a X-ray diffraction pattern
$B(2\theta)$	Peak width in a X-ray diffraction pattern
$\varepsilon$	Permittivity of the Helmholtz layer
$\text{pH}_{pzc}$	pH value for which the dielectric surface is electrically neutral
$p_r$	Porosity factor of an inkjet-printed pH sensing electrode
$V_{GS}$	Potential difference between gate and source
$E_{ref}$	Potential of reference electrode
$p$	Pressure
$C_F$	Pseudocapacitance
$C_0$	Pseudocapacitance of the pH sensing material per unit area
$r_i$	Ratio between the time constant and the pH measurement time at a pH value
$E_{cal}$	Recorded voltage when the sensor is in a pH = 7 calibration solution
$R_{REF}$	Reference resistance at 25 °C
$T_{REF}$	Reference temperature
$\Delta R_{sen}$	Resistance change of a sensing film before and after testing
$R_{Ag1,2}$	Resistance of inkjet-printed Ag films
$R_{PdO1,2}$	Resistance of inkjet-printed Pd/PdO films
$R_{P1,2}$	Resistance of the drawn PEDOT:PSS film covered by waterproof layer
$R_{sen}$	Resistance of the exposed PEDOT:PSS film before test
$R_{A1,2}$	Resistance of the silver contacts
$K$	Scherrer's constant
$C_{spec}$	Specific pseudocapacitance of the pH sensing material
$E^0$	Standard cell potential
$\phi^0$	Standard electrode potential
$C_S$	Stern layer capacitance
$G_s$	Strain energy release rate
$\sigma_f$	Stress in a film
$\chi^{sol}$	Surface dipole potential of the solution
$\Psi$	Surface potential at the dielectric
$\gamma$	Surface tension
$\alpha_{TCR}$	Temperature coefficient of resistance

$t_{90}$	The time needed for 90% change of voltage from initial to final values
$\Delta E_{sen}$	Theoretical pH sensitivity of the sensor
$h$	Thickness of a film
$h_{surf}$	Thickness of the electrode surface that participate in the redox reaction
$x_{HL}$	Thickness of the Helmholtz layer
$V_{TH}$	Threshold voltage
$t$	Time
$\tau_i$	Time constant of the exponential term $i$
$t_s$	Time used for the measurement at a pH value
$N_S$	Total number of surface binding sites per unit area
$L_c$	Transistor's channel length
$W_c$	Transistor's channel width
$z$	Valence of the ion
$\eta$	Viscosity
$V_{vol}$	Volume of a system
$\lambda$	Wavelength
$W$	Width of a film
$\phi_M$	Work function of metal
$\phi_{SC}$	Work function of semiconductor

# Declaration of Academic Achievement

This thesis was written by Yiheng Qin under the supervision of Dr. Matiar M. R. Howlader, Dr. M. Jamal Deen, and Dr. Yaser M. Haddara from McMaster University. The research described in Chapter 2 to 4, and 6 (pH and temperature sensor part) was carried out in collaboration with Xerox Research Centre of Canada (XRCC). The research presented in Chapter 5 and 6 (free chlorine sensor part) was carried out in collaboration with Department of Chemical Engineering, McMaster University.

- Chapter 1: I conducted the literature review, and summarized the research results.
- Chapter 2: I designed the devices and experiments. Sandra Gardner (XRCC) recorded the scanning electron microscopy images. I conducted all other experiments. Dr. Yiliang Wu (XRCC, now at TE connectivity) assisted in data analysis.
- Chapter 3: I designed the devices and experiments. Jonathan Lee and Geoff Allen (XRCC) assisted in the viscosity and surface tension measurements. Arif U. Alam (McMaster) helped in the atomic force microscopy imaging. I conducted all other experiments. Dr. Nan-Xing Hu (XRCC) supported the data analysis.
- Chapter 4: I designed the devices and experiments. Sandra Gardner (XRCC) recorded the scanning electron microscopy images. Arif U. Alam (McMaster) carried out the Fourier transform infrared spectroscopy measurements. I conducted all other experiments. Dr. Nan-Xing Hu (XRCC) supported the data analysis.
- Chapter 5: I designed the devices and experiments, and did all experiments and analysis.
- Chapter 6: I designed the devices and experiments. Si Pan (McMaster) assisted in the fabrication of free chlorine sensors. Zeng Cheng (McMaster, now at AMD) provided help in programming the field-programmable gate array. I did all other experiments and data analysis.

# Chapter 1

## Introduction\*

Continuous, real-time monitoring of the level of pH and free chlorine concentration in drinking, recreational, and food processing water is of great importance to public health. However, it is challenging when conventional analytical instruments, such as bulky pH electrodes and expensive free chlorine meters, are used. These instruments have slow response, are difficult-to-use, prone to interference from operators, and require frequent maintenance. In contrast, microfabricated electrochemical sensors are cheaper, smaller in size, and highly sensitive. Therefore, these sensors are desirable for online and on-demand monitoring of pH and free chlorine in drinking water.

In this chapter, we introduce the importance and conventional approaches of pH and free chlorine sensing for drinking water quality monitoring. Next, we discuss different physical configurations of microfabricated sensors. These configurations include potentiometric electrodes, ion-sensitive field-effect transistors, and chemoresistors/chemotransistors for electrochemical pH sensing. Also, we identified that micro-amperometric sensors are the dominant ones used for free chlorine sensing. We summarized and compared the structures, operation/sensing mechanisms, applicable materials, and performance parameters in terms of sensitivity, sensing range, response time and stability of each type of sensor. Then, the motivation of this research is described, with the specifications of the proposed system and each sensor utilized in the system. Finally, the research contribution and thesis organization is presented.

---

\* Adapted from Y. Qin, H.-J. Kwon, M. M. R. Howlader, and M. J. Deen, "Microfabricated electrochemical pH and free chlorine sensors for water quality monitoring: Recent advances and research challenges," *RSC Adv.*, vol. 5, no. 85, pp. 69086–69109, 2015, with permission from The Royal Society of Chemistry (Appendix E).

## 1.1. Research background

### 1.1.1. pH and free chlorine sensing for drinking water quality monitoring

The quality of drinking water is determined by bio-physico-chemical parameters including, but are not limited to pH, free chlorine concentration, turbidity, dissolved oxygen (O<sub>2</sub>), conductivity, organic carbon, and some types of microorganisms [1]. Among them, the pH value and free chlorine concentration is critical to the natural environment and our health. The pH of an aqueous solution is defined as the negative common logarithm of the molar concentration of hydronium ions (H<sub>3</sub>O<sup>+</sup>), given by:

$$\text{pH} = -\log[\text{H}_3\text{O}^+]. \quad (1.1)$$

The usual range of pH is 0 to 14, where pH = 7 is the neutral value, pH < 7 indicates an acidic solution, and pH > 7 denotes a basic solution [2].

According to the World Health Organization (WHO), the recommended optimum level of pH for drinking water is in the range of 6.5 to 9.5 [3]. The Canadian government has a narrower range of 6.5 to 8.5 [4]. If the pH of water in the distribution system is outside the recommended range, it may indicate some problems in water treatment and could eventually affect our health. For example, the leaching and nitrification of water is indicated by lower pH values [5]; the presence of microorganisms in water changes the pH by producing acidic or basic metabolic species [6]; accidental spills of disinfecting chemicals and breakdown of treatment system can even result in extreme pH values (pH outside the range of 4 to 10) [7]. Water with unusual pH values may have abnormal odor and taste. It may cause gastrointestinal irritation [8], corrosion of metal pipes [9], and indicate inefficient disinfection [10]. Therefore, pH has to be regularly monitored at all stages of water treatment [11].

On the other hand, chlorine is introduced into the water treatment system for disinfection due to its capability to bond with and destroy the outer surfaces of bacteria and viruses [12], such as *Escherichia coli* O157:H7, *Salmonella*, *Salmonella typhi*, *Shigella*, *Campylobacter*,

*Vibrio cholera* and *Pseudomonas*, which could cause water-borne diseases. However, chlorine should be used in a controlled manner to safely and effectively disinfect drinking water. The WHO states that 2 to 3 parts per million (ppm) chlorine should be added into water to get an effective disinfection and acceptable residual concentration [13]. In U.S. standards, the maximum concentration of residual chlorine in drinking water is 2 ppm [14]. Also, the suggested concentration for free chlorine in a well-maintained swimming pool is 1.5 to 2 ppm [15], [16]. For food processing, the water should contain 50 to 200 ppm free chlorine [17].

Underfeeding of chlorine may result in incomplete disinfection that threatens public health. Overfeeding may generate objectionable odor and increase the level of trihalomethanes (suspected carcinogens) in the treated water [18]. Moreover, chlorine is a costly chemical whose production requires a large amount of energy (around 3,000 kWh electricity is needed for producing 1 ton chlorine from brine) [19]. As a result, the free chlorine level in drinking water is a critical parameter that should be monitored routinely and frequently.

### **1.1.2. Conventional ways of pH sensing**

Conventional technologies for pH measurement for water quality monitoring are mainly depending on glass electrode-based pH meters, which were invented by Arnold Beckman in 1934 and commercialized in 1936 [20]. The first pH meter included a glass-indicating electrode that was developed by F. Haber and Z. Klemensiewicz in 1909 and integrated with a vacuum tube amplifier [21]. In the next several decades, different types of pH sensors emerged, and they could be mainly categorized into chemo-mechanical sensors, electrochemical sensors, and optical sensors [11]. Even today, the most commonly used pH sensors are still the glass-membrane-based electrochemical electrodes.

A typical glass electrode consists of a bulb made from a specific glass (for example, a glass containing lithium or sodium ions), internal solution (usually 0.1 M hydrochloride acid or buffered chloride solution), internal electrode (usually silver/silver chloride, Ag/AgCl, or

calomel electrode), and glass or plastic electrode body [22]. During pH measurement, the outer surface of the bulb is hydrated by forming a silicate skeleton layer, which is designed to be selectively permeable to  $\text{H}_3\text{O}^+$ . Similarly, a hydrated layer is created on the inner side of the bulb. The amount of charges at the inner side is proportional to the amount of permeated  $\text{H}_3\text{O}^+$  at the outer side (relating to the concentration of  $\text{H}_3\text{O}^+$  in the external solution). The potential difference across the glass bulb membrane ( $E$ ) is given by Nernst equation [23]:

$$E = E^0 + \frac{2.303RT}{zF} \log[\text{H}_3\text{O}^+], \quad (1.2)$$

where  $E^0$  is the standard cell potential, which is a function of the standard potential of the internal reference electrode (relative to standard hydrogen electrode) and the resistivity of the internal solution.  $R$  is the gas constant ( $8.314 \text{ J/K}\cdot\text{mol}$ ),  $T$  is the absolute temperature,  $z$  is the valence of the ion (1 for  $\text{H}_3\text{O}^+$ ),  $F$  is Faraday's constant ( $9.649 \times 10^4 \text{ C/mol}$ ), and  $[\text{H}_3\text{O}^+]$  is the ion activity (relating to the molar concentration of  $\text{H}_3\text{O}^+$ ). At  $25 \text{ }^\circ\text{C}$ , the electrode potential as a function of solution pH is:

$$E = E^0 - 0.05916\text{pH}, \quad (1.3)$$

which shows the ideal pH sensitivity of the glass electrode is  $59.16 \text{ mV/pH}$ . This value is known as the Nernstian slope in the pH-voltage plot and has been treated as the reference value in the development of novel pH sensors.

### 1.1.3. Conventional ways of free chlorine sensing

Free chlorine in water consists of hypochlorous acid ( $\text{HOCl}$ ) and hypochlorite ion ( $\text{OCl}^-$ ). When chlorine gas is introduced into water for disinfection,  $\text{HOCl}$  is produced [24]:



where  $\text{HOCl}$  is a weak acid and can be partially dissociated into  $\text{H}^+$  and  $\text{OCl}^-$  in water:



Thus, at a certain temperature, the percentage distribution of  $\text{HOCl}$  and  $\text{OCl}^-$  is a function of the concentration of  $\text{H}^+$  ( $\text{H}_3\text{O}^+$ ), which is the pH of the solution (Figure 1-1). This relation can be generally expressed by:

$$\log \frac{[\text{OCl}^-]}{[\text{HOCl}]} = \log K_a + \text{pH}, \quad (1.6)$$

where  $[\text{OCl}^-]$  and  $[\text{HOCl}]$  are the equilibrium concentrations of  $\text{OCl}^-$  and  $\text{HOCl}$ , respectively, and  $K_a$  is the dissociation constant of  $\text{HOCl}$  (around  $10^{-7.53}$  at  $25^\circ\text{C}$ ) [25]. One can measure the solution pH together with the concentration of either  $\text{HOCl}$  or  $\text{OCl}^-$  to obtain the level of free chlorine concentration. Two commonly used analytical methods for free chlorine monitoring are colorimetric and electrochemical analysis, including: absorptiometry methods using *N,N*-diethyl-*p*-phenylenediamine (DPD) [26], *o*-tolidine [27] or other chemicals [28]–[30]; iodometric titration [31]; chromatography [32]; chemiluminescence [33]; and amperometric methods [34], [35].

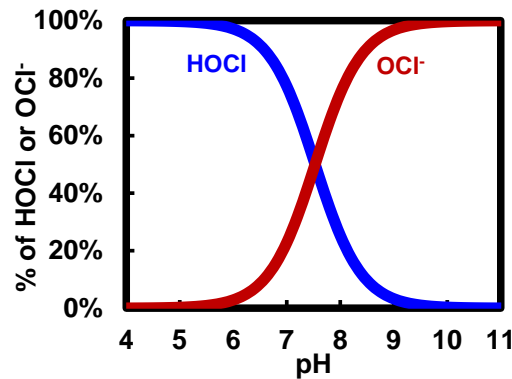


**Figure 1-1.** Distribution of hypochlorous acid and hypochlorite ion in water at different pH values at  $25^\circ\text{C}$ .

The DPD-based absorptiometry method has been extensively used owing to its high sensitivity. When the solution pH is around 7, free chlorine oxidizes DPD to form a colored magenta compound [26]. The color can be photometrically read out to determine the amount/concentration of chlorine. This method usually can detect free chlorine in the concentration range of 0 to 5 ppm with an accuracy of 0.04 ppm. It has been considered as a standard analytical approach and approved by the United States Environmental Protection Agency for online monitoring of free chlorine [36].

#### 1.1.4. Conventional ways of temperature sensing

The temperature of a water sample may not directly tell the water quality, however, the temperature affects most of the bio-physico-chemical parameters in water. To monitor the

drinking water quality with a high accuracy, the water sample temperature should be measured. For example, according to the Nernst equation (equation (1.2)), the sensitivity of a glass-electrode-based pH sensor is a function of the water temperature. Also, in free chlorine monitoring, the dissociation constant of HOCl varies with the water temperature [25].

Electronic temperature sensor can be categorized as resistance temperature detectors (RTD, including thermistors), thermocouples, and junction semiconductor sensors. A RTD uses a pure metal (such as platinum, Pt), whose resistance changes is linearly proportional to temperature (a positive temperature coefficient of resistance, TCR) [37]. The Pt-based RTD typically has a wide sensing range of  $-270\text{ }^{\circ}\text{C}$  to  $+850\text{ }^{\circ}\text{C}$  with a sensitivity of  $0.00385\ \Omega/^{\circ}\text{C}$  and an accuracy of  $\sim 0.25\text{ }^{\circ}\text{C}$  (between  $0\text{ }^{\circ}\text{C}$  and  $100\text{ }^{\circ}\text{C}$ ). A RTD can also use a semiconductor material (such as silicon, Si) that exhibits large changes in resistance for a small change in temperature (thermistor) [38]. This device has a negative TCR, meaning that the resistance decreases as the temperature increases. The accuracy of such device is  $0.1\text{ }^{\circ}\text{C}$  to  $0.2\text{ }^{\circ}\text{C}$  in the range of  $0\text{ }^{\circ}\text{C}$  to  $100\text{ }^{\circ}\text{C}$ . One of the advantages of RTDs is their small dimensions and low cost.

In a thermocouple, two dissimilar metals are connected at their two ends. If the two metal-metal junctions are exposed to two different temperatures, a thermoelectric potential will be produced in the circuit (Seebeck effect) [39]. The magnitude of the thermoelectric potential depends on the nature of the two metals and the temperature difference between the junctions. The sensing range of a thermocouple can be up to  $2000\text{ }^{\circ}\text{C}$  [40], depending on the metals used. However, the accuracy of thermocouples is lower ( $\sim 1\text{ }^{\circ}\text{C}$ ) than RTDs.

A p-n junction diode and bipolar junction transistor (BJT) have strong temperature dependence in their electrical characteristics. If a diode or a BJT is biased by a constant current, the forward biased voltage will change depending on the temperature change [41].

The junction semiconductor sensors have a sensing range up to  $\sim 500$  °C, and their sensitive can be greater than  $1$  mV/°C.

### **1.1.5. Future pH and free chlorine sensors**

Traditional analytical approach for drinking water quality monitoring consists of multiple steps: water sampling, sample transportation to laboratories, and laboratory analysis [42]. This approach is time-consuming, expensive and laboratory-dependent. Also, the results are easily affected by anthropogenic interference as well as long-term storage of the water samples [43], [44]. For example, the operation of inexpensive multi-parameter water quality test kits (85 CAD for a 15-parameter test kit) are based on the colorimetric method. The colors of different reagents change when they react with the analytes. These test kits are qualitative, have a low measurement accuracy, and can only be used for a limited number of times (2 to 5 times). Glass pH electrodes are brittle, large in dimensions, slow in response, costly, and they need regular maintenance such as calibration and refilling of the reference buffer solution [45]. For free chlorine monitoring, the commonly used DPD analyzers have high sensitivity and can provide accurate results in a limited detection range if they are calibrated frequently. However, such analyzers rely on expensive optical instruments, generate environmentally harmful chemicals, are prone to the interference of certain iron and manganese species, and are difficult to miniaturize [36], [46]. Therefore, alternative sensing technologies need to be developed to address these challenges.

The utilization of accurate, easy-to-use, small-footprint and inexpensive sensors is an attractive alternative approach. Recent developments in microfabrication technologies enable the realization of such sensors. The advantages of the microfabrication technologies include the precise control of material surface morphologies (such as roughness), the ability to tailor material properties (such as conductivity), and the reduction of the amount of materials used. Also, micro-scale sensors can be integrated with other sample processing, signal processing and transmission components to create high-functionality integrated systems for automatic operation [47], [48].

There are reports of several hydrogel-based sensors using micro chemical-mechanical transducers for the measurement of pH [49]–[52]. However, these sensors are more difficult to implement due to their brittle structures and long response time (hundreds of minutes). In contrast, micro-optical sensors are highly accurate and sensitive, but their sensing range is limited and linearity is poor. Also, the components for optical sensors such as lasers and detectors are expensive [53]–[56], and usually, the sensors require chemical reagents for the measurement [57]. Therefore, chemo-mechanical and optical sensors are challenging to implement for continuous, low-cost and easy-to-use water quality monitoring. The advantages of the microfabricated electrochemical sensors over other types of sensors and analytical methods include:

- Wider sensing range and faster response with comparable sensitivity.
- Easier integration with microelectronic components for automatic operation.
- Smaller dimensions and higher structural compatibility with existing water distribution systems.
- Better compatibility with additive fabrication technologies.
- Lower cost so that they can be deployed more widely.

## **1.2. Microfabricated electrochemical pH sensors**

In the literature, more than seven mechanisms were described to explain the working principles of solid-state electrochemical pH sensors [58]–[60]. These mechanisms include:

- $\text{H}_3\text{O}^+$  ion exchange in a membrane rich in hydroxyl groups (-OH). It is the mechanism for conventional glass electrodes.
- Redox equilibrium involving  $\text{H}_3\text{O}^+$  ions between a metal and its oxides, such as an antimony electrode.
- Redox equilibrium involving  $\text{H}_3\text{O}^+$  ions between metal oxides with different metal valences, such as iridium oxide ( $\text{IrO}_x$ ) electrodes.

- Redox equilibrium involving a solid-phase material and  $\text{H}_3\text{O}^+$  ions, whose hydrogen content can be changed by applying an electrical current, such as conductive polymer-based electrodes.
- Steady-state corrosion of the electrode material by  $\text{H}_3\text{O}^+$  ions, but this is not suitable for practical uses.
- Change of surface potential of a solid-state material due to the pH change of the contacting solution, based on the site-dissociation and double-layer models at the solid-liquid interface. Such theory was applied in transistor-based pH sensors.
- Variation of electrical properties (such as resistivity) of a material with changes in the pH of the solution.

Based on these transduction mechanisms, different configurations of pH sensors were developed. In addition to these methods, other mechanisms and sensor structures, such as voltammetric [61], [62], impedimetric [63], and diode-based sensors [64], were reported. In subsection 1.2.1 to 1.2.3, we focus on the more widely reported pH sensors structured as potentiometric electrodes, ion-sensitive field-effect transistors (ISFETs), and chemoresistors/chemotransistors.

## **1.2.1. Potentiometric sensor**

### **1.2.1.1. Sensor configuration and sensing mechanism**

A typical potentiometric sensor has a two-electrode structure, one electrode being the sensing electrode and the other, the reference electrode with Ag/AgCl being the most commonly used reference electrode in micro-scale pH sensors [65]–[67]. When both electrodes contact the solution, the electrical potential difference between them is measured to determine the  $\text{H}_3\text{O}^+$  concentration in the solution. Figure 1-2 shows a schematic of a potentiometric pH sensor and its possible sensing mechanisms.

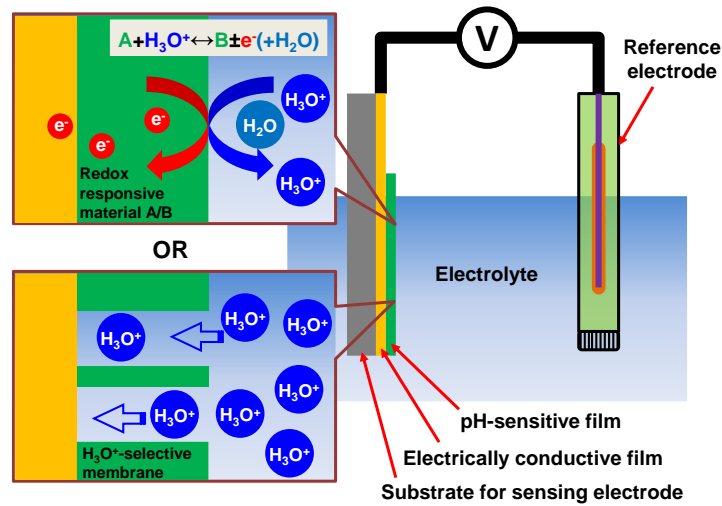


**Figure 1-2.** Schematic of a potentiometric pH sensor and its possible sensing mechanisms.

For potentiometric sensors, two possible mechanisms for pH sensing were observed: redox reactions and ion-selective permeation. First, if the material on the sensing electrode has redox reactions with  $H_3O^+$ , then a potential difference is generated by the free energy change as reversible chemical reactions approaching their equilibrium conditions [67]. Second, if the sensing material acts as an ion-selective membrane, the concentration gradient of ions across the membrane also generates a potential difference. For both cases, the potential can be quantitatively determined by the Nernst equation, as discussed previously in section 1.1.2. Ideally from equation (1.3), the change of 1 pH unit at 25 °C will result in a 59.16 mV change in the potential difference between the sensing and reference electrodes.

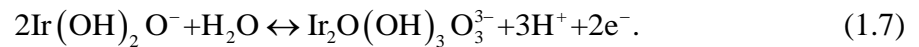
The potentiometric configuration is simple when compared to other sensor structures. It only requires two electrodes and no power supply is needed for its operation. Thus, the dimensions of potentiometric sensors can be reduced. The potential difference between the sensing and reference electrodes is normally hundreds of millivolts, which can be easily read out by inexpensive, commercial voltmeters. Therefore, potentiometric sensors are widely used in laboratories for the characterization of newly developed pH sensitive materials.

### 1.2.1.2. Applicable materials and sensor performance

The electrical conductivity of pH sensitive material being used for the potentiometric sensing electrode should not be low for the transfer of electrons generated by the redox reactions. Thus, conductive and semiconductive metal oxides and organic materials are used. Several of these are now described.

$\text{IrO}_x$  was reported as an outstanding material for pH measurement over wide ranges, with fast responses, and high durability and stability [68]. Several approaches for the preparation of microfabricated  $\text{IrO}_x$  electrodes were used. They include: thermal oxidation of iridium (Ir) [69], electroplating [70], [71], anodization [72], sputtering [64], [73], and sol-gel processing [74]. Generally, the  $\text{IrO}_x$  electrodes have near-Nernstian response (59.16 mV/pH), because the amount of transferred electrons equals to the amount of reacted  $\text{H}_3\text{O}^+$ . However,  $\text{IrO}_x$  prepared by electrochemical deposition showed super-Nernstian response (pH sensitivity greater than 59.16 mV/pH), with a sensitivity of around 70 mV/pH.

To explain the super-Nernstian response, it is proposed that the electrochemically deposited  $\text{IrO}_x$  can become hydrated in an aqueous environment and contains Ir ions with different valences (+3 and +4) [70], [71]. If  $\text{IrO}_x$  is fully hydrated, the redox reaction is:



This reaction shows that every 3 hydronium ions will lead to the transfer of 2 electrons. As a result, the pH response for this reaction is  $(3/2)(RT/F) = 88.74$  mV/pH at 25 °C. If  $\text{IrO}_x$  is partially hydrated, then a Nernstian slope between 59.16 and 88.74 mV/pH should be obtained. The  $\text{IrO}_x$  electrodes can cover a pH sensing range between 1 and 13 with short response times. It is worth noting that a less porous sensing surface gives faster response due to a shorter diffusion length of the  $\text{H}_3\text{O}^+$  in the sensing electrode [74]. For example, nano-porous  $\text{IrO}_x$  exhibited a response time of 100 s while that of a dense film is less than 2 s.

Other metal oxides have also been studied, but their pH sensitivities were not as high as  $\text{IrO}_x$ . Nano-copper oxide ( $\text{CuO}$ ) [75], cobalt oxide ( $\text{Co}_3\text{O}_4$ ) [76], tungsten oxide ( $\text{WO}_3$ ) [77] were synthesized by hydro-thermal growth and their pH sensitivities were 28, 58.5, and 56.7 mV/pH, respectively. Sputtered ruthenium oxide ( $\text{RuO}_2$ ) sensors were reported with a sensitivity of about 69 mV/pH [78]. However, the explanation for this phenomenon of super-Nernstian response was not given.

A super-Nernstian response of 84 mV/pH was achieved with  $\beta$ -phase lead dioxide nanoparticles (NPs) deposited electrochemically [79]. The pH sensing range of this sensor was from 0.12 to 13, which is the widest in recent publications. The superior response was attributed to the multiple oxidation states of lead oxide ( $\text{PbO}_x$ ), which was similar to the electrochemically deposited  $\text{IrO}_x$ . In addition, palladium(II) oxide ( $\text{PdO}$ ) generated from solution-processed palladium (Pd) precursor was tested and a pH sensitivity around 65 mV/pH was obtained [80]. Also, because this sensor was prepared at a low temperature (200 °C), it could potentially be integrated with polymeric substrates to reduce the cost of the pH sensors [81].

In addition to metal oxides, many conductive polymers (CPs) were also used as potentiometric electrodes. Their pH sensitivity is attributed to their acidic and/or basic functional groups, which can be protonated or deprotonated at different pH levels [82]. Deprotonation of CPs results in a decrease of charge carrier density along the polymer chains, which alters the materials' redox, electrical and optical properties. Two widely studied CPs are polyaniline (PANI) and polypyrrole (PPY). The amino groups in their polymer chains have affinity towards  $\text{H}_3\text{O}^+$ . Hence, PANI and PPY thin films can be considered as  $\text{H}_3\text{O}^+$  permeable membrane and a Nernstian response was observed in pH buffers [83]–[85]. Another contributor to the Nernstian response of CP-based pH sensors is the redox equilibrium, similar to metal oxide-based sensors.

PANI electrodes prepared by electropolymerization showed a slight super-Nernstian response (62.4 mV/pH) in the pH range of 2 to 9 [84]. Due to the reliable near-Nernstian performance and fast response time <25 s in the physiological pH range (3 to 8), PANI-based wearable sensors were used to measure the pH values of bio-fluids [86], [87]. Compared to PANI-based sensors, PPY was tested in a wider pH range of 2 to 12, but a lower sensitivity (~50 mV/pH) was measured [83], [85], [88]. Such sensors were shown to be stable over 30 days.

Considering other organic materials, parylene-C normally used as an insulating material, also displayed a pH sensitivity of 16.3 mV/pH between pH of 4 and 10 [89]. Although the sensitivity of parylene-C was low, its process compatibility with existing microelectronics fabrication technologies makes it suitable for low-cost applications. Carbon nanotubes (CNTs) were also evaluated as a pH sensitive material with a Nernstian response [90].  $\text{H}_3\text{O}^+$  and hydroxide ion ( $\text{OH}^-$ ) can dope CNT walls by behaving as electron acceptors and donors [91]. Thus, the Fermi level of CNTs changes with the pH value, leading to a change in the measured open-circuit potential.

## 1.2.2. ISFET

### 1.2.2.1. Sensor configuration and sensing mechanism: ISFET

The ISFET was described by Bergveld in 1970. Its configuration was a metal-oxide-semiconductor field-effect transistor (MOSFET) with the gate separated from the chip by the solution to be monitored. The gate metal was replaced by a reference electrode and the dielectric layer is normally critical to the sensing performance (Figure 1-3) [59], [92], [93].

Based on the simple theory of MOSFET, the drain current ( $I_D$ ) of the ISFET in the linear regime is given by [59], [94]:

$$I_D = C_{ox} \mu \frac{W_c}{L_c} \left[ (V_{GS} - V_{TH}) V_{DS} - \frac{1}{2} V_{DS}^2 \right], \quad (1.8)$$

where  $C_{OX}$  is the gate dielectric capacitance per unit area;  $\mu$  is the charge carrier mobility;  $W_c$  and  $L_c$  are the transistor's channel width and length, respectively;  $V_{GS}$  is the potential difference between gate and source electrode; and  $V_{TH}$  is the threshold voltage of the transistor. The threshold voltage can be further expressed as [59], [94]:

$$V_{TH} = E_{ref} - \Psi + \chi^{sol} - \frac{\phi_{SC}}{q} - \frac{Q_{OX} + Q_{SS} + Q_B}{C_{OX}} + 2\phi_f, \quad (1.9)$$

where  $E_{ref}$  is the potential of reference electrode;  $\Psi$  is the surface potential at the dielectric-electrolyte interface, which results from a chemical reaction (usually governed by the dissociation of oxide surface groups) and is a function of pH;  $\chi^{sol}$  is the surface dipole potential of the solution;  $\phi_{SC}$  is the work function of semiconductor;  $q$  is the elementary charge;  $Q_{OX}$  is the accumulated charge per unit area in the dielectric;  $Q_{SS}$  is the accumulated charge per unit area at the dielectric-semiconductor interface;  $Q_B$  is the depletion charge per unit area in the semiconductor; and  $\phi_f$  is the Fermi voltage.

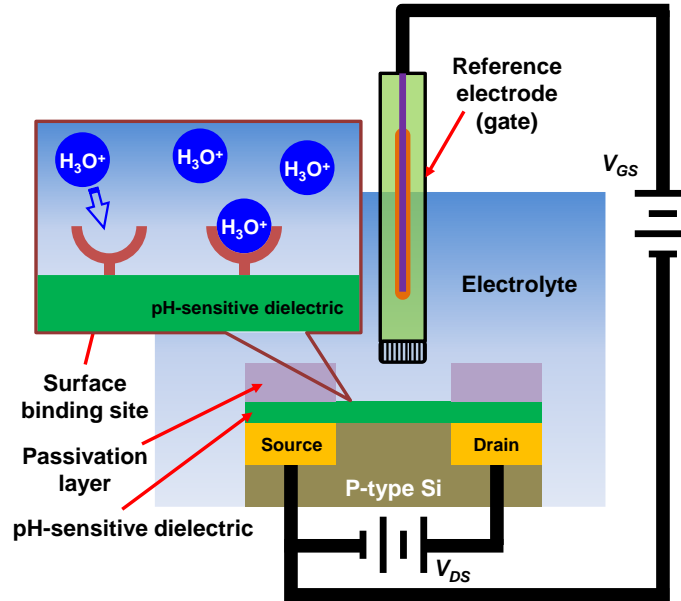


**Figure 1-3.** Schematic of an ISFET-based pH sensor and its sensing mechanism.

From equation (1.8) and (1.9), one can see that the electrolyte-insulator-semiconductor (EIS) structure determines the threshold voltage and consequently the current-voltage behavior of the ISFET. A theory from site-dissociation and double-layer models was developed to express the surface potential ( $\Psi$ ) [59], [94]:

$$\Psi = 2.3 \frac{kT}{q} \frac{\beta}{\beta + 1} (\text{pH}_{pzc} - \text{pH}), \quad (1.10)$$

where  $k$  is the Boltzmann's constant;  $T$  is the absolute temperature;  $\beta$  is the acidic and basic equilibrium constants of the related surface reactions;  $\text{pH}_{pzc}$  is the pH value for which the dielectric surface is electrically neutral. Among these parameters,  $\beta$  represents the capability of chemical sensing of the oxide or dielectric. If  $\beta$  is large enough, we can assume  $\beta/(\beta+1) = 1$ . In this case, at 25 °C, the change of 1 pH unit will result in the change of surface potential of 59.16 mV (also known as Nernstian-response). In terms of pH sensors,  $\beta$  is related to the surface binding sites for  $\text{H}_3\text{O}^+$  (such as -OH groups) and is defined as [95]:

$$\beta = \frac{2q^2 N_s (K_b / K_a)^{1/2}}{kTC_{DL}}, \quad (1.11)$$

where  $N_s$  is the total number of surface binding sites per unit area;  $K_a$  and  $K_b$  are the equilibrium constants of acid and base points, respectively;  $C_{DL}$  is the double-layer capacitance at the dielectric-electrolyte interface derived from the Gouy-Chapman-Stern model. As a result, if a gate dielectric has a significant amount of surface binding sites for  $\text{H}_3\text{O}^+$ , then the surface potential of the dielectric can be shifted by a measurable amplitude. For ISFETs, the variation of threshold voltage or drain current can be recorded to determine the pH variation. Furthermore, the thin-film-transistor-based ISFET follows the same relation between surface potential and solution pH.

### 1.2.2.2. Applicable materials and sensor performance: ISFET

The sensing material in an ISFET should have extensive surface binding sites for  $\text{H}_3\text{O}^+$ . Most ISFETs, or EIS devices, were fabricated on doped Si substrates. The insulation materials functioning as the pH-sensitive layer include metal oxides and semiconductor-based ceramics. Titanium oxide ( $\text{TiO}_2$ ) has been used in both EIS structures and ISFETs. The pH sensitivity of sputtered  $\text{TiO}_2$  film was ~57 mV/pH [96], [97], while the sensitivity was ~63 mV/pH for the  $\text{TiO}_2$  film prepared by metal-organic chemical vapor deposition (MOCVD) [98]. The sensitivity of  $\text{TiO}_2$  is attributed to the hydrogen bonds formed at the

oxide surface acting as binding sites. However, the formation of titanium hydroxide introduces large hysteresis during measurements. In addition, to get a densely-packed TiO<sub>2</sub> layer, high-temperature annealing is required (normally above 500 °C).

Another attractive material for pH sensing is tantalum pentoxide (Ta<sub>2</sub>O<sub>5</sub>). A near-Nernstian response of about 57 mV/pH was obtained for this material prepared by MOCVD [99] or thermal oxidation [100]. The challenge of using Ta<sub>2</sub>O<sub>5</sub> is to avoid exposure to light. This is because light can generate charge carriers in Ta<sub>2</sub>O<sub>5</sub> and result in drift of the output signals. Other materials such as zinc oxide (ZnO) [101], hafnium oxide (HfO<sub>2</sub>) [102], gadolinium oxide (Gd<sub>2</sub>O<sub>3</sub>) [103], titanium (Ti)-based binary oxides [104], aluminum-gallium-nitride/gallium nitride (AlGaN/GaN) [105], and semiconductor nanowires [106], [107] were used and they demonstrated a sub-Nernstian or near-Nernstian pH responses.

Low-temperature (normally below 300 °C) deposition of the pH sensing layer is attractive for sensor development on a polymeric substrate due to their low glass transition temperatures. Solution-processed aluminum oxide (Al<sub>2</sub>O<sub>3</sub>) was spin coated onto graphene and annealed at 250 °C, offering a pH sensitivity of 36.8 mV/pH in the pH range of 3 to 10 [108]. Ta<sub>2</sub>O<sub>5</sub> layer was deposited onto graphene using atomic layer deposition (ALD) at low temperatures [109]. The pH sensing range of the graphene-based sensor is between 3 and 8 with a sensitivity of 55 mV/pH.

Besides inorganic materials, organic semiconductors were also used for the channel in an ISFET. Poly(3-hexylthiophene) (P3HT) and pentacene were also used in ISFET-based pH sensors [110]–[113]. They can be integrated not only with metal oxide sensing layers, but also with organic thin films having hydrogen ionophores or H<sub>3</sub>O<sup>+</sup> binding sites. Polytriarylamine (PTAA) has superior electrical stability to other organic semiconductors. It was coated with the insulating material Al<sub>2</sub>O<sub>3</sub> and polyisobutylmethacrylate-Teflon as a bilayer [114], [115]. Depending on the insulating material, the pH sensitivity varied from 33 mV/pH (Al<sub>2</sub>O<sub>3</sub>) to over 60 mV/pH (polyisobutylmethacrylate-Teflon). Importantly,

PTAA enabled the stable operation of such sensors for >5000 cycles of measurement [115]. Due to the low mobility of charges in organic semiconductors, the operation voltage of these sensors are higher (normally tens of volts) than that of Si-based ones.

### 1.2.2.3. Sensor configuration and sensing mechanism: ExGFET

The extended-gate field-effect transistor (ExGFET), invented in 1983, is a modified version of the ISFET [116]. An ExGFET is a MOSFET or thin film transistor with an extended gate electrode, in which a large part of the extended gate is away from the active area of the transistor, as shown in Figure 1-4.

During sensing, only the extended-gate is in the solution while the other parts stay dry. Due to its structure, the ExGFETs have several advantages over traditional ISFETs [117]:

- Lower cost since the pH sensing electrodes can be connected to the gate of commercial MOSFETs (users do not have to fabricate their own transistors).
- Easier packaging because the whole ExGFET is physically connected (without solution between gate and dielectric).
- Better stability since the major part of the sensor can be used in a dry environment.

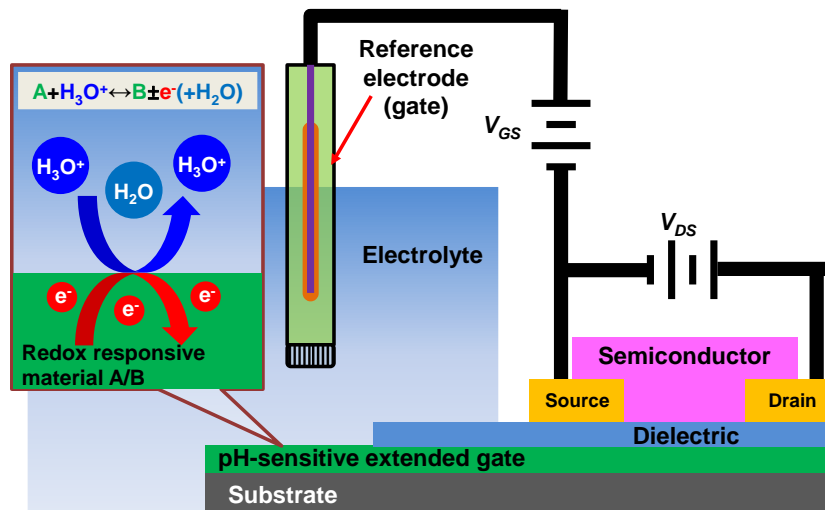


**Figure 1-4.** Schematic of an ExGFET-based pH sensor and its sensing mechanism.

The major difference between ISFETs and ExGFETs is the impedance of the sensing films [118]. In an ISFET, the sensing layer is the gate dielectric, which has to be defect-free and

of high-impedance. The sensing membrane in an ExGFET has to be low-impedance and  $\text{H}_3\text{O}^+$  changes the potential at the gate. The effective threshold voltage of an ExGFET when performing sensing can be written as [119]:

$$V_{TH,ExG} = V_{TH} + E_{ref} - \Psi + \chi^{sol} - \frac{\phi_M}{q}, \quad (1.12)$$

where  $V_{TH}$  is the threshold voltage of the ExGFET when not performing sensing;  $\Psi$  is the surface potential at the electrolyte-gate interface, which is a function of pH; and  $\phi_M$  is the work function of gate metal. Since the pH-surface potential relation for ExGFETs is identical to that for ISFETs, then different pH values will result in different threshold voltages and drain currents.

#### 1.2.2.4. Applicable materials and sensor performance: ExGFET

In case of ExGFET, low-impedance sensing layers have to be used. In contrast to insulating  $\text{TiO}_2$  films in ISFETs, semiconductive  $\text{TiO}_2$  nanostructures were used in ExGFETs.  $\text{TiO}_2$  NPs deposited by sol-gel methods exhibited pH responses between 50 and 61 mV/pH in the pH range between 1 and 11 [119]–[121]. However, significant hysteresis and drift were observed, which might be due to the nanoporous nature of the sensing films made from NPs. Furthermore, such sensing films require high temperature ( $>500$  °C) annealing as a post-treatment to achieve optimized performance.

To address the issue of high-temperature processing, hydrothermal growth of  $\text{TiO}_2$  nanowires [122] and nanorods [123] were performed at 150 °C. However, the processing time with this approach is much longer than that of other growth methods. Similarly,  $\text{ZnO}$  nanowalls [117] and nanowires [124] prepared by chemical bathing and ALD, respectively, were sensitive to pH change. But their response was poorer than  $\text{TiO}_2$ . Other metal oxides that were used in an ExGFET-based pH sensor include niobium pentoxide [125],  $\text{PdO}$  [126], and tin oxide [127]. They were less widely studied due to either their relatively poor sensing performance, or the requirement for extreme fabrication conditions such as the use of high temperatures.

Organic-inorganic hybrid materials were studied to utilize the benefits from both types of materials. For instance, CNTs were used with indium oxide in a bilayer and core-shell configurations [128], [129]. CNTs and nickel have been plated together to form CNT-nickel oxide composite structure [130]. The metal oxides normally behave as the  $\text{H}_3\text{O}^+$  binder and CNTs are employed to regulate the conductivity of the film. Although these composite materials did not perform as well as metal oxides, the ease in adjusting material properties by varying processing steps and parameters are important advantages.

Pure organic materials are less frequently reported as the sensing component in an ExGFET. Parylene-C, one of the few examples, was treated with  $\text{O}_2$  plasma to generate surface functional groups for  $\text{H}_3\text{O}^+$  binding [131]. The resulting pH sensitivity of 23 mV/pH in the pH range of 4 to 10 was relatively low. This poor performance left room for more research work in this area.

### **1.2.3. Chemoresistor and chemotransistor**

#### **1.2.3.1. Sensor configuration and sensing mechanism: Chemoresistor**

A chemoresistor-based pH sensor is a two-terminal device with the pH sensitive material deposited between two electrodes (Figure 1-5). The sensing material has an intrinsic electrical resistance/conductance, which will change accordingly upon exposure to solutions with different pH values. The mechanisms for the change in resistance/conductance are the following [132]:

- The chemical reactions between  $\text{H}_3\text{O}^+$  or  $\text{OH}^-$  with the sensing material that generates new materials with different electrical properties.
- The  $\text{H}_3\text{O}^+$ -induced changes in the charge depletion/accumulation layer in the semiconductive sensing material.

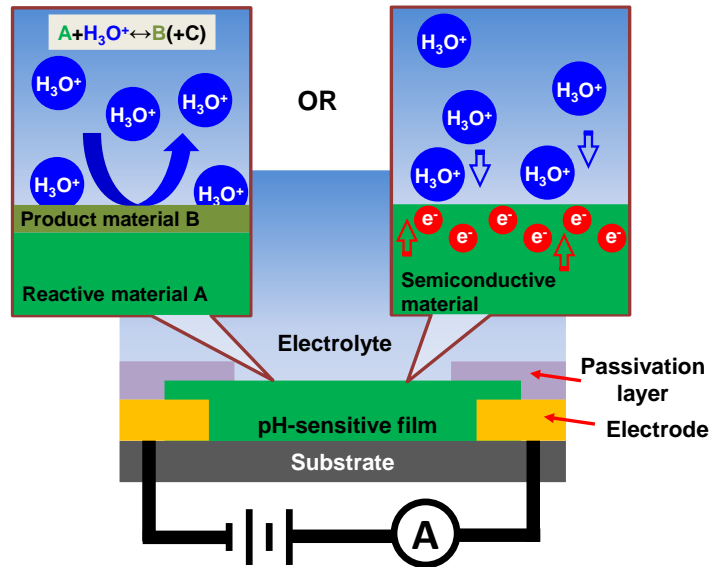


**Figure 1-5.** Schematic of a pH sensor in chemoresistor structure and its possible sensing mechanisms.

The chemoresistor has a simple physical structure and it does not require a reference electrode. These two features are preferred for miniaturization of the sensor.

### 1.2.3.2. Applicable materials and sensor performance: Chemoresistor

For chemoresistors,  $TiO_2$  nanowires have been synthesized at the surface of Ti/Carbon nanofibers by electrospinning and hydrothermal growth [133]. The high-concentration  $H_3O^+$  in the solution reduces the depletion layer at the surface of n-type  $TiO_2$  nanowires, thus increasing the electrical conductivity of the material. In the pH range between 2 and 12, such a sensor showed a response of 5.7 nS/pH. On the other hand, Pd is known as a hydrogen storage material owing to the formation of hydride of Pd, which possesses an electrical resistivity 1.3 to 2 times higher than Pd [134]. Based on the resistivity change, Lee et al. used standard photolithography processes were used to fabricate Pd resistors and gold (Au) electrodes [134]. Hydrogen gas generated during electrolysis was sensed by the Pd resistor and its resistance was proportional to the concentration of  $H_3O^+$  in the solution (higher concentration generated more hydrogen gas). A change of 1 unit pH caused the Pd resistance to vary 5% from its initial value.

Graphene and CNTs were also studied in chemoresistors [132], [135]. Their pH sensing mechanism can be attributed to the adsorption of  $\text{H}_3\text{O}^+$  and  $\text{OH}^-$  at their surface sites. The adsorbed ions make the carbon nanomaterials doped or de-doped, resulting in the variation of resistance. Annealed graphene had a pH sensitivity of  $2000 \text{ } \Omega/\text{pH}$  between pH of 4 and 10, while the value was  $65 \text{ } \Omega/\text{pH}$  in the pH range from 5 to 9 for multi-wall CNTs. Note that it is more meaningful to compare the response using resistivity rather than resistance. However, the resistivity values were not reported in these articles.

### **1.2.3.3. Sensor configuration and sensing mechanism: ECT**

Sometimes, the pH sensing material is not easily affected by the  $\text{H}_3\text{O}^+$ , so sensitivity is low. Therefore, an extra electrode can be incorporated into the chemoresistor to form a chemotransistor. The extra electrode is the gate of the chemotransistor and its function is to modulate the output current [136]. If the gate electrode is separated from the transistor and placed in the solution, then the device could be an electrochemical transistor (ECT, Figure 1-6).

In contrast to an ISFET, there is no oxide/dielectric layer between the semiconductor and solution [137]. The conductivity of the channel is controlled by the electrochemical doping/de-doping process at the semiconductor-solution interface. The doping/de-doping process comprises reversible transportation of mobile ions into/out of the semiconductor. Also, the channel can be switched between different doping levels by the gate bias [138]. Organic semiconductors are the preferred materials in ECTs because the modification of their electrical properties is relative easier when compared to inorganic ones. When there is no gate voltage applied, the output current is determined by the intrinsic conductance of the organic semiconductor (assume it is p-type) [139]. If the gate voltage is positive, the  $\text{H}_3\text{O}^+$  (can be other cations) in the solution will be pushed into the semiconductor by the electrical field to dope the material, which increases the charge carrier density in the channel. Thus, the output current will increase. However, reversibility of the sensor is poor, which is attributed to the electrochemical-process-induced material degradation.

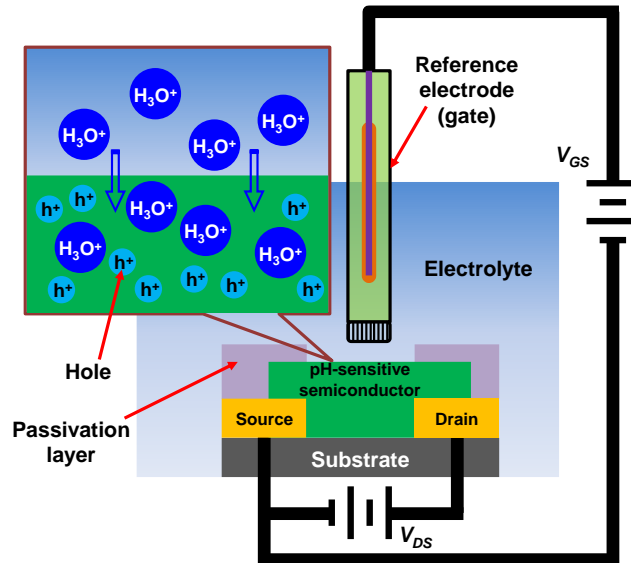


Figure 1-6. Schematic of an ECT-based pH sensor and its sensing mechanism.

#### 1.2.3.4. Applicable materials and sensor performance: ECT

ECT-based pH sensors generally use organic materials as the channel and sensing layer. The influence of  $H_3O^+$  on charge transport in the P3HT channel in an ECT was observed. The output current had a 10 nA/pH response when the pH was varied between 4 and 10 [140]. However, due to the electrochemical reaction of the sensing material, the lifetime of this ECT-based sensor was short, around 12 hours. To improve the lifetime of the sensor by reducing material degradation and delamination, AC measurement can be used.

Poly(3,4-ethylenedioxythiophene) doped with poly(styrenesulfonate) (PEDOT:PSS) is a conductive polymer whose conductivity can be tuned by the extra doping of  $H_3O^+$  [141]. The injection of  $H_3O^+$  could turn highly conductive PEDOT<sup>+</sup> into less conductive PEDOT<sup>0</sup>. Thus, in order to get the identical output current, the effective gate voltage had to be increased. A pH sensitivity of 64.2 mV/pH was realized. Since reliability is of great concern for ECT-based sensors, Single-walled CNTs were oxidized and functionalized with poly(1-aminoanthracene) (PAA) to prepare the pH sensing material [58]. The response of the sensor was 73 mS/pH and demonstrated a wide pH sensing range between pH of 2 and 12. Also, very importantly, this sensor had a long lifetime of over 120 days.

### 1.2.3.5. Sensor configuration and sensing mechanism: EGFET

An electrolyte-gated field-effect transistor (EGFET) has the identical physical structure as an ECT. It consists of the semiconductor which does not react with the solution. Instead, an electrical double layer (EDL, or Debye Helmholtz double layer) at the electrolyte-semiconductor interface is formed [139], [142]. In a p-channel EGFET (Figure 1-7), if the gate voltage is negative, the anions in the solution migrate to the semiconductor-solution interface while the cations travel to the solution-gate interface, resulting in the formation of EDLs. According to the Gouy-Chapman-Stern model, the EDL consists of excess electrons (or holes) along the metal gate (semiconductor) surface, and a layer of cations (anions) at the electrolyte side. The cations (anions) layer is composed of two layers, the compact layer (or Helmholtz layer, HL) and the diffusion layer [143]. Because ions are solvated in the solution, the HL is composed of a single layer of solvent molecules and a single layer of solvated ions [144]. The diffusion layer consists of free cations (anions) driven by the electrostatic interaction and thermal motion. The concentration of cations (anions) decreases with the distance from the gate (semiconductor). The electrical potential drops at the gate (semiconductor)-solution interface in the EDLs, which is an analogue of a capacitor. The capacitance of the EDL ( $C_{DL}$ ) can be expressed as [143]:

$$\frac{1}{C_{DL}} = \frac{x_{HL}}{\varepsilon} + \frac{1}{\left(\frac{2\varepsilon n^2 e^2 \alpha}{kT}\right)^{\frac{1}{2}} \cosh\left(\frac{zq\phi_{HD}}{2kT}\right)}. \quad (1.13)$$

In equation (1.13),  $x_{HL}$  is the thickness of the HL,  $\varepsilon$  is the permittivity of the HL,  $\alpha$  is the ion concentration in the bulk solution,  $z$  is the charge of the ion, and  $\phi_{HD}$  is the electrical potential at the HL-diffusion layer interface, which is also the plane having a distance  $x_{HL}$  to the gate (semiconductor). This distance  $x_{HL}$  is also a function of the ion concentration in the bulk solution:

$$x_{HL} = \frac{3.3 \times 10^6 \varepsilon}{z\alpha^{\frac{1}{2}}}. \quad (1.14)$$

Because the thickness of the EDL is extremely small (typically less than 0.1 Å in metals and 10 Å in solutions), the capacitance can be as high as a few to hundreds of  $\mu\text{F}/\text{cm}^2$

(typical values are between  $10 \mu\text{F}/\text{cm}^2$  and  $500 \mu\text{F}/\text{cm}^2$ , compared to  $10 \text{nF}/\text{cm}^2$  for 300 nm thick silicon dioxide) [139], which enables low operation voltage of the transistor. The pH sensitivity is determined by the gate capacitance as a function of  $\text{H}_3\text{O}^+$  concentration. When pH increases,  $\alpha$  decreases,  $x$  increases,  $C_d$  decreases, and the output current decreases. The disadvantages of EGFET-based sensors include their long response time due to the construction of the EDL, the difficulty in sensing highly acidic solutions (such as  $\text{pH} = 1$ ), as well as the poor selectivity of ions.

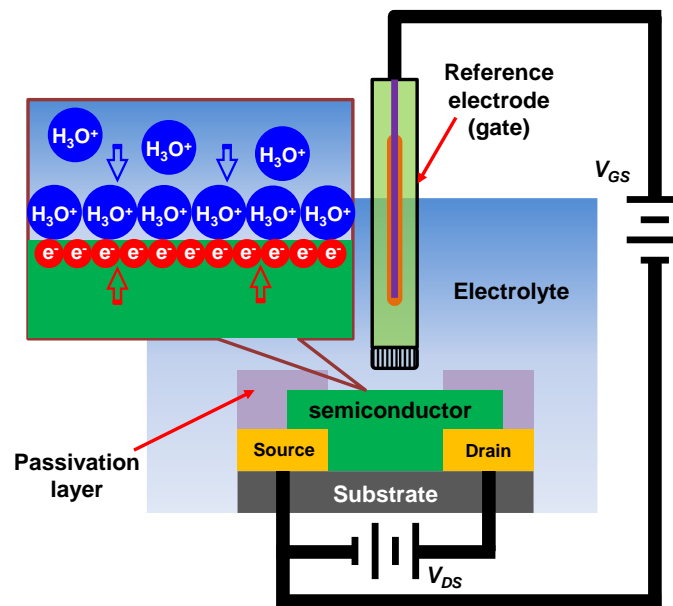


**Figure 1-7.** Schematic of an EGFET-based pH sensor and its sensing mechanism.

### 1.2.3.6. Applicable materials and sensor performance: EGFET

Using an EGFET, a pH response was observed in the output current when the solution pH is between 7 and 9 [145]. In such a device, ZnO nanowires were decorated by Pd or Au NPs, which induced quasi-spherical charge depletion regions in the 1D (nanowire) transport channel. However, important performance parameters such as sensitivity were not reported. Graphene, CNTs, and P3HT, deposited by low-temperature technologies were characterized in EGFET-based pH sensors [146]–[148]. They displayed low sensitivities around  $28 \text{ mV}/\text{pH}$ , which may be due to the instability of the materials in an aqueous environment. However, a few-layer graphene film was grown at  $1100 \text{ }^\circ\text{C}$  and mounted to an EGFET as the sensing layer [149]. A sensitivity of about  $100 \text{ mV}/\text{pH}$  was achieved in

the pH range from 2 to 12. This high sensitivity indicated the combined effect of surface potential modulation and ion adsorption.

### 1.2.3.7. Sensor configuration and sensing mechanism: FET

The ECT- and EGFET-based sensors discussed above are not preferred for miniaturized devices due to the floating gate. An alternative way to reduce the dimensions of the device is to fabricate the gate beneath the semiconductor and dielectric, the same as a bottom-gate thin-film transistor (Figure 1-8) [136]. In such FET-based sensor, the sensing mechanisms include [136]:

- The direct interaction between the semiconductor and ions (for example, charge transfer and doping/de-doping can alter the conductivity of the semiconductor).
- The adsorption and diffusion of ions along the grain boundaries in the semiconductor, which may create deep-energy traps and increase the resistance of inter-grain charge transport.
- The local screening of the electrical field, due to the accumulation of ions at the semiconductor-solution interface.

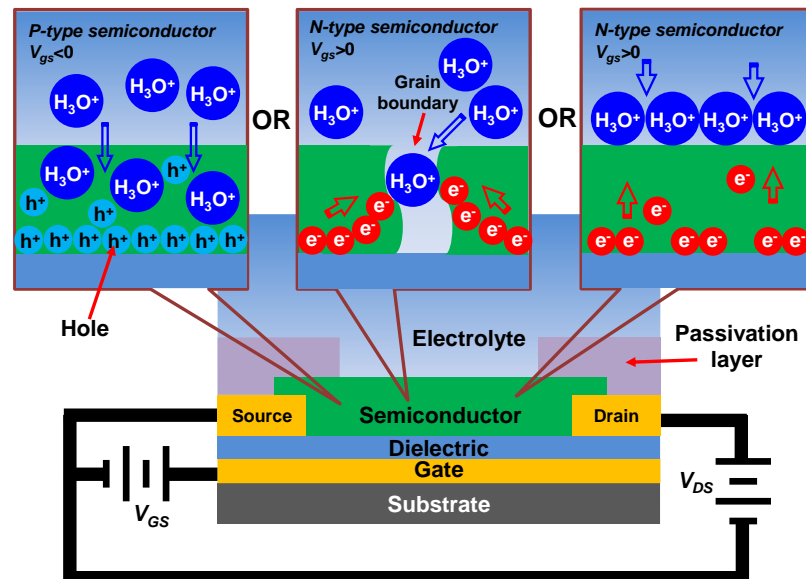


Figure 1-8. Schematic of a pH sensor in FET structure and its possible sensing mechanisms.

During operation, the gate bias and the source-drain bias are set to generate a current flow through the channel [150]. The presence of  $\text{H}_3\text{O}^+$  adsorption or interaction is subsequently transduced to a change in the source-drain current. To make the sensing process reversible, an opposite polarity bias can be applied to the gate to desorb the weakly bonded ions [151]. The challenges for FET-based sensors are the high operating voltage, the drift of output current induced by gate-bias stress, and the stability of the sensing material in an aqueous environment [152]–[154].

#### **1.2.3.8. Applicable materials and sensor performance: FET**

For FET-based sensors, a dual-gate transistor with Si nanowires as the channel on a silicon-on-insulator platform was introduced [155]. These sensors had a sensitivity of 68 mV/pH, but the drift rate of 27 mV/h made it unsuitable for long-term monitoring. Instead, some organic materials with a high stability in water were developed [153], [156]. For example, 5,5-bis-(7-dodecyl-9H-fluoren-2-yl)-2,2-bithiophene was synthesized as a p-type semiconductor that could trap diffused  $\text{H}_3\text{O}^+$  in the grain boundaries [156]. The output current of the FET responded to the change of pH value at 50 nA/pH over  $10^4$  measurement cycles.

#### **1.2.4. Research challenges**

Although many microfabricated electrochemical pH sensors have been reported, several challenges remain. One challenge is related to the performance of the sensors. For sensors with sub-Nernstian response, studies should focus on improving sensitivity. Many sensors exhibited near-Nernstian or super-Nernstian response. For these sensors, their stability and repeatability were the major concern. The instability and poor repeatability in long-term use most likely originate from the following phenomena:

- **Degradation of sensing materials.**

The degradation can be either physical or chemical. Physical degradation indicates that the sensing material at the sensor surface mechanically leaves the substrate and enters the

solution. This is likely to happen in a pH sensor in an online water quality monitoring system since the flow rate of water is typically fast and it can physically impact the sensor surface. This physical process influences the sensitivity by exposing the underlying material which may not be as sensitive as the surface material. Also, the surface of the sensing area may become rougher and result in a longer response time. Moreover, voids and pinholes may be generated in the sensing film, reducing the mechanical stability and reliability of the sensor.

Chemical degradation happens when irreversible reactions happen between the sensing material and  $\text{H}_3\text{O}^+$ , or when the redox reaction is not fully reversible. In water quality monitoring systems, treated water contains residual chlorine, which is a strong oxidizing reagent for many organic materials. These reactions alter the chemical composition of the sensing material which affects sensitivity, and also may introduce slow-reaction sites which results in increased hysteresis. Both physical and chemical degradation can result in increases in the drift rate of the sensor since the properties of the sensor surface keep changing with time. Thus, new sensing materials with better physical and chemical stability (except for the reversible reactions with  $\text{H}_3\text{O}^+$ ) have to be developed.

- **Interference from the test solution**

The interference can originate from the adsorption of other ions or from bio-fouling. pH sensors based on ISFETs, ECTs, EGFETs, and FETs are more prone to alkaline ions since they can be adsorbed on pH sensing surfaces. The interfering ions introduce an electrical field to the channel of the transistor, thus affecting its output electrical characteristics. Bio-fouling commonly happens in water quality monitoring devices. The fouling layer may deteriorate the functionality of sensors by blocking the redox reaction between the sensing material and  $\text{H}_3\text{O}^+$ , or by preventing the adsorption of  $\text{H}_3\text{O}^+$  onto the sensor surface. To reduce interference from the solution, an ion-selective membrane and an anti-fouling coating should be applied to the surface of the sensors.

- **Instability of the electronic components**

This mostly happens in pH sensors using transistor configurations with organic semiconductors. The electrical properties of organic semiconductors change with time, which is less stable than conventionally used silicon. As a consequence of the non-predictable behavior of the organic semiconductor, the repeatability of the pH sensor will be poor. Therefore, more research in the area of organic electronics is needed to obtain stable and reliable device performance using improved organic materials.

Another challenge is related to the microfabrication technologies. The cost of the sensors for drinking water quality monitoring should not be high. This requires the fabrication to be cheap and use small amount of materials. Also, process conditions at high temperatures and in vacuum environment should be avoided. Solution-based low-cost and large-area processing is potentially promising, but the quality of deposited materials is problematic (usually high-temperature treatment should be done after solution processing for a high-performance sensor). Therefore, there is a trade-off between performance and cost of sensors. High-quality sensing materials that can be deposited using cost-effective ways are desired.

Microfabricated pH sensors based on potentiometric electrodes, ISFETs, and chemoresistors/chemotransistors have been reviewed in terms of their physical configurations and sensing mechanisms. The physical structures of the pH sensors are determined by the electrical properties (such as conductivity) and chemical features (such as solubility in water and chemical reactivity) of the sensing materials. The widely studied sensing materials include metal oxides, ceramics, polymers, and carbon nanomaterials. The sensing performance of microfabricated electrochemical pH sensors varies a lot (for example, from sub-Nernstian response to super-Nernstian response). This variation could be attributed to the intrinsic properties of the materials and their properties after processing. Therefore, the physical design, material selection, and microfabrication conditions are three key factors in the quest for low-cost, highly sensitive, efficient, and easy-to-use pH sensors.

**Table 1-1.** Comparison of glass pH electrodes and different types of microfabricated electrochemical pH sensors.

		Advantages	Disadvantages
Glass electrode		<ol style="list-style-type: none"> <li>1. Wide application temperature (from <math>&lt;0^{\circ}\text{C}</math> to <math>&gt;100^{\circ}\text{C}</math>)</li> <li>2. Ideal Nernstian response independent of redox interferences</li> <li>3. High accuracy and resolution (0.001 pH unit)</li> <li>4. High stability and long lifetime (several years)</li> </ol>	<ol style="list-style-type: none"> <li>1. Unstable in strong alkaline and hydrofluoric acid solutions</li> <li>2. Large in size</li> <li>3. Brittle</li> <li>4. Require frequent maintenance and calibration</li> <li>5. Expensive</li> </ol>
Microfabricated electrochemical pH sensor	General	<ol style="list-style-type: none"> <li>1. Small size</li> <li>2. Easy for integration</li> <li>3. Can be stored in dry condition</li> <li>4. Low cost</li> <li>5. Less frequent maintenance</li> </ol>	<ol style="list-style-type: none"> <li>1. Low accuracy and resolution</li> <li>2. Large hysteresis and drift</li> <li>3. Poor ion selectivity</li> <li>4. Sometimes sensitive to light</li> <li>5. Limited application temperature</li> <li>6. Require water-stable sensing materials</li> </ol>
	Potentiometric electrode	<ol style="list-style-type: none"> <li>1. Simple structure</li> <li>2. Power supply not needed</li> </ol>	<ol style="list-style-type: none"> <li>1. Require reference electrode</li> <li>2. No internal signal amplification</li> </ol>
	ISFET	<ol style="list-style-type: none"> <li>1. Semiconductor protected by dielectric</li> <li>2. Compatible with complementary metal-oxide-semiconductor (CMOS) fabrication process</li> <li>3. Internal signal amplification</li> </ol>	<ol style="list-style-type: none"> <li>1. Require reference electrode</li> <li>2. Dielectric surface difficult to be functionalized for higher selectivity</li> </ol>
	ExGFET	<ol style="list-style-type: none"> <li>1. Transistor can be used in dry condition</li> <li>2. Compatible with CMOS fabrication process</li> <li>3. Internal signal amplification</li> </ol>	<ol style="list-style-type: none"> <li>1. Require reference electrode</li> <li>2. Larger size due to extended gate</li> </ol>
	Chemoresistor	<ol style="list-style-type: none"> <li>1. Simple structure</li> <li>2. Reference electrode not needed</li> </ol>	<ol style="list-style-type: none"> <li>1. Low reversibility</li> <li>2. Poor selectivity</li> <li>3. Lower sensitivity comparing to ECT</li> <li>4. No internal signal amplification</li> </ol>
	ECT	<ol style="list-style-type: none"> <li>1. Dielectric not needed</li> <li>2. Low operation voltage</li> <li>3. Higher sensitivity comparing to chemoresistor</li> <li>4. Internal signal amplification</li> </ol>	<ol style="list-style-type: none"> <li>1. Require reference electrode</li> <li>2. Low reversibility</li> <li>3. Poor selectivity</li> <li>4. Difficult in integration</li> </ol>
	EGFET	<ol style="list-style-type: none"> <li>1. Dielectric not needed</li> <li>2. Low operation voltage</li> <li>3. Internal signal amplification</li> </ol>	<ol style="list-style-type: none"> <li>1. Require reference electrode</li> <li>2. Sensing is difficult in high-concentration electrolyte</li> <li>3. Low switching speed</li> <li>4. Poor selectivity</li> </ol>
	FET	<ol style="list-style-type: none"> <li>1. Compact structure</li> <li>2. Easy for integration</li> <li>3. Reference electrode not needed</li> <li>4. Internal signal amplification</li> </ol>	<ol style="list-style-type: none"> <li>1. Require water-stable semiconductors</li> <li>2. High operation voltage</li> <li>3. Large hysteresis</li> <li>4. Low reversibility</li> </ol>

The conventional glass pH electrode is compared with different types of microfabricated electrochemical pH sensors (Table 1-1). In Table A-1 (Appendix A), a listing of recent microfabricated electrochemical pH sensors is provided. The list includes sensor structures,

sensing materials, key performance parameters, and corresponding fabrication processes. It has been observed that the size and cost disadvantages of the glass electrodes stimulated research in microfabrication of different kinds of electrochemical pH sensors. However, further research is needed to develop new materials and microfabrication processes, as well as to optimize their compatibility for low-cost and high-performance pH sensors.

### **1.3. Microfabricated electrochemical free chlorine sensors**

As discussed in subsection 1.1.3, two most commonly used approaches for free chlorine detection are DPD-based colorimetric and amperometric-based electrochemical methods. However, their large footprint limits their applications in drinking water quality monitoring. A briefly review of the miniaturized free chlorine sensors was given in reference [11]. It focused on microwire-based amperometric sensors and interferometry sensors. In this subsection, electrochemical free chlorine sensors having planar structures are reviewed due to their potential of miniaturization and integration with microelectronic devices.

#### **1.3.1. Amperometric sensor configuration and sensing mechanism**

Amperometric sensing is based on the voltammetric sensing method, which requires three electrodes: working, counter, and reference, for precise measurement [67]. A time-dependent electrical potential is applied to the working electrode, while the current flowing between the working and counter electrodes is measured (Figure 1-9). The reference electrode is used to provide a fixed potential of the electrolyte. The potential sweep from a small to a large value can generate a current peak if the analyte is oxidized in that potential range. The creation of the peak is due to the oxidation of the analyte while the decline of the peak is because of the depletion of the analyte at the electrode surface. Conversely, when the potential sweeps from high to low, a reduction peak will be generated.

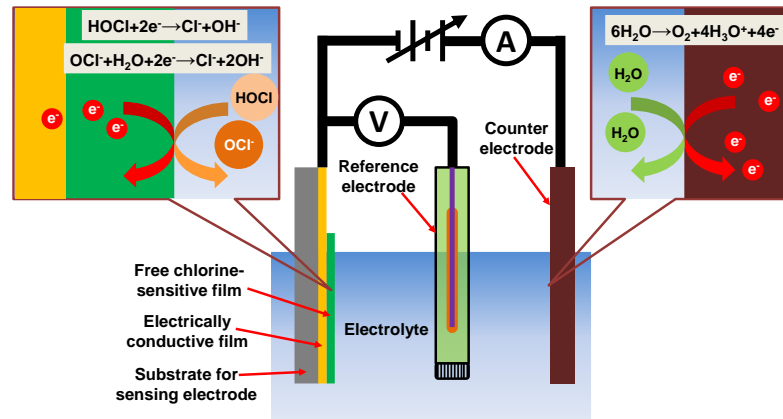
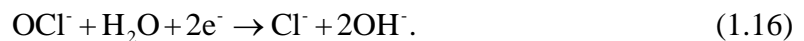


**Figure 1-9.** Schematic of an amperometric free chlorine sensor and its sensing mechanism.

In amperometric sensing, a constant potential is applied between the working and reference electrodes and the current is monitored between the working and counter electrodes [67]. The constant potential is determined based on the position of redox peaks in the corresponding voltammetric waveform. At the selected potential, the redox reaction of the analyte should take place, and the interference of other ions should be avoided. The amplitude of measured current is proportional to the analyte concentration in the solution.

In an amperometric free chlorine sensor, the working electrode is normally made of noble metals such as Au and Pt, and is sometimes coated with a selective membrane for hypochlorite ions. At the working electrode, free chlorine is electrochemically reduced by applying a constant potential versus the reference electrode [157]. For example, at pH = 5.5, the reduction peak of HOCl and/or OCl<sup>-</sup> was observed at +0.4 V on a Au electrode with respect to a Ag/AgCl reference electrode. The electrochemical reactions at the working electrode can be written as the following equations:



The transfer of electrons generates a current which is proportional to the free chlorine concentration. Note that the pH, temperature, flow rate and pressure of the solution must be carefully controlled for an accurate measurement.

### 1.3.2. Applicable materials and sensor performance

A limited range of electrode materials has been demonstrated to create miniaturized free chlorine sensors using microfabrication technologies. For example, Au working and counter electrodes were deposited by electron-beam evaporation on cyclic olefin copolymer, where the Ag/AgCl reference electrode was electrochemically deposited [158]. Both electrodes were capped by microfluidic channels through which the analyte flowed. This low-cost and disposable sensor was operated under 0.1 V bias, and had a linear detection range of  $\text{OCl}^-$  from 1.5 to 8 ppm. The current density in the counter electrode showed a sensitivity of about  $69 \mu\text{A}/\text{cm}^2/\text{ppm}$ . The lifetime of this sensor was about 100 s, which was longer than the signal stabilization time of 20 s. A stable free chlorine sensor using a similar structure and fabrication process was developed in another study [159]. The resulting sensitivity of  $0.23 \mu\text{A}/\text{ppm}$  in the concentration range of 0.2 to 5 ppm makes this sensor suitable for monitoring the free chlorine levels in swimming pools (lifetime >10 days, applied potential = 0.35 V). Moreover, a lower detection limit of 0.08 ppm were realized using 0.15 V applied potential on Au electrode [35]. The sensor maintained a stable sensitivity of 68.8 nA/ppm for over 7 days.

Pt electrodes were also used to detect free chlorine concentration and they showed similar performance to those with Au electrodes [34], [160]. The operation voltage of a Pt electrode is higher than that of a Au electrode because the reduction of free chlorine at a Pt electrode happens at a higher potential. Another reason for the higher potential is to minimize the overlap of  $\text{O}_2$  and hypochlorite reduction peaks, which is required for precise measurements [35].

For electrodes made of materials other than noble metals, carbon has been studied due to its chemical stability. Screen printed carbon electrode coated with potassium iodide exhibited a sensing range up to 20 ppm for free chlorine, with a sensitivity of  $0.2 \mu\text{A}/\text{ppm}$  [161]. The sensing mechanism was based on the reaction between chlorine and iodide ions, which produced tri-iodide ions that could be titrated using sodium thiosulphate.

Polymelamine has been electropolymerized onto carbon electrode to detect from 5.5  $\mu\text{M}$  to 7 mM free chlorine (sensitivity of 58  $\mu\text{A}/\text{mM}$ ) [16]. Such an electrode exhibited an enhanced reduction peak current, which was attributed to the reduction of the azo group (-N=N-) and then oxidized by free chlorine in a cyclic manner. Free chlorine concentration in swimming pool water and tap water was measured using the polymelamine/carbon-based sensors.

In another study, a boron-doped diamond electrode showed reduced fouling rates compared to carbon electrodes [162]. The free chlorine electrodes made of this material exhibited a lifetime over 3 months. Recently, benzethonium chloride was used in electrochemical deposition of Prussian Blue for a higher surface coverage on glassy carbon electrodes [163]. Free chlorine concentration between 9 ppb and 10 ppm could be detected in a short time (<5 s) with a sensitivity of 12  $\mu\text{A}/\text{cm}^2/\text{ppm}$ . This is believed to be the first publication reporting free chlorine measurement results for real water samples (tap water) using laboratory-fabricated sensors. This sensor demonstrated a measurement accuracy over 93%. Finally, ferrocene compounds were also electrochemically deposited on glassy carbon electrodes to measure the concentration of  $\text{ClO}^-$  [164]. However, their responses were not linear, making it difficult to be used in real sensing applications. Recently, CuO NPs were mixed with multi-wall CNTs in an epoxy matrix as an amperometric electrode for free chlorine measurement [165]. CuO NPs and CNTs increased the electrocatalytic active areas of the working electrode so that the electron transfer in the reduction of hypochlorite was promoted. In this study, a low detection limit of  $\sim 0.6$  ppb and high sensitivity of 446 nA/ppm was realized.

### 1.3.3. Research challenges

It can be noted that microfabricated electrochemical free chlorine sensors are not as well developed as pH sensors. The major challenge is the lack of reversible sensing materials for HOCl or  $\text{OCl}^-$ . A promising electrochemical sensing material should either react with free chlorine in a reversible manner, or selectively transport HOCl or  $\text{OCl}^-$  to the target

substrate. The chemical reagents used in optical detection techniques (such as DPD) can react with free chlorine, but the process is irreversible. While ion-selective transport membrane exists for many ions, very few were found for HOCl or OCl<sup>-</sup> due to their oxidizing nature. Therefore, developing advanced materials for free chlorine sensing is urgently needed.

The limitation in sensing material forces the utilization of amperometric electrodes for electrochemical sensing of free chlorine. Normally, cyclic voltammetry measurement has to be done first to determine the optimized voltage bias for amperometric measurement, which increases the difficulty in using the sensors. Moreover, dissolved O<sub>2</sub> is electroactive in the usual voltage range between +1 and -1 V for amperometric sensing of free chlorine. The interference from dissolved O<sub>2</sub> decreases the sensing accuracy. Finally, the requirement of a potentiostat for an amperometric sensor increases the complexity as well as the cost of the sensor. Hence, alternative sensor configurations are needed when a suitable sensing material is available. Once the above challenges are properly addressed, the concern for free chlorine sensors would become similar to those for pH sensors. Such concerns include the improvement of reliability and the reduction of fabrication costs.

The literature on electrochemical free chlorine sensors is limited. Within the limited scope, the amperometric sensors have been identified as the widely used structure for the electrochemical detection of free chlorine. The comparison between conventional electrochemical free chlorine sensor and microfabricated ones is given in Table 1-2.

**Table 1-2.** Comparison of conventional and microfabricated electrochemical free chlorine sensors.

	Advantages	Disadvantages
Conventional electrochemical free chlorine sensors	<ol style="list-style-type: none"> <li>1. Accurate</li> <li>2. Fast response</li> </ol>	<ol style="list-style-type: none"> <li>1. Interference from pH, pressure, flow rate, and temperature</li> <li>2. Large size and difficult in integration</li> </ol>
Microfabricated electrochemical free chlorine sensors	<ol style="list-style-type: none"> <li>1. Eliminate electrolyte replenishment</li> <li>2. Small</li> <li>3. Low-cost</li> <li>4. Easy integration with other sensors</li> </ol>	<ol style="list-style-type: none"> <li>1. Limited lifetime of coated membrane</li> <li>2. Low accuracy</li> </ol>

A list of microfabricated electrochemical free chlorine sensors are provided in Table A-2 (Appendix B) with their structures, electrode/sensing materials, key performance parameters, and corresponding fabrication processes. The comparison shows that more works were focused on the optimization of working electrodes than the development of active sensing materials. Although microfabricated free chlorine sensors can be developed for cost-effective applications, their sensitivity varies widely and they are less accurate and reliable than the conventional sensors. This indicates that the microfabricated electrochemical free chlorine sensor is a challenging area of research that requires further intensive investigations.

## 1.4. Research motivation

Although numerous research activities has been carried out to develop advanced pH and free chlorine sensors (subsection 1.2 and 1.3), very few of them were ready for field applications. This research is devoted to developing an integrated drinking water quality monitoring system that is capable for the on-demand measurement of the pH, free chlorine concentration, and temperature of water samples accurately and regularly. Such a drinking water quality monitoring system should be:

- **Highly accurate.** The system should consist of sensors that have high sensitivity, reversibility, stability, and selectivity.
- **Responding in real-time.** The sensors in the system should response fast towards target analyte so that the users can obtain the results on-site.
- **Easy-to-use.** The system should be designed for users who do not possess comprehensive technical training. Also, the output of the system should be easily understandable by the public.
- **Low-cost.** A low-cost system can be distributed over a wide geographical areas, and is affordable by individuals in underdeveloped regions.

To obtain the abovementioned goals, this research focuses on the development of microfabricated pH, free chlorine, and temperature sensors. The proposed specifications of

these sensors are listed in Table 1-3. For the pH sensor, we are targeting the sensitivity close to a commercial pH meter (59 mV/pH), which is required for a resolution of 0.1 pH. The sensor should be usable in the pH range for common water samples (e.g. drinking, recreation, and food processing water). The accuracy of  $\pm 0.1$  pH guarantees the distinguishing between qualified and unqualified water. For the free chlorine sensor, the sensing range should be wide enough for different water samples. When the sensor is used to monitor drinking water, its accuracy should be better than  $\pm 0.1$  ppm. Regarding the temperature sensor (used to compensate the pH and free chlorine sensing signals), the accuracy of  $\pm 2.5$  °C is required to ensure an accurate readout for the pH and free chlorine sensors. Besides, all three sensors should have a short response time, a small footprint, a stability around 1 month, a low cost, an application temperature between 0 to 40 °C, a simple storage condition, and a low maintenance frequency.

**Table 1-3.** Proposed specifications for pH, free chlorine, and temperature sensors.

Parameters	pH	Free chlorine	Temperature
Sensitivity	59 mV/pH	0.1 $\mu\text{A}/\text{cm}^2/\text{ppm}$	1 mV/°C
Resolution	0.1	0.1 ppm	1 °C
Sensing range	6 - 10	0 - 6 ppm	0 - 40 °C
Accuracy	$\pm 0.1$ pH	$\pm 0.1$ ppm	$\pm 2.5$ °C
Response time	<1 min		
Stability	~1 month		
Size	<1 cm <sup>3</sup>		
Cost <sup>a</sup>	<\$100	<\$100	<\$50
Storage condition	Dry or water		
Application temperature	0 to 40 °C		
Maintenance frequency	Once a month		
Easy-to-use?	Yes		

<sup>a</sup> Material and fabrication cost.

The design goals for the pH sensor are realized by using a simple two-electrode potentiometric configuration. The sensing electrode uses metal/metal oxide due to its wide sensing range, high sensitivity, and high stability. The reference electrode is a Ag/AgCl electrode that provides a stable reference voltage (insensitive to pH and other common ions). To fabricate the potentiometric sensor at a low cost, we aim to develop low-temperature, solution-based processes that do not rely on cleanroom environment and high-vacuum equipment. The sensors' temporal response, sensitivity, hysteresis, drift, temperature dependence, and selectivity are characterized.

The free chlorine sensor is implemented using either a chemoresistor configuration or an amperometric configuration. The chemoresistor-based free chlorine sensor uses a conductive polymer as the sensing material, attributed to its instability in a solution containing free chlorine. An easy-to-implement and cost-effective process is developed to fabricate the free chlorine sensor. The reusability, sensitivity, stability, and selectivity of the sensor is studied for its practical applications. In this research, we also explore the feasibility to simplify an amperometric free chlorine sensor developed by our group. The performance of the simplified sensor in the integrated drinking water quality monitoring system is studied.

The temperature sensor uses a Wheatstone bridge circuit to realize a high sensitivity. The thermistors in the circuit are fabricated using the same material combinations and similar fabrication technologies as the pH sensor. We focus on studying the effect of processing parameters on the electrical properties of the deposited materials. Physical, thermal, chemical, and electrical characterizations are carried out to study the electrical conduction mechanisms in the deposited films.

Finally, this research aims to demonstrate a fully integrated drinking water quality monitoring system using the three types of sensors. The integration process is developed to fabricate the sensors on a common substrate. An electronic system is designed and programmed to sample and process the sensor signals, followed by displaying the water quality parameters.

## **1.5. Research contributions**

The research work conducted in this thesis aims at developing an integrated, easy-to-use, accurate, and low-cost sensing system for drinking water quality monitoring. The major contributions of this work are summarized as follows:

- **The development of pH sensing electrodes using Pd/PdO.** A spin coating process and a low-temperature annealing process were developed and optimized to deposit Pd/PdO thin films. The chemical composition, film morphology, surface roughness of the films were characterized and correlated with their pH sensing properties. A linear pH response with sensitivity of  $\sim 64.71$  mV/pH was obtained for pH between 2 and 12.
- **Inkjet printing technologies were developed to deposit Pd, Ag, epoxy, sodium hypochlorite (NaOCl), poly(vinyl chloride) (PVC) inks for integrated pH sensors.** A two-step thermolysis process was developed to convert the printed Pd ink to continuous and uniform Pd films with good adhesion to different substrates. Using only one printing pass, a low electrical resistivity of  $2.6 \mu\Omega \cdot \text{m}$  of the Pd film was obtained. Accurate pH values of real water samples were obtained by using the printed sensors with a low-cost multimeter.
- **Temperature-sensitive Pd/PdO films were prepared by inkjet printing and thermolysis in a low-vacuum environment.** The film formation mechanism was studied via morphological, chemical, and thermogravimetric characterization. The TCR of the films can be adjusted from  $0.067\% / ^\circ\text{C}$  to  $-0.189\% / ^\circ\text{C}$  by tuning the amount of semiconductive PdO in the conduction path. Also, the humidity dependence of the printed films was studied.
- **A paper-based, hand-drawn, chemoresistor-type free chlorine sensor was developed using poly(3,4-ethylenedioxythiophene):poly(styrenesulfonate) (PEDOT:PSS).** The resistivity of PEDOT:PSS increased when it was exposed to free chlorine in water due to oxidation reactions. The fabrication steps were all at room temperature, required no instrumentation or equipment, and could be carried out by untrained personnel. The fabricated sensor was mechanically stable, reusable, had a wide sensing range, and could accurately measure free chlorine concentrations in real water samples.
- **A field-programmable gate array (FPGA)-based drinking water quality monitoring system was developed to sample, process, and display the signals from an integrated sensor.** The integrated sensor consisted of an inkjet-printed pH sensor,

an inkjet-printed temperature sensor, and a pencil-lead-based amperometric sensor on a common substrate. The temperature sensor was a Wheatstone bridge circuit including two PdO thermistors and two Ag thermistors. The sensitivity of the temperature sensor was  $\sim 3.5$  mV/°C. The amperometric free chlorine sensor was simplified to a two-electrode configuration that eliminates the use of a potentiostat. The sensitivity of  $\sim 1$   $\mu\text{A}/\text{cm}^2/\text{ppm}$  ensured accurate monitoring of real water samples.

### Publications:

- Y. Qin, S. Pan, M. M. R. Howlader, R. Ghosh, N.-X. Hu, M. J. Deen, “Portable water quality monitoring system with integrated pH, free chlorine and temperature sensors,” (*in preparation*)
- Y. Qin, A. U. Alam, M. M. R. Howlader, N.-X. Hu, and M. J. Deen, “Morphology and electrical properties of inkjet-printed palladium/palladium oxide,” *J. Mater. Chem. C*, vol. 5, no. 8, pp. 1893–1902, 2017.
- Y. Qin, S. Pan, M. M. R. Howlader, R. Ghosh, N.-X. Hu, and M. J. Deen, “Paper-based, hand-drawn free chlorine sensor with poly(3,4-ethylenedioxythiophene):poly(styrenesulfonate),” *Anal. Chem.*, vol. 88, no. 21, pp. 10384–10389, Nov. 2016.
- Y. Qin, A. U. Alam, M. M. R. Howlader, N.-X. Hu, and M. J. Deen, “Inkjet printing of a highly loaded palladium ink for integrated, low-cost pH sensors,” *Adv. Funct. Mater.*, vol. 26, no. 27, pp. 4923–4933, Jul. 2016.
- Y. Qin, H.-J. Kwon, A. Subrahmanyam, M. M. R. Howlader, P. R. Selvaganapathy, A. Adronov, and M. J. Deen, “Inkjet-printed bifunctional carbon nanotubes for pH sensing,” *Mater. Lett.*, vol. 176, pp. 68–70, Apr. 2016.
- Y. Qin, A. U. Alam, S. Pan, M. M. R. Howlader, R. Ghosh, P. R. Selvaganapathy, Y. Wu, and M. J. Deen, “Low-temperature solution processing of palladium/palladium oxide films and their pH sensing performance,” *Talanta*, vol. 146, pp. 517–524, 2016.
- Y. Qin, M. M. R. Howlader, and M. Deen, “Low-temperature bonding for silicon-based micro-optical systems,” *Photonics*, vol. 2, no. 4, pp. 1164–1201, Dec. 2015.

- Y. Qin, H.-J. Kwon, M. M. R. Howlader, and M. J. Deen, “Microfabricated electrochemical pH and free chlorine sensors for water quality monitoring: Recent advances and research challenges,” *RSC Adv.*, vol. 5, no. 85, pp. 69086–69109, 2015.
- Y. Qin, M. M. R. Howlader, M. J. Deen, Y. M. Haddara, and P. R. Selvaganapathy, “Polymer integration for packaging of implantable sensors,” *Sensor. Actuat. B Chem.*, vol. 202, pp. 758–778, Oct. 2014.
- A. U. Alam, Y. Qin, M. M. R. Howlader, and M. J. Deen, “Direct bonding of liquid crystal polymer to glass,” *RSC Adv.*, vol. 6, no. 109, pp. 107200–107207, 2016.

## 1.6. Thesis organization

In Chapter 1, an introduction to the significance of drinking water quality monitoring is presented. The recent research activities in microfabricated electrochemical pH and free chlorine sensors are discussed and compared with conventional pH and free chlorine meters. Then, the motivation of developing accurate, easy-to-use, and low-cost drinking water quality monitoring systems is presented. Finally, a brief summary of the main contributions of this research and the structure of this thesis are given.

In Chapter 2, a solution-processed Pd/PdO-based pH sensing electrode is presented. Details of fabrication approaches, material characterization methods, and sensor characterization set-ups used in this research are given. In particular, efforts are devoted to studying the sensing mechanisms, and to optimizing the sensor performance in terms of sensitivity, response time, hysteresis, and stability. The optimal sensor performance is obtained by tuning the fabrication parameters such as the thermolysis temperature of the precursor solution and the annealing time of the deposited Pd film. We find that the chemical composition of the sensing electrode determines the sensitivity, the surface roughness affects the response time, and the nano-morphology decides the stability of the electrode.

In Chapter 3, an inkjet printing process for a highly loaded Pd ink is developed to deposit and pattern Pd thin films for an integrated pH sensor. The formulation of the Pd ink is

described, and a two-step thermolysis step is used to convert the printed ink to continuous, uniform, and highly conductive Pd films with good adhesion to different substrates. Also, solid-state reference electrodes are inkjet-printed with the use of Ag, epoxy, NaOCl, and PVC inks. Accurate pH values of real water samples are obtained by using the printed sensors with a low-cost multimeter

In Chapter 4, the effect of thermolysis atmosphere for the inkjet-printed Pd ink on the film morphology and electrical properties is studied. The morphology, chemical composition, crystal structure, and thermogravimetric property of the deposited films is analyzed. A thin film formation mechanism is also proposed. The TCR of the films can be adjusted from 0.067% /°C to -0.189% /°C by tuning the amount of semiconductive PdO in the conduction path, so that the films can be used as temperature sensors. For the application of water quality monitoring, the electrical stability of the films is studied under different humidity levels. The surface-adsorbed hydroxyl groups and/or molecular water increases the resistance drift of the films.

In Chapter 5, a free chlorine sensor is drawn by hand on a paper substrate. The sensor design, sensing mechanism, and operation method is discussed with a focus on the practical use of the sensor. The mechanical stability, sensing range, reusability, sensitivity, selectivity, and stability of the sensor is characterized. Also, the measurement results for real water samples are presented. We show that the sensor is of great significance for drinking water quality monitoring in less developed areas where fabrication facilities, analytical equipment, and trained personnel are limited, but the need for analytical devices is critical.

In Chapter 6, an integrated drinking water quality monitoring system is presented. Such a system includes an inkjet-printed pH sensor discussed in Chapter 3, a Wheatstone-bridge-based temperature sensor fabricated by the inkjet printing Pd/PdO and Ag, and a free chlorine sensor. The free chlorine sensor is a simplified version of an amperometric sensor

with an amine-modified pencil lead as the sensing electrode. The three sensors are fabricated on a common substrate and their sensing performance is characterized. A programmed FPGA board is used as the user interface to sample, process, and display the sensor signals.

In Chapter 7, this thesis is concluded with a summary of the research and several recommendations for future improvements for pH, free chlorine, temperature sensors, and the integrated sensing system for drinking water quality monitoring.

## Chapter 2

# Solution-processed Pd/PdO: pH sensing mechanisms and properties\*

Highly sensitive, easy-to-fabricate, and low-cost pH sensors with small dimensions are required for drinking water quality monitoring. In this chapter, a low-temperature, solution-based process is developed to prepare Pd/PdO thin films for pH sensing. A precursor solution for Pd is spin coated onto pre-cleaned glass substrates and annealed at low temperature to generate Pd and PdO. The percentages of PdO at the surface and in the bulk of the electrodes are correlated to their sensing performance, which is studied using X-ray photoelectron spectroscopy. Large amounts of PdO introduced by prolonged annealing improve the electrode's sensitivity and long-term stability. Atomic force microscopy study showed that the low-temperature annealing results in a smooth electrode surface, which contributed to a fast response. Nano-voids at the electrode surfaces are observed by scanning electron microscopy, indicating a reason for the long-term degradation of the pH sensitivity. Using the optimized annealing parameters of 200 °C for 48 h, a linear pH response with sensitivity of  $64.71 \pm 0.56$  mV/pH is obtained for pH between 2 and 12. These electrodes showed a response time shorter than 18 s, hysteresis less than 8 mV and stable operation for more than 60 days.

---

\* Adapted with permission from Y. Qin, A. U. Alam, S. Pan, M. M. R. Howlader, R. Ghosh, P. R. Selvaganapathy, Y. Wu, and M. J. Deen, "Low-temperature solution processing of palladium/palladium oxide films and their pH sensing performance," *Talanta*, vol. 146, pp. 517–524, 2016. Copyright (2016) Elsevier (Appendix E).

## 2.1. Background

pH sensors are of significant importance for regular/continued monitoring of drinking water quality [11]. Since conventional glass pH electrodes are fragile, large in dimensions (typically in the centimeter range), difficult to handle, and require frequent calibration and maintenance [11], [22], it is challenging to apply them in confined spaces for continuous use in many environmental monitoring applications. Therefore, small-size, easy-to-use, and low-cost pH sensors with sensitive and reliable performance are needed. Among the various types of pH sensors that include chemical-mechanical sensors, optical sensors, ion-sensitive field-effect transistor-based sensors, and resistor-based sensors [57]–[59], [166], the potentiometric sensor is one of the most commonly studied configurations owing to its straightforward and compact structure, potential for miniaturization, ease in fabrication and integration, low power consumption, as well as compatibility with both organic and inorganic materials.

The pH sensing behavior of a number of metal oxides were studied for potentiometric sensors. For example, CuO [75], IrO<sub>x</sub> [70]–[72], Co<sub>3</sub>O<sub>4</sub> [76], WO<sub>3</sub> [77], [167], RuO<sub>2</sub> [78], TiO<sub>2</sub> [168], ZnO [169], PdO [126], and PbO<sub>x</sub> [79] were used in pH sensors. Among these materials, PdO is promising due to its demonstrated higher (super-Nernstian) sensitivity than that of many materials. Also, it has fast response (<10 s) in a wide sensing range of pH between 2 and 12, and long lifetime (up to several years) [126], [170]–[172]. However, the fabrication of high-quality PdO films at low temperature and low cost is challenging.

Currently, thermal oxidation [171], [173], physical vapor deposition [126], [174], [175] and electrochemical deposition [170], [176], [177] are being used to fabricate Pd/PdO films. In these processes, the challenges are the requirements of high temperatures (above 400 °C), vacuum environment and high electrical energy. Moreover, it is challenging to pattern electrodes on electrochemically deposited films because of the requirements of masks and additional lithographic steps [71], [72], [178], [179]. These process conditions are incompatible with the development of cost-effective pH sensors on inexpensive polymeric

substrates [180], as well as their integration with electronics for sensing systems [181]. Thus, alternative approaches for material deposition such as low-temperature solution processing have to be employed. Earlier, screen-printed Pd was investigated for electrochemical sensing [182]. The fabricated electrodes were porous and contained PdO, but they were not pH sensitive. On the other hand, while solution-processed IrO<sub>x</sub> [72], TiO<sub>2</sub> [119] and ZnO [95] were reported for pH sensors, so far, PdO-based pH sensing electrodes have not yet been prepared from solution.

In the following subsections, details of fabrication approaches, material characterization methods, and sensor characterization set-ups used in this research are given. The Pd/PdO pH sensing electrodes were fabricated using a simple, low-temperature, and low-cost solution-based process. Pd precursor solution was spin coated onto glass substrates, followed by annealing in ambient air at low temperatures. The annealing process converted organic Pd complex to metallic Pd and further oxidized Pd to PdO. We optimized the processing parameters and characterized the fabricated Pd/PdO films to achieve high quality of sensing electrodes. Potentiometric measurements were used to characterize the pH sensing performance of the electrodes. Also, we investigated their reproducibility and long-term stability.

## 2.2. Experimental set-up

### 2.2.1. Chemicals and reagents

Isopropanol (IPA, 8600-1), acetic acid (HOAc, 1000-1), potassium sulfate (K<sub>2</sub>SO<sub>4</sub>, 6760-1-70), zinc chloride (ZnCl<sub>2</sub>, 9120-1), and toluene (PhMe, 9200-1) were purchased from Caledon Laboratory Chemicals. Isobutylbenzene (IBB, 113166), sodium hypochlorite (NaOCl) solution (239305), a poly(3,4-ethylenedioxythiophene):poly(styrenesulfonate) (PEDOT:PSS) solution (483095), silver chloride (AgCl, 227927), poly(vinyl chloride) (PVC, 389293), cyclohexanone (C102180), phosphoric acid (H<sub>3</sub>PO<sub>4</sub>, 695017), boric acid (H<sub>3</sub>BO<sub>3</sub>, 339067), phosphate buffered saline (PBS) tablet (P4417), sodium chloride (NaCl,

793566), sodium acetate (NaOAc, S2889), sodium phosphate dibasic ( $\text{Na}_2\text{HPO}_4$ , S0876), potassium sulfate ( $\text{K}_2\text{SO}_4$ , 221325), ammonium carbamate (292834), propylene glycol monomethyl ether acetate (PGMEA, 484431), Triton™ X-100 (X-100), and sodium hydroxide (NaOH) pellets (S5881) were from Sigma-Aldrich. Pd precursor solution (Pd-25c) and silver nanoparticle (Ag NP) ink (xcm-nsIJ) were obtained from Xerox Research Centre of Canada. Urea (URE001.1) was from BioShop. Potassium chloride (KCl, PX1405), sodium carbonate ( $\text{Na}_2\text{CO}_3$ , SX0395-1), sodium bicarbonate ( $\text{NaHCO}_3$ , SX0320-1), ammonium sulfate ( $(\text{NH}_4)_2\text{SO}_4$ , AX1385-3), and magnesium chloride ( $\text{MgCl}_2$ , MX0045-2) were from EMD Millipore. Potassium nitrate ( $\text{KNO}_3$ , 74336-300) was from Anachemia. Calcium chloride ( $\text{CaCl}_2$ , C77-500), copper(II) sulfate pentahydrate ( $\text{CuSO}_4 \cdot 5\text{H}_2\text{O}$ , C493-500), and ethylene glycol (E178-500) were from Fisher Scientific. SU-8 3035 photoresist was purchased from MicroChem. Conductive Ag paste (product No. CI-1001) was purchased from Engineered Materials Systems Inc.

Britton-Robinson pH buffer solutions (pH = 2, 4, 5, 6, 7, 8, 9, 10, and 12) were prepared by mixing an acid solution comprising 0.04 M  $\text{H}_3\text{PO}_4$ , 0.04 M HOAc, 0.04 M  $\text{H}_3\text{BO}_3$  with an appropriate amount of 0.2 M NaOH solution. The pH levels of the buffer solutions were monitored by a commercial pH meter (PHB-600R, OMEGA) with a glass electrode (PHE1311, OMEGA) during preparation.

Free chlorine solutions with different concentrations were prepared by diluting the as-received NaOCl solution using a PBS solution (0.01 M, pH = 7.4). The free chlorine concentrations of the prepared solutions were calibrated using a DPD-based colorimetric test kit (CN-70, Hach).

## **2.2.2. Methods for characterizing solutions and thin films**

### **2.2.2.1. Characterization of solution properties**

The surface tension of different solutions was measured using a tensiometer (K100, Krüss) at 22 °C in ambient conditions. About 15 mL of the solution equilibrated to 22 °C was

transferred to a pre-cleaned and dust-free crystallizing dish (diameter = 48 mm, height = 30 mm) and placed in the tensiometer equipped with a Wilhelmy plate. The surface tension data was averaged from 30 to 60 s after the immersion of the Wilhelmy plate. The viscosity of different solutions was measured using a rheometer (RFS3, TA Instruments).

To obtain the solution viscosity, a shear rate sweep run was carried out both clockwise and counter clockwise at 25 °C, and the average viscosity was calculated. The rate sweep was from 1 /s to 400 /s in the low-to-high sweep, and 400 /s to 1 /s in high-to-low sweep. Before the initial low-to-high rate sweep, the sample was equilibrated for 300 s. The high-to-low rate sweep has an equilibration time of 120 s right after the low-to-high rate sweep.

The solid content of different solutions was measured using a thermogravimetric (TG) analyzer (Q5000 IR, TA Instruments) with Pt pans as solution carriers. Two temperature profiles were used. For the 1-step profile, the temperature was increased from room temperature to 200 °C at 80 °C/min, followed by an isothermal step at 200 °C for 4 min. Then, the temperature was increased to 250 °C at 80 °C/min. For the 2-step profile, the temperature was increased from room temperature to 120 °C at 80 °C/min, followed by an isothermal step at 120 °C for 1 min. Next, the temperature was increased to 200 °C at 80 °C/min, followed by an isothermal step at 200 °C for 4 min. Then, the temperature was increased to 250 °C at 80 °C/min. All measurements were done under nitrogen (N<sub>2</sub>) purge (25 mL/min).

#### **2.2.2.2. Physical characterization of deposited thin films**

The thickness of the deposited thin films was measured by using a stylus profiler (Dektak XT, Bruker). A pair of stainless steel tweezers was used to gently scratch the deposited thin film to expose the substrate. The stylus was scanned at a speed of 50 μm/s between the exposed substrate and the thin film with 3 mg applied force.

The pattern of the deposited thin films was observed using a stereo microscope (AZ100, Nikon). The surface morphology of the thin films was observed using field-emission scanning electron microscopy (SEM, SU-8000, Hitachi) with a landing voltage of 700 V and 200 V for Pd/PdO on glass and PEDOT:PSS on paper, respectively. The surface morphology of the Pd/PdO thin films was also observed using field-emission SEM (JSM-7001F, JEOL) with an acceleration voltage of 10 kV and emission current of  $\sim 80 \mu\text{A}$ . Thin-film X-ray diffraction (XRD) patterns were obtained on a Rigaku MiniFlex diffractometer using copper  $K_\alpha$  ( $\lambda = 0.15418 \text{ nm}$ ) radiation. The XRD patterns were used to calculate the size of the crystallites in the deposited thin films.

Atomic force microscopy (AFM, Dimension Icon, Bruker) was used to measure the surface roughness of the thin films. The AFM measurements were based on tapping mode with  $20 \mu\text{m} \times 20 \mu\text{m}$  and  $1 \mu\text{m} \times 1 \mu\text{m}$  scanning areas using a 1 Hz scanning rate. The surface roughness was calculated using NanoScope Analysis software.

To check the adhesion between deposited thin films and substrates, water rinse tests were performed by rinsing the thin films under tap water (flow rate  $\sim 3 \text{ m/s}$ ) for 60 s. Scotch tape test was performed manually by pressing transparent scotch tapes (S-9782, 3M) onto the thin films firmly and pulling off slowly. The delamination of printed films in both cases was visually observed.

### **2.2.2.3. Chemical characterization of deposited thin films**

X-ray photoelectron spectroscopy (XPS, JPS-9200, JEOL) was used to analyze the chemical composition of sensing electrodes. Narrow-scan spectra (resolution of 0.1 eV) were obtained using a magnesium X-ray source (10 keV and 15 mA). Depth profiling spectra were acquired after every 40 s of argon (Ar) ion etching (3 keV and 20 mA) at a pressure of 0.08 Pa. Four etching steps were carried out at one analysis location. XPSPEAK 4.1 software was used for curve fitting and to calculate the area under peaks to determine the films' chemical composition.

Raman spectra were recorded on Renishaw inVia Raman spectrometer with an excitation wavelength of 633 nm. The obtained spectra were an accumulation of 10 measurements. Fourier transform infrared (FTIR) spectra of the thin film surfaces were recorded using a spectrometer (Vertex 70, Bruker) coupled to a microscope (Hyperion 3000, Bruker) with an attenuated total reflection objective.

The PdO content in the printed Pd/PdO thin films were measured using a Q5000 IR (TA Instruments) thermogravimetric (TG) analyzer with Pt pans as powder carriers. About 15 mg Pd/PdO powder was obtained by scraping thin films off from glass substrates. The TG analysis was performed from room temperature to 950 °C at a temperature ramp rate of 20 °C/min with a N<sub>2</sub> purge (20 mL/min).

#### **2.2.2.4. Electrical characterization of deposited thin films**

The resistance of deposited thin films was measured by a semiconductor analyzer (4200-SCS, Keithley) equipped with a probe station (S-1160, Signatone) using the 4 point probe method. The measurement bias current was 1 mA to minimize self-heating. The resistance of deposited thin films was also measured in vacuum ( $\sim 10^{-6}$  mbar) at varying temperatures using a probe station (ST-500, Janis Research) equipped with a temperature control unit (Model 9700, Scientific Instruments). A reliability test chamber (ESL-2CA, ESPEC) was used to provide an ambient measurement environment with varying temperatures and relative humidity (RH) levels.

Bending tests were carried out using a tensile pulling tester (AG-X, Shimadzu) by compressing the deposited thin films (2 cm × 4 cm, on a flexible substrate) by 1 cm (bending radius  $\sim 1.6$  cm) at a speed of 1 mm/s. The bending tests were performed cyclically at a frequency of 0.05 Hz (once every 20 seconds). The electrical resistance of the thin film during bending was measured simultaneously using a semiconductor parameter analyzer (4200-SCS, Keithley).

### 2.2.3. Solution processing of Pd/PdO pH sensing electrodes

The glass substrates (7525M, J. Melvin Freed Brand microscope slides) were manually cut into 2.5 cm × 3.8 cm pieces using a diamond scribe, followed by rinsing with IPA and deionized (DI) water, and then dried under compressed dry air (Figure 2-1(a)). About 0.5 mL of the Pd precursor solution (used without further purification) was dispensed onto glass substrates using a pipette and left settling for 2 min before spin coating. The coating was performed at 500 rpm for 10 s with 800 rpm/s acceleration and subsequently 3000 rpm for 60 s with 800 rpm/s acceleration (Figure 2-1(b)). Then, the samples were baked on a hotplate, in ambient air, at different temperatures (200 °C and 250 °C) and for different durations (4 min, 24 h, and 48 h) (Figure 2-1(c)). The area of the sensing electrode was ~9.5 cm<sup>2</sup>. After annealing, the electrodes were characterized (Figure 2-1(d)).

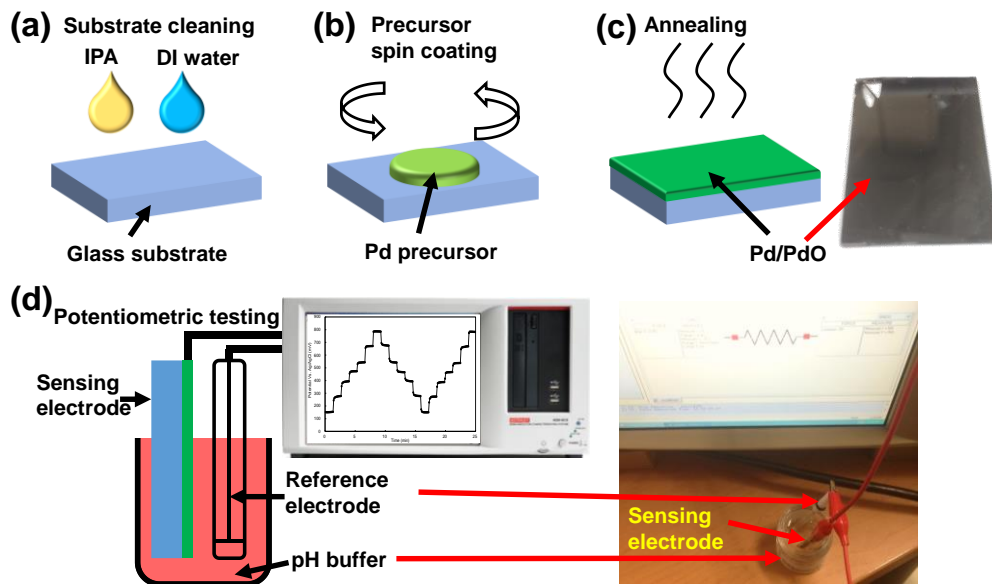


**Figure 2-1.** (a)-(c) Fabrication process of Pd/PdO-based pH sensing electrodes. (a) Glass substrate cleaning by rinsing with IPA and DI water. (b) Spin coating of Pd precursor solution. (c) Pd precursor conversion by baking and sample annealing at different conditions. (d) Characterization set-up for pH sensing behavior of fabricated electrodes.

The fabrication of pH sensing electrodes was straightforward, including spin coating and annealing in ambient air. The annealing temperature of 200 °C was decided based on two reasons. First, such temperature should be higher than the decomposition temperature of

the Pd precursor (~190 °C). Second, a low annealing temperature is preferred to allow the precursor being processed on a wide range of substrates (e.g. low-cost polymeric substrates). The annealing included 2 steps: a short-term conversion step and a long-term oxidation step. In the conversion step, the clear light-yellow precursor solution turned to black color within 1 min upon heating, indicating the precursor decomposition and the formation of Pd NPs. After annealing for another 1 to 2 min, metallic silver color appeared because of the fusing of Pd NPs to a thin film. Since the conversion was performed in air, a certain amount of PdO was produced in this step. In addition, good adhesion between the deposited Pd/PdO films and the glass substrate were confirmed by scotch tape tests.

To study the effect of PdO percentage on the pH sensing behavior, the samples were annealed in air for 4 min, 24 h, and 48 h at 200 °C. Another conversion and annealing temperature (250 °C) was used to accelerate the generation of PdO for 4 min, 24 h, and 48 h. In total, 6 groups of samples (A to F) were prepared and are listed in Table 2-1. The average thickness (taken over 5 locations) of a sample annealed at 200 °C for 4 min was 85.7 nm. The Pd/PdO thin films became thicker if a higher annealing temperature or a longer annealing time was used. The increased thickness was attributed to the volume expansion induced by the generation of PdO.

**Table 2-1.** Summary of preparation conditions, thickness, chemical composition, and performance parameters of pH sensing electrodes.

Sample ID	Annealing temperature, °C	Annealing time	Thickness, nm	PdO% at the surface	PdO% in the bulk	pH sensitivity, mV/pH	Linearity <sup>a</sup>
A	200	4 min	85.7 ± 4.9	51%	18%	54.53 ± 1.70	0.9988
B	200	24 h	121.3 ± 7.2	82%	47%	68.93 ± 1.74	0.9995
C	200	48 h	125.1 ± 5.9	98%	49%	64.71 ± 0.56	0.9991
D	250	4 min	93.6 ± 5.3	89%	26%	65.64 ± 1.46	0.9996
E	250	24 h	125.0 ± 6.2	97%	49%	64.62 ± 1.65	0.9993
F	250	48 h	125.3 ± 4.0	99%	53%	63.19 ± 1.47	0.9994

<sup>a</sup>Linearity is compared using the correlation coefficient R<sup>2</sup>.

#### 2.2.4. Set-up for pH sensing tests

The pH sensing performance of the fabricated electrodes/sensors was characterized based on a potentiometric configuration against a Ag/AgCl reference electrode with 1 M KCl

filling solution (CHI111, CH Instruments). The bottom half of the sensing electrode and reference electrode (~2 cm distance between them) was immersed in static pH buffer solutions at the same time and connected to a Keithley 4200-SCS semiconductor analyzer using alligator clamps. The semiconductor analyzer was set for measuring the open circuit voltage by forcing the current flowing through the sensing and reference electrodes to be 0 A with a “Best Fixed” source range. This voltage sampling interval was defined to be 2 or 6 s. The deposited Pd/PdO was used for the dual purpose of sensing as well as electrical contact because it was electrically conductive. The open circuit potential between the sensing and reference electrode was recorded as a function of time at room temperature ( $27 \pm 2$  °C). The sensing electrodes were tested in each pH buffer for ~80 s and immediately transferred into the next pH buffer without rinsing with DI water or drying.

## **2.3. Characterization of Pd/PdO thin films**

### **2.3.1. Chemical composition**

The chemical composition at the surface and in the bulk of deposited Pd/PdO electrodes was characterized by XPS. XPS spectra for the surface were obtained without Ar ion etching while those for the bulk were measured after 160 s of etching (etch rate ~0.44 nm/s, XPS spectra after 40 s of etching are identical at each location for analysis). Figure 2-2(a-d) show XPS spectra of Pd 3d region for the surface and bulk of sensing electrodes annealed at 6 different conditions.

For the surface of the electrode prepared at 200 °C for 4 min (sample A), peaks for Pd 3d<sub>5/2</sub> and Pd 3d<sub>3/2</sub> doublet were at binding energies around 334.90 eV and 340.22 eV, respectively (Figure 2-2(a), solid line). These peak positions indicate the presence of metallic Pd (Pd<sup>0</sup>) [183], [184]. Noteworthy, shoulders could be observed on the left side (high-energy side) of Pd peaks, which suggests the existence of Pd<sup>2+</sup> because PdO has been considered as a stable oxide form of Pd [37]. In the bulk of the same sample (Figure 2-2(b),

solid line), peaks for Pd 3d<sub>5/2</sub> and Pd 3d<sub>3/2</sub> do not shift, but the shoulders are less obvious, designating a smaller amount of Pd<sup>2+</sup>.

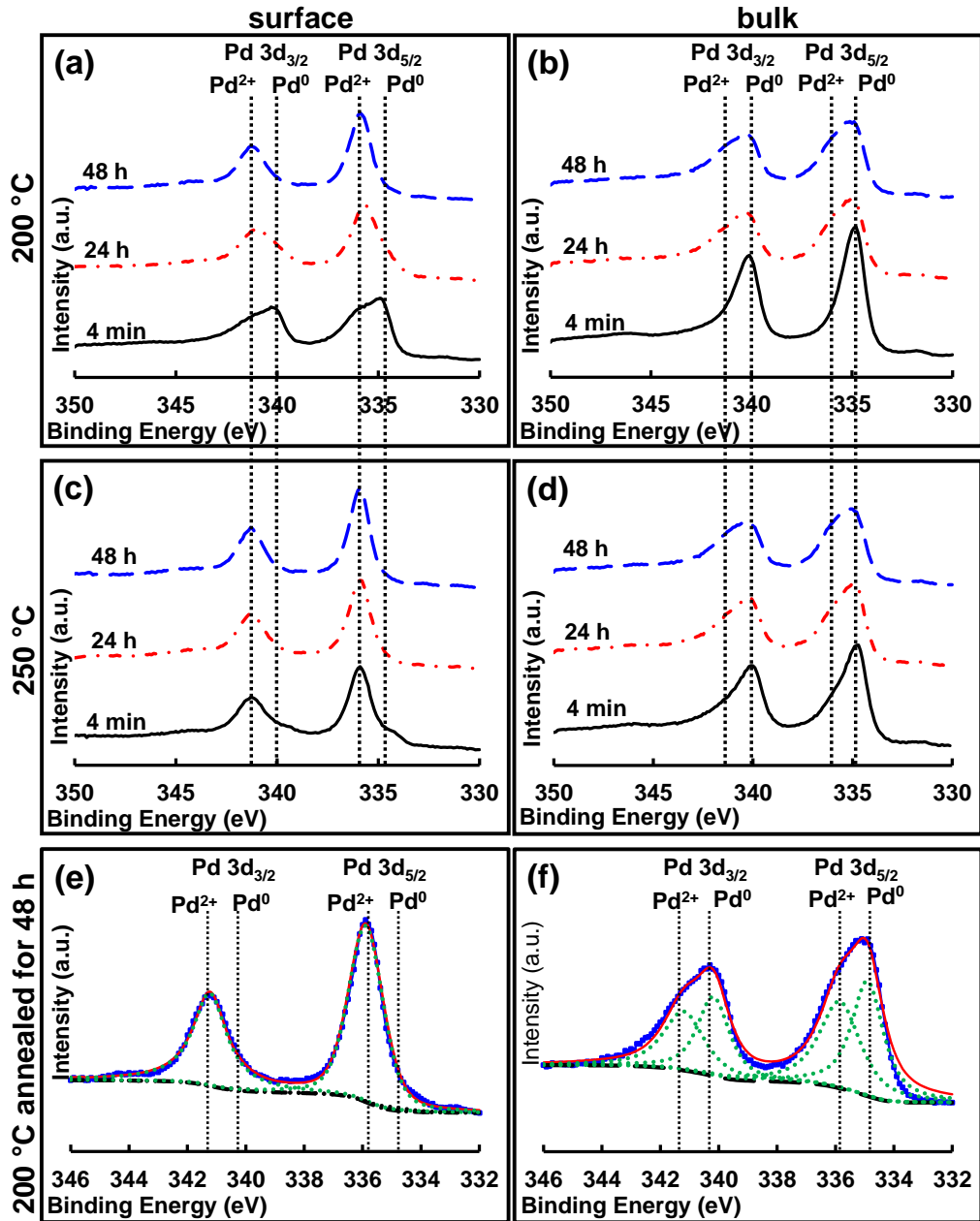


**Figure 2-2.** (a-d) Pd 3d XPS spectra of the surface and bulk of sensing electrodes annealed at different temperatures for 4 min (solid lines), 24 h (dot-dash lines), and 48 h (dashed lines). (a) Surface, 200 °C. (b) Bulk, 200 °C. (c) Surface, 250 °C. (d) Bulk, 250 °C. (e) and (f) Curve fitting of XPS spectra for calculating atomic ratio between Pd<sup>0</sup> and Pd<sup>2+</sup>; square boxes are original data, solid lines are fitted curves, dotted lines are fitted peaks for Pd<sup>0</sup> and Pd<sup>2+</sup>, and dashed lines are background lines. (e) Surface of a sample annealed at 200 °C for 48 h (the intensity of 2 Pd<sup>0</sup> peaks is too low to be seen). (f) Bulk of the same sample annealed at 200 °C for 48 h.

Next, we studied the effects of annealing on the film properties. With increasing annealing times, peaks for Pd 3d<sub>5/2</sub> and Pd 3d<sub>3/2</sub> shift to higher binding energies for both surface and bulk spectra. This shift can be explained by the increased amount of Pd<sup>2+</sup>. For the sample annealed at 250 °C for 4 min (sample D, Figure 2-2(c), solid line), Pd<sup>2+</sup> is the major surface composition because peaks for Pd 3d<sub>5/2</sub> and Pd 3d<sub>3/2</sub> have higher binding energies than the sample annealed at 200 °C for 4 min. In its bulk spectrum (Figure 2-2(d), solid line), we can also observe a significant amount of Pd<sup>2+</sup>. Longer annealing time at 250 °C resulted in slightly shifted peaks to the high-energy side (sample E and F, Figure 2-2(c) and (d), dot-dash and dashed lines), which means that the amount of Pd<sup>2+</sup> gradually reaches saturation.

To quantitatively find the atomic percentage of Pd<sup>2+</sup>, the XPS spectra of Pd 3d doublet were fitted using 4 peaks (each of Pd 3d<sub>3/2</sub> and Pd 3d<sub>5/2</sub> was fitted by one Pd<sup>0</sup> and one Pd<sup>2+</sup> peak). Figure 2-2(e) and (f) shows the curve fitting of the surface and bulk spectra of the sample annealed at 200 °C for 48 h (sample C). The atomic percentage of Pd<sup>2+</sup> (PdO) for all types of electrodes were calculated and are listed in Table 2-1. At the beginning of annealing, the amount of PdO at the surface and in the bulk increased quickly (compare sample A and D with B and E), since O<sub>2</sub> in air diffused into the film and reacted with metallic Pd. Later, it was more difficult for O<sub>2</sub> to diffuse into the film because the surface became denser. Therefore, the difference in PdO% between the 48h-annealed and 24h-annealed samples was not significant (compare sample B and E with C and F). Besides, the time for PdO formation can be shortened by using higher annealing temperature, or annealing in an oxidation atmosphere, such as in O<sub>2</sub>.

### 2.3.2. Surface morphology

Figure 2-3 shows AFM images that illustrate the surface roughness of the sensing electrodes prepared at different temperatures. Similar roughness values were obtained on samples annealed at the same temperature for different durations. When the precursor was converted to Pd at 200 °C, the nucleation and coalescence of generated Pd/PdO nanoparticles, together with the decomposition of organic compounds, introduced peaks

and valleys in the deposited film [185]. The resulting surface roughness for the electrodes annealed at 200 °C had a root-mean-square (RMS) value of  $8.1 \pm 1.1$  nm over a  $20 \mu\text{m} \times 20 \mu\text{m}$  area (3 measurements were done on each sample). Figure 2-3(a) shows an example of an electrode annealed at 200 °C for 48 h. Its RMS roughness was 8.2 nm. Elevating the conversion temperature to 250 °C resulted in a faster solvent evaporation. Thus, agglomerates with smaller sizes were formed, and more peaks/valleys with larger amplitudes were created. The formation of such rough surfaces was due to the fast solvent evaporation, which shortened the time for self-leveling and smoothing of the film [186]. Hence, a higher surface roughness (RMS value of  $17.9 \pm 3.0$  nm) was observed for the electrode annealed at 250 °C. The AFM image of an electrode annealed at 250 °C for 48 h (sample F) is shown in Figure 2-3(b). The RMS roughness of the sample was 18.0 nm.

The surface morphology was analyzed in more detail by shrinking the scanning area to  $1 \mu\text{m} \times 1 \mu\text{m}$  (Figure 2-3(c)). Similar AFM images were obtained for the electrodes annealed at all 6 different conditions (RMS roughness was  $1.7 \pm 0.4$  nm). As one example, nanoparticles with diameters around 10 nm were densely packed at the surface of the electrode annealed at 200 °C for 48 h. The RMS value of the surface roughness in this case is 1.30 nm.

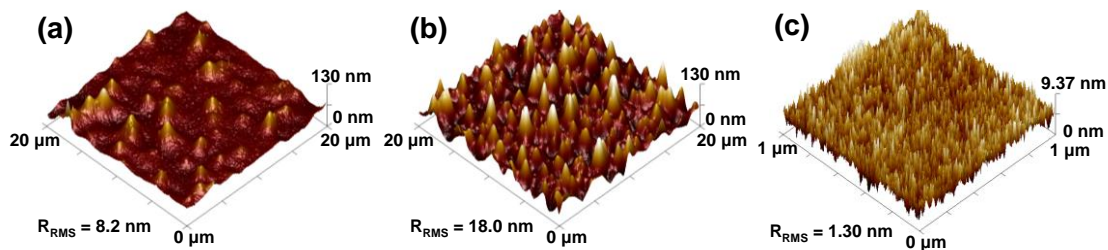


**Figure 2-3.** (a-b) AFM images over a  $20 \mu\text{m} \times 20 \mu\text{m}$  area of surfaces of pH sensing electrodes annealed at (a) 200 °C; (b) 250 °C for 48 h. (c) AFM image over a  $1 \mu\text{m} \times 1 \mu\text{m}$  area of surfaces of a pH sensing electrode annealed at 200 °C for 48 h.

SEM observations were done in addition to AFM measurements. Voids of nanoscale dimensions are observed among crystal domains in all samples. These voids were probably generated by the decomposition of organic compounds in the precursor. Inside the crystal domains, Pd/PdO nanoparticles are closely fused, which agrees with the results from AFM

analysis. With an increase of the annealing time from 4 min to 48 h, a less porous film was obtained. Also, the size and amount of nano-voids were reduced (compare Figure 2-4(a) with Figure 2-4(c)). With an increase of the annealing temperature from 200 °C to 250 °C, a denser film could be obtained as well. Figure 2-4(d) is the surface of an electrode annealed at 250 °C for 4 min, which appears to be similar to the surface of the electrode annealed at 200 °C for 48 h. Moreover, the annealing time does not affect the surface morphology when annealed at 250 °C (Figure 2-4(e-f)). Thus, a dense electrode surface with few nano-voids can be produced by increasing the annealing time or by elevating the annealing temperature.

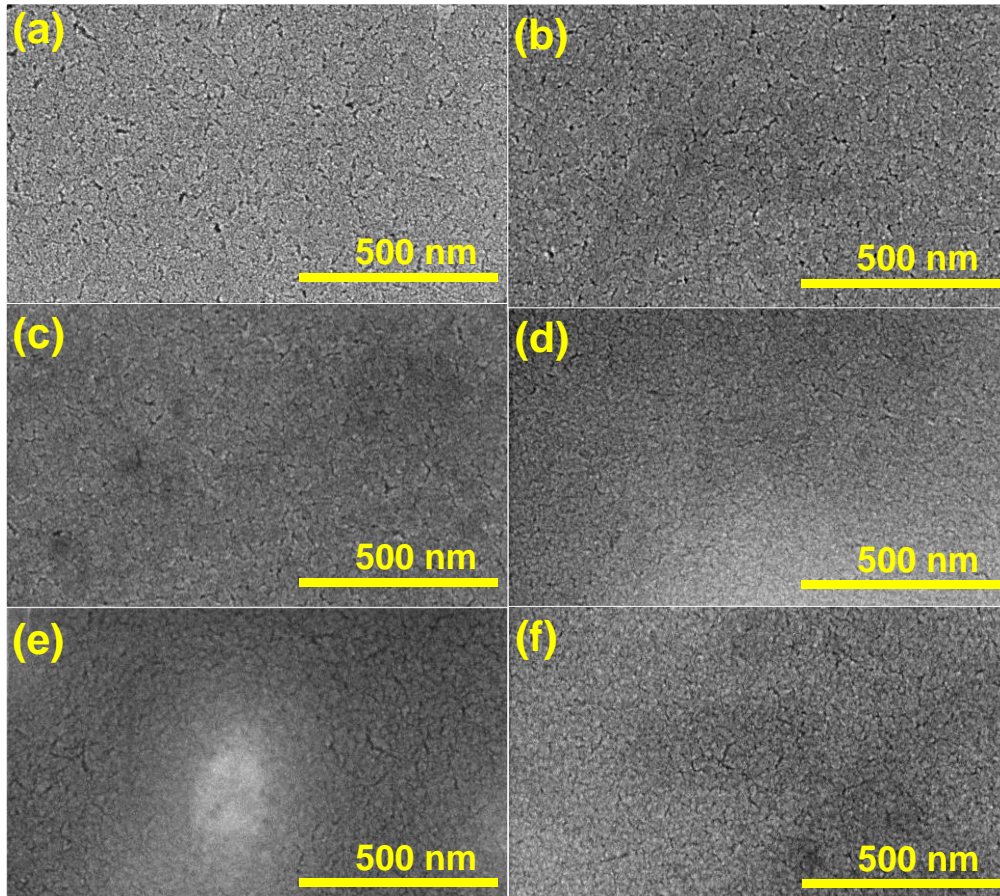
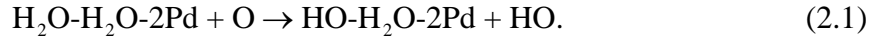


**Figure 2-4.** SEM images of surfaces of sensing electrodes annealed at (a) 200 °C for 4 min. (b) 200 °C for 24 h. (c) 200 °C for 48 h. (d) 250 °C for 4 min. (e) 250 °C for 24 h. (f) 250 °C for 48 h.

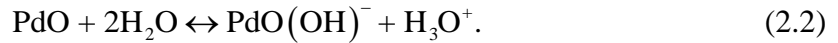
### 2.3.3. pH sensing mechanism

Even though the pH sensing behavior of Pd/PdO electrodes was studied for many years, the sensing mechanism is still not fully understood [187]. According to a previous study

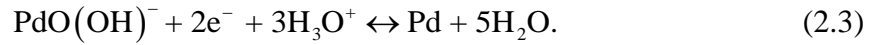
[22], the free valences in the PdO lattice is saturated by the adsorption of water molecules (Figure 2-5(a-b)). The adsorbed water molecules aggregate and convert to a HO-H<sub>2</sub>O complex (Figure 2-5(c)) via [188]:



Thus, when the Pd/PdO electrode is immersed into a solution, we can write:



If H<sub>3</sub>O<sup>+</sup> ions are present in the solution, the hydrated PdO has the tendency to dissociate into metallic Pd and water according to [189]:



By combining reaction (2.2) and (2.3), we can get the commonly accepted redox reaction between PdO and H<sub>3</sub>O<sup>+</sup> ions that determines the pH sensing mechanism [190]:



where every involved H<sub>3</sub>O<sup>+</sup> ion leads to the transfer of one electron.

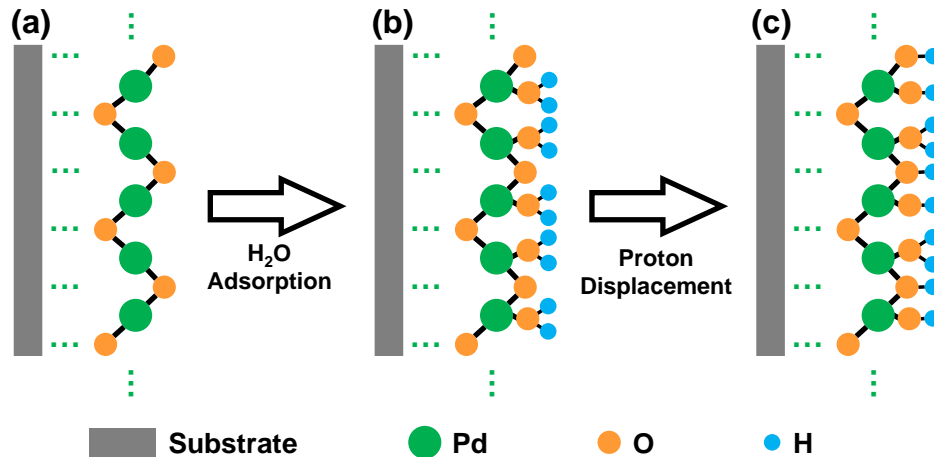


**Figure 2-5.** Dissociative adsorption of water at the surface of PdO. (a) Pristine surface of PdO. (b) Water adsorption. (c) Proton displacement at the PdO surface.

The Pd/PdO electrode in a solution undergoes the redox reaction (2.4), so a boundary/interface between the solid phase (electrode) and the liquid phase (solution) is formed with different concentrations of H<sub>3</sub>O<sup>+</sup> ions (pH of the solution) [191]. When an electrochemical equilibrium condition with regard to species *I* (H<sub>3</sub>O<sup>+</sup> ion in this case) is

reached at the boundary, the value of the electrochemical potential  $\tilde{\mu}$  of this species is the same in the solution phase ( $\tilde{\mu}_I^{sol}$ ) and in the electrode phase ( $\tilde{\mu}_I^{ele}$ ) [192]:

$$\tilde{\mu}_I^{sol} = \tilde{\mu}_I^{ele}. \quad (2.5)$$

The electrochemical potential of a species located in a certain part within the phase relates to the chemical potential ( $\mu_I$ ) of this species and the electrical potential ( $\phi$ ) in this part of the phase [192]:

$$\tilde{\mu}_I = \mu_I + z_I F \phi, \quad (2.6)$$

where  $z_I$  is the charge number of the species, and  $F$  is Faraday's constant. Combining equation (2.5) and (2.6), we obtain the boundary potential ( $\phi_b$ ) at equilibrium:

$$\phi_b = \phi^{ele} - \phi^{sol} = -\frac{\mu_I^{ele} - \mu_I^{sol}}{z_I F}, \quad (2.7)$$

where  $\phi^{ele}$  and  $\phi^{sol}$  is the electrical potential of the electrode phase and the solution phase, respectively. On the other hand, the chemical potential of a charged species in a system is defined as the partial Gibbs free energy ( $G$ ) of the system related to species  $I$  [193]:

$$\mu_I = \left( \frac{dG}{dn_I} \right)_{p, T, n_{j \neq I}}, \quad (2.8)$$

where  $p$ ,  $T$ , and  $n_I$  denotes the pressure, the absolute temperature, and the number of moles, respectively. Thus, the chemical potential of  $I$  is the partial derivative of the Gibbs free energy over the number of moles of  $I$  at a constant pressure, temperature, and numbers of moles of all other species in the system. Note that the Gibbs free energy can only be determined by the difference in  $G$  ( $\Delta G$ ) between the current state and some standard state  $G^0$ :

$$G = G^0 + \Delta G, \quad (2.9)$$

where  $G^0 = U^0 - TS^0$ , with  $U^0$  and  $S^0$  is the internal energy and the entropy of the system at the standard state, respectively. Because  $U^0$  and  $S^0$  are extensive values that are proportional to the mass of the system, then:

$$\left( \frac{dG^0}{dn_I} \right)_{p, T, n_{j \neq I}} = \mu_I^0 \neq 0. \quad (2.10)$$

Therefore, the chemical potential of a system  $\mu$  can only be determined in relation to some standard state  $\mu^0$ . For an ideal system undergoing a reversible change at a constant temperature, when no chemical work is being performed, the derivative of the Gibbs free energy is related to the volume  $V_{vol}$  and the derivative of the pressure of the system:

$$dG = V_{vol} dp. \quad (2.11)$$

Thus, the Gibbs free energy difference between two states (the standard state 0 and an arbitrary state 1) can be written as:

$$\Delta G = \int_0^1 dG = \int_0^1 V_{vol} dp. \quad (2.12)$$

According to the ideal gas law  $pV_{vol} = nRT$  ( $R$  is the gas constant), equation (2.12) can be written as:

$$\Delta G = \int_0^1 V_{vol} dp = \int_0^1 \frac{nRT}{p} dp = nRT \ln \left( \frac{p}{p_0} \right). \quad (2.13)$$

If the pressure at the standard state is 1 atm, we obtain the Gibbs free energy at an arbitrary state by combining equation (2.12) and (2.13):

$$G = G^0 + nRT \ln p. \quad (2.14)$$

In a system with many species in equilibrium, the concentration of a species  $I$  ( $C_I$ ) is proportional to its partial pressure ( $p_I$ ), so the partial Gibbs free energy of  $I$  ( $G_I$ ) can be written as:

$$G_I = G_I^0 + nRT \ln C_I, \quad (2.15)$$

where  $G_I^0$  is the partial Gibbs free energy of  $I$  at the standard state. In a practical solution system, the relation between the concentration and pressure in equilibrium is affected by the interaction between different molecules in the solution [194]. This molecular interaction leads to a deviation from the constant proportionality between the pressure and concentration. Hence, this deviation is compensated by considering activities instead of concentrations. The activity of species  $I$  ( $a_I$ ) and  $C_I$  is related by an activity coefficient ( $\gamma_I$ ):

$$a_I = \gamma_I C_I. \quad (2.16)$$

In water quality monitoring applications, the water samples in most cases are diluted solutions. The activity coefficient ( $\gamma_I$ ) approaches unity so that equation (2.15) still can be used. Thus, the chemical potential can be determined by combining equation (2.8), (2.10), and (2.15):

$$\mu_I = \mu_I^0 + RT \ln C_I. \quad (2.17)$$

Then, the electric potential difference between the electrode and solution (the boundary potential) can be calculated by using equation (2.7) and (2.17):

$$\phi_b = \phi^{ele} - \phi^{sol} = -\frac{\mu_I^{0,ele} - \mu_I^{0,sol}}{z_I F} - \frac{RT}{z_I F} \ln \frac{C_I^{ele}}{C_I^{sol}} = \phi^0 - \frac{RT}{z_I F} \ln \frac{C_I^{ele}}{C_I^{sol}}, \quad (2.18)$$

which is known as the Nernst equation.  $C_I^{ele}$  and  $C_I^{sol}$  is the concentration of species  $I$  in the electrode phase and the solution phase, respectively.  $\phi^0 = -(\mu_I^{0,ele} - \mu_I^{0,sol})/z_I F$  represents the standard electrode potential, and is used to simplify the equation. For a solid-state Pd/PdO pH sensing electrode without a liquid junction, the diffusion potential can be neglected, and the electrode potential is approximately the boundary potential. Referring to the sensing mechanism shown in reaction (2.4), we can consider the concentrations for the Pd (solid phase), PdO (solid phase), and water as unity [195]. Because the  $H_3O^+$  ion in the solution is the target analyte to be monitored, the Pd/PdO electrode potential can be expressed by:

$$\phi_{Pd/PdO} = \phi^0 + \frac{RT}{F} \ln [H_3O^+]. \quad (2.19)$$

According to the definition of pH in equation (1.1), equation (2.19) can be rewritten as:

$$\phi_{Pd/PdO} = \phi^0 - \frac{2.303RT}{F} \text{pH}. \quad (2.20)$$

In a potentiometric sensing set-up shown in Figure 2-1(d), the open-circuit potential between the Pd/PdO sensing electrode and the Ag/AgCl/KCl reference electrode is the output sensing signal, which can be calculated by:

$$E = \phi_{Pd/PdO} - \phi_{Ag/AgCl/KCl} = \phi^0 - \frac{2.303RT}{F} \text{pH} - \phi_{Ag/AgCl/KCl}, \quad (2.21)$$

where  $\phi_{Ag/AgCl/KCl}$  is the electrode potential of a commercial reference electrode (CRE, CHI111, CH Instruments, with 1 M KCl filling solution) used in this study, which is a fixed value of  $\sim 0.235$  V. Therefore, the expression for the sensor output is:

$$E = \phi^0 - \frac{2.303RT}{F} \text{pH} - 0.235 = E^0 - \frac{2.303RT}{F} \text{pH}, \quad (2.22)$$

where  $E^0 = \phi^0 - 0.235$  (V) is the standard potential for the sensing electrode with respect to the reference electrode. At 25 °C, the slope of the  $E$ -pH plot is  $2.303RT/F = 59.16$  mV/pH, which defines the theoretical pH sensitivity.

### 2.3.4. pH sensitivity

pH sensing electrodes prepared under 6 different conditions (A to F in Table 2-1) were characterized potentiometrically by recording the open circuit potential in Britton-Robinson buffer solutions with pH values of 2, 4, 6, 7, 8, 10, and 12. Four consecutive measurement cycles (2 to 12 to 2 to 12 to 2) were performed and the average potential values were plotted versus pH. The plots in Figure 2-6 were used to determine the pH sensitivity of fabricated electrodes. Sensitivity values calculated from these plots are summarized in Table 2-1. For the sample annealed at 200 °C for 4 min, a relatively lower sensitivity and linearity was obtained. Such sensing behavior can be attributed to the relatively small fraction of PdO at the electrode surface, where the redox reaction takes place, compared to the samples annealed for longer times or higher temperatures. Although metallic Pd is also sensitive to pH, its sensing mechanism is believed to be different from that of PdO [196]. Metallic Pd exhibited poorer sensitivity in basic solutions than in acid solutions, which lowered its sensitivity and linearity over the pH range of 2 to 12 (Figure 2-6(a)).

If the samples were annealed at a higher temperature or for a longer time, the electrode surfaces consisted of  $>80\%$  PdO and super-Nernstian response (sensitivity higher than 59.16 mV/pH) could be observed, as shown in Table 2-1. The super-Nernstian behavior of Pd/PdO sensing electrodes was reported previously [126], [170], but a detailed explanation for this phenomenon was lacking.

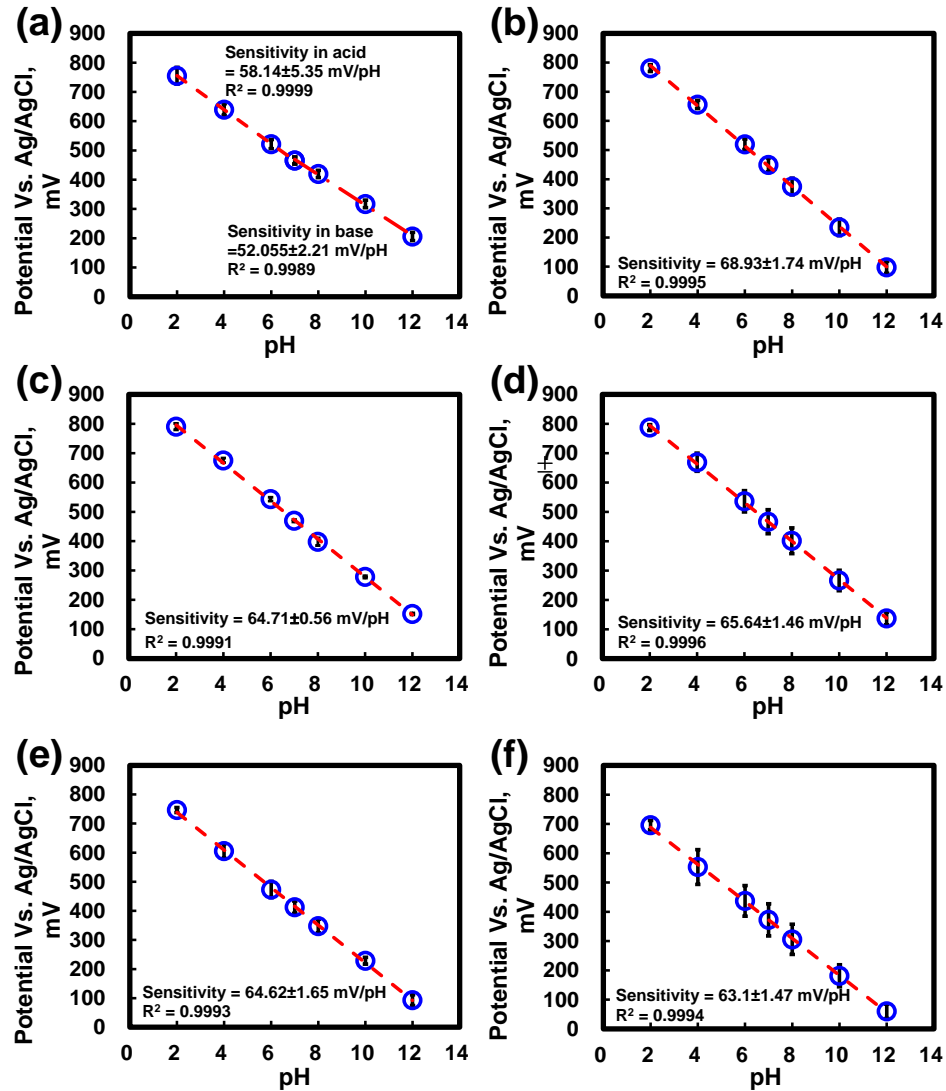
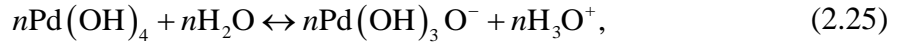
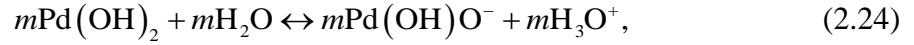


**Figure 2-6.** Open circuit potential versus pH values for an electrode annealed at (a) 200 °C for 4 min. (b) 200 °C for 24 h. (c) 200 °C for 48 h. (d) 250 °C for 4 min. (e) 250 °C for 24 h. (f) 250 °C for 48 h.

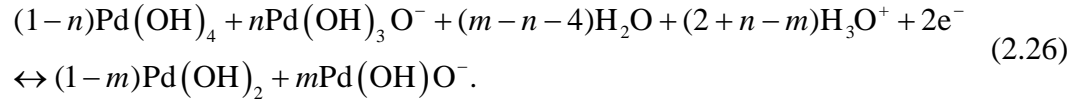
We believe that this super-Nernstian behavior of Pd/PdO is similar to that observed in solution-processed  $\text{IrO}_x$  pH sensing electrodes. The origin of such super-Nernstian response in  $\text{IrO}_x$  electrodes was described in detail in reference [71]. We believe that oxides of Pd ( $\text{PdO}_x$ ) and  $\text{IrO}_x$  may possess similar behavior. It was found that  $\text{PdO}_x$  can be hydrous [197] and Pd may have higher valence in its oxides (for example,  $\text{PdO}_2$ ) [198]. Hence, the super-Nernstian response of Pd/PdO electrodes may be attributed to the uptake/release of  $\text{H}_3\text{O}^+$  of hydrous  $\text{PdO}_x$  without transferring electrons. The most common hydroxides of palladium ( $\text{Pd}(\text{OH})_2$  and  $\text{Pd}(\text{OH})_4$ ) can convert between each other according to [190]:



where  $\text{Pd}(\text{OH})_2$  and  $\text{Pd}(\text{OH})_4$  can partially dissociate in a solution:



where  $0 \leq m \leq 1$  and  $0 \leq n \leq 1$ . Combining reactions (2.23), (2.24), and (2.25), we obtain:



Therefore, when  $2+n-m > 2$  or  $m < n$  ( $m$  electrons and  $n$  hydronium ions ( $m < n$ ) are transferred in the reaction), the pH sensitivity is enhanced by a factor of  $(2+n-m)/2$  according to the Nernst equation. Then the resulting sensitivity can be written as  $(2+n-m)(RT/F)/2 > 59.16$  mV/pH at 25 °C. If  $m = 0$  and  $n = 1$ , a super-Nernstian sensitivity of  $3/2 \times 59.16 = 88.74$  mV/pH can be obtained.

XPS analysis was carried out to observe Pd with higher valences in the deposited film. However, the high-resolution XPS spectra did not show visible peaks for Pd with higher valences. This suggests the amount of  $\text{PdO}_x$  ( $x > 1$ ) is not in the detectable range of the XPS. This result agrees with the pH sensitivity of  $\sim 65$  mV/pH in this study. In addition, the increase of annealing time or annealing temperature decreased the sensitivity slightly (neglect the electrode annealed at 200 °C for 4 min). The degradation of the performance might be related to the decomposition of unstable  $\text{PdO}_x$  ( $x > 1$ ) to PdO [198]. The reduced amount of  $\text{PdO}_x$  ( $x > 1$ ) limited the reactions between hydrous  $\text{PdO}_x$  and drove the sensitivity to the theoretical value of 59.16 mV/pH. On the other hand, the anhydrous  $\text{PdO}_x$  films deposited under vacuum or high-temperature conditions resulted in lower sensitivity [126], [172]–[175], [199]. In contrast,  $\text{PdO}_x$  prepared by electrochemical methods had more hydrous oxides and the sensitivity was higher ( $\sim 71$  mV/pH) [170] than that in this study ( $\sim 65$  mV/pH). Therefore, the super-Nernstian behavior may be related to the hydrous  $\text{PdO}_x$  ( $x > 1$ ) obtained at low temperatures without using vacuum processing. Further

investigation is required to understand the detailed mechanism of the super-Nernstian behavior of the Pd/PdO pH sensing electrodes.

### 2.3.5. Response time

Response time and reversibility of Pd/PdO sensing electrodes were studied by continuous testing. The electrodes were tested in each pH buffer for about 80 s and immediately transferred into the next pH buffer without rinsing with DI water or blow drying. The open circuit potential as a function of time for the electrode annealed at 200 °C for 48 h is plotted in Figure 2-7(a) with an enlarged view in Figure 2-7(b). Smooth transition of the potential signals could be observed. The response time ( $t_{90}$  in Figure 2-7(b)), which is defined as the time required for 90% change of measured voltage from initial values to final values ( $\Delta V_{90}$  in Figure 2-7(b)), can be extracted from Figure 2-7(a).

For our sensing electrodes, the response time was less than 18 s for all pH values, but this response time is longer than the values reported in other studies (less than 2 s) [70], [74]. The faster response achieved in these studies relied on a smoother and denser electrode surface, which was prepared by high-temperature or high-pressure treatment. These process conditions are not compatible with low-cost, flexible substrates. In our case, this response time of <18 s is fast enough for practical use in applications such as drinking water quality monitoring. Also, such relatively slower response may be due to the diffusion of  $\text{H}_3\text{O}^+$  ions into the nano-voids among Pd/PdO crystal domains (shown in Figure 2-4) [68], [74], [75]. Further, the response was slightly faster in the acid region than in the basic region. This difference was explained in reference [173] as due to some minor reaction (such as the reaction between Pd and hydroxide ions) that happens at the electrode surface. Comparing the electrodes annealed at different temperatures, the response time is shorter when electrodes were annealed at 200 °C (<18 s) than at 250 °C (<30 s) (see Table 2-2 and Figure 2-8 for the detailed values of response time of different electrodes at various pH levels). This faster response may be related to the smoother electrode surface, which allows faster redox equilibrium between Pd/PdO and  $\text{H}_3\text{O}^+$  ions at surface and buried sites [200].

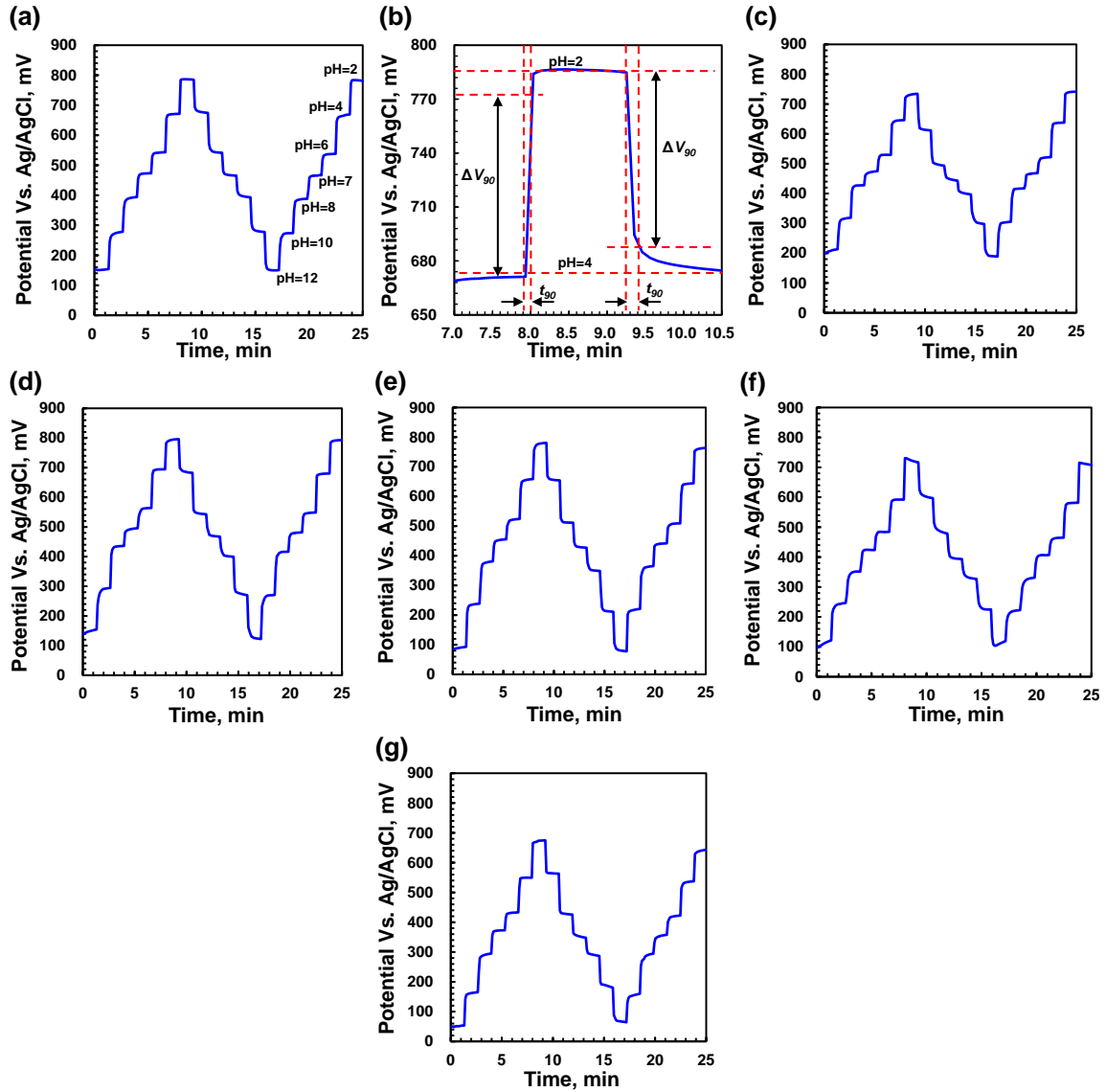


**Figure 2-7.** (a) Real-time response of an electrode annealed at 200 °C for 48 h between pH of 2 and 12; full-scale view. (b) Enlarged view of the voltage transition between pH = 2 and 4, indicating how the response time was determined. (c-g) Real-time response of an electrode annealed at (c) 200 °C for 4 min. (d) 200 °C for 24 h. (e) 250 °C for 4 min. (f) 250 °C for 24 h. (g) 250 °C for 48 h.

**Table 2-2.** Response time at different pH values for electrodes annealed at different conditions (unit: s).

Sample ID	Annealing Condition	pH=2	pH=4	pH=6	pH=7	pH=8	pH=10	pH=12
A	200 °C 4 min	6-12 <sup>a</sup>	6-12	6-12	18-24	12-18	18-24	12-18
B	200 °C 24 h	6-12	6-12	6-12	6-12	12-18	12-18	6-12
C	200 °C 48 h	<6	6-12	6-12	6-12	12-18	12-18	6-12
D	250 °C 4 min	<6	6-12	6-12	12-18	12-18	12-18	12-18
E	250 °C 24 h	<6	12-18	12-18	12-18	24-30	12-18	24-30
F	250 °C 48 h	6-12	6-12	6-12	18-24	24-30	12-18	18-24

<sup>a</sup> The sampling interval was 6 s.

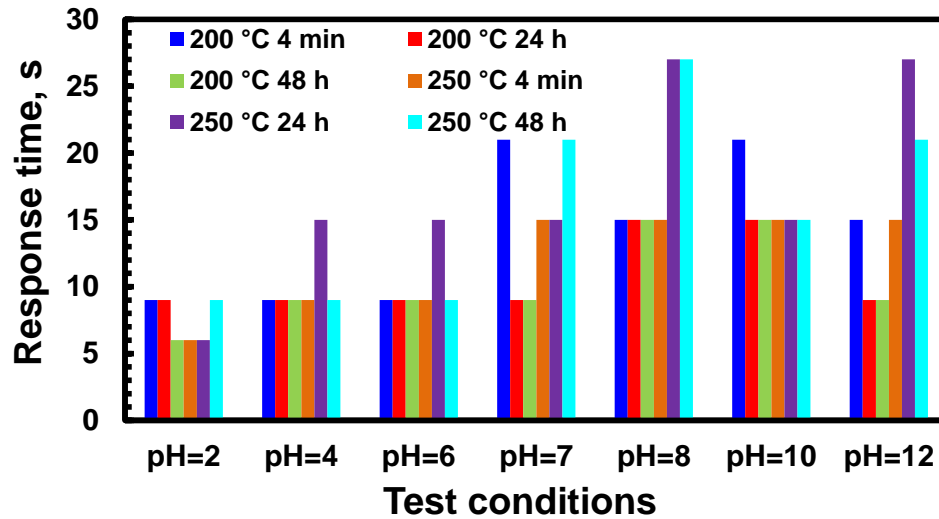


Figure 2-8. Response time at different pH values for electrodes annealed at different conditions.

### 2.3.6. Reversibility and drift

The hysteresis at each pH level was calculated to examine the reversibility behavior of the sensing electrode. For the electrode annealed at 200 °C for 48 h, hysteresis less than 7.81 mV (1.24% as the normalized value over the testing pH range) at all pH levels was obtained, indicating that the redox reaction between PdO and  $\text{H}_3\text{O}^+$  ion was highly reversible. Furthermore, no apparent correlation was found between annealing conditions and hysteresis characteristics (see Table 2-3 and Figure 2-9 for detailed values of hysteresis of different electrodes at various pH levels).

Table 2-3. Hysteresis at different pH values for electrodes annealed at different conditions.

Sample ID	Annealing condition		pH=2	pH=4	pH=6	pH=7	pH=8	pH=10	pH=12
A	200 °C 4 min	Absolute value, mV	6.93	8.40	7.41	6.57	10.88	13.56	24.35
		Normalized value	1.29%	1.56%	1.38%	1.22%	2.03%	2.52%	4.53%
B	200 °C 24 h	Absolute value, mV	16.70	9.94	2.02	14.56	16.34	9.75	15.28
		Normalized value	2.43%	1.45%	0.29%	2.12%	2.38%	1.42%	2.22%
C	200 °C 48 h	Absolute value, mV	4.12	5.22	5.21	7.81	6.00	4.63	3.58
		Normalized value	0.65%	0.83%	0.83%	1.24%	0.95%	0.73%	0.57%
D	250 °C 4 min	Absolute value, mV	3.05	2.45	5.86	14.12	16.74	0.76	32.04
		Normalized value	0.46%	0.37%	0.89%	2.15%	2.55%	0.12%	4.88%
E	250 °C 24 h	Absolute value, mV	9.24	10.29	13.66	13.69	4.04	2.71	2.33
		Normalized value	1.56%	1.74%	2.31%	2.31%	0.68%	0.46%	0.39%
F	250 °C 48 h	Absolute value, mV	3.11	12.03	3.21	9.88	7.61	5.00	10.50
		Normalized value	5.17%	2.00%	0.53%	1.65%	1.27%	0.83%	1.75%

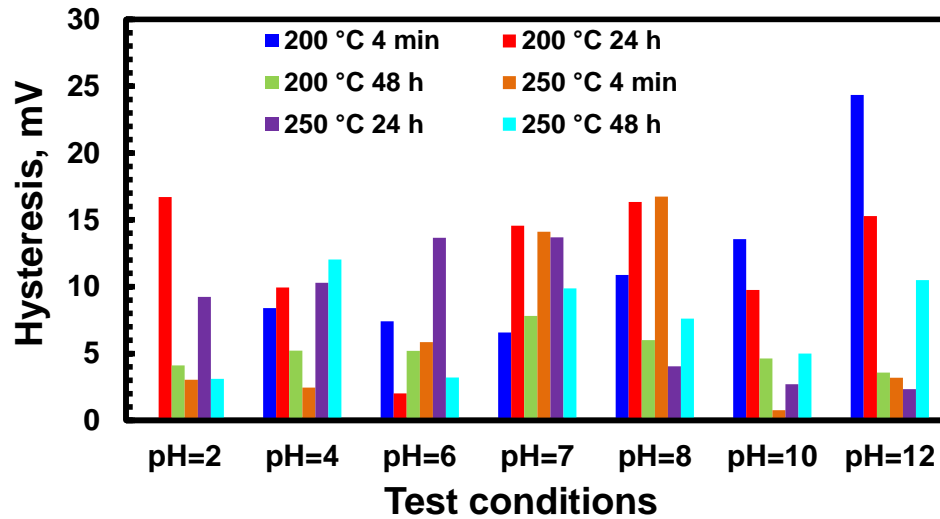


**Figure 2-9.** Hysteresis at different pH values for electrodes annealed at different conditions.

In addition, the electrode annealed at 200 °C for 48 h was continuously monitored in the pH = 7 buffer solution for ~18 h. The drift rate of ~3.25 mV/h of this electrode was comparable with Pd/PdO pH sensing electrodes prepared from thermal oxidation [126], [172]. As a consequence, we suggest the optimized process condition for the Pd/PdO pH sensing electrode was annealing at 200 °C for 48 h.

### 2.3.7. Stability

The stability of pH sensing electrodes is essential for their long-term usage, and can be categorized into operation stability and storage stability. The operation stability was studied by carrying out pH measurements every few days over a 60-day period. Each pH measurement involved 4 pH cycles (2 to 12 to 2 to 12 to 2) with a measurement time of 80 s at each pH level, after which, the average sensitivity was recorded. The electrodes were stored in ambient air at room temperature without any maintenance or special precaution. The evolution of the sensitivity values for electrodes (annealed at 200 °C for 48 h, 250 °C for 4 min, and 250 °C for 48 h) up to 60 days is plotted in Figure 2-10.

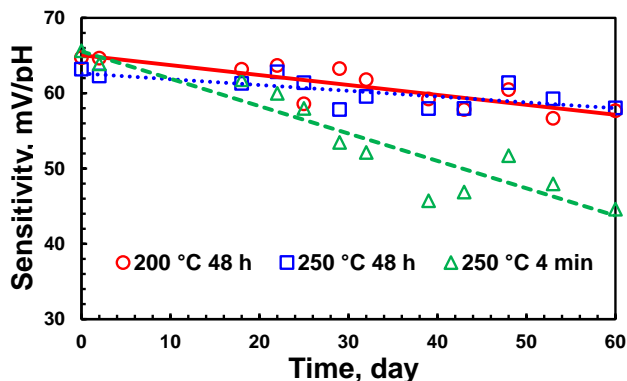


**Figure 2-10.** Operation stability of Pd/PdO pH sensing electrodes over a 60-day period.

For all monitored electrodes, a decrease in sensitivity values was observed. The sensitivity of the electrode annealed at 250 °C for 4 min showed a fast decrease, while the sensitivity degradation of the other 2 electrodes was much slower. Linear fitting of the scattered data was used to calculate the degradation rate of sensitivity, which was -0.36 mV/pH/day for the electrode annealed at 250 °C for 4 min. Electrodes annealed at 200 °C and 250 °C for 48 h exhibited a slow degradation rate (-0.13, and -0.08 mV/pH/day, respectively). In addition, both electrodes still maintained near-Nernstian performance (57.66, and 58.04 mV/pH, respectively) after 60 days.

By comparing the characteristics (chemical composition and surface morphology) of the 3 types of electrodes, it can be inferred that the different operation stability may be caused by the presence of surface nano-voids and the dissimilar percentage of PdO in the bulk. First, acid solutions containing chloride ions ( $\text{Cl}^-$ , from the filling solution of the reference electrode) may enter the nano-voids and react with the Pd in the bulk. The formation of chlorides of Pd gradually degrades the electrodes [201], hence reducing the amount of surface PdO and decreasing the sensitivity. XPS analysis was performed after the operation stability test for the electrode annealed at 250 °C for 48 h. The percentage of surface PdO reduced to ~46%, indicating the degradation of the electrode surface. Second, the reactions between  $\text{Cl}^-$  ions and Pd are accompanied by the transferring of electrons. In the overall reaction, more electrons ( $x$ ) than  $\text{H}_3\text{O}^+$  ions ( $y$ ) are transferred (i.e.  $x > y$ ). Therefore, the sensitivity  $(y/x)(RT/F)$  becomes lower than 59.16 mV/pH at 25 °C. As a result, if a larger

amount of metallic Pd is presented in the bulk of the electrode, then the electrode's surface degrades faster and more electrons are transferred in the overall redox reaction. Both phenomena lead to a faster decrease of sensitivity, which agrees with our observation. Moreover, other studies also found that the electrode aging may include dissolution and reaction of surface Pd when exposed to pH buffer solutions [77], [126]. Thus, the operation stability could be improved by coating the electrode with a  $\text{H}_3\text{O}^+$ -permeable passivation material such as Nafion latex [170]. However, the transport of  $\text{H}_3\text{O}^+$  from the solution to the electrode surface through the coating would result in an increased response time. On the other hand, because of the similar chemical composition but different surface roughness of electrodes annealed at 200 °C and 250 °C for 48 h, it could be inferred that the surface roughness is not an important factor for the operation stability.

Storage stability is a measure of sensitivity degradation during storage before the first measurement. Since the electrode annealed at 200 °C for 48 h showed optimized performance in terms of sensitivity, response time, and operation stability, it was selected to study the storage stability. The electrode was kept in ambient air at room temperature for 60 days before the first pH test. The resulting pH sensitivity after storage was  $64.15 \pm 1.85$  mV/pH (5 measurement cycles), which was comparable with the sensitivity value of newly fabricated electrodes. This result demonstrated that the Pd/PdO sensing film has a minimum shelf-life of 60 days without any special care.

### **2.3.8. Reproducibility**

To study the reproducibility of the fabrication process and sensitivity of Pd/PdO electrodes, 7 electrodes were fabricated with annealing at 200 °C for 48 h. The sensitivity values of these electrodes were: 64.13, 64.92, 64.16, 63.85, 65.08, 63.61, and 64.71 mV/pH, with the average value of 64.35 mV/pH and standard deviation (SD) of 0.56 mV/pH. These consistent results demonstrated that the fabrication process was reliable and repeatable, and the performance of fabricated sensors was reproducible.

## 2.4. Conclusions

Solution-processed Pd/PdO thin films were shown to be a promising pH-sensitive material. XPS, SEM, and AFM studies were used to determine the chemical composition and surface morphology of deposited Pd/PdO films. High sensitivity can be realized by forming more PdO at the electrode surface and in the bulk. Dense and flat surface morphology of the electrode can lead to a fast response. The presence of both metallic Pd and surface nano-voids in the electrodes causes the decreasing of long-term sensitivity. pH sensing electrodes prepared by annealing Pd precursor solution at 200 °C for 48 h exhibited a linear super-Nernstian pH sensitivity of  $64.71 \pm 0.56$  mV/pH in the pH range of 2 to 12 with a short response time less than 18 s, small hysteresis less than 7.81 mV, and high reproducibility with a SD of 0.56 mV/pH in sensitivity. The super-Nernstian behavior may be related to the hydrous PdO<sub>x</sub> ( $x > 1$ ) produced from the solution-based process at low temperatures. Our proposed fabrication process uses solution-based material and does not require high temperature or vacuum equipment, which is compatible with large-area and low-cost manufacturing of high-performance pH sensors on flexible substrates.

## Chapter 3

# Inkjet-printed Pd/PdO for integrated pH sensors\*

An inkjet printing process for depositing Pd thin films from a highly loaded ink (>14 wt%) is reported in this chapter. The viscosity and surface tension of a Pd-organic precursor solution is adjusted using toluene to form a printable and stable ink. A two-step thermolysis process is developed to convert the printed ink to continuous and uniform Pd films with good adhesion to different substrates. Using only one printing pass, a low electrical resistivity of  $2.6 \mu\Omega \cdot \text{m}$  of the Pd film is obtained. To demonstrate the electrochemical pH sensing application, the surfaces of the printed Pd films are oxidized for ion-to-electron transduction and the underlying layer is left for electron conduction. Then, solid-state reference electrodes are integrated beside the bifunctional Pd electrodes by inkjet printing. These potentiometric sensors have sensitivities of  $60.6 \pm 0.1 \text{ mV/pH}$  and  $57 \pm 0.6 \text{ mV/pH}$  on glass and polyimide substrates, and short response times of 11 s and 6 s, respectively. Also, accurate pH values of real water samples are obtained by using the printed sensors with a low-cost multimeter.

### 3.1. Background

Inkjet printing is an easy-to-use and low-cost approach to simultaneously deposit and pattern thin film materials from solutions. This technology can produce structures with fine patterns, consumes a small amount of materials, does not need complicated equipment, and

---

\* Adapted with permission from Y. Qin, A. U. Alam, M. M. R. Howlader, N.-X. Hu, and M. J. Deen, "Inkjet printing of a highly loaded palladium ink for integrated, low-cost pH sensors," *Adv. Funct. Mater.*, vol. 26, no. 27, pp. 4923–4933, Jul. 2016. Copyright (2016) John Wiley and Sons (Appendix E).

is compatible with large-area processing lines for flexible and non-planar substrates [202]. Numerous applications, for example, high-resolution electrodes [203], field-effect transistors [178], solar cells [204], light-emitting devices [205], bio/chemical sensors [206], and bio-printed tissues [207], were enabled by using inkjet printing technology. In these applications, metal nanoparticles, oxides, polymers, and many other materials were inkjet-printed [202]. However, the inkjet printing of an essential material for electrochemistry applications, Pd, is less commonly reported. The lack of printability of Pd and Pd-based materials limited their applications in low-cost electrochemical systems.

Pd and Pd-based materials can be deposited via hydrothermal growth, electrochemical deposition, thermal oxidation, and physical vapor deposition [126], [208], [209]. These processing techniques require a large amount of chemicals, high-pressure chambers, high temperatures, and vacuum equipment. We have demonstrated that spin-coated Pd/PdO thin films can be used as pH sensing electrodes in Chapter 2 [80]. However, the spin coating process consumes a large amount of materials. Also, additional patterning steps are needed to integrate the deposited materials into functional systems. These processing and patterning steps result in costly manufacturing. Therefore, the less complicated and more cost-efficient inkjet printing technique for Pd deposition should be developed.

To the best of my knowledge, inkjet printing of Pd was used to deposit and pattern seed layers for electroless deposition [210]–[212], and also as the contact electrodes for thin-film resistors [213]. The Pd inks used in these studies had low metal content (normally <5 wt%), which resulted in very thin, discontinuous, and high-resistance Pd films. Such Pd films are undesirable for electrochemical sensing because the inefficient electron transfer in the high-resistance films results in a poor sensing performance [166]. One method to reduce the resistance is to print the lightly loaded ink using multiple passes, but this is time-consuming [213]. Alternatively, highly loaded Pd inks and their inkjet printing processes can be developed to deposit continuous, homogenous, and conductive Pd films using a single print pass, thus making it a fast film deposition technique.

In this chapter, we developed an ink loaded with >14 wt% Pd for inkjet printing. The inkjet printing process for such ink is optimized for the deposition of continuous, uniform and low-resistivity thin films with good adhesion to the underlying substrates. Utilizing this ink and printing process, we demonstrate the practical and cost-effective fabrication of an integrated pH sensing platform on both rigid and flexible substrates. Bifunctional sensing electrodes are fabricated by oxidizing the printed Pd. The PdO-rich surfaces function as pH sensing layers and the conductive portion beneath the surfaces are electron conduction paths. Solid-state reference electrodes are inkjet-printed besides the sensing electrodes to form potentiometric sensors. The integrated sensors exhibited high sensitivity, fast response, good stability, and were highly accurate in measuring real water samples.

## **3.2. Inkjet printing of Pd/PdO pH sensing electrodes**

### **3.2.1. Pd Ink formulation and properties**

The as-received Pd precursor solution contains a Pd-organoamine complex. Since the specific amine ligand significantly increases the solubility of the Pd complex in toluene, the metal load for this precursor solution can be as high as ~18.5 wt% (Table 3-1). In addition, the organoamine ligand helps to prevent crystallization of the precursor upon solvent evaporation. Therefore, it is possible to use this Pd precursor solution for thin film deposition.

Two important parameters, viscosity and surface tension, must be considered when developing inks for inkjet printing. For the printhead used in this study, the ink's viscosity ( $\eta$ ) <9 cP and surface tensions ( $\gamma$ ) of ~30 mN/m is preferred. Regarding the as-received Pd precursor solution, its viscosity was 31.54 cP and its surface tension was 33 mN/m, as listed in Table 3-1. Although the surface tension was in the suitable range, its high viscosity made jetting difficult even at the maximum firing voltage (40 V) and a printhead temperature of

50 °C (higher temperature was not desired due to fast solvent evaporation). Thus, the viscosity of the Pd precursor solution was reduced by dilution.

Six criteria should be considered when formulating low-viscosity Pd inks:

1. The dilution solvent should be miscible with the precursor solution.
2. The Pd content should stay high to attain a thick and conductive layer after one printing pass.
3. The dilution solvent should have a surface tension of ~30 mN/m and a viscosity <9 cP.
4. Low jetting voltages should be applied to avoid the formation of satellite droplets.
5. Printhead temperatures <50 °C should be used to prevent nozzle clogging caused by fast solvent evaporation.
6. The dilution solvent should have a boiling point (BP) >100 °C to avoid rapid ink drying during storage.

**Table 3-1.** Physical properties, key jetting parameters, and thermolysis parameters for the functional inks.

Ink	Functionality	Solvent	Major ink properties				Key jetting parameters <sup>b</sup>		Thermolysis parameters	
			Solvent BP, °C	Solid content, wt%	$\eta^a$ (25 °C), cP	$\gamma$ (22 °C), mN/m	$T$ , °C	Peak voltage, V	$T$ , °C	$t$ , min
Pd precursor	pH sensing electrode	Toluene	110	18.5	31.54	33.0	Not jettable			
Pd-PhMe	pH sensing electrode	Toluene	110	14.8	12.99	30.5	40	26	120 & 200	2 & 4
Pd-IBB	pH sensing electrode	Isobutylbenzene	170	14.1	12.44	29.9	40	26	170 & 200	2 & 4
SU-8	Adhesion layer for Ag	PGMEA	145	7.4	1.96	27.5	25	17	90 & 200	2 & 60
Ag NP	Reference electrode	Hydrocarbon	110	50	4.5	29.0	30	22	120	10
NaOCl	Chlorinate Ag to AgCl	DI water + 2 vol% Triton X-100	100	0.4	0.92	31.1	25	26	-	-
PVC/KCl/AgCl	Electrolyte for reference electrode	Cyclohexanone	155	2.0	8.18	34.5	40	26	160	10

<sup>a</sup>  $\eta$ , viscosity;  $\gamma$ , surface tension;  $T$ , temperature;  $t$ , time.

<sup>b</sup> Substrate temperature = 25 °C in all cases.

Based on the 6 criteria, Pd-IBB and Pd-PhMe, as low-viscosity Pd inks, were prepared by mixing 80 wt% precursor solution with 20 wt% isobutylbenzene (IBB) and 20 wt% toluene (PhMe), respectively. TG analysis (TGA) test results in Figure 3-1 showed that the Pd

contents of both Pd-IBB and Pd-PhMe were greater than 14 wt%, ~3 times higher than other Pd precursor solutions [214]. After dilution, the viscosities of Pd inks reduced to 12-13 cP at 25 °C while their surface tensions were kept ~30 mN/m (Table 3-1). At 40 °C, the viscosity of Pd-IBB and Pd-PhMe was 8.50 cP and 8.93 cP, respectively. Consequently, using a peak firing voltage of 26 V at 40 °C nozzle temperature, both inks could be jetted stably at a droplet velocity of ~10 m/s without forming satellite droplets. Also, cleaning cycles for unclogging nozzles were not required for a 1-hour printing job. To study storage stability, newly prepared Pd inks were kept in capped cartridges at  $27 \pm 2$  °C in ambient air. After 2 weeks, both inks could be jetted using the same parameters shown in Table 3-1.

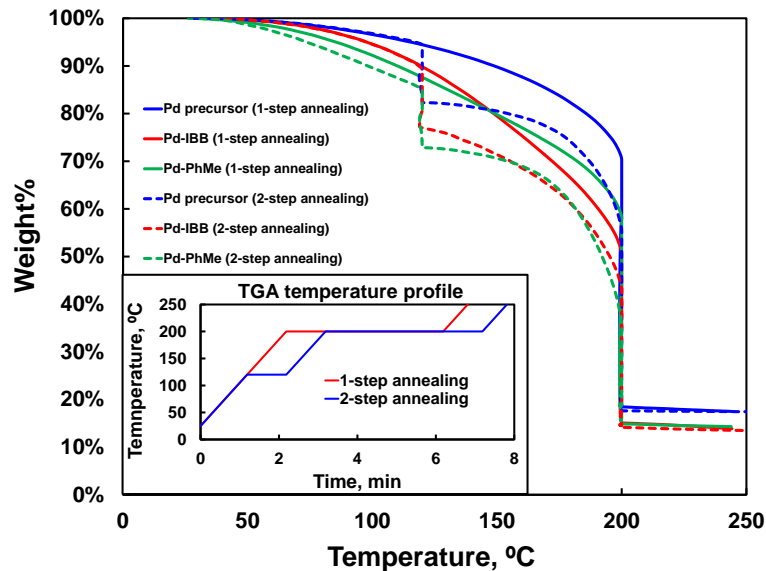


**Figure 3-1.** TGA test results of as-received Pd precursor solution, Pd-PhMe, and Pd-IBB using 1-step and 2-step thermolysis methods (inset: temperature profiles of 1-step and 2-step thermolysis).

### 3.2.2. Formation of Pd thin films

The inkjet printer used in this study was a Dimatix DMP-2831 materials printer (Fujifilm), equipped with DMC-11610 Dimatix materials cartridges (Fujifilm). The cartridge was accompanied with a 16-nozzle piezoelectric printhead, which could jet ~10  $\mu$ L ink per droplet. All inks (~1.5 mL each) were filtered through Whatman GD/X syringe filters (polytetrafluoroethylene membrane, pore size 0.2  $\mu$ m, WHA68741302, Sigma-Aldrich) before loading to the cartridges. The jetting waveforms for Pd is shown in Figure 3-2. Other parameters include the firing frequency of 2 kHz and the meniscus vacuum of 0.18 psi.

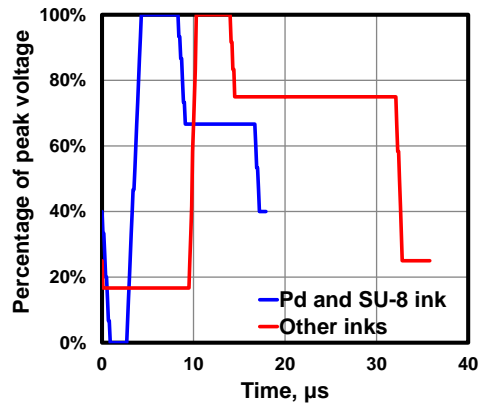


**Figure 3-2.** Voltage waveforms of the printhead for jetting different inks.

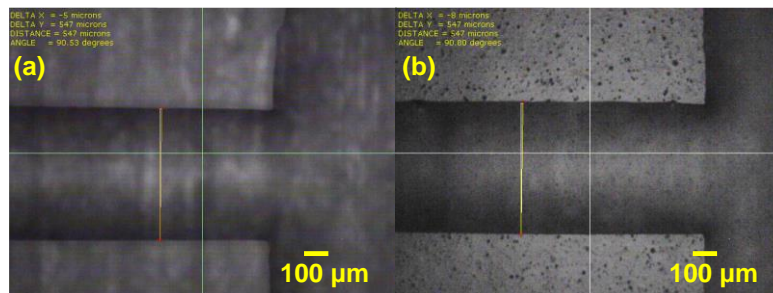


**Figure 3-3.** Photographs showing wetting behaviors of inkjet-printed Pd-PhMe ink on different substrates. (a) On glass, 547  $\mu\text{m}$ -wide lines. (b) On PI treated by air plasma for 2 min, 547  $\mu\text{m}$ -wide lines. (Droplet pitch = 30  $\mu\text{m}$ , designed line width = 520  $\mu\text{m}$  in both cases.)

The wetting behaviors of as-received Pd precursor, Pd-IBB, and Pd-PhMe were studied on glass and polyimide (PI, Kapton<sup>®</sup> 200HN, DuPont) surfaces. Before inkjet printing, all glass and PI substrates were cleaned by rinsing with IPA and DI water, followed by drying under compressed dry air. On glass substrates, all 3 types of inks showed good wetting. Figure 3-3(a) display the printed Pd-PhMe on a glass substrate. As shown, a continuous and uniform ink layer was obtained. The measured line width of a printed Pd-PhMe layer was 547  $\mu\text{m}$ , close to the designed values of 520  $\mu\text{m}$ . The surfaces of some glass substrates were also treated using air plasma for 2 min using a plasma cleaner (PDC-32G, Harrick Plasma) with a background pressure of 200 mTorr and an RF power of 18W. However, the Pd inks printed on plasma-treated glass substrates showed poor wettability. Therefore, we focused on using the glass substrates cleaned by IPA and DI water here. More investigation is needed to study the mechanism for the dewetting of the Pd inks, but this is out of the scope of the current study. On the as-received PI substrates, the Pd inks showed a poor

wetting behavior due to the low surface energy of PI. Thus, the surface of PI was treated using air plasma for 2 min to increase its surface energy for better pattern definition (treatment for longer times had no significant effect). Figure 3-3(b) shows a printed Pd-PhMe layer on a treated PI substrate with a well-defined line of 547  $\mu\text{m}$  wide (close to the designed value of 520  $\mu\text{m}$ ).

Printed Pd-PhMe were converted to metallic Pd using thermolysis. Two thermolysis temperature profiles (Figure 3-1) were compared to optimize the morphology of the printed Pd films. On the one hand, Pd inks were heated up to 200  $^{\circ}\text{C}$  on a hotplate in air for 4 min (1-step thermolysis). During this period, the solvent of the ink evaporated, the precursor decomposed to Pd NPs, and metallic Pd films formed. Figure 3-4(a) is a SEM image showing the morphology of a Pd film prepared by 1-step thermolysis of printed Pd-PhMe (30  $\mu\text{m}$  droplet pitch) on a glass substrate. Pinholes with diameters <100 nm and a non-uniform film can be observed. Such surface morphology was caused by the decomposition of organic compounds in the Pd precursor and the unevenly distributed agglomeration of Pd NPs. When the ink was heated up to 200  $^{\circ}\text{C}$  in 1 step, the solvent evaporation and the generation of Pd NPs happened simultaneously. When the ink was not fully dried, Pd NPs were surrounded by residual solvent. Pd NPs in the liquid phase could move and aggregate with nucleation centers more easily than in the solid phase. Since the Pd NPs were transported unevenly, thicker and thinner regions were formed once the solvent evaporation and precursor thermolysis were completed. The thicker regions were denser while the thinner regions consisted of pinholes or cracks.

Based on the 1-step thermolysis discussed above, a 2-step thermolysis was used to improve the film morphology. In the first step, the printed Pd ink was heated up to 120  $^{\circ}\text{C}$  in air for 1 min to evaporate most of the solvent. Then, the temperature was increased to 200  $^{\circ}\text{C}$  to decompose the precursor and produce a uniform Pd layer ~100 nm in thickness. In the second step, Pd NPs were generated in solid phase and immobilized on the substrate to coalesce into a uniform film. Figure 3-4(b) is the SEM image of a homogeneous Pd film

prepared by the 2-step thermolysis of printed Pd-PhMe on a glass substrate. Pd printed on PI (2 min plasma treatment, 2-step thermolysis) exhibited a dense morphology with few pinholes (Figure 3-4(e)). During plasma treatment, nitrogen moieties (such as  $-N=C<$ ) were generated on the surface of PI and served as bonding sites for Pd atoms [215]. The bonded Pd atoms behaved as nucleation centers and were uniformly distributed, resulting in a homogeneous Pd film of  $\sim 80$  nm thick.

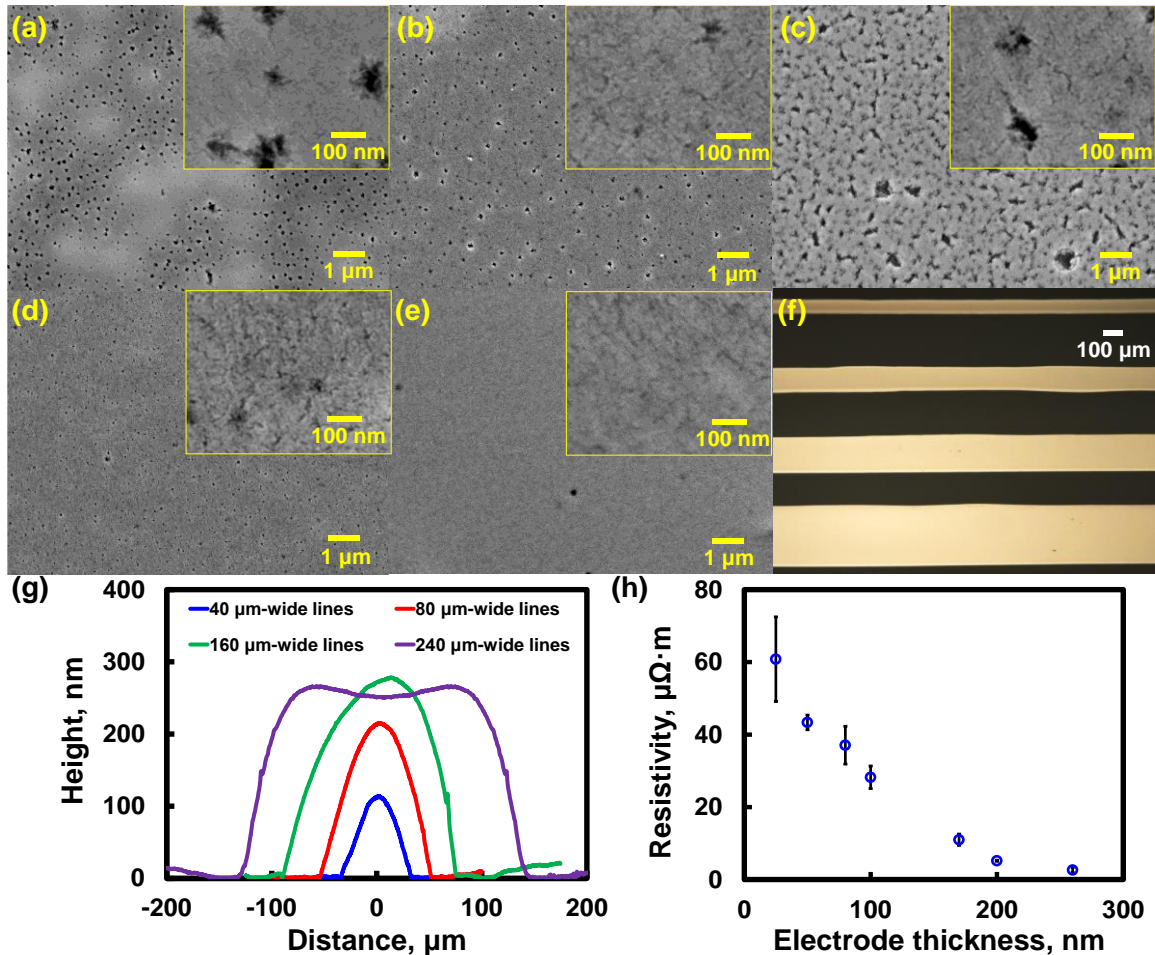


**Figure 3-4.** (a-e) SEM images of surface morphologies of Pd films printed using Pd-PhMe ink. (a) 30  $\mu\text{m}$  droplet pitch, glass substrate, 1-step thermolysis; (b) 30  $\mu\text{m}$  droplet pitch, glass substrate, 2-step thermolysis; (c) 40  $\mu\text{m}$  droplet pitch, glass substrate, 2-step thermolysis; (d) 20  $\mu\text{m}$  droplet pitch, glass substrate, 2-step thermolysis; (e) 30  $\mu\text{m}$  droplet pitch, PI substrate, 2-step thermolysis; (f) Optical microscopy image of 2-step thermalized Pd lines printed using Pd-PhMe ink with 20  $\mu\text{m}$  droplet pitch on a glass substrate. (g) Thickness profiles of printed Pd lines shown in (f). (h) Thickness dependence of the resistivity of printed Pd.

Regarding Pd-IBB, a 2-step thermolysis was also performed. However, a rough film was obtained after thermolysis at 170  $^{\circ}\text{C}$  (170  $^{\circ}\text{C}$  was selected due to the higher BP of IBB) for

1 min and 200 °C for 4 min (Figure 3-5). The rough surface indicated that a large amount of residual solvent (IBB) existed on the substrate when Pd NPs were generated. IBB evaporated slowly because of its low vapor pressure (~1.8 hPa, comparing to ~29 hPa of PhMe and ~23 hPa of water at 20 °C). Since a 15-min evaporation step was needed to remove the IBB in the ink, the process was inefficient and not used in following studies.

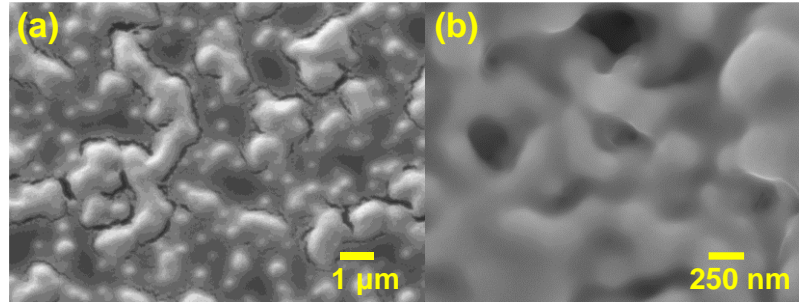


**Figure 3-5.** SEM images of surface morphologies of a printed Pd layer using Pd-IBB as ink and 2-step thermolysis. (a) A typical inhomogeneous surface morphology. (b) Magnified view of (a).

The surface morphology of printed Pd was also a function of film thickness. Pd films of 50 nm (Figure 3-4(c)), 100 nm (Figure 3-4(b)), and 200 nm (Figure 3-4(d)) thick was obtained by printing Pd-PhMe on a glass substrate with a droplet pitch of 40 μm, 30 μm, and 20 μm, respectively. In the 50 nm thick film, pinholes were larger (comparing to the 100 nm thick film) and multiple pinholes connected to form cracks. In the 200 nm thick film, the pinholes were smaller. These results indicated the importance of having a large amount of metal in deposited the ink to attain a thick Pd film free of pinholes and cracks.

The “coffee-stain” effect also reduces the uniformity of inkjet-printed films and is not desired for many applications [216]. To reduce this effect, increasing the solid content in the inks, adding cosolvents with high BPs to the inks, and increasing the substrate temperature were shown to be effective [216]. In our study, Figure 3-4(f) shows the optical microscopy image of printed Pd lines using Pd-PhMe with 20 μm droplet pitch on a glass substrate. The thickness profiles of these lines are shown in Figure 3-4(g). As the designed line width increased from 40 μm to 240 μm, the thickness of Pd film increased from ~100 nm to ~260 nm. Due to the high metal content (~14 wt%) of the ink, the “coffee-stain”

effect was not apparent although the ink was single-solvent-based and the substrate was at  $27 \pm 2$  °C.

### 3.2.3. Electrical resistivity of inkjet-printed Pd thin films

A low resistance of the printed metal layer is required for electrical interconnections and low-impedance electrochemical sensing electrodes. From subsection 3.2.2, we qualitatively observed that a thicker printed Pd film consisted of less pinholes and cracks. The elimination of pinholes and cracks would result in a low electrical resistance of the films. From section 3.2.2 and Figure 3-4(b-d), one can observe that the morphology of the printed Pd film strongly depends on the film thickness. Also, the film morphology is not affected by the width or length of the film (Figure 3-4(f)). Thus, the effective resistivity of the printed Pd films was measured and calculated as a function of film thickness (Figure 3-4(h)). Pd lines with different thicknesses were printed on glass (Pd-PhMe, 2-step thermolysis) by varying the designed line width and the droplet pitch. From resistance ( $R_{ele}$ ) measurements, the effective resistivity ( $\rho$ ) was calculated using:

$$\rho = R_{ele} h \frac{W}{L}, \quad (3.1)$$

where  $h$ ,  $W$  and  $L$  are the measured thickness, width and length of the printed Pd lines, respectively (Figure 3-6).

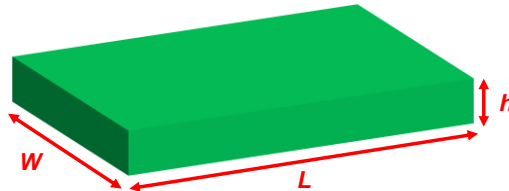


**Figure 3-6.** Schematic of the physical dimensions of a printed Pd/PdO film.

For a 25 nm thick Pd film, its effective resistivity was  $60 \mu\Omega \cdot m$ , much higher than that of bulk Pd ( $\sim 0.1 \mu\Omega \cdot m$ ). When the Pd thickness increased, the effective resistivity decreased as expected, since the films became denser (Figure 3-4(b-e)). A printed Pd film of 260 nm thick had a low effective resistivity of  $2.6 \mu\Omega \cdot m$ , which is close to a previous result obtained by printing 5 passes of a lightly loaded ink [213]. Here, we take advantage of the highly

loaded Pd ink to get a low-resistance film using only 1 printing pass. However, this effective resistivity is still higher than that of metallic Pd. This higher effective resistivity suggested a dependence on factors other than the film morphology. Therefore, the chemical composition of the printed Pd films was investigated.

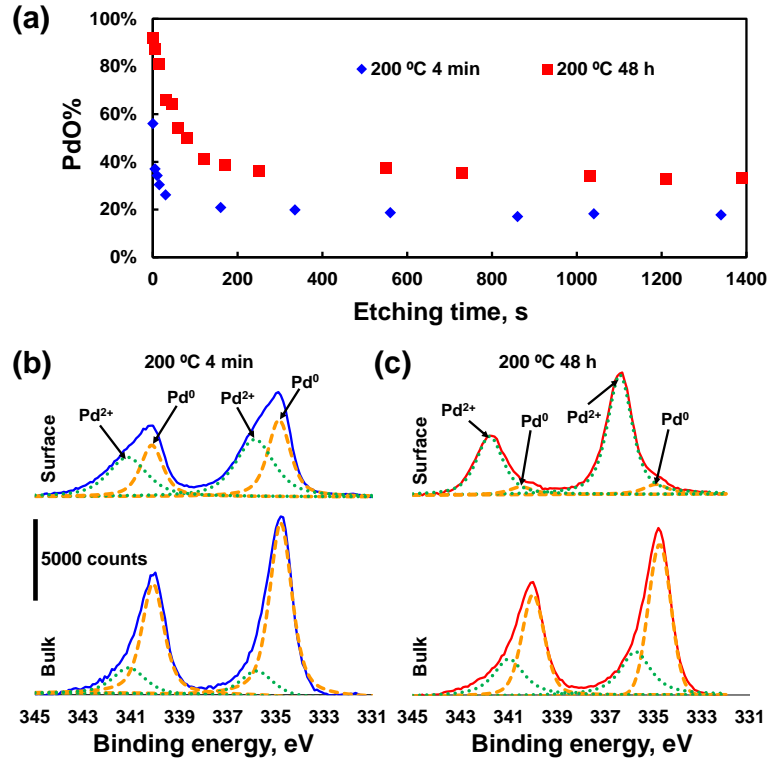


**Figure 3-7.** (a) Depth-dependent chemical compositions of printed Pd films thermalized at 200 °C for 4 min and 48 h obtained by XPS depth profiling. (b) Pd 3d XPS spectra and curve fitting of the surface and bulk of printed Pd thermalized at 200 °C for 4 min. (c) Pd 3d XPS spectra and curve fitting of the surface and bulk of printed Pd annealed at 200 °C for 48h.

Figure 3-7(a) shows the depth profiles of PdO percentage for 100 nm thick Pd films based on XPS analyses. For the film obtained right after thermolysis (200 °C, 4 min), its surface contained ~56% PdO (curve fitting is shown in Figure 3-7(b)) while its bulk contained ~17% PdO. The PdO was formed by the oxidation of Pd by O<sub>2</sub> in air during the thermolysis at 200 °C [209]. Therefore, the presence of PdO resulted in the effective resistivity of the printed film being higher than metallic Pd. When the film thickness decreased, the effect of surface PdO and pinholes were more pronounced. As a result, the effective resistivity of thinner films was higher than that of thicker films. In summary, the effective electrical resistivity of a printed Pd film was dominated by two factors: film morphology and

chemical composition. Moreover, the distribution of PdO in the XPS depth profiling results showed a diffusion-limited profile. This profile was formed because the oxidation of Pd during thermolysis is primarily supported by O<sub>2</sub> in air. Thus, a bilayer structure with higher PdO concentration close to the surface and a more conductive layer underneath. In order to obtain a highly conductive Pd film, the concentration of PdO should be low.

### 3.2.4. Adhesion of inkjet-printed Pd thin films

In printed flexible devices, adhesion between the printed structures and the underlying substrates is critical for the devices' stability and reliability. Film adhesion is especially important when it is used in a severe environment such as in a liquid [217]. The adhesion test results of printed Pd films on glass and PI substrates are listed in Table 3-2. On glass substrates, thin Pd films could pass the water rinse and scotch tape tests, but thick Pd films could be peeled off with the tape. The better adhesion of the thinner Pd films may be attributed to two reasons: the larger amount of pinholes/cracks in the films and the smaller film thickness. First, in thin Pd films, pinholes and cracks (Figure 3-4(b-d)) created many inter-domain boundaries. The Pd atoms at the boundaries had a less ordered structure, hence a higher surface energy [218]. A thin film with a higher surface energy has a stronger tendency to be attracted to another surface, which results in a stronger adhesion between deposited films and substrates [219], [220]. Thus, the adhesion between thin Pd films and the substrates were better. Second, the stress in thin films promotes their delamination [221]. The adhesion between a thin film and a substrate can be quantitated by strain energy release rate ( $G_s$ ), which is proportional to the film thickness ( $h$ ) according to [222]:

$$G_s = \frac{Z_c \sigma_f^2 h}{E_f}, \quad (3.2)$$

where  $Z_c$  is a dimensionless cracking parameter,  $\sigma_f$  is the stress in the film, and  $E_f$  is the modulus of elasticity. A thicker film has a larger strain energy release rate, indicating the film delaminates from the substrate more easily for stress release. In addition to this theoretical explanation, our observation also agrees well with previous experimental results [219], [223], [224].

**Table 3-2.** Adhesion test results of inkjet-printed thin films.

Printed material	Substrate	Film thickness, nm	Water rinse test	Scotch tape test
Pd	Glass	35	Pass	Pass
Pd	Glass	70	Pass	Pass
Pd	Glass	100	Pass	Fail
Pd	Glass	150	Pass	Fail
Pd	Glass	200	Pass	Fail
Pd	PI	100	Pass	Pass
Pd	PI	200	Pass	Pass
Ag	Glass	300	Pass	Fail
Ag	Glass	650	Fail	Fail
Ag	PI	300	Fail	Fail
Ag	PI	650	Fail	Fail
Ag	SU-8	300	Pass	Pass
Ag	SU-8	650	Pass	Pass
SU-8	Glass	200	Pass	Pass
SU-8	PI	200	Pass	Pass
PVC/KCl/AgCl	Glass	100	Pass	Fail
PVC/KCl/AgCl	Glass	100000 <sup>a</sup>	Fail	Fail
PVC/KCl/AgCl	PI	100	Pass	Pass
PVC/KCl/AgCl	PI	100000 <sup>a</sup>	Pass	Fail
PVC/KCl/AgCl	SU-8	100	Pass	Pass
PVC/KCl/AgCl	SU-8	100000 <sup>a</sup>	Pass	Pass

<sup>a</sup> Manually printed.

In contrast, on the PI substrates treated by air plasma for 2 min, thick Pd films exhibited good adhesion. Although the plasma-introduced oxygen-containing groups are reactive to the deposited Pd, we believe the improved adhesion was mainly attributed to the generation of nitrogen-containing groups at the surface of PI during the plasma treatment [215]. The presence of the nitrogen-containing groups was proven in previous studies by using XPS and FTIR spectroscopy [215], [225]. The nitrogen atoms in the nitrogen-containing groups have unbonded electron pairs, which can serve as ligands for Pd [215], [226]. Therefore, the improved adhesion of Pd on PI was due to the higher affinity of nitrogen towards Pd than that of oxygen towards Pd. Figure 3-8 shows the AFM images of glass and PI surfaces. After the 2-min plasma treatment, the PI surface had a RMS roughness of 0.83 nm, which was about a half of the roughness of the glass substrate. The smooth PI surface indicated insignificant mechanical interlocking between Pd and PI. Thus, chemical bonding was the major factor for a strong adhesion between the printed Pd and PI substrates.

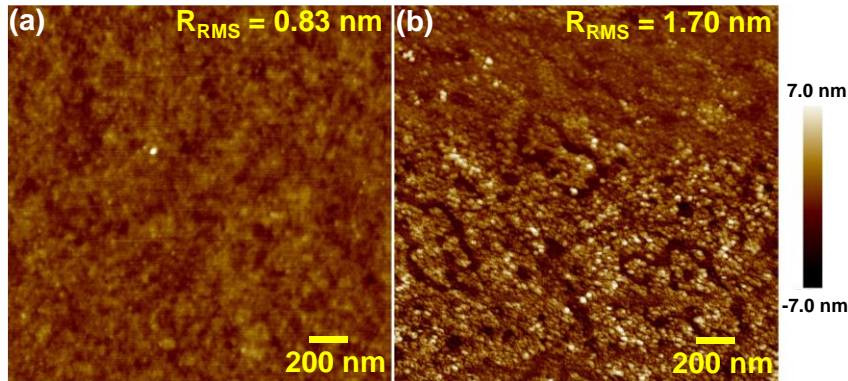


**Figure 3-8.** AFM images of different substrates. (a) PI treated by air plasma for 2 min. (b) Glass.

### 3.2.5. Modeling the response of the pH sensing electrodes

According to Chapter 1 and Chapter 2, in a Pd/PdO electrochemical pH sensor, the sensing electrode should possess the following characteristics.

- An oxide-rich surface for the ion-to-electron transduction based on the redox reaction (see reaction (2.4)).
- A low-resistance bottom layer for electron conduction.
- A good adhesion with the substrate for stable operation in the aqueous environment.

To demonstrate the usability of the printed Pd films, Pd/PdO printed sensing electrodes (PSEs) were fabricated by annealing the printed Pd at 200 °C for 48 h. After annealing, the PdO-rich surfaces (Figure 3-7(a) and (c)) functioned as the pH sensitive layers. The bulk of the electrodes had less PdO and a higher conductivity, functioning as the electron conducting layers. Thus, even though the PSEs were deposited using only one material, they played a dual role. This makes our fabrication process simpler than that in other studies where the sensing and electron conduction layers were deposited separately [166].

When the Pd/PdO PSE is immersed into an electrolyte solution, the fast and reversible redox reaction (2.4) occurs at or near the electrode-electrolyte interface for charge transfer [227]. Such a redox reaction involves electron exchange, hence, a pseudocapacitor ( $C_F$ ) and a charge transfer resistance ( $R_F$ , in series with  $C_F$ ) can be used to model this electrochemical reaction (Figure 3-9). In addition, a double layer capacitor ( $C_{DL}$ , in parallel with  $C_F$  and  $R_F$ )

consisting of a diffusion layer capacitor ( $C_D$ ) and a Stern layer capacitor ( $C_S$ , in series with  $C_D$ ) can be used to represent the formation of the electrical double layer at the electrode-electrolyte interface. The specific capacitance of the pseudocapacitor at a transition metal oxide surface (can be  $>1000$  F/g) is much larger than that of the double layer capacitor (normally  $<100$  F/g) [227]. Therefore, the charge exchange behaviors or the pH sensing properties at the PSE surface is mainly determined by the pseudocapacitor and the charge transfer resistance. Considering the electrode resistance ( $R_e$ ), the PSE immersed in a solution can be modeled as a lumped resistor ( $R_m$ ) with a lumped capacitor ( $C_m \approx C_F$ ). The charge transfer resistance is usually small ( $<1$  k $\Omega$ ) and has a negligible effect on the signal readout [228], [229], so  $R_m$  is mainly determined by the electrode resistance ( $R_m \approx R_e$ , tens of k $\Omega$ ). In addition, the same Pd/PdO film is used as the electrical connection that is not immersed in the electrolyte, so charges generated in the PSE can be stored in the dry part of the Pd/PdO film, so a parasitic capacitor ( $C_e$ ) is used to represent this charge storage effect. Moreover, the electronic set-up (Figure 2-1(d), including cables, clamps, and the semiconductor parameter analyzer) has a small lumped capacitance  $C_c$  ( $<10$  nF), and a large input resistance  $R_c$  ( $R_c > 1$  T $\Omega$  for the set-up in this study).

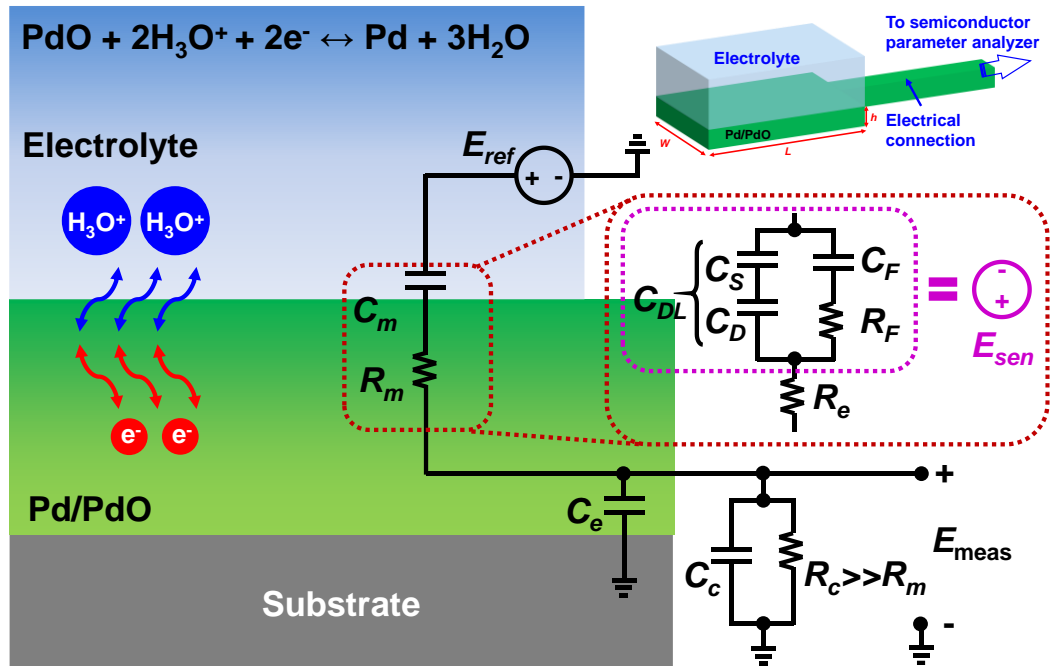


Figure 3-9. Equivalent circuit model for determining the pH response at the Pd/PdO-electrolyte interface.

When the pH value of a solution undergoes a step change, the sensor output cannot response to this pH change immediately. Instead, a certain amount of time is needed for the sensor output to vary from the initial value to another stable value [230]–[232]. This delayed response is believed to consist of a series of responses with different speed, which can be expressed by different time constants. Thus, the normalized sensor output ( $O(t)$ ) can be written using a multiple time constant model [230]–[232]:

$$O(t) = \Delta E_{sen} \times \Delta \text{pH} \times \left[ 1 - \sum_{i=1}^n \varepsilon_i \exp\left(-\frac{t}{\tau_i}\right) \right] \quad (t > 0), \quad (3.3)$$

where  $t$  is time,  $\Delta E_{sen}$  is the theoretical pH sensitivity of the sensor ( $\sim 65$  mV/pH, according to section 2.3.4),  $\varepsilon_i$  and  $\tau_i$  are the normalized amplitude and time constant of the corresponding exponential term  $i$ , respectively. The time constant  $\tau$  with a smaller value indicates a faster response. In our Pd/PdO-based pH sensors, several factors affect the delayed response:

- The fast response is determined by the reaction of surface sites, which forms the pseudocapacitor ( $C_F$ ). This process can be modeled using the equivalent circuit in Figure 3-9, and the time constant is a resistor-capacitor constant with a small value (within several seconds) [230]–[232].
- In addition to the fast response, a dispersive transport model can be used to illustrate the reaction between the  $\text{H}_3\text{O}^+$  ions in the solution and the buried sites in the sensing electrode [233], [234]. This dispersive transport process also exhibits an exponential relation with time, which is considered to be the cause of the long-term drift of the sensor. The time constant of this process is in the order of minutes to tens of hours, depending on the density of reaction sites, the physical/chemical defects, and many other electrical properties of the sensing material. Due to the lack of the study on these properties of Pd/PdO, the theoretical calculation of the time constant of the dispersive transport process is extremely difficult.
- Moreover, the delayed sensor response also depends on other factors, such as the leaching of the electrolyte in the reference electrode and the mechanical delamination of the sensing material from the substrate. These processes may not show a significant

effect on the sensor response in a short period of time, but may cause a large drift in the sensor output in hours and days (or even a longer period of time).

Because the dispersive transport process, the electrolyte leaching, and the material delamination is not a reversible process (or not reversible in a short period of time), the sensor response shows hysteresis when the solution pH is cycled between different values. The hysteresis ( $W_{hyst}$ ) also depends on the time constant of each process, and it can be expressed by [230]–[232]:

$$W_{hyst} = \Delta E_{sen} \times \sum_{i=1}^n 2\varepsilon_i r_i \left[ 1 - \frac{2 \exp(0.5/r_i)}{1 + \exp(1/r_i)} \right], \quad (3.4)$$

where  $r_i = \tau_i/t_s$ , and  $t_s$  is the time used for the measurement at a pH value (90 s in our study).

To extract the time constants from experimental results using the abovementioned model, pH sensing measurements were carried out in buffer solutions with pH = 4, 5, 6, 7, 8, 9, and 10. Each pH step change is 1 pH unit. The normalized experimental data was fitted using equation (3.3) and plotted in Figure 3-10. The extracted normalized amplitude values and time constants are shown in Table 3-3.

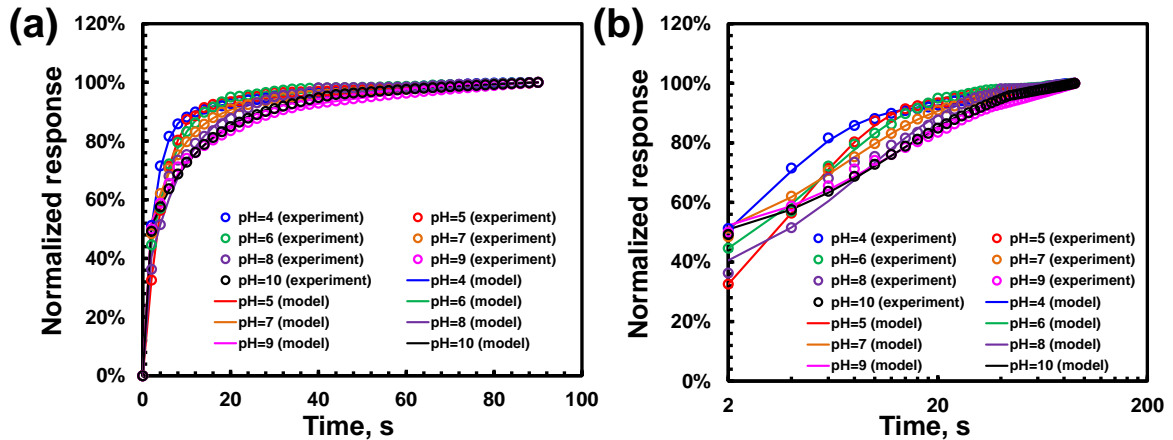


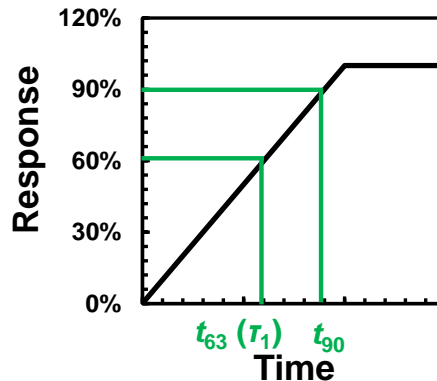
**Figure 3-10.** Comparison between experimental data and modeling results (two time constant model) of the sensor response towards a pH step change. (a) Linear time scale. (b) Logarithm time scale.

**Table 3-3.** Extracted parameters for a two time constant model for the modeling of the pH step response.

pH	4	5	6	7	8	9	10
$\varepsilon_1$	0.70	0.83	0.63	0.44	0.62	0.36	0.45
$\tau_1$ , s	2.93	4.12	5.93	7.23	9.15	10.38	11.99
$\varepsilon_2$	0.19	0.22	0.16	0.23	0.13	0.26	0.16
$\tau_2$ , s	141.67	347.52	369.35	265.78	280.60	159.57	171.20
$t_{90}$ (model), s	4.40	6.19	8.90	10.85	13.73	15.57	17.99
$t_{90}$ (experiment), s	7.00	7.67	10.33	11.00	14.00	15.33	18.00
Hysteresis (model), mV	5.26	6.3	6.49	6.34	9.48	8.17	9.42
Hysteresis (experiment), mV	7.41	8.02	8.50	8.10	9.28	11.03	11.66

From Table 3-3, we can observe that  $\tau_1$  has a larger amplitude  $\varepsilon_1$  (than  $\varepsilon_2$ ) at all pH values, indicating the response time of the sensor is mainly determined by the fast process (the “formation” of the pseudocapacitor due to the redox reactions). In addition,  $\tau_2$  has a larger value but smaller amplitude than  $\tau_1$ , which suggests that the dispersive transport of ions is a slower process and does not significantly affect the overall sensor response in a short period of time (90 s in this case). Because the sensor response curves are steep for  $t < 15$  s (Figure 3-10), a linear approximation can be used to calculate the response time ( $t_{90}$ ) of the sensor (Figure 3-11). The time constant is defined as the time required for the output to reach ~63% of its final value, thus the response time can be calculated by:

$$t_{90} \approx 1.5\tau_1. \quad (3.5)$$

**Figure 3-11.** The linear approximation of the sensor response for the calculation of response time using the time constant extracted from the two time constant model.

In Figure 3-12, we can observe that the response time values obtained by experimental measurements agree well with the theoretical calculations using the extracted  $\tau_1$  and equation (3.5), showing the feasibility of using the two time constant model to predict the sensor performance. Another feature in Figure 3-12 (for both experimental and modeling

results) is that the response time is longer in solutions with larger pH values. This slower response in basic solutions may be due to the abundance of  $\text{OH}^-$  ions, whose mobility is lower than that of  $\text{H}_3\text{O}^+$  ions.

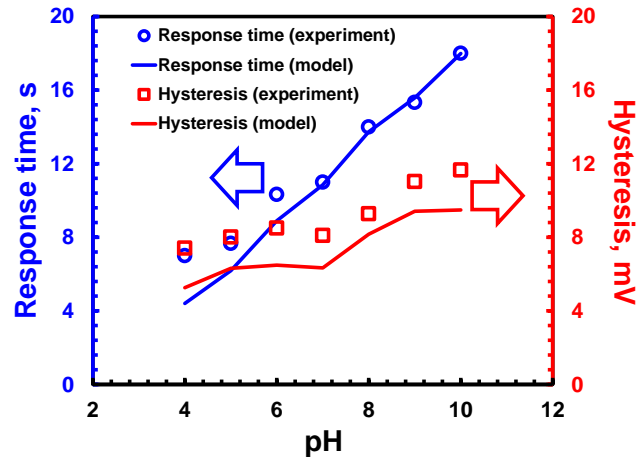


**Figure 3-12.** Comparison between the sensor response time and hysteresis obtained by experimental measurements and theoretical calculation using the two time constant model.

In addition to the response time, the hysteresis of the sensor at different pH values are calculated using equation (3.4) and the extracted time constant parameters in Table 3-3. Generally, the theoretical calculation can predict the trend of the hysteresis, but its values are underestimated. The underestimation may be due to other non-reversible processes that are not considered in the two time constant model, for example the mechanical delamination of the sensing material.

### 3.2.6. Design of Pd/PdO pH sensing electrodes

To optimize the physical dimensions of the printed pH sensing electrode, the optimal thickness and area of the electrodes are obtained by theoretical modeling, whose results are compared with experimental observations.

The electrode with a thickness ( $h$ ) of 100 nm and sensing area of  $10 \text{ mm}^2$  ( $W = 2 \text{ mm}$ ,  $L = 5 \text{ mm}$ ) is used as the start condition. Because the response time of the sensor (average value of 11.1 s) is mainly determined by the fast redox reaction process (discussed in section 3.2.5), the average time constant of 7.4 s can be estimated using equation (3.5). In the

equivalent circuit in Figure 3-9, the time constant of this redox reaction process is determined by the lumped electrode capacitance and resistance. Thus, we can write:

$$\tau_1 = R_m C_m = R_e C_F = R_e C_{spec} m_e = R_e C_{spec} \rho_{PdO} W L h_{surf} = 7.4 \text{ s}, \quad (3.6)$$

or

$$\tau_1 = R_e C_0 W L = 7.4 \text{ s}, \quad (3.7)$$

where  $R_e \approx 40 \text{ k}\Omega$  is the measured electrode resistance,  $C_{spec}$  is the specific pseudocapacitance of the Pd/PdO sensing material,  $m_e$  is the mass of the electrode surface layer, and  $\rho_{PdO}$  is the density of PdO,  $h_{surf} \approx 10 \text{ nm}$  is the thickness of the surface Pd/PdO which participate in the redox reaction [235],  $C_0 = \rho_{PdO} h_{surf} C_{spec}$  is the pseudocapacitance of the Pd/PdO sensing material per unit area. Note that the parasitic capacitance  $C_e$  can be neglected here because its value is much smaller than the pseudocapacitance  $C_F$ . Therefore, we can find:

$$C_{spec} = 223 \text{ F/g} \quad \text{or} \quad C_0 = 1850 \text{ }\mu\text{F/cm}^2, \quad (3.8)$$

which agrees with previously reported values for transition metal oxide electrodes [227].

First, we study the size effect on the sensing performance of the PSEs on glass substrates by keeping the electrode thickness constant (100 nm). In total 5 sizes are studied with different electrode widths and lengths ( $W \times L = 0.5 \text{ mm} \times 2 \text{ mm}$ ,  $2 \text{ mm} \times 5 \text{ mm}$ ,  $3 \text{ mm} \times 8 \text{ mm}$ ,  $4 \text{ mm} \times 10 \text{ mm}$ ,  $5 \text{ mm} \times 10 \text{ mm}$ ). According to a previous study [236], if the pH of a solution changes by 1 and assume the potential at the reference electrode ( $E_{ref}$ ) is constant, the measured output voltage of the pH sensor ( $\Delta E_{meas}$ ) will change by (Figure 3-9):

$$\Delta E_{meas} = \Delta E_{sen} \times \frac{C_m}{C_m + C_e + C_c}, \quad (3.9)$$

where  $\Delta E_{sen} = 65 \text{ mV/pH}$  is the intrinsic pH sensitivity of the electrode (section 2.3.4). Because  $C_m$  is a function of the electrode geometry while  $C_c$  and  $C_e$  are independent of the electrode geometry, the measured pH sensitivity can be written as:

$$\Delta E_{meas} = \Delta E_{sen} \times \frac{C_0 W L}{C_0 W L + C_e + C_c}. \quad (3.10)$$

When the electrode with  $W = 2$  mm,  $L = 5$  mm,  $h = 100$  nm, and  $\Delta E_{meas} = 65$  mV/pH, is used as the reference condition, the parasitic capacitance of the PSE ( $C_e$ ) is found to be  $\sim 15$   $\mu$ F using equation (3.10). This large parasitic capacitance may be caused by the large surface area of the NP-fused Pd/PdO electrical connection (Figure 2-1(d) and Figure 3-9). More study is needed to find the exact value of the specific capacitance of the inkjet-printed Pd/PdO film. Using equation (3.10) with the extracted values for  $C_0$  and  $C_e$ , the size effect on the sensitivity of the PSEs can be studied and plotted in Figure 3-13. We find that the theoretical calculation results agree well with the experimental data. Also, near-Nernstian sensitivities were obtained when the PSEs were larger than 10  $\text{mm}^2$ . If the PSEs were smaller than 10  $\text{mm}^2$ , a sensitivity drop could be observed. This observation suggests that a larger sensing area is preferred for a highly sensitive sensor. Importantly, this calculation also indicates that, for further miniaturization of the sensor, the sensitivity can be improved by using a dense and highly conductive material (such as Au and Pt used in other studies) as the electrical connection and the underlayer of the sensing electrode.

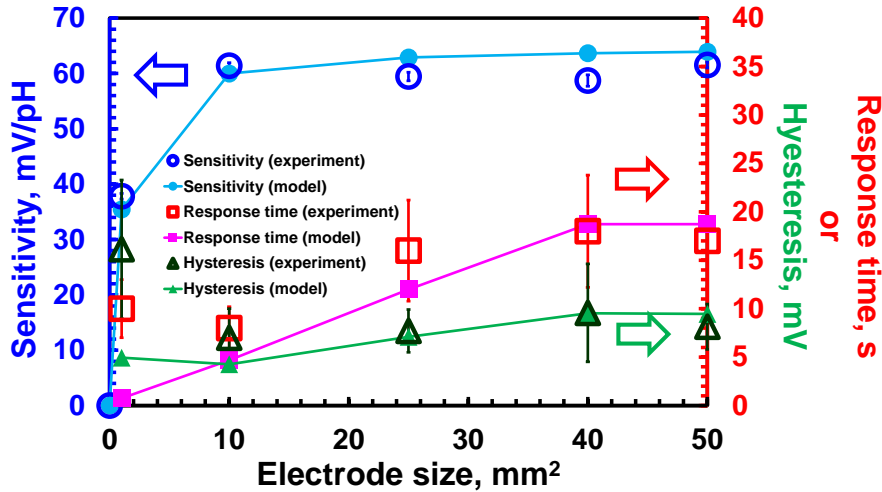


**Figure 3-13.** Effect of Pd/PdO electrode size on the pH sensitivity, response time, and hysteresis.

The response time of the sensor can be estimated using equations (3.5) and (3.6):

$$t_{90} = 1.5\tau_1 = 1.5R_e C_0 WL = 1.5\rho \frac{L}{Wd} C_0 WL = 1.5 \frac{\rho L^2 C_0}{d}, \quad (3.11)$$

where the response time only depends on the length and thickness of the electrode, not the electrode width. Therefore, in Figure 3-13, we can observe similar response time values for

the electrodes with an area of 40 mm<sup>2</sup> and 50 mm<sup>2</sup> (because both their lengths are 10 mm). Note that the deviation between the calculated and the experimental response time is large for the electrode of 1 mm<sup>2</sup>. This large difference may be caused by the relatively significant effect of  $\tau_2$ , because  $\tau_1$  for such a small electrode is tiny ( $\sim 0.5$  s). However, the dispersive transport process is difficult to be modeled for Pd/PdO due to the lack of parameters such as the density of reaction sites, the amount physical-chemical defects, the relaxation time for traps, and many other properties of the sensing material.

The hysteresis of the sensors can be calculated by equation (3.4), where the values of  $\tau_1$  are calculated based on equation (3.11). In addition,  $\varepsilon_1 \approx 0.5$ ,  $\tau_2 \approx 200$ , and  $\varepsilon_2 \approx 0.1$  are extracted from the fitted response curves (similar to Figure 3-10). The agreement between the modeling and experimental results is shown in Figure 3-13. Similar to the response time, the experimentally observed hysteresis is much larger than the modeling result for the electrode of 1 mm<sup>2</sup>. This deviation is caused by the inaccurate estimation of  $\tau_2$  for an electrode with a small sensing area.

Next, we study the thickness effect on the sensing performance of the PSEs by keeping the electrode area constant (2 mm  $\times$  5 mm). According to section 3.2.2 and 3.2.3, we can observe that the Pd/PdO film contains more defects and pores as its thickness reduces. Thus, we introduce a porosity factor ( $p_r$ ) for the correction of the length of the Pd/PdO film. So equation (3.10) is modified for calculating the pH sensitivity as a function of electrode thickness ( $C_c$  is neglected due to its small value comparing with  $C_e$ ):

$$\Delta E_{meas} = \Delta E_{sen} \times \frac{C_0 W L p_r}{C_0 W L p_r + C_e}, \quad (3.12)$$

where  $p_r$  is an empirical parameter and its values for different electrode thicknesses are listed in Table 3-4. Figure 3-14 shows that a thicker PSE had a higher sensitivity, which saturates at the Nernst limit for PSEs over 100 nm thick. The low sensitivity of thin PSEs was caused by both the poor morphologies and the large electrical resistance of the Pd/PdO films. On the one hand, pinholes and cracks exposed the substrates and reduced the effective surface area (Figure 3-4(b-d)), resulting in a reduced sensitivity. On the other hand,

the redox reactions between PdO and  $\text{H}_3\text{O}^+$  ions generated electrons, which had to be transferred to external circuits for potentiometric sensing. The pinholes and cracks in the PSEs increased the electrode resistance (Figure 3-4(h)) and hindered the conduction of electrons, thus lowering the pH sensitivity.

**Table 3-4.** Extracted parameters for a two time constant model for the modeling of the pH step response of electrodes with different thicknesses.

Electrode thickness, nm	25	35	70	80	100	150	170
$\varepsilon_1$	0.70	0.73	0.77	0.71	0.75	0.79	0.76
$\tau_1$ , s	25.0	16.2	5.1	4.6	3.4	4.0	4.8
$\varepsilon_2$	0.39	0.36	0.33	0.35	0.29	0.30	0.24
$\tau_2$ , s	998	911	532	445	254	223	220
$p_r$	0.50	0.60	0.80	0.85	1.00	1.10	1.15
$t_{90}$ (model), s	37.5	24.3	7.7	6.9	5.1	6.0	7.1
$t_{90}$ (experiment), s	24.5	13.7	5.6	5.1	7.9	8.2	9.5
Hysteresis (model), mV	18.8	15.9	6.4	6.1	5.8	6.5	7.3
Hysteresis (experiment), mV	23.4	21.0	7.6	10.8	7.0	4.0	5.4

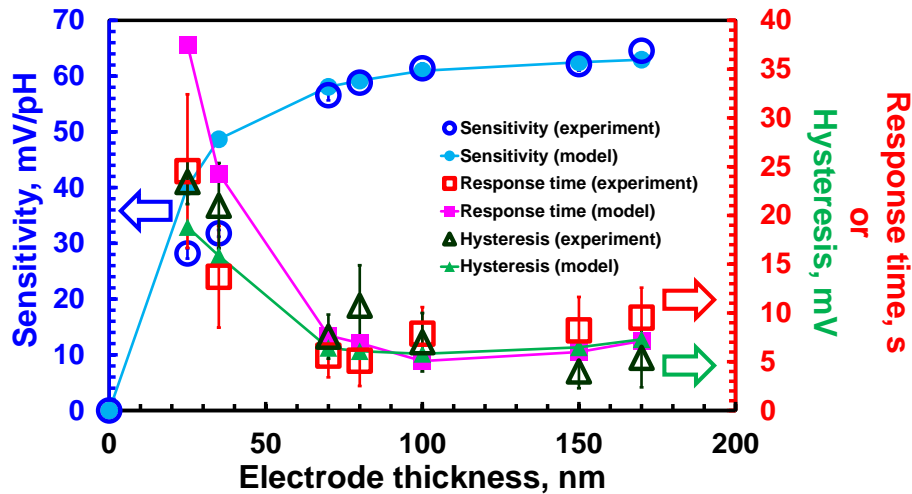


**Figure 3-14.** Effect of Pd/PdO electrode thickness on the pH sensitivity, response time, and hysteresis.

In terms of response time, equation (3.11) is modified using the porosity factor:

$$t_{90} = 1.5 \frac{\rho L^2 p_r^2 C_0}{d}. \quad (3.13)$$

Fast responses ( $\sim 8$  s) were found for the PSEs thicker than 80 nm. Below this thickness, the response time increased significantly. The slow response for thin PSEs was attributed to the loosely-packed films that increased the migration path for  $\text{H}_3\text{O}^+$  [237]. PSEs thicker than 170 nm were not studied here because of their poor adhesion to the glass substrate

when immersed in solutions. Using equation (3.4), the hysteresis values are calculated, which are close to the experimental results. Finally, we conclude that an optimal PSE had a size of 10 mm<sup>2</sup> and a thickness of 100 nm.

### 3.3. Integrated pH sensors

#### 3.3.1. Fabrication process

To prove the potential application of the PSEs in future compact, low-cost electrochemical monitoring systems, potentiometric pH sensors were integrated on glass and PI substrates using Pd/PdO PSEs and Ag/AgCl/KCl printed reference electrodes (PREs). The integration process is shown in Figure 3-15.

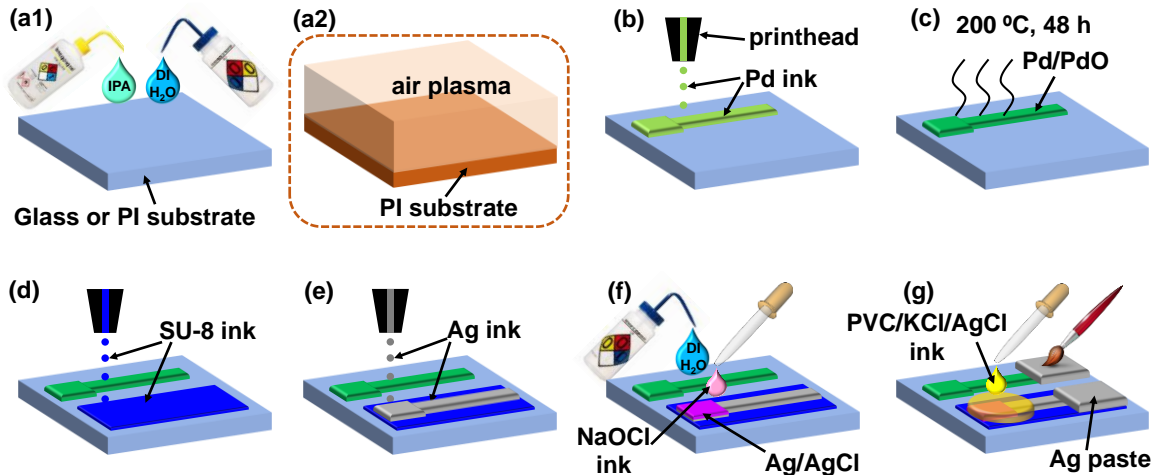


**Figure 3-15.** Integration process of a pH sensor using printing techniques. (a1) Substrate cleaning. (a2) Air plasma treatment of PI substrate. (b) Inkjet printing of Pd ink. (c) Thermolysis and annealing of printed Pd to form Pd/PdO sensing electrode. (d) Inkjet printing of SU-8 ink as adhesion between Ag and the substrate. (e) Inkjet printing of AgNP ink for the reference electrode. (f) Pipette printing of NaOCl ink for the chlorination of the surface of Ag. (g) Pipette printing of PVC/KCl/AgCl ink to form the solid electrolyte of the reference electrode, and painting of Ag paste for electrical contacts.

First, glass and PI substrates were cleaned by rinsing with IPA and DI water and dried under compressed dry air (Figure 3-15(a1)). For PI substrates, a 2-min air plasma treatment was performed before the printing processes (Figure 3-15(a2)). Next, one layer of Pd-PhMe ink was inkjet-printed onto the substrates (Figure 3-15(b)). The printed Pd-PhMe was converted to a PSE (100 nm thick and 10 mm<sup>2</sup> large) using 2-step thermolysis and annealed

at 200 °C for 48 h (Figure 3-15(c)). Afterwards, an SU-8 ink was prepared by diluting the as-received SU-8 3035 photoresist to 7.4 wt% using PGMEA (Table 3-1). The SU-8 ink was inkjet-printed beside the PSE and cured to form an 8 mm × 25 mm block with a thickness of ~100 nm (Figure 3-15(d)). The printed SU-8 layer adhered to glass and PI substrates well, and could be used as an interfacial layer between Ag (to be printed in the next step) and the substrates (Table 3-2). Then, the PRE was fabricated based on previous reports [238], [239] with modifications, as explained below.

Figure 3-15(e) shows a Ag NP ink (Table 3-1) that was inkjet-printed on the SU-8 layer and annealed at 120 °C for 10 min to form a 300 nm thick Ag layer (5 mm × 10 mm). Subsequently, a NaOCl ink was prepared by diluting the as-received NaOCl solution to 0.4 wt% using DI water. The high surface tension (~72 cP) of the aqueous solution was reduced to ~31 cP by adding 2 vol% Triton™ X-100 surfactant so that the ink was printable (Table 3-1). To chlorinate the top part of the printed Ag, ~0.1 mL NaOCl ink was required. This amount of ink could not be deposited within 100 layers of printing because the jetting capability of the printhead was ~10 pL per droplet. Therefore, to improve the process efficiency, ~0.1 mL NaOCl ink was printed from a pipette to the Ag surface and allowed to chlorinate the Ag for ~30 s before rinsing with DI water (Figure 3-15(f)). The SEM images of the printed Ag layer before and after chlorination is shown in Figure 3-16(a) and (b). XPS analyses shown in Figure 3-16(c) confirmed the formation of AgCl on top of Ag.

A printable ink for the solid electrolyte was formulated by dissolving 2 wt% PVC in KCl- and AgCl-saturated cyclohexanone (Table 3-1). Also due to the limited jetting capability of the printhead, ~0.2 mL PVC/KCl/AgCl ink was printed from a pipette on top of Ag/AgCl (Figure 3-15(g)) to form a thick (~1 μm) solid electrolyte layer. Finally, Ag paste was manually painted and annealed at 160 °C for 10 min as electrical connections. The sensors with integrated PSE and PRE were conditioned in 1 M KCl solution for 12 h before testing.

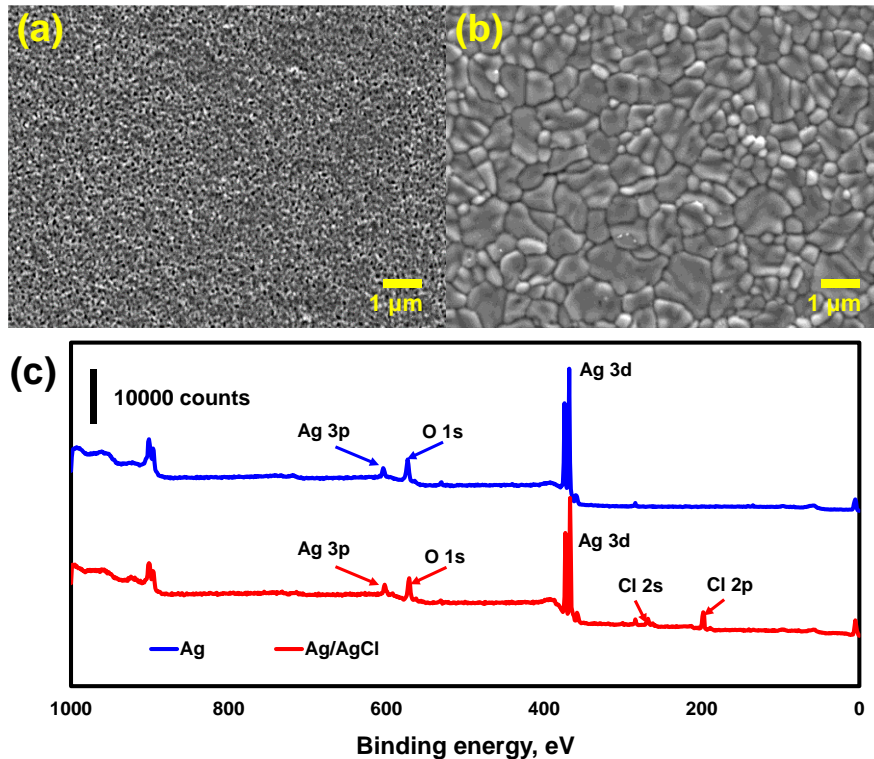


**Figure 3-16.** (a) SEM image of the surface morphology of a printed Ag layer. (b) SEM image of the surface morphology of a printed AgCl layer. (c) XPS analysis of the surfaces of printed Ag and AgCl layers.

### 3.3.2. Evaluation of pH sensing performance

#### 3.3.2.1. pH sensitivity

Figure 3-17(c) displays the sensitivity of an integrated sensor on a glass substrate. Due to the constant PRE potential ( $SD = 1.5 \text{ mV}$ ), the sensitivity of the integrated sensor ( $60.6 \pm 0.1 \text{ mV/pH}$ ) was almost identical to that of a PSE ( $60.6 \text{ mV/pH}$ , referenced to a CRE). On PI (Figure 3-17(d)), the  $SD$  of the PRE potential was  $2.4 \text{ mV}$  and the sensitivity of the integrated sensor was  $57 \pm 0.6 \text{ mV/pH}$ . Because the thermal conductivity of PI ( $0.12 \text{ W/m}\cdot\text{K}$ ) was lower than that of glass ( $0.8 \text{ W/m}\cdot\text{K}$ ) [180], it took a longer time for the Pd ink on PI to reach its decomposition temperature. A longer time before precursor decomposition resulted in more spreading and a thinner ink layer. Hence, the thinner PSE on PI ( $\sim 80 \text{ nm}$  comparing to  $\sim 100 \text{ nm}$  on glass) may be the reason for this lower sensitivity.

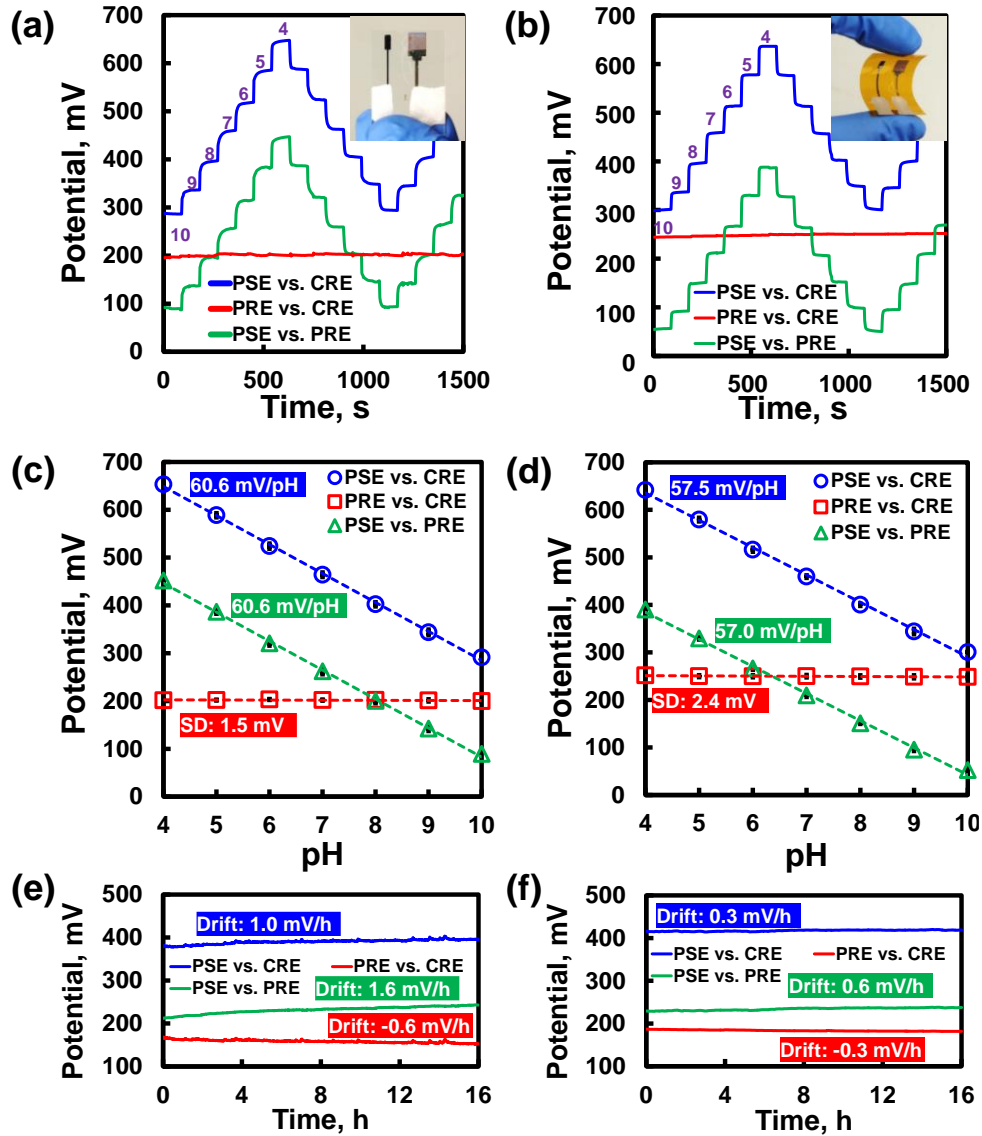


**Figure 3-17.** (a) Temporal response of an integrated sensor on glass when the pH of buffer solutions cycles between 4 and 10; inset: photograph of an integrated sensor on glass. (b) Temporal response of an integrated sensor on PI when the pH of buffer solutions cycles between 4 and 10; inset: photograph of an integrated sensor on PI. (c) Open circuit potential versus pH values for an integrated sensor on glass. (d) Open circuit potential versus pH values for an integrated sensor on PI. (e) Drift behavior an integrated sensor on glass. (f) Drift behavior an integrated sensor on PI.

According to the Nernst equation (2.22), the pH sensitivity is a function of temperature. To verify this dependence, the sensitivity of the pH sensor was measured at 3 °C, 15 °C, 27 °C and 40 °C. The pH sensitivity showed a linear temperature dependence of  $\sim 0.23$  mV/pH/°C, which was close to the theoretical value of 0.2 mV/pH/°C (Figure 3-18).

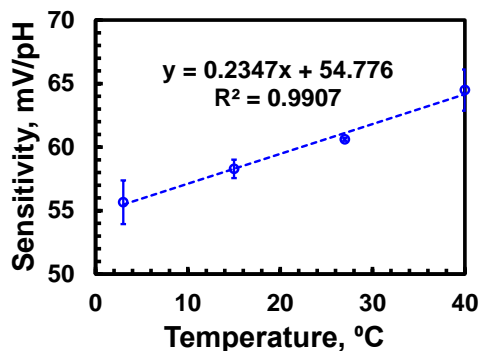


Figure 3-18. The measured sensitivity of the pH sensor as a function of temperature.

### 3.3.2.2. Response time

The temporal pH response of the printed sensors on glass and PI were measured after 12-h conditioning in 1 M KCl. The results are shown in Figure 3-17(a) and (b). The PREs exhibited negligible response between pH = 4 and 10 (referenced to a CRE), suggesting that the PREs could replace CREs in integrated sensors. Also, fast responses of the PSE were observed upon pH variations, which is important for real-time measurements. The response time is determined by the transportation speed of  $\text{H}_3\text{O}^+$  ions from the bulk solution to the PSE surface, as well as the rate of reactions between  $\text{H}_3\text{O}^+$  ions and the surface sites of the PSE. The integrated sensor displayed a response time of 11 s and 6 s on a glass and on a PI substrate, respectively. The difference in response time was mainly due to the different film morphologies on the two types of substrates. The 100 nm thick Pd films on glass contained pinholes and cracks (Figure 3-4(b)), which increased the migration path for  $\text{H}_3\text{O}^+$  ions and slowed the response [237]. On PI substrates, the redox reaction (2.4) was limited at the surface of the closely-packed films, which resulted in a fast response.

### 3.3.2.3. Reversibility and drift

Another important factor limiting the sensors' accuracy is hysteresis, which is difficult to avoid. It is a combined effect of buried and slow-reaction sites in the PSEs, and is also affected by the mechanical stability of the sensing material [166]. In our study, the hysteresis was 8.9 mV for the sensor on glass, and was 5.3 mV for the sensor on PI. These response time and hysteresis values are comparable with other studies [80], [126], [166]. We believe that the hysteresis is caused by the presence of Pd in the PSE, because Pd can

have irreversible redox reactions with  $\text{H}_3\text{O}^+$  in the solution, especially at low pH values [196].

The drift behavior of the integrated sensors was studied in 1 M KCl solution at  $27 \pm 2$  °C in the dark for 16 h. On glass (Figure 3-17(e)), the drift of the PSE was 1 mV/h, and for the PRE, -0.6 mV/h. The drift of both electrodes resulted in the integrated sensor's drift of 1.6 mV/h, which is similar to previous studies [166]. The printed Pd/PdO film delaminated at a slower rate on PI than on glass, due to the surface nitrogen atoms induced better adhesion of Pd to PI. Thus, a lower drift rate of 0.6 mV/h was obtained for the integrated sensor (Figure 3-17(f)).

#### 3.3.2.4. Stability

A very important parameter for practical sensors is stability which specifies how the sensor's characteristics change with time. Therefore, we studied the stability of the integrated sensors stored in 1 M KCl solution at  $27 \pm 2$  °C and in dark over a period of 70 days. Figure 3-19 shows the change of sensitivity with storage time. After sensor fabrication (day 0, before being stored in 1 M KCl), the sensitivities of the PSEs were measured against a CRE because the PREs must be conditioned before use (triangles at day 0). The PSEs on glass and PI had a high sensitivity of 63.6 mV/pH (blue triangle at day 0) and 60.2 mV/pH (red triangle at day 0), respectively. The difference in sensitivity may be due to the different PSE thicknesses, as discussed above. After storage in 1 M KCl, the sensor on PI had a slightly lower but stable sensitivity of  $\sim 57$  mV/pH (red squares between day 1 and 31). The sensitivity drop was due to the rearrangement of surface Pd and oxygen atoms, the formation of surface -OH groups, and the relief of stress in the Pd/PdO film [240]. After 35 days of storage, the PRE delaminated from the substrate. The sensitivity of the PSE between day 38 and 70 was then assessed using a CRE, and was found to be stable during this period (red triangle between day 38 and 70). In contrast, the sensitivity of the sensor on glass kept decreasing (blue circles between day 1 and 20) until the PSE

delaminated after 23 days of storage. The low stability of such sensors was primarily due to the poor adhesion between the printed Pd film and glass.

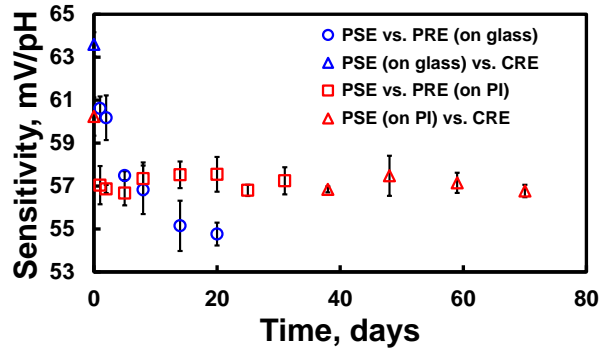


Figure 3-19. Stability of integrated sensors on glass and PI.

### 3.3.2.5. Selectivity

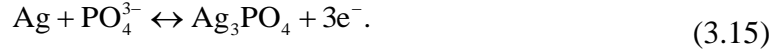
In addition, the selectivity was studied by immersing the sensor into solutions containing different concentrations of interfering ions. The solid electrolyte layer on top of the Ag/AgCl electrode is very critical for maintaining a stable electrical potential at the reference electrode. Without such a layer, the PRE showed a sub-Nernstian response ( $\sim 50$  mV/decade of  $\text{Cl}^-$  ion concentration) towards  $\text{Cl}^-$  ions (Figure 3-20(a)) in the solution due to the reaction [238]:



If the solid electrolyte layer is used, the electrical potential at the PRE was stable in solutions with  $10 \mu\text{M}$  to  $1 \text{ M}$  of  $\text{Cl}^-$  ions (SD of potential =  $1.83 \text{ mV}$ ). This was because the relatively constant  $\text{Cl}^-$  ion concentration in the electrolyte layer kept reaction (3.14) in equilibrium.

Although reaction (3.14) only indicates the dependence of  $\text{Cl}^-$  ion concentration of the PRE, the un-protected AgCl layer exhibited an unstable potential in solutions with different pH values. At high pH levels ( $\text{pH} > 9$ ), the solubility of AgCl increases so the amount of AgCl on the PRE reduces [241], and the equilibrium of reaction (3.14) is deteriorated. In the acid solution ( $\text{pH} < 4$ ), the amount of  $\text{H}_3\text{PO}_4$  (in the pH buffer solution) increased. The

potential at the PRE was also affected by phosphate ions (in addition to reaction (3.14)) [242]:



Therefore, the bare Ag/AgCl could only show a stable potential between pH = 4 and 9, while the SD of the potential of the solid-electrolyte-coated PRE was 1.65 mV in a wider pH range of 3 to 10 (Figure 3-20(b)).

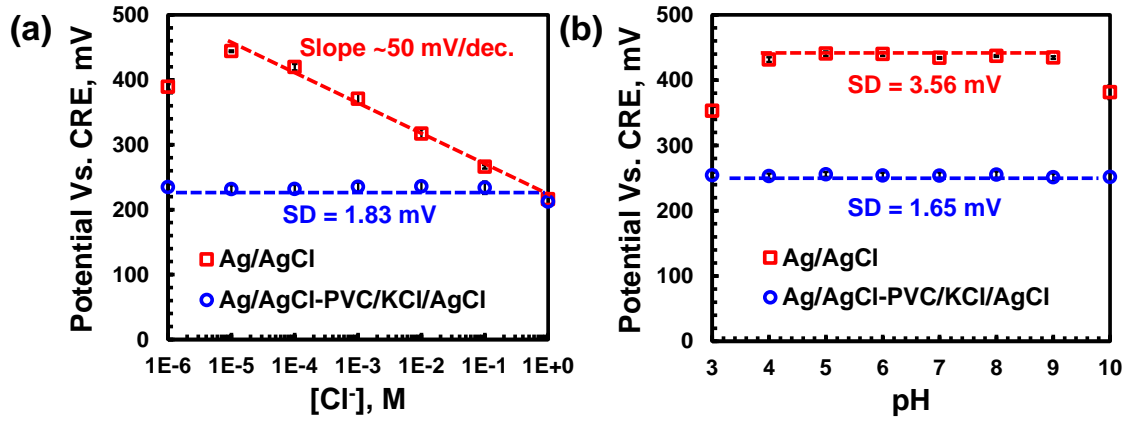


**Figure 3-20.** The electrical potential stability of a PRE in solutions with: (a) Different concentrations of Cl<sup>-</sup> ions. (b) Different pH values.

Once the PRE provides a stable potential, the sensor revealed negligible response to common anions and cations (Figure 3-21) due to the specific redox reaction (2.4). We believe the only minor voltage variations shown in Figure 3-21 were attributed to the exchange of potassium ions (K<sup>+</sup>) or Cl<sup>-</sup> ions between the solutions and the solid electrolyte layer on the PRE.

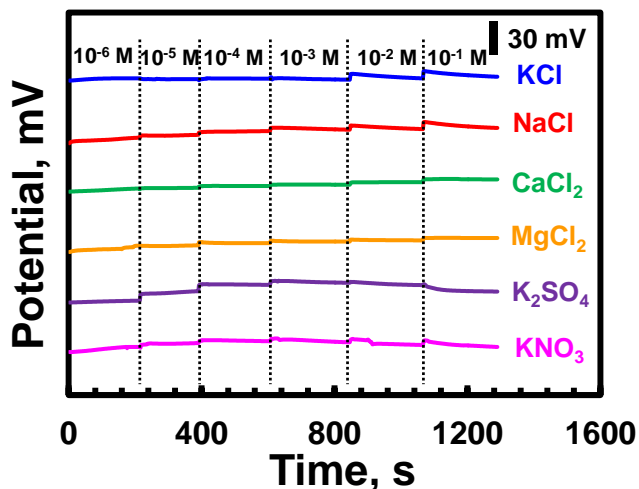


Figure 3-21. The response of a printed pH sensor in interfering solutions with different concentrations.

### 3.3.2.6. Biofouling of the sensing electrode

Microorganisms may present in real water samples, and the sensitivity of the sensor may be reduced due to the biofouling of the surface of the PSE. One researcher in our group found that the sensitivity of the Pd/PdO sensing electrode decreased by ~4% in 7 days when it was stored in DI water, tap water, and a humic acid solution [243]. However, if the electrode was stored in an accelerated biofouling condition (1% yeast extract solution), a sensitivity decrease of ~20% was observed in 7 days. The decline in the sensitivity in the accelerated biofouling condition can be attributed to adhesion and growth of the microbes on the electrode surface. The study on biofouling indicates that a pre-processing step may be required to remove the microbes in the water sample for a long sensor lifetime [243].

### 3.3.2.7. Sensing performance in flowing water

To simulate real-world water quality monitoring situations better, it is important to study the sensing performance of the electrodes in flowing water. One researcher in our group carried out computational fluid dynamics simulation (Ansys Fluent) to study the pH sensor performance when it is used in water with different flow rates [244]. The simulation results suggest the sensitivity of the sensor will decrease by 50% when the flow rate is increased from 0.05 m/s to 0.2 m/s. This study also shows that localized turbulence at the electrode surface can be used to maintain a high sensitivity when the sensor is used in the flowing

water. The localized turbulence can be created by introducing groove structures on top of the electrodes in the water flowing channel [244].

### 3.3.3. Test of real water samples

To prove the practical usability of the integrated sensors, the PSE and PRE (stored in 1 M KCl for 12 h) were connected to a commercial multimeter (72-7730, TENMA) for recording the open-circuit potential. The output potential was converted to the pH value of real water samples using the calibration curves shown in Figure 3-17(c) and (d). A single-point calibration using the pH = 7 buffer solution was done prior to the measurements for an accurate result. Figure 3-22 is the summary of the test results for 9 types of water samples. In all cases, the differences between the calculated pH values (using measured potential) for the printed sensors and the pH readings for a commercial pH meter were less than 2%. In addition, these accurate results were obtained using a simple test setup without using complicated instruments. This indicated the possibility of building highly accurate, easy-to-use, low-cost pH sensing systems that incorporate the printed sensors developed in this study.

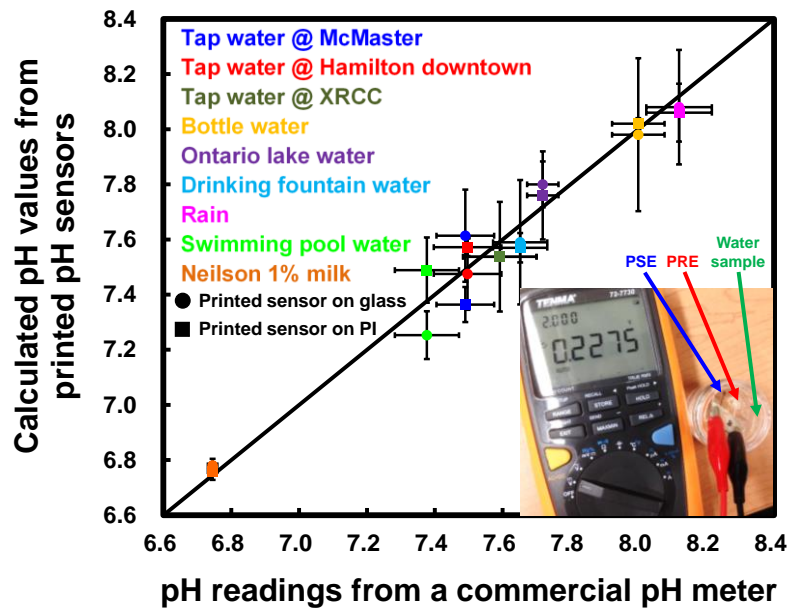


Figure 3-22. pH measurement results of real water samples using the integrated sensors on glass and on PI.

### 3.4. Conclusions

We have developed an inkjet printing process for a highly loaded Pd ink to deposit Pd thin films. The viscosity and surface tension of as-received Pd precursor solution was adjusted by 20 wt% toluene to form a printable ink. The printed ink was converted to continuous, homogenous, low-resistivity Pd films using a 2-step thermolysis. The printed Pd films exhibited good adhesion to air-plasma-treated PI substrates. To demonstrate the electrochemical application of the printed Pd films, an annealing step was carried out at 200 °C in air. The resulted PdO-rich surface served as a pH sensing layer while the underlying conductive layer provided a path for electrons. The bifunctional Pd/PdO PSEs were designed with a size of 10 mm<sup>2</sup> and a thickness of 100 nm for an optimal sensitivity and response time. These PSEs were then integrated with solid-state PREs to form potentiometric sensors. The integrated sensors on glass and PI showed a fast and repeatable pH response with a sensitivity of  $60.6 \pm 0.1$  mV/pH and  $57 \pm 0.6$  mV/pH, respectively. Also, accurate pH values of real water samples were obtained with the printed sensors. Because the drop-on-demand inkjet printing process consumes a small amount of functional materials and can be easily scaled up, these printed sensors can be very cost-effective for large-scale manufacturing. Finally, since the developed sensors are of high sensitivity and with a fast response, and are stable, low-cost, and easy-to-use, then an electrochemical sensing platform based on such sensors can be built for monitoring drinking water quality.

# Chapter 4

## Inkjet-printed Pd/PdO for temperature sensors\*

In this chapter, inkjet-printed Pd films with different morphologies are prepared using different precursor thermolysis atmospheres. The temperature dependence of the electrical properties of the Pd films are characterized for the development of inkjet-printed temperature sensors. First, the Pd precursor is reductively decomposed into amine-stabilized Pd clusters. In air, O<sub>2</sub> assists the decomposition of the organoamine ligands for the Pd clusters. Small NPs are formed and fused into smooth films. In N<sub>2</sub>, the residual ligands facilitate the formation of sub-micron spherical aggregates. In low vacuum, a bilayer film containing a bottom layer with fused NPs and a top layer with spherical aggregates is formed. Such morphology is caused by the competition between the film formation processes in air and in N<sub>2</sub>. The electrical properties of the films are determined by the whole film for the smooth film and by the bottom layer for the bilayer film. The TCR value of the films can be adjusted from 0.067% /°C to -0.189% /°C by tuning the amount of semiconductive PdO in the conduction path. In addition, humid air increases the resistance drift of the films by forming surface-adsorbed -OH groups and/or molecular water. This study suggests that printed temperature sensors can be fabricated by adjusting the atmosphere for the thermolysis of the Pd precursor.

---

\* Adapted from Y. Qin, A. U. Alam, M. M. R. Howlader, N.-X. Hu, and M. J. Deen, "Morphology and electrical properties of inkjet-printed palladium/palladium oxide," *J. Mater. Chem. C*, vol. 5, no. 8, pp. 1893–1902, 2017, with permission from The Royal Society of Chemistry (Appendix E).

## 4.1. Background

In Chapter 2 and Chapter 3, we showed that the sensitivity of a pH sensor is a function of temperature. Thus, a temperature sensor needs to be integrated with the pH sensor for accurate monitoring of the pH of a drinking water sample. One of the commonly used temperature sensor is a RTD, whose resistivity changes with temperature. The TCR of a metallic material is positive [37], while that of a semiconductor is negative [38]. In Chapter 3, we have demonstrated inkjet-printed metallic Pd and semiconductive PdO films, whose electrical resistivity should depend on temperature. Therefore, sensitive temperature sensors can be prepared using the printed Pd and PdO if they show large absolute TCR values (can be either positive or negative).

The electrical properties of vacuum-processed Pd/PdO films were reported [245]–[247]. For example, the TCR was 3.3% /°C for a sputtered Pd film and -3.6% /°C for a thermally oxidized PdO film. However, these values could not be used for the inkjet-printed films due to the organic additives in the Pd ink and the different deposition atmospheres [248].

One important factor affecting the electrical properties (including TCR) of an inkjet-printed Pd/PdO film is its morphology. For example, small (sub-10 nm) and dispersed Pd/PdO NPs in power sources ensure a high catalytic activity, fuel efficiency, and power density [208], [249]. Nano/micro-textured Pd/PdO films used in hydrogen sensors are responsible for a high sensitivity and a fast response [250]–[252]. Dense and smooth Pd films are required for highly conductive electrical interconnections and highly sensitive electrochemical sensors [81], [166], [253]. To obtain these Pd/PdO films with different morphologies, lithographical steps or structural templates are needed [250]–[252], which increases the complexity and cost of the fabrication processes. Although our developed inkjet printing process can simplify the deposition of Pd/PdO films, its capability to produce films with different morphologies was not studied.

In addition to the film morphology, the electrical properties of the Pd/PdO films are influenced by the variations of the moisture or RH levels in the application environment. This humidity dependence is critical for water quality monitoring sensors because water may modify the electronic structures of the metal oxide surfaces by introducing hydroxyl groups (-OH) [254], [255]. Previously, the surface chemistry and electrical properties of Pd/PdO were studied with numerical simulations [255]–[257], but these theoretical calculations were not used to predict the electrical properties of Pd/PdO in real-world conditions. Experimentally, the response of hydrogen sensors changed when the Pd/PdO sensing resistors were used at different RH levels [258], [259]. These studies were unable to decouple the effect of moisture-interfering hydrogen-oxide interaction and moisture-induced resistance change. To the best of my knowledge, the electrical properties of inkjet-printed Pd/PdO films has not been examined.

In this chapter, we investigated the thermolysis process for the inkjet-printed Pd precursor ink in different atmospheres. We found that the morphology of the deposited Pd/PdO films can be adjusted by controlling the O<sub>2</sub> content in the thermolysis atmosphere. At 200 °C, the precursor is reductively decomposed into amine-stabilized Pd clusters. In air, O<sub>2</sub> can assist the decomposition of the organic ligands for the Pd clusters and facilitates the fusion of small NPs to dense and smooth films. When O<sub>2</sub> is lacking (in N<sub>2</sub>), the residual organic ligands trigger the aggregation of NPs, generating sub-micron spheres. In low vacuum, the competition between the two abovementioned mechanisms (thermolysis in air and in N<sub>2</sub>) results in a bilayer Pd film with a bottom layer of fused NPs and a top layer of spherical aggregates. The Pd/PdO films with different morphologies and PdO contents display different electrical properties. The TCR can be adjusted from 0.067% /°C (smooth metallic films) to -0.189% /°C (bilayer semiconductive films). In humid conditions, a large resistance drift is caused by the formation of -OH groups in the oxide-rich films, so the semiconductive Pd/PdO films had a lower electrical stability than the Pd-rich metallic films. The -OH groups increase the inter-grain energy barrier which results in an increased resistance. Also, the adsorbed -OH groups and/or molecular water provide extra conduction

paths for the oxidized bilayer films. These results suggest that the inkjet-printed Pd/PdO films can be used as RTD-based temperature sensors. However, importantly, the effect of moisture on the resistance drift of the films must be minimized for real-world applications.

## 4.2. Thin film formation in air, low vacuum, and nitrogen

The Pd ink used in this study was the same as the one formulated in Chapter 3 (Pd-PhMe). The thermolysis of the Pd ink was done in two steps. The first step was the preheating of the printed ink on a hotplate in air at 120 °C for 4 min to evaporate the solvent. The second step was carried out in a chamber (Isotemp 280A, Fisher Scientific) at 200 °C for 20 min with three different atmospheres:

1. Air, short for ANOX.
2. Low vacuum (~2.7 mbar), short for VNOX.
3. N<sub>2</sub> (after purging for 10 min), short for N2NOX.

For oxidized samples, a thermal treatment step at 200 °C for 48 h in air was carried out after the precursor thermolysis step. The oxidized samples corresponding to the three thermolysis atmospheres are named as AOX, VOX, and N2OX (Table 4-1).

**Table 4-1.** Summary of the morphologies and electrical properties of the inkjet-printed Pd/PdO films.

Sample	Description	Morphology	NP size, nm	Organic%	PdO%	Resistivity (25 °C), $\mu\Omega$ m	TCR (vacuum), /°C	R drift (vacuum), /h	TCR (humid air), /°C	R drift (humid air), /h
ANOX	Thermolysis in air, not oxidized	Dense and smooth	7	1.3%	21.8%	2.3	0.067%	-0.015%	0.058%	0.003%
VNOX	Thermolysis in low vacuum, not oxidized	Thin bottom layer with spheres on top	12	8.3%	28.1%	31.2	0.041%	-0.023%	0.022%	0.035%
N2NOX	Thermolysis in N <sub>2</sub> , not oxidized	Discontinuous, spherical aggregates	-	7.0%	19.7%	-	-	-	-	-
AOX	Thermolysis in air, oxidized	Dense and smooth	7	0%	77.5%	67.5	-0.091%	0.046%	-0.100%	0.222%
VOX	Thermolysis in low vacuum, oxidized	Thin bottom layer with spheres on top	12	0%	59.1%	277.5	-0.189%	-0.016%	-0.247%	-0.330%
N2OX	Thermolysis in N <sub>2</sub> , oxidized	Discontinuous, spherical aggregates	-	0%	62.8%	-	-	-	-	-

### 4.2.1. Film morphologies

The morphologies of the Pd/PdO films can be changed by using different thermolysis atmospheres for the inkjet-printed Pd precursor. When the thermolysis atmosphere was air (ANOX), a dense, smooth, and continuous film of ~200 nm thickness was formed (Figure 4-1(a), (d), and (g)). Such a film consisted of fused Pd NPs with a particle size of ~7 nm (inset of Figure 4-1(d)). From the SEM images in Figure 4-1(d) and (g), clear grain boundaries can be observed among the domains of fused Pd NPs. These grain boundaries were caused by inter-domain voids, which might be attributed to the removal of organic ligands in the film. Despite these nanoscale voids, the film prepared in air was dense in the microscale with a close-to-zero porosity.

When the Pd precursor was thermally decomposed in low vacuum (VNOX), the deposited film displayed a bilayer morphology (Figure 4-1(b), (e), and (h)). The bottom layer was thin (~100 nm thick) and contained nanocracks. These nanocracks might be generated by the stress induced by the uneven film thickness. The top layer in VNOX contained spherical aggregates with a diameter of ~600 nm. The high magnification SEM image (inset of Figure 4-1(e)) revealed that the spherical aggregates were formed by aggregated Pd NPs (~12 nm in diameter), in contrast to the fused NPs in ANOX. In VNOX, the grain boundaries were not as obvious as those in ANOX, because the inter-domain voids were filled by the residual organic ligands. In the microscale, the film (VNOX) also had a low porosity.

If N<sub>2</sub> was the thermolysis atmosphere (N<sub>2</sub>NOX), the generated film was semitransparent (due to the exposure of the glass substrate to ambient), and only contained large spheres (~900 nm in diameter) without a continuous bottom layer (Figure 4-1(c), (f), and (i)). The spheres were loosely-packed, with small interconnecting areas. Microscale voids could be observed among the spheres, indicating a very porous film. A clear SEM image with high magnification was difficult to obtain due to the charging effect of the exposed glass substrate. Because the spheres were loosely-packed and adhered poorly to the substrate, a cross section of the spheres was difficult to make.

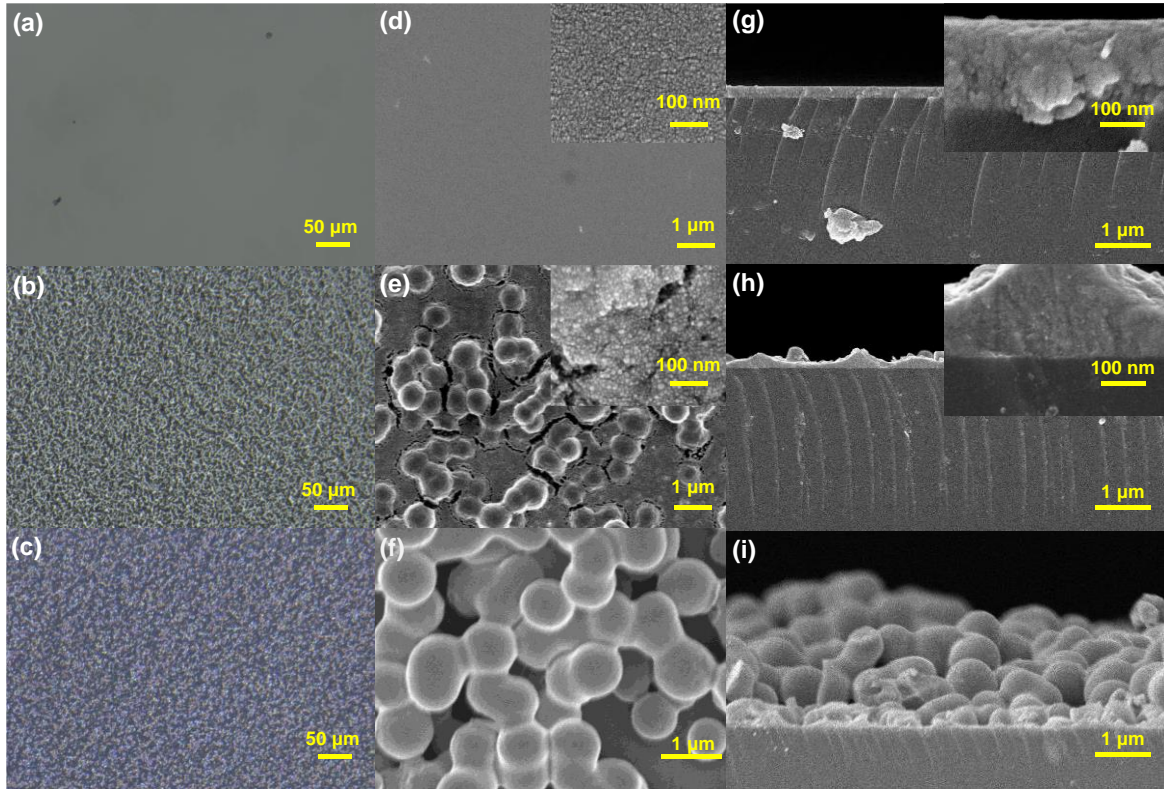


**Figure 4-1.** (a)-(c) Top-view optical images of Pd/PdO films for the thermolysis atmosphere of: (a) Air (ANOX). (b) Low vacuum (VNOX). (c) N<sub>2</sub> (N<sub>2</sub>NOX). (d)-(f) Top-view SEM images of Pd/PdO films for the thermolysis atmosphere of: (d) Air (ANOX). (e) Low vacuum (VNOX). (f) N<sub>2</sub> (N<sub>2</sub>NOX). (g)-(i) Cross-sectional SEM images of Pd/PdO films for the thermolysis atmosphere of: (g) Air (ANOX). (h) Low vacuum (VNOX). (i) N<sub>2</sub> (N<sub>2</sub>NOX).

XRD patterns of the films (Figure 4-2) were used to calculate the Pd crystallite size. In each XRD pattern, the diffraction peak around 40.1° was attributed to the (111) facet of Pd (JCPDS card No. 46-1043) [260]. The slight shift in the peak position may be due to stress in the films [261]. Also, the peak for PdO (~34°) was negligible because of the relatively large background noise. Thus, the films mainly contained Pd crystallites. The sizes of Pd crystallites are calculated based on the Gaussian-fitted Pd(111) peak using Scherrer's equation [262]:

$$L_{crystallite} = \frac{K\lambda}{B(2\theta)\cos\theta}, \quad (4.1)$$

where  $L_{crystallite}$  is the crystallite size,  $K = 0.89$  is the Scherrer's constant,  $\lambda = 0.15418$  nm is the X-ray wavelength,  $B(2\theta)$  is the peak width, and  $\theta$  is the peak position. The Pd crystallite

size is 5.4 nm, 4.7 nm, and 3.5 nm, respectively, for the thermolysis atmosphere of air, low vacuum, and N<sub>2</sub>. The smaller crystallite size indicates a shorter crystal growth time.

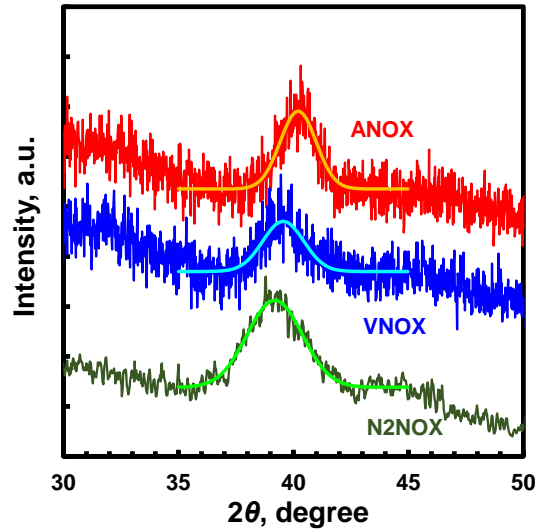


**Figure 4-2.** XRD patterns of the Pd/PdO films with different precursor thermolysis atmospheres.

#### 4.2.2. Chemical compositions

In addition to the physical characterization of the inkjet-printed Pd/PdO films, Raman analysis (Figure 4-3) was used to determine the chemical compositions of these films. For the thermolysis atmosphere of N<sub>2</sub> (N2NOX), a tilted baseline and two weak peaks at ~553 cm<sup>-1</sup> and ~1100 cm<sup>-1</sup> can be observed, which was caused by the exposed glass substrate. For the thermolysis atmosphere of air (ANOX), the glass background had negligible effect on the spectrum, which confirmed the dense morphology of such films. A broad peak with low intensity between 1100 cm<sup>-1</sup> and 1700 cm<sup>-1</sup> can be found in the spectrum for ANOX. Because the Pd precursor contains organoamines ligands, this broad peak was attributed to the residual organic species after thermolysis (e.g., N-H deformation vibrations at ~1615 cm<sup>-1</sup>, C-N stretching vibrations at 1130 cm<sup>-1</sup>, C-H deformation vibrations at 1460 cm<sup>-1</sup>, and C-C skeletal vibrations at 1300 cm<sup>-1</sup>) [263]. For the thermal decomposition in low vacuum (VNOX), the peak representing the organic species became more prominent, which indicated a larger content of residual organic species in the film. Besides, the peak for PdO at ~650 cm<sup>-1</sup> was difficult to be observed for the non-oxidized samples. These observations are in agreement with the XRD results and implies a metallic behavior of the films.

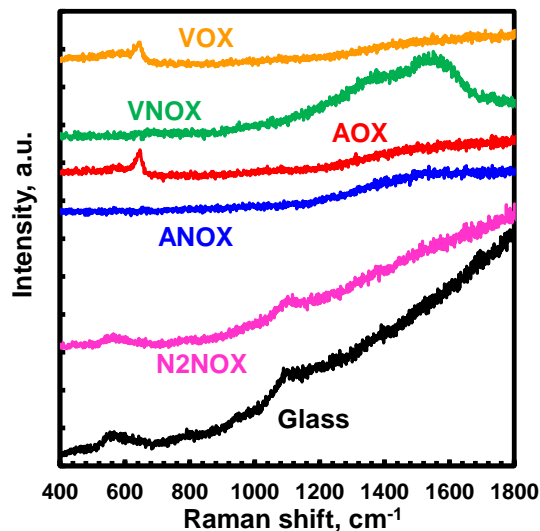
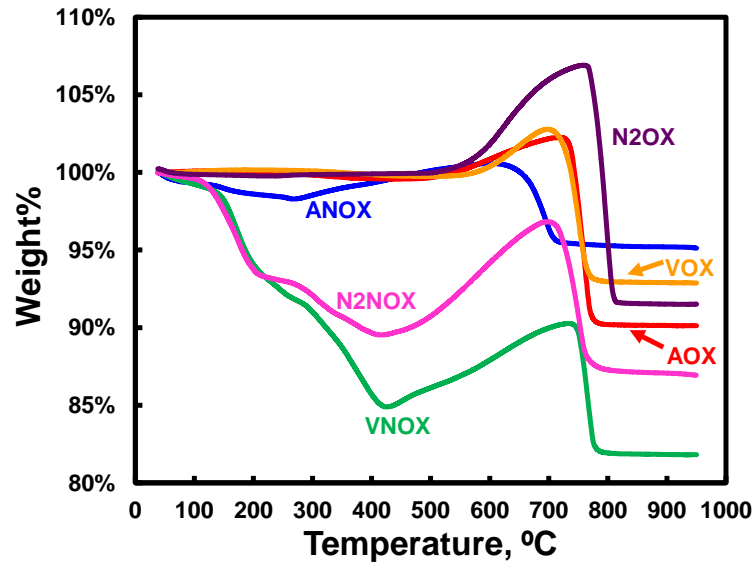


Figure 4-3. Raman spectra of Pd/PdO films with different precursor thermolysis atmospheres.

### 4.2.3. Thermogravimetric analysis

TG analysis was used to quantify the content of the residual organic species and PdO in the films. Figure 4-4 illustrates the weight change of the Pd/PdO mixture from room temperature to 950 °C. In this study, a typical TG curve (no matter what atmosphere was used for the thermolysis) included four weight loss steps and one weight gain step. At ~100 °C, the weight loss was due to the removal of molecular water [264]. At 200-400 °C, the decomposition of the residual organic species caused the weight loss [81]. At 300-500 °C, -OH groups on the PdO surface dissociated and the weight was reduced [264]. From 300 °C to above 600 °C, the Pd metal in the mixture reacted with chemically adsorbed O<sub>2</sub> (when the samples were transferred from the thermolysis oven to the TG analyzer in air) and resulted in a weight gain [255], [265]. Note that the temperature range for the loss of -OH groups and the uptake of O<sub>2</sub> overlapped. Between 600 °C and 800 °C, the TG curve showed a significant weight loss, which originated from the decomposition of PdO to Pd [264], [265]. Therefore, the weight difference between ~150 °C and ~300 °C can be used to calculate the content of residual organic species. The weight difference between the ~400 °C and ~900 °C can be used to estimate the PdO content. The calculated weight contents for the residual organic species and PdO are shown in Table 4-1.



**Figure 4-4.** TG analysis of Pd/PdO mixture with different precursor thermolysis atmospheres.

As a comparison, *in-situ* TG measurements were carried out in N<sub>2</sub> in the furnace of the TG analyzer to eliminate the effect of O<sub>2</sub> uptake (Figure 4-5). In the first test (curve 1 in Figure 4-5), the Pd precursor was decomposed inside the furnace of the TG analyzer (120 °C for 4 min and 200 °C for 4 min) and heated up to ~950 °C. The weight loss was due to the evaporation of the solvent and the decomposition of Pd precursor at ~200 °C. Metallic Pd was generated in this process. A slight weight loss above 200 °C could also be observed, indicating residual organic species remained in the generated Pd.

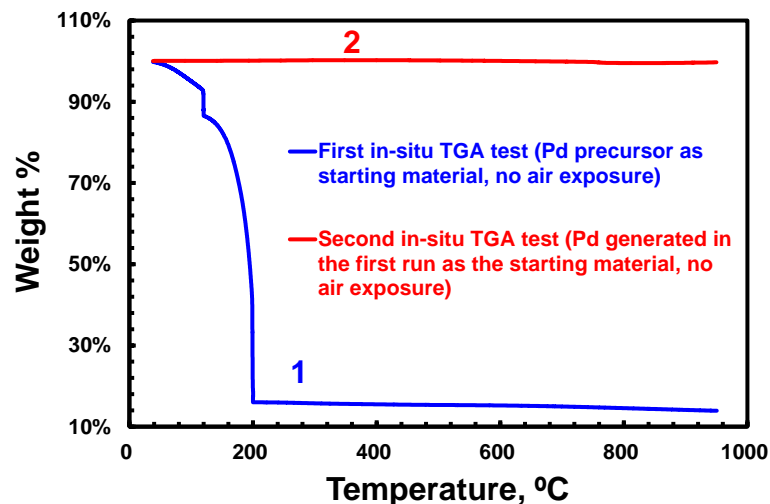


**Figure 4-5.** TGA curves of Pd precursor and Pd/PdO mixture.

In the second test (curve 2 in Figure 4-5), the Pd generated in the first test was cooled down to  $\sim 30$  °C inside the furnace of the TG analyzer with  $N_2$  purge. Then, the furnace was heated up to  $\sim 950$  °C again. In this process, the weight gain between 300 °C and 600 °C was negligible and almost no weight change could be observed in the whole temperature range, suggesting that PdO was not generated under  $N_2$ .

For the sample prepared in air (ANOX),  $O_2$  assisted the precursor thermolysis so that little residual organic species remained in the film after the thermolysis process [266]. However, in low vacuum (VNOX) and  $N_2$  (N2NOX), the thermal decomposition of the organoamines was slow due to the lack of  $O_2$ . Thus,  $\sim 8\%$  residual organic species was found in the films (VNOX and N2NOX). On the other hand, PdO was formed in all non-oxidized samples (ANOX, VNOX, and N2NOX).

The presence of PdO could not be determined from the XRD and Raman analyses due to the large background noise (small film thickness). Based on the SEM images in Figure 4-1, sub-micron spherical aggregates were formed in  $N_2$  (N2NOX), and the Pd at the surface was easily oxidized to PdO after exposure to air. In low vacuum (VNOX), the spherical aggregates were smaller, and a thin bottom layer existed. This morphology had a larger surface area than that formed in  $N_2$  (N2NOX). Thus, more PdO was obtained after the thermolysis step in low vacuum (VNOX). The film prepared in air (ANOX) was dense and smooth, and the oxidation was caused by the penetration of  $O_2$  into the film. If a Pd NP has a Pd core-PdO shell structure with a NP diameter of 7 nm (Figure 4-1(a)) and a native oxide thickness of 0.8 nm [267], then this NP contains  $\sim 27\%$  PdO. Because the TGA-measured PdO content in the film prepared in air was  $\sim 22\%$ , the Pd NPs were partially covered by PdO. The PdO contents calculated by the TG tests and by the core-shell model are in agreement with our previous studies using XPS ( $\sim 20\%$ ) [80], [81].

After the oxidation step, the PdO content of all samples (AOX, VOX, and N2OX) increased (Table 4-1). For the sample prepared in air (AOX),  $\sim 77.5$  wt% PdO presented in the film,

which was more than that in VOX and N2OX (both ~60 wt%). The lower PdO contents in VOX and N2OX could also be attributed to the spherical aggregates in the films. In the spherical aggregates (in VNOX/VOX and N2NOX/N2OX), the penetration depth for O<sub>2</sub> was the radius of the spheres (~300 to ~450 nm), while the O<sub>2</sub> penetration depth in the smooth film (ANOX/AOX) was ~200 nm. Therefore, the oxidation of ANOX is easier than that of VNOX and N2NOX.

#### 4.2.4. Film formation mechanisms

Based on the characterization results above, film formation mechanisms are proposed for the inkjet-printed Pd precursor in different thermolysis atmospheres, as shown in Figure 4-6. The printed Pd precursor solution contained an organometallic complex formed by a Pd salt (Pd-X) as the Pd source and an organoamine (R-NH<sub>2</sub>) as the ligand [268]. Regardless of the thermolysis atmosphere, the Pd precursor was first subjected to reductive decomposition into amine-stabilized Pd clusters at ~200 °C [248].

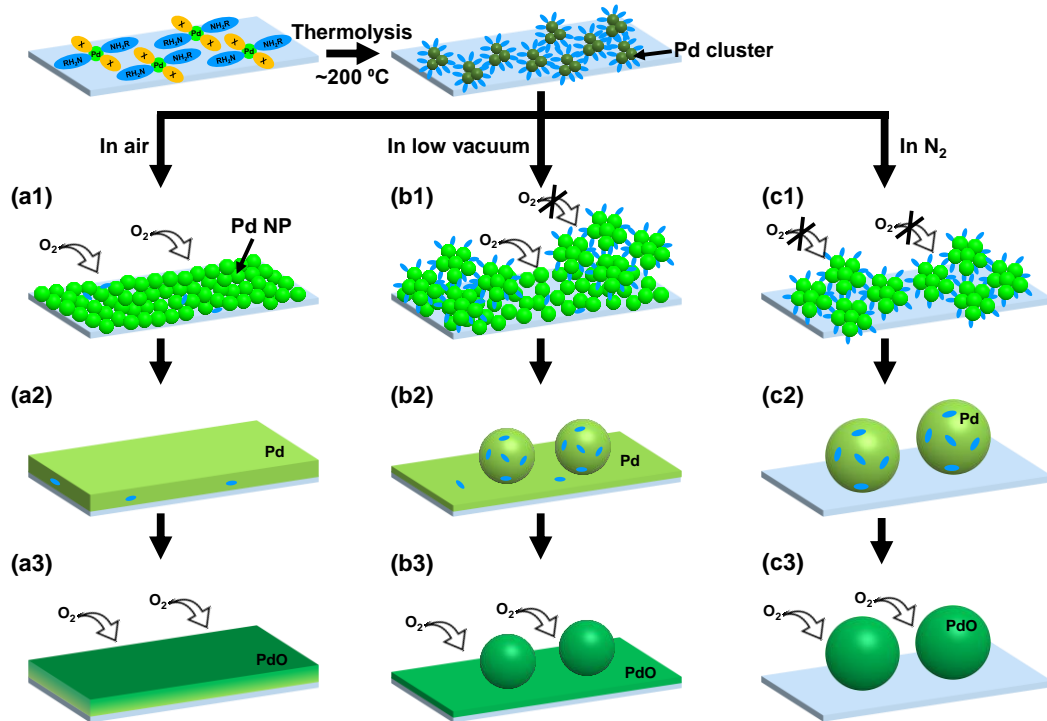


**Figure 4-6.** Proposed Pd/PdO film formation mechanisms in different precursor thermolysis atmospheres: (a) air, (b) low vacuum, and (c) N<sub>2</sub>.

In air, O<sub>2</sub> reacted with the organic ligands and quickly exposed the surface of the Pd clusters. The clusters could grow and merge together to form NPs (Figure 4-6(a1)). These clean NPs were small in size (sub-10 nm) and had a low melting point [269]. When the process temperature was kept at 200 °C, the surfaces of these Pd NPs melted, fused together, and eventually a smooth and dense film was formed (Figure 4-6(a2) and Figure 4-1(a)). The absence of residual organic ligands was confirmed by Raman and TG analysis.

In contrast to air, when in N<sub>2</sub>, the decomposition of the organic ligands was inhibited due to the lack of O<sub>2</sub>. The residual ligands remained on the surface of the Pd clusters and prevented their growth. Therefore, the size of the Pd clusters was smaller than those generated in air (confirmed by XRD analysis). Also, the slow decomposition of the ligands indicated a low reduction rate of Pd<sup>2+</sup> in the precursor, which resulted in larger Pd NPs (confirmed by SEM imaging) [270]. Because the NPs were large in size and were covered with residual organic species, they were difficult to fuse into a homogenous film at ~200 °C (Figure 4-6(c1)). Instead, these NPs formed spherical aggregates with residual organic species embedded (Figure 4-6(c2) and Figure 4-1(c)). The inset of Figure 4-1(b) confirmed that the NPs were aggregated rather than fused together.

In low vacuum, due to the low concentration of O<sub>2</sub>, the film was deposited as a result of the competition between the two mechanisms (thermolysis in air and in N<sub>2</sub>) discussed above. The melted and fused NPs were at the bottom, and the large aggregates were at the top of the film (Figure 4-6(b1) and (b2)). As a result, a bilayer morphology was formed in low vacuum (Figure 4-1(b)).

### **4.3. Electrical properties of inkjet-printed Pd/PdO films**

A study of the electrical properties of inkjet-printed Pd/PdO films at different temperatures and RH levels is important for their applications as temperature sensors for water quality monitoring. Because the films prepared in N<sub>2</sub> (N<sub>2</sub>NOX) were discontinuous (not conductive), only the films prepared in air and low vacuum (ANOX and VNOX) are studied

here. An oxidation step can be carried out at 200 °C for 48 h in air to increase the content of PdO (Figure 4-6(a3) and (b3)) and adjust the electrical properties of the printed films. Note that the film morphologies were not altered by the oxidation step and/or the tests in humid air.

### 4.3.1. Effect of temperature

The electrical properties of the inkjet-printed films were studied by measuring their electrical resistance at different temperatures in vacuum. At 25 °C, the calculated electrical resistivity values of the samples are listed in Table 4-1. The sample prepared in air before oxidation (ANOX) showed a dense and smooth morphology and a low resistivity of 2.3  $\mu\Omega\cdot\text{m}$ , which agreed with our previous results [81]. When the film was oxidized (AOX), the resistivity increased to 67.5  $\mu\Omega\cdot\text{m}$ . This increased resistivity was attributed to the increase in the amount of semiconductive PdO in the film. From the Raman spectrum in Figure 4-3(a), a PdO peak at  $\sim 650\text{ cm}^{-1}$  could be observed after oxidation. Also, the calculation based on the TG curves in Figure 4-4 showed that the PdO content increased from  $\sim 22\%$  to  $\sim 78\%$ .

For the sample prepared in low vacuum (VNOX), it showed a resistivity of 31.2  $\mu\Omega\cdot\text{m}$  at 25 °C. Compared to ANOX, VNOX had a higher measured resistivity, which was caused by their different morphologies. For VNOX, the electrical conduction was in the thin bottom layer, which was thinner than the film thickness (200 nm, measured from ANOX) used in Ohm's law for the calculation of equivalent resistivity. In other words, the top spherical spheres did not participate in the electrical conduction. When the film was oxidized (VOX), the resistivity of 277.5  $\mu\Omega\cdot\text{m}$  was a consequence of the high PdO percentage in the thin conduction path.

When the measurement temperature changed, all samples showed stable resistance values with a drift rate less than 0.05% /h (Figure 4-7(a-d)). The low drift rates indicated that the

printed Pd/PdO films were stable in dry conditions. The TCR values ( $\alpha_{TCR}$ ) of the samples can be calculated using:

$$\alpha_{TCR} = \frac{1}{R_{REF}} \frac{dR_{ele}}{dT}, \quad (4.2)$$

where  $R_{REF}$  is the resistance at 25 °C, and  $dR_{ele}/dT$  is the slope of the resistance-temperature curve in Figure 4-7(e).

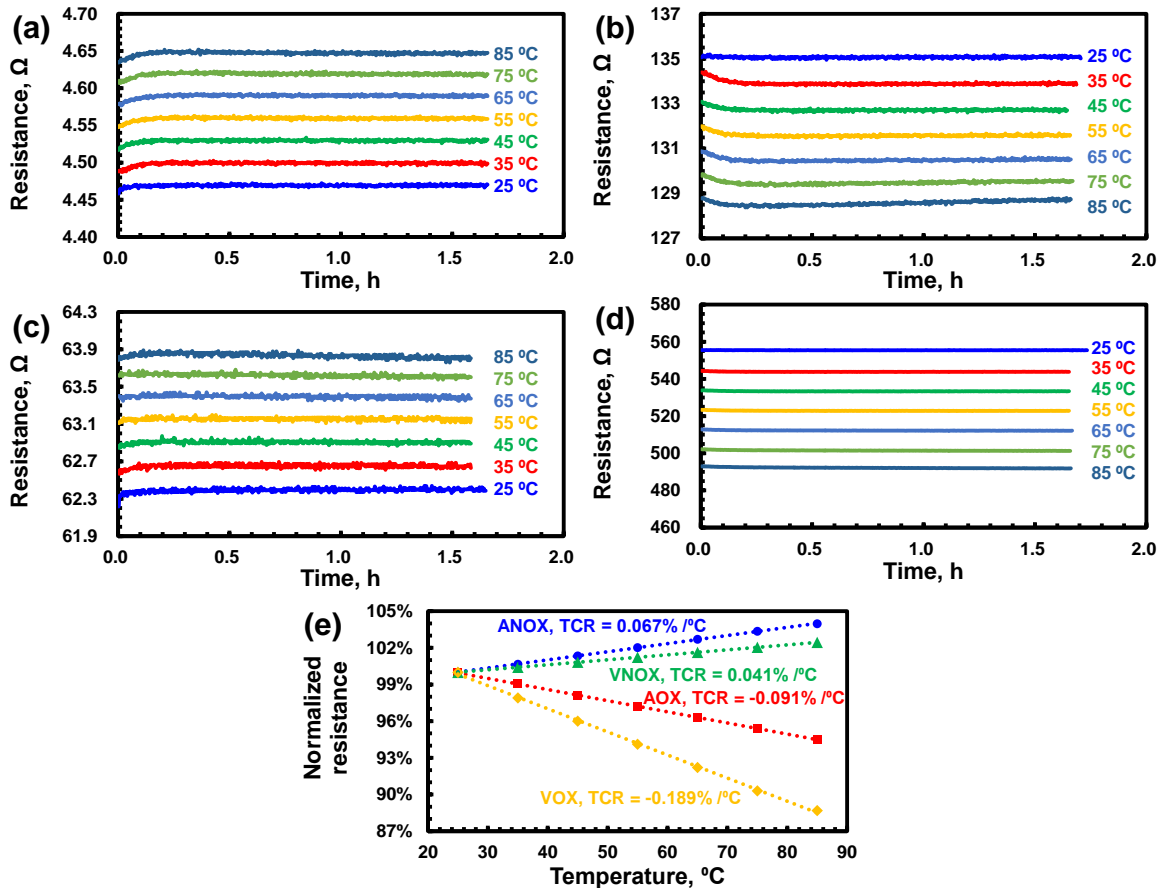


**Figure 4-7.** Resistance drift in vacuum for the Pd/PdO films prepared: (a) In air before oxidation (ANOX). (b) In air after oxidation (AOX). (c) In low vacuum before oxidation (VNOX). (d) In low vacuum after oxidation (VOX). (e) Temperature dependence of resistance for the 4 samples for TCR calculations.

The non-oxidized samples showed positive TCR values (Table 4-1 and Figure 4-7(e)), indicating a metallic behavior. However, the TCR values (0.067% /°C for ANOX and 0.041% /°C for VNOX) were smaller than that of vacuum-deposited Pd films (~0.3% /°C) [246]. Such small TCR values may be due to two reasons: (1) the printed films contained semiconductive PdO with a negative TCR, which reduced the overall TCR value. The film

prepared in vacuum (VNOX) had a thin bottom conductive layer, where the effect of PdO was more prominent than in the films prepared in air (ANOX). Therefore, the TCR of VNOX was smaller than that of ANOX. (2) The inter-grain charge transport in the NP-constructed films is a thermally activated process, which has a negative TCR [271]. In other words, the charge transport was more efficient (resistance was lower) at higher temperatures. Thus, the overall TCR values were reduced.

For the oxidized samples, semiconductive properties were obtained with negative TCR values. Although the film prepared in air after oxidation (AOX) contained more PdO (~75%) than the film prepared in low vacuum after oxidation (VOX, ~57% PdO), its TCR value was closer to zero. In AOX, the conduction path was the entire film which consisted of both Pd and PdO. The presence of Pd increased the TCR value. In VOX, the conduction path was the thin bottom layer. Such a thin layer was fully oxidized to PdO easily, making it highly semiconductive, and hence a smaller TCR value. In other words, the ~43% Pd in VOX was mainly in the spherical aggregates, which did not affect the electrical conduction.

By choosing a proper thermolysis atmosphere and an oxidation step, the TCR value of an inkjet-printed Pd/PdO film can be tuned between a small positive value and a relatively large negative value. A Pd/PdO film with a large negative TCR can be integrated with a resistor having a large positive TCR [272] to form a highly sensitive bridge-type temperature sensor.

### **4.3.2. Effect of relative humidity**

Figure 4-8 shows the drift behavior and RH dependence of the resistance of Pd/PdO films in humid air at 30 °C. The resistance values of the non-oxidized films (ANOX and VNOX) showed small positive drifts and their RH dependence was weak (Table 4-1 and Figure 4-8(e)). The small positive drift may be due to the formation of -OH groups at the surface of PdO [255], [259]. Because PdO is a p-type semiconductor, its resistivity is increased (positive drift) when the adsorbed -OH groups donate electrons to the PdO conduction band.

In other words, the presence of -OH groups at the PdO surface increased the energy barriers for the inter-grain hole transport. In the non-oxidized films, the amount of PdO was small, so that the drift was insignificant.

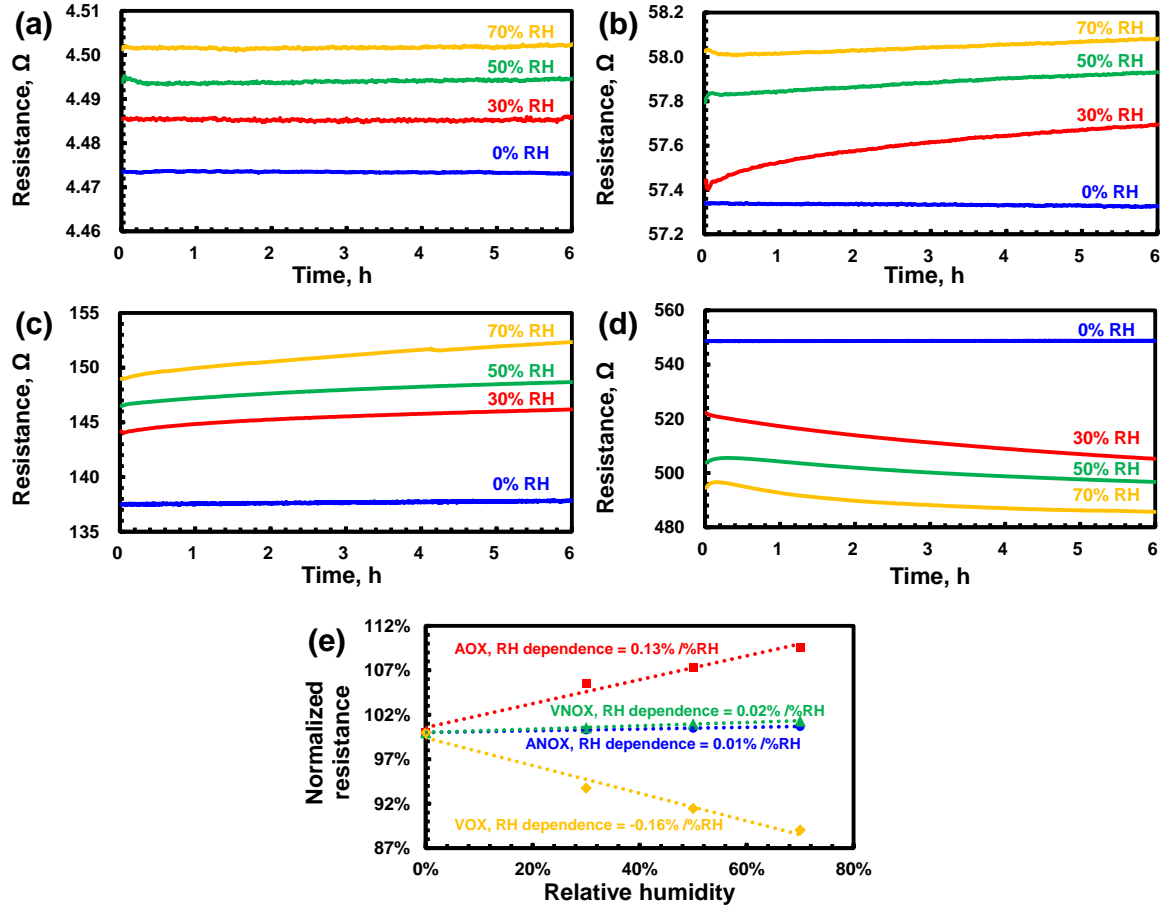


**Figure 4-8.** Resistance drift in humid air for the Pd/PdO films prepared: (a) In air before oxidation (ANOX). (b) In air after oxidation (AOX). (c) In low vacuum before oxidation (VNOX). (d) In low vacuum after oxidation (VOX). (e) RH dependence of resistance for the 4 samples.

For the oxidized films, the drift rates were ~10 times larger than those of the non-oxidized films (Table 4-1). Also, the oxidized films exhibited a strong dependence on RH (Figure 4-8(e)). The oxidized film prepared in air (AOX) had a positive resistance drift of 0.222% /h. The larger amount PdO in the film resulted in the adsorption of more -OH groups, hence a larger positive drift in resistance. However, the oxidized film prepared in low vacuum (VOX) exhibited a negative resistance drift of -0.330% /h. Therefore, we proposed that the main contribution of the adsorbed -OH groups and/or molecular water was to create more

conduction bridges in this defective film, while the effect of increasing inter-grain barriers was less important. More electrical conduction paths decreased the resistance of the film and resulted in a negative resistance drift. In the non-oxidized film (VNOX), this bridging effect may also exist. These conduction bridges were formed by -OH groups or adsorbed molecular water, which were more resistive than the metallic Pd. In such a case, even if more conduction paths were formed, charge carriers would still be transported in the original paths which were more conductive. Therefore, the overall resistance drift was positive in the non-oxidized film.

FTIR spectroscopy analyses (Figure 4-9) were carried out to confirm the effect of moisture on the resistance drift of the Pd/PdO films. The intensity increase of the O-H stretching peak ( $\sim 3400\text{ cm}^{-1}$ ) [263] indicated that the adsorption of -OH groups during the test in humid air. Also, the oxidized samples showed more -OH groups than the non-oxidized samples, which meant a faster reaction with moisture. The faster adsorption of -OH groups caused a larger drift. Besides, at  $\sim 1600\text{ cm}^{-1}$ , the peaks for H-O-H bending became more intense after the test in humid air [263]. Such observations indicated the adsorption of molecular water on the films. Therefore, we confirmed the origin of the resistance drift of the printed films was the moisture in air.

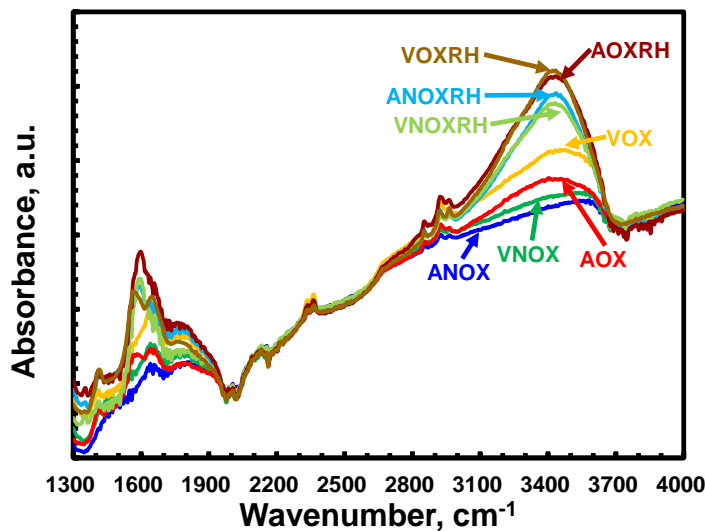


**Figure 4-9.** FTIR spectra of Pd/PdO films with different precursor thermolysis atmospheres before and after testing in humid air.

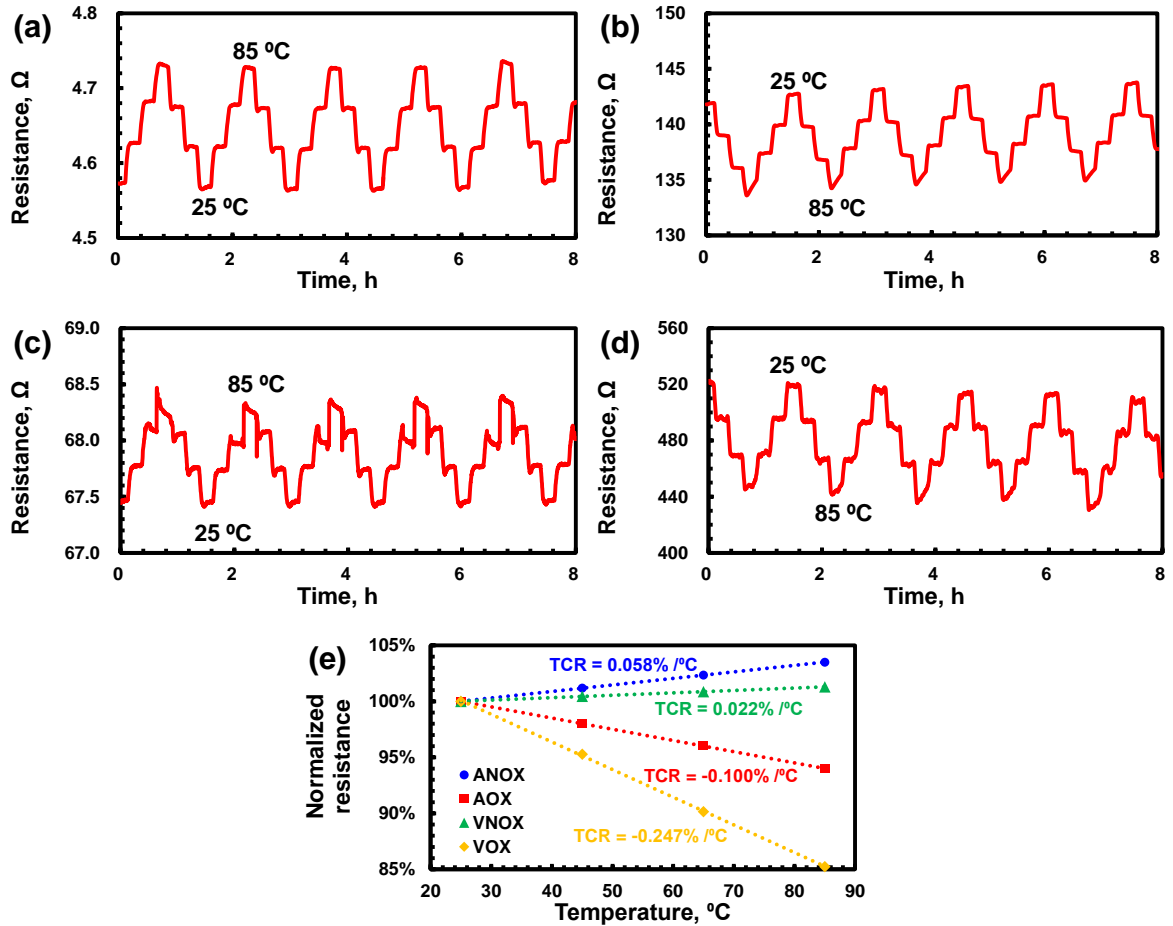


**Figure 4-10.** Resistance change during temperature cycling tests of Pd/PdO films prepared: (a) In air before oxidation (ANOX). (b) In air after oxidation (AOX). (c) In low vacuum before oxidation (VNOX). (d) In low vacuum after oxidation (VOX). (e) Temperature dependence of resistance in humid air for the 4 samples for TCR calculation.

Temperature cycling tests were carried out at 50% RH to find the TCR values of the films in humid conditions. Table 4-1 and Figure 4-10 show that the TCR values of all 4 types of films were reduced (more negative). Considering a semiconductive PdO film, its resistance ( $R_{ele}$ ) at a certain temperature ( $T$ ) can be expressed by [271]:

$$R_{ele} = R_{0B} \exp\left(\frac{E_a}{kT}\right), \quad (4.3)$$

where  $R_{0B}$  is the resistance of the film without barriers,  $E_a$  is the activation energy, and  $k$  is Boltzmann's constant. According to equation (4.2), the expression of TCR ( $\alpha_{TCR}$ ) can be written as:

$$\alpha_{TCR} = \frac{\frac{R_{ele}}{R_{REF}} - 1}{T - T_{REF}}, \quad (4.4)$$

where  $R_{REF}$  is the resistance at the reference temperature  $T_{REF}$  (25 °C in this study). By combining equation (4.3) and (4.4), the TCR can be calculated using:

$$\alpha_{TCR} = \frac{\exp\left[\frac{E_a}{k}\left(\frac{1}{T} - \frac{1}{T_{REF}}\right)\right] - 1}{T - T_{REF}}. \quad (4.5)$$

Because -OH groups are electron donors and trap holes in a p-type semiconductor, the inter-grain energy barriers (activation energies,  $E_a$ ) in the Pd/PdO films were increased when the films were exposed to moisture. According to equation (4.5), a higher activation energy ( $E_a$ ) will result in a larger (more negative) TCR value. This theory explained our experimental observations shown in Figure 4-10. Since the electrical resistance of the oxide-rich films showed a large RH dependence, the films should be encapsulated with materials with a high thermal conductivity and a low moisture adsorption rate [180], [273] for the application as temperature sensors.

### 4.3.3. Electrical conduction mechanisms

Based on the electrical measurement and characterization results above, electrical conduction mechanisms are proposed for the Pd/PdO films with different morphologies shown in Figure 4-11.

- **Precursor thermolysis in air, non-oxidized film (ANOX, Figure 4-11(a)).** The electrical conduction path was the whole film, and its resistivity was mainly determined by the PdO content in the film. The film exhibited a metallic property due to its major composition of Pd. When the film was exposed to moisture, the surface of PdO became hydrated. The adsorbed -OH groups at the oxide surface increased the inter-grain barrier (Figure 4-11(f)), which resulted in an increased film resistance and a reduced TCR.

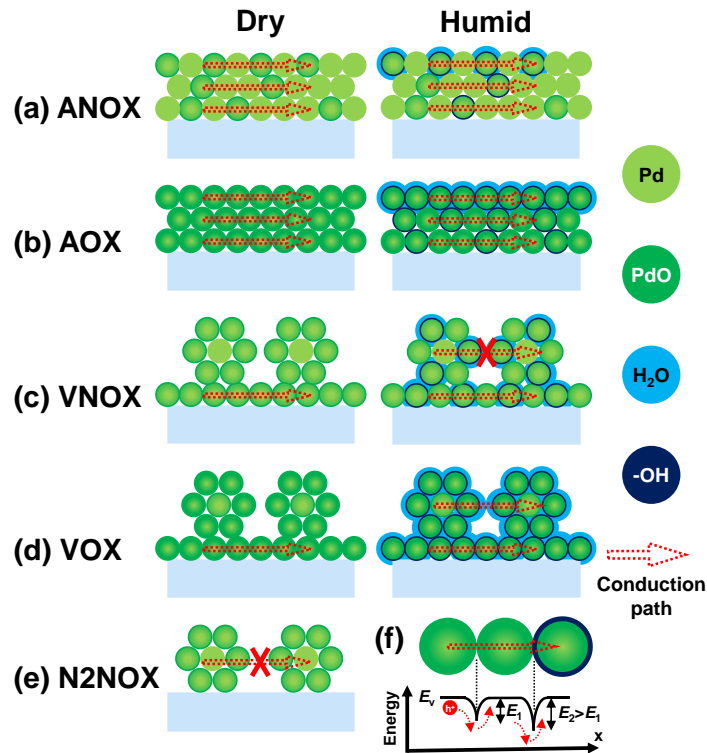


**Figure 4-11.** Proposed electrical conduction mechanisms of Pd/PdO films with different morphologies prepared: (a) In air before oxidation (ANOX). (b) In air after oxidation (AOX). (c) In low vacuum before oxidation (VNOX). (d) In low vacuum after oxidation (VOX). (e) In  $N_2$  before oxidation (N2NOX). (f) Schematic illustrating the inter-grain charge transport mechanism.

- Precursor thermolysis in air, oxidized film (AOX, Figure 4-11(b)).** The electrical conduction was throughout the whole film. PdO was the major composition in the film, making it semiconductive. In humid air, the -OH groups significantly altered the inter-grain charge transport in the film. Therefore, the film showed a large resistance drift and a more negative TCR.
- Precursor thermolysis in low vacuum, non-oxidized film (VNOX, Figure 4-11(c)).** The electrical conduction path was the metallic bottom layer in the film, suggesting its resistivity was determined by both the morphology and the PdO content. During test in the humid environment, the adsorbed -OH groups and/or molecular water may form additional conductive paths among the spherical aggregates. However, these newly-formed paths were not as conductive as the Pd-rich film at the bottom. Thus, the electrical conduction in the film was not significantly changed. The -OH groups in the

bottom layer slightly increased the film's resistance and reduced its TCR, similar to the case of ANOX.

- **Precursor thermolysis in low vacuum, oxidized film (VOX, Figure 4-11(d)).** The electrical conduction path was the semiconductive bottom layer in the film. The film resistance was greatly influenced by the amount of semiconductive grains (conduction paths) participating in the conduction. When the RH was high, additional conduction paths were formed by adsorbed -OH groups and/or molecular water. These newly-formed paths were effective because the initial conduction path was not highly conductive. Consequently, such film showed a negative resistance drift in the humid environment.
- **Precursor thermolysis in N<sub>2</sub>, non-oxidized film (N<sub>2</sub>NOX, Figure 4-11(e)).** Because the film consisted of discontinuous spherical aggregates, it was not conductive.

#### 4.4. Conclusions

The thermolysis process of an inkjet-printed Pd precursor ink was investigated. It was found that the morphology of the Pd/PdO films could be tuned by using different thermolysis atmospheres and that the precursor was reductively decomposed into amine-stabilized Pd clusters at 200 °C. The O<sub>2</sub> in air facilitated the decomposition of the ligands for the Pd clusters and clean Pd NPs were formed. The fusion of the small NPs with a low melting point resulted in a smooth and dense film. In N<sub>2</sub>, the generated NPs were larger and were embedded with organic species. Such NPs form sub-micron spherical aggregates. In low vacuum, a bilayer morphology was formed due to the competition between the film formation processes in air and in N<sub>2</sub>. The electrical properties of the films with different morphologies were different. The smooth film had a lower resistivity since the electrical conduction was throughout the film. For the bilayer film, only the bottom layer participated in the conduction and a higher resistivity was observed. The TCR value of the films can be tuned from 0.067% /°C to -0.189% /°C due to the different amounts of PdO in the

conduction paths. When the Pd/PdO films were studied in humid air, the adsorbed -OH groups raise the inter-grain barrier for the charge carrier transport and caused a positive resistance drift. In the oxidized bilayer film, additional conductive paths were created by the adsorbed -OH groups and/or molecular water, resulting in a negative resistance drift. This chapter showed that the inkjet-printed Pd/PdO films with different electrical properties can be easily prepared for applications such as temperature sensors. However, the devices should be encapsulated in order to obtain a stable performance.

# Chapter 5

## Paper-based, hand-drawn free chlorine sensor\*

The concentration of free chlorine used for disinfecting drinking water, recreational water, and food processing water is critical for environmental and human health safety, and should be controlled within stipulated ranges. This chapter describes a paper-based electrochemical free chlorine sensor fabricated by hand-drawing. The electrical resistivity of a PEDOT:PSS chemoresistor increases when it is exposed to free chlorine in water due to oxidation reactions. Because the relative change of the electrical resistance represents the sensor's response, the sensor can be fabricated by hand-drawing with different shapes and dimensions. The fabrication steps are all at room temperature, require no instrumentation or equipment, and can be carried out by untrained personnel. The fabricated sensor is mechanically stable, reusable, has a wide sensing range, and can accurately measure free chlorine concentrations in real water samples. Therefore, the low-cost, hand-drawn free chlorine sensor is of great significance for drinking water quality monitoring in less developed areas where fabrication facilities, analytical equipment, and trained personnel are limited, but the need for analytical devices is critical.

### 5.1. Background

Free chlorine sensors are important for monitoring the quality of water for drinking, recreation, and food processing [166]. In U.S. standards, the maximum concentration of

---

\* Adapted with permission from Y. Qin, S. Pan, M. M. R. Howlader, R. Ghosh, N.-X. Hu, and M. J. Deen, "Paper-based, hand-drawn free chlorine sensor with poly(3,4-ethylenedioxythiophene): poly(styrenesulfonate)," *Anal. Chem.*, vol. 88, no. 21, pp. 10384–10389, Nov. 2016. Copyright (2016) American Chemical Society (Appendix E).

residual chlorine in drinking water is 2 ppm [166]. The recommended free chlorine concentration in a swimming pool is 1.5 to 2 ppm [166]. The food processing water should contain 50 to 200 ppm free chlorine [166]. Free chlorine concentrations outside these ranges either cause inefficient disinfection or adversely affect human health. However, conventional free chlorine sensors are expensive, difficult-to-use, have narrow sensing ranges, and require maintenance by trained personnel. Thus, alternative sensors and sensing methods need to be developed for accurate free chlorine monitoring in different types of water samples at low cost.

Paper-based analytical devices are emerging for various applications including environmental monitoring, biochemical sensing, food processing, and point-of-care clinical diagnostics [274]–[276]. Paper also has the advantages of light weight, mechanical flexibility, intrinsic hydrophilicity, porous structures with a high surface-to-volume ratio, ease of surface functionalization, biocompatibility and biodegradability, abundance, cost-effectiveness, and high accessibility [275], [276]. Capitalizing on these unique properties, paper-based low-cost voltammetric cells [277], ion-selective electrodes [278], colorimetric sensors [279], fluorescent probes [280], microfluidic assays [281] and other types of devices [282], [283] were developed for analytical purposes. However, free chlorine sensors have not been demonstrated on paper substrates.

For the fabrication of these analytical devices, functional materials are deposited and patterned on papers utilizing different techniques. Photolithography was employed to pattern high-resolution structures, but its process complexity and expensive photomasks limited its application for low-cost devices [283]. On the other hand, wax printing [282], inkjet printing [91], screen printing [284], flexographic printing [285] and laser printing [286] provide simpler fabrication methods by combining material deposition and patterning steps. However, such printing processes rely on customized equipment and trained personnel. These requirements are difficult to be satisfied in resource-limited areas, remote or rural communities, and the underdeveloped world, where the need for analytical devices

is pronounced [281]. Therefore, easy-to-implement, highly accessible, and cost-effective fabrication methods are needed.

For such critical requirements, hand-drawing processes have emerged for fabricating electronic devices. The hand-drawing process is instrument-free, fast, and compatible with paper substrates [287]. These features offer the possibility to fabricate low-cost paper-based devices on demand for specific on-site applications by untrained personnel. Conductive patterns [288], transistors [289], physical sensors [290], and electrochemical sensors [291] drawn on various substrates have been reported. However, the potential of the hand-drawing process has not been widely demonstrated for analytical devices.

In this chapter, we describe a hand-drawn free chlorine sensor consisting of a drawn PEDOT:PSS chemoresistor as the sensing element on a paper strip. All fabrication steps are at room temperature and require no instrumentation or equipment. The sensing of free chlorine depends on the oxidation-induced electrical resistivity increment of the PEDOT:PSS film. Comparing to commercial colorimetric free chlorine strips, the developed drawn sensor can provide a quantitative reading over a wide concentration range (0.5-500 ppm), which covers the range for monitoring of drinking, recreation, and food processing water. Also, the sensor has a high bending stability, and is reusable, which further reduces the cost of each measurement. The inexpensive draw-on-demand sensor is especially important for less industrialized or resource-limited areas where fabrication facilities, analytical equipment, and trained personnel are limited.

## **5.2. Sensor design and operation**

PEDOT:PSS was chosen for free chlorine sensing due to its solution processability, tunable electrical conductivity, and reactivity with free chlorine [292]. In a free chlorine solution, PEDOT is oxidized (Figure 5-1(a)) and its electrical resistivity increases due to the disruption of  $\pi$ - $\pi$  conjugation in its chemical structures [292]. The resistance change of a PEDOT:PSS film is determined by the free chlorine concentration and reaction time. Based

on this mechanism, a PEDOT:PSS chemoresistor was designed. Its layout design and equivalent circuit is shown in Figure 5-1(b).

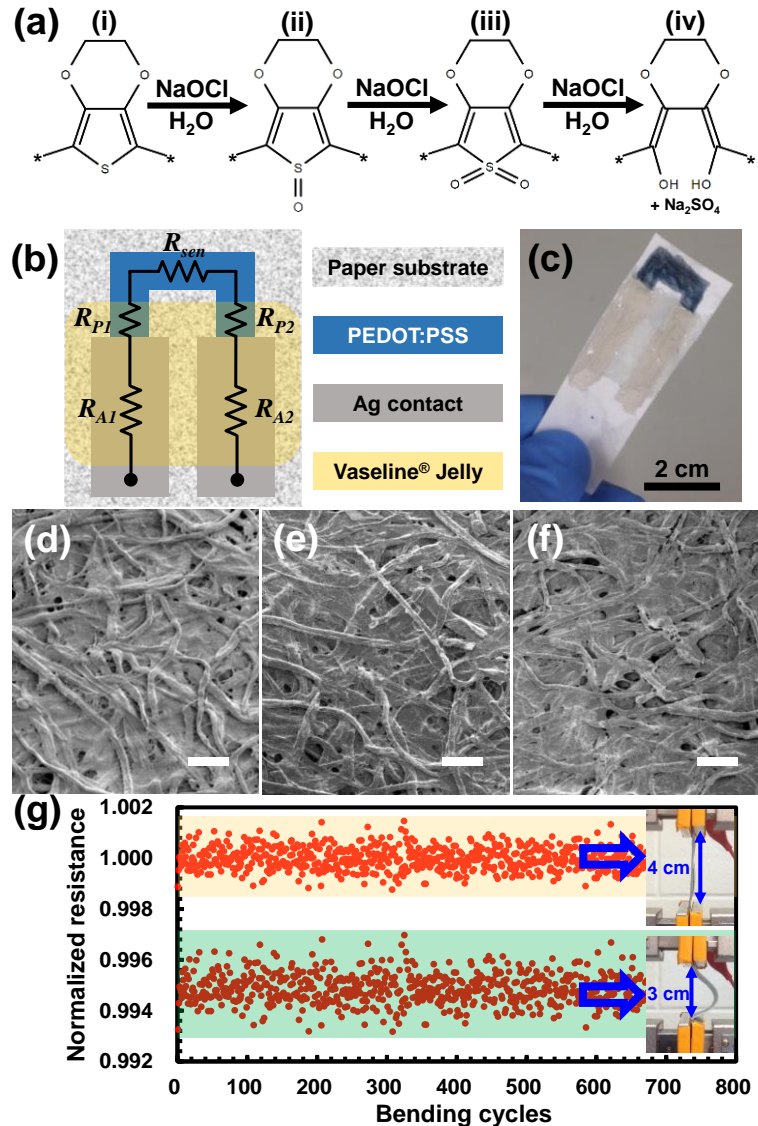


**Figure 5-1.** (a) Oxidation of PEDOT in a free chlorine solution (adopted from reference 23). (b) Top view schematic and equivalent circuit of the drawn sensor. (c) Image of a drawn sensor after fabrication; (d-f) SEM images (scale bars represent  $100\ \mu\text{m}$ ) of the surface of: (d) Paper substrate. (e) Drawn PEDOT:PSS film. (f) Drawn PEDOT:PSS after testing in 100 ppm NaOCl solution for 15 s. (g) Resistance variation of a 4 cm long drawn PEDOT:PSS chemoresistor during bending tests.

The response of the free chlorine sensor is quantified using the relative resistance change ( $\Delta R/R_0$ ) of the chemoresistor as:

$$\frac{\Delta R}{R_0} = \frac{\Delta R_{sen}}{R_{A1} + R_{A2} + R_{P1} + R_{P2} + R_{sen}}, \quad (5.1)$$

where  $\Delta R$  is the measured resistance difference at the Ag contacts before and after oxidation,  $R_0$  is the measured resistance before oxidation,  $R_{A1}$ ,  $R_{A2}$  are the resistance of the contacts,  $R_{P1}$ ,  $R_{P2}$  are the resistance of the drawn PEDOT:PSS film covered by the waterproof layer,  $R_{sen}$  is the resistance of the exposed PEDOT:PSS film before testing, and  $\Delta R_{sen}$  is the resistance difference of the exposed PEDOT:PSS film before and after testing. Since the resistance of the Ag contacts ( $<1 \Omega$ ) is much lower than that of the drawn PEDOT:PSS (5-100 k $\Omega$ ) film (Figure 5-1(c)), equation (1) is simplified to:

$$\frac{\Delta R}{R_0} \approx \frac{\Delta R_{sen}}{R_{P1} + R_{P2} + R_{sen}}. \quad (5.2)$$

Therefore, to maximize the response of the sensor, the values of  $R_{P1}$ ,  $R_{P2}$  should be minimized by reducing the overlapped area between the PEDOT:PSS film and the waterproof layer. To reduce the sensor-to-sensor variation of the overlapped area, a stencil can be used to cover the PEDOT:PSS film when depositing the waterproof layer. In this study, the overlapped area is  $\sim 10 \text{ mm}^2$ , and the exposed sensing area is  $\sim 150 \text{ mm}^2$ . The advantages of using the relative resistance change ( $\Delta R/R_0$ ) to express the sensor response include:

- The sensing element (chemoresistor) can be fabricated with different shapes and dimensions, which eliminate the need for precision equipment and enables hand-drawing as the fabrication technique. Also, the fabrication process has a high tolerance for the variation in the sensor geometry.
- The relative change of resistance of a chemoresistor can be calculated for multiple tests as long as the resistance is within the range of the measuring instrument (e.g., multimeter). Thus, the sensor is reusable.
- The effect of the degradation of the sensing material (PEDOT:PSS) during storage can be reduced because the resistance is measured before each test. This step sets the baseline of each test, which is similar to a calibration step.

### 5.3. Sensor fabrication and usage

Figure 5-2 shows the fabrication process of a paper-based free chlorine sensor strip. The as-received PEDOT:PSS solution was filled in the ink cartridge of a fountain pen, manually drawn onto a filter paper (type 542, Whatman) and dried naturally in air (Figure 5-2(a)). The drawn PEDOT:PSS film formed a chemoresistor as the sensing element. The paper substrate we selected was based on its strength in water and its adhesion to PEDOT:PSS. Table 5-1 shows the comparison of different paper substrates.

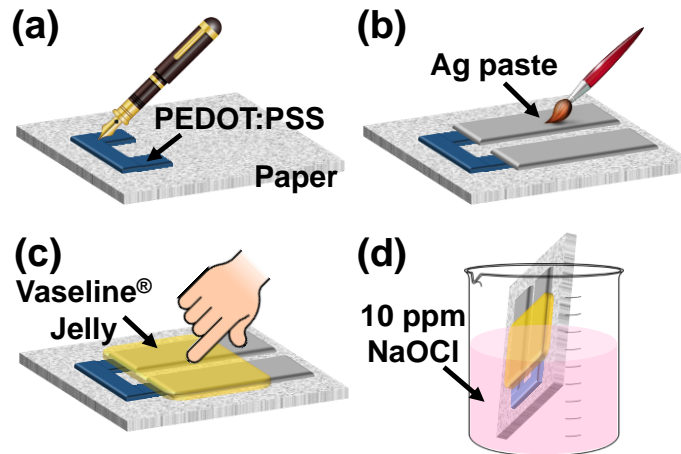


**Figure 5-2.** Fabrication process of a paper-based free chlorine sensor. (a) Drawing a PEDOT:PSS film as a chemoresistor. (b) Drawing Ag films for electrical contacts. (c) Coating waterproof Vaseline® Jelly. (d) Sensor conditioning in a NaOCl solution.

**Table 5-1.** Comparison of 6 types of paper substrates and their adhesion to PEDOT:PSS films.

Substrates	Pore size, $\mu\text{m}$	Porosity, %	Strength	Adhesion to PEDOT:PSS
Whatman filter paper #542	2.5	-	Good	Good
Whatman filter paper #1	11	-	Poor	Good
Polycarbonate membrane filter (TTTP04700, EMD Millipore)	2	5.9	Poor	Poor
Nitrocellulose membrane filter (SMWP04700, EMD Millipore)	5	84	Poor	Poor
PVDF membrane filter (GVHP04700, EMD Millipore)	0.22	75	Good	Poor
Normal writing paper	-	-	Poor	Good

Then, a Ag paste was drawn onto the PEDOT:PSS film using a painting brush and dried naturally in air to form the contacts (Figure 5-2(b)). Finally, a petroleum jelly (Vaseline® Jelly Original) was manually applied on both sides of the paper (Figure 5-2(c)) to protect the Ag contacts from water. To accurately monitor free chlorine concentrations of  $<5$  ppm,

the sensor should be conditioned in 10 ppm NaOCl solution for 5 min and dried before use (Figure 5-2(d)).

All free chlorine sensing tests were performed at  $27 \pm 2$  °C in freshly prepared free chlorine solutions. To obtain the sensor response, the sensor strips were dipped into free chlorine solutions for different durations, then rinsed with tap water for 2 s and dried in air. The drying time is about 10 min and it can be shortened by reducing the exposed area of the paper substrate and the PEDOT:PSS film. The resistance of the drawn PEDOT:PSS chemoresistor before and after testing was measured using a commercial multimeter (72-7730, TENMA). Figure 5-3 shows the real-time resistance change during the drying period of a PEDOT:PSS chemoresistor after free chlorine testing (10 ppm, 5 min). The sensor strip was left in ambient air at room temperature for drying. The measured electrical resistance of the sensing chemoresistor is affected by two factors:

- The oxidation of PEDOT by the free chlorine in the residual solution. This effect causes the increase of the resistance.
- The evaporation of water, which was absorbed by the paper during free chlorine testing. Water absorption increases the distance between cellulous fibers in the paper, loosens the PEDOT conductive network, and increases the resistance of the sensing chemoresistor. Thus, water evaporation causes the decrease of the resistance.

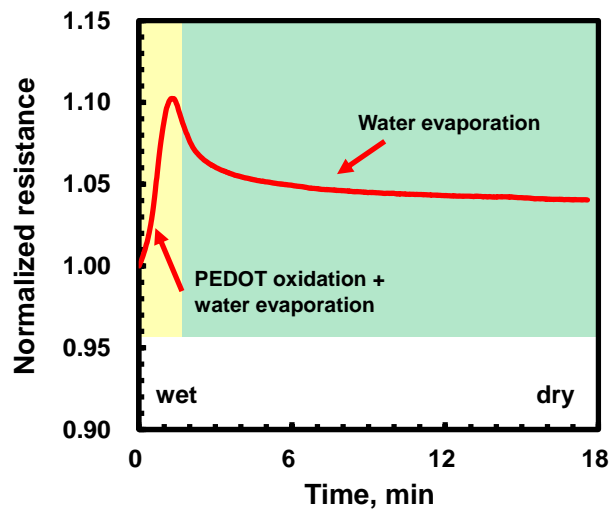


Figure 5-3. Resistance change during the drying period of the PEDOT:PSS film after free chlorine sensing.

In the first stage (yellow background), the oxidation reaction dominates so the resistance increases. In the second stage (green background), the residual free chlorine depletes and the effect of water evaporation dominates. Therefore, a decrease of the resistance is observed. At the drying time of ~10 min, the resistance reaches a relative stable value. Hence, the resistance of the chemoresistor after free chlorine sensing is measured after 10 min of drying.

## **5.4. Sensor characterization**

### **5.4.1. Test in DI water**

For the practical use of the drawn sensor, the adhesion between PEDOT:PSS and the substrate is important. Delamination of the sensing material increases the resistance of the chemoresistor which increases the error of the test. Due to the porous nature of paper (Figure 5-1(d)), PEDOT:PSS adheres well to the substrate and forms conductive networks (Figure 5-1(e)). After rinsing the PEDOT:PSS film with DI water or dipping the sensor in a 100 ppm free chlorine solution for 15 s, the film morphologies did not show much difference (Figure 5-1(f)). The consistency in the morphologies before and after free chlorine sensing indicates that the electrical resistance change is due to the oxidation reactions of the PEDOT (not physical delamination).

### **5.4.2. Mechanical stability**

Another important factor for the practical use of the sensor strip is its bending stability. A PEDOT:PSS chemoresistor of 2 cm × 4 cm was bent for >750 times in air and its resistance changes were repeatable (Figure 5-1(g)). The average relative resistance change was -0.51% (negative sign means the resistance decreases upon bending), indicating that bending had a minor effect on the resistance change. This high bending stability is attributed to the mechanical flexibility of the paper and the good adhesion of PEDOT:PSS to it. To further reduce the effect of mechanical bending, a stress/strain sensor can be integrated on the

paper for signal compensation. Also, the paper-based sensor can be laminated onto a rigid substrate.

### 5.4.3. Reusability

The reusability of the drawn sensor was studied by repeatedly measuring the relative resistance changes of the PEDOT:PSS chemoresistor in free chlorine solutions with different concentrations for different durations (Figure 5-4). Once the paper substrate is deformed by water in the first measurement, its flatness doesn't change much in the consequent wetting-drying cycles. Similar to the mechanical bending, the deformation of the paper has negligible effect on the sensor response. In the solution with 0 ppm free chlorine (DI water), the resistance increases slightly ( $\Delta R/R_0 \sim 0.02$ ) due to the natural degradation of PEDOT:PSS in air and water [293].

In solutions with low free chlorine concentrations (<5 ppm, Figure 5-4(b-d)), the testing duration should be longer than 5 min to obtain a relative resistance change ( $\Delta R/R_0$ ) of at least 0.06. Also, the values of relative resistance change gradually increase in the first few tests and then stabilize, which was not observed in another report when high free chlorine concentrations (>25 ppm) were used [292]. This phenomenon may be explained by the generation of intermediate species (ii) and (iii), shown in Figure 5-1(a). Species (ii) and (iii) includes thiophene-1-oxide and thiophene-1,1-dioxide structures, respectively. These structures provide species (ii) and (iii) with smaller electronic band gaps (hence lower electrical resistivity) than species (i) with a thiophene structure [294]. The final oxidation species (iv) has disrupted  $\pi$ - $\pi$  conjugation, and its resistivity is the highest. At low free chlorine concentrations, the oxidation of PEDOT is reaction-limited [292], and species (ii-iv) all contribute to the measured resistance. Therefore, in the first few tests, the amount of species (iv), hence the resistance of the chemoresistor increases slowly (even resistance decrease can be observed due to the relatively larger amount of species (ii) and (iii) than (iv)). After this initialization stage, the generation of species (ii-iv) approach constant speeds, so the resistance increases at a constant rate.

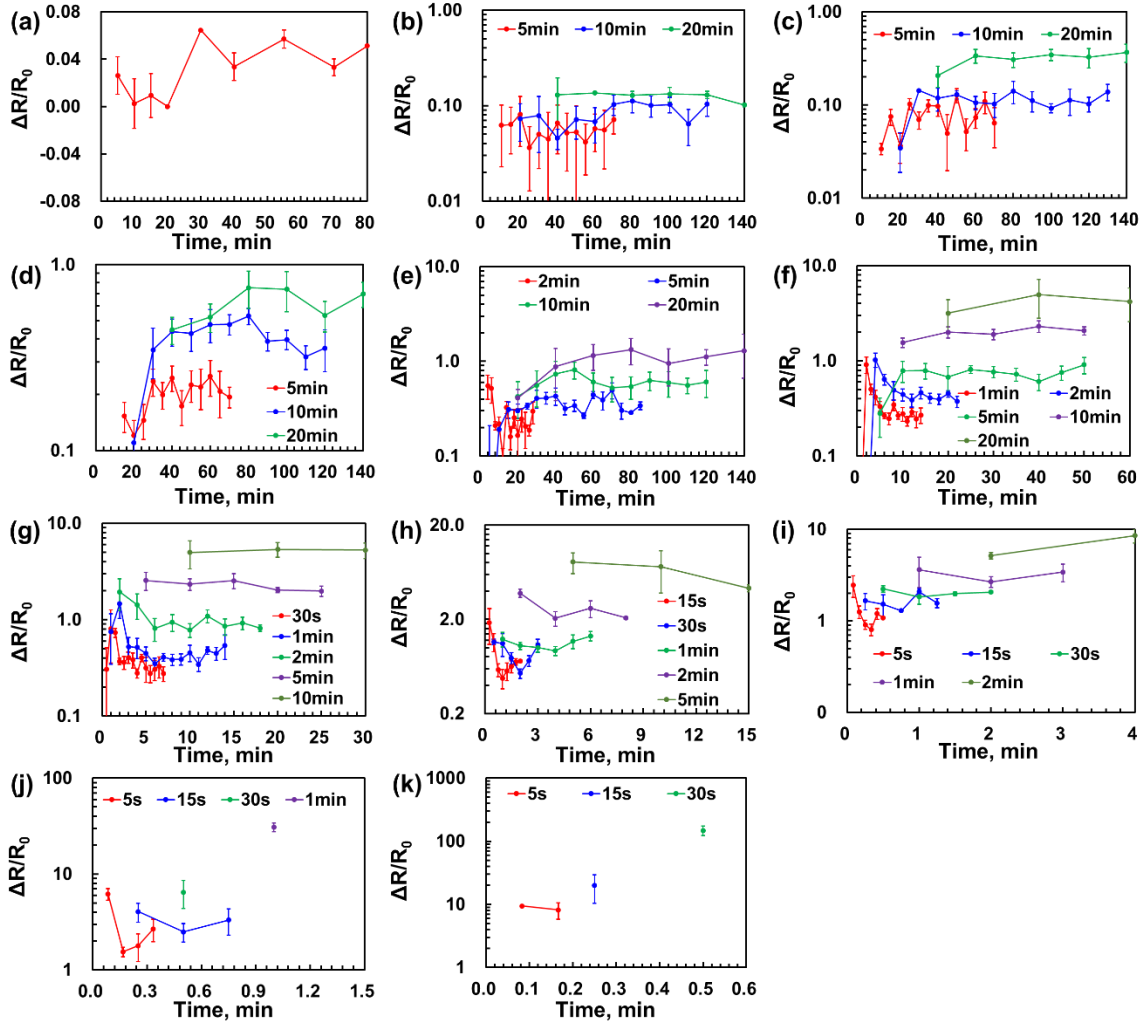


**Figure 5-4.** Reusability of paper-based drawn PEDOT:PSS sensor stripes in solutions with different free chlorine (NaOCl) concentrations. (a) 0 ppm (DI water). (b) 0.5 ppm. (c) 1 ppm. (d) 2 ppm. (e) 5 ppm. (f) 10 ppm. (g) 20 ppm. (h) 50 ppm. (i) 100 ppm. (j) 200 ppm. (k) 500 ppm. Legend in each figure: time of each test. X axis: accumulated testing time.

In solutions with medium free chlorine concentrations (5-50 ppm, Figure 5-4(e-g)), response peaks can be observed after the second test if short testing duration (<2 min) is used. This observation can be explained by the same mechanism discussed above. Both species (ii) and (iii) are accumulated in the first test due to the reaction-limited process. In the second test, low-resistance species (ii) and (iii) are oxidized to the high-resistance species (iv) so that the response is large. Longer reaction time reduces the effect of species (ii) and (iii), and the response peak in Figure 5-4(e-g) is less pronounced.

In solutions with high free chlorine concentrations (>50 ppm, Figure 5-4(h-k)), PEDOT is oxidized quickly to species (iv) and the effect of intermediate species (ii) and (iii) is not significant. Also, due to the fast oxidation, the resistance of the chemoresistor quickly exceeded the measurement range (0-20 M $\Omega$ ) of the used multimeter. Thus, the reusability of the sensor is higher for low free chlorine concentrations.

According to the abovementioned results, to monitor low free chlorine concentrations (<5 ppm) accurately, a pre-conditioning step (e.g., in 10 ppm NaOCl solution for 5 min) has to be carried out. After conditioning, the sensor response becomes reproducible, as shown in Figure 5-5. For the free chlorine concentration of 1, 10, and 100 ppm, the sensor can be reused for 19 (5 min testing duration), 9 (5 min testing duration), and 5 (15 s testing duration) times, respectively.

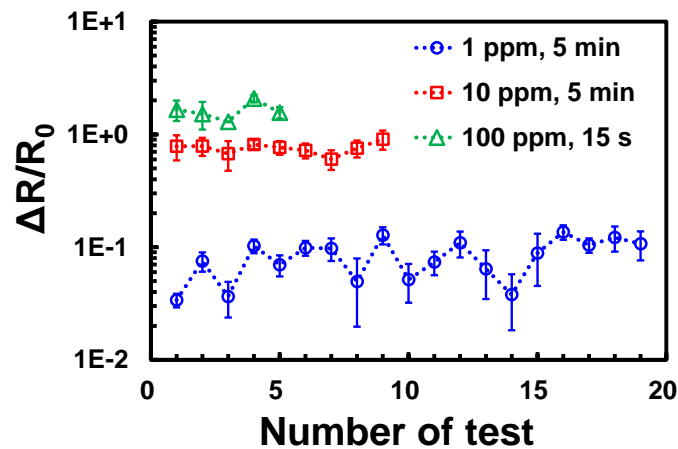


**Figure 5-5.** Reusability of the free chlorine sensor after conditioning in a 10 ppm NaOCl solution for 5 min

#### 5.4.4. Sensitivity

Figure 5-6 shows the sensor response in solutions with different free chlorine concentrations using different testing durations. Based on the sensing range, test efficiency, and regression coefficient, the sensor response is divided into two segments. For the concentrations of 0.5-50 ppm and 50-500 ppm, a testing duration of 5 min and 15 s is selected, respectively. The use of a shorter testing duration for higher concentrations could

offer the sensor a longer lifetime (more tests can be done before resistance exceeds the measurement range). The sensor response can be expressed as:

$$\frac{\Delta R}{R_0} = 0.091 \exp(2.428 \times \log_{10} [\text{NaOCl}]), \quad 0.5 \text{ ppm} \leq [\text{NaOCl}] \leq 50 \text{ ppm}; \quad (5.3)$$

$$\frac{\Delta R}{R_0} = 0.0016 \exp(3.425 \times \log_{10} [\text{NaOCl}]), \quad 50 \text{ ppm} \leq [\text{NaOCl}] \leq 500 \text{ ppm}. \quad (5.4)$$

The detection limit of the sensor is defined as 3 times of the sensor response in a blank solution ( $\Delta R/R_0 \sim 0.02$ ). Here, the detection limit is 0.5 ppm free chlorine ( $\Delta R/R_0 \sim 0.06$ ). Extending the testing duration can improve the detection limit, but the test efficiency and reusability of the sensor will be reduced. In addition, the sensor response towards 0.5 ppm free chlorine is  $>10$  times larger than its response to mechanical bending ( $\Delta R/R_0 \sim -0.0051$ ).

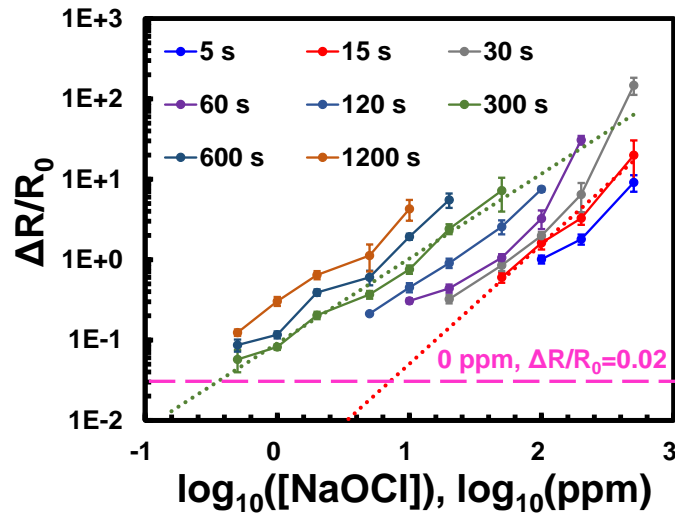


**Figure 5-6.** Sensor responses in different free chlorine solutions using different testing durations.

For practical use, a drawn sensor strip is first dipped into the test solution for 15 s, and the relative resistance change is measured. If the response is larger than 0.6 (the sensor response in a 50 ppm free chlorine solution for 15 s), equation (5.4) is used to calculate the free chlorine concentration. On the other hand, if the response is less than 0.6, it is dipped into the test solution again for 5 min. The sensor response from the 5-min test is used to calculate the free chlorine concentration according to equation (5.3). The flow chart of this procedure is shown in Figure 5-7.

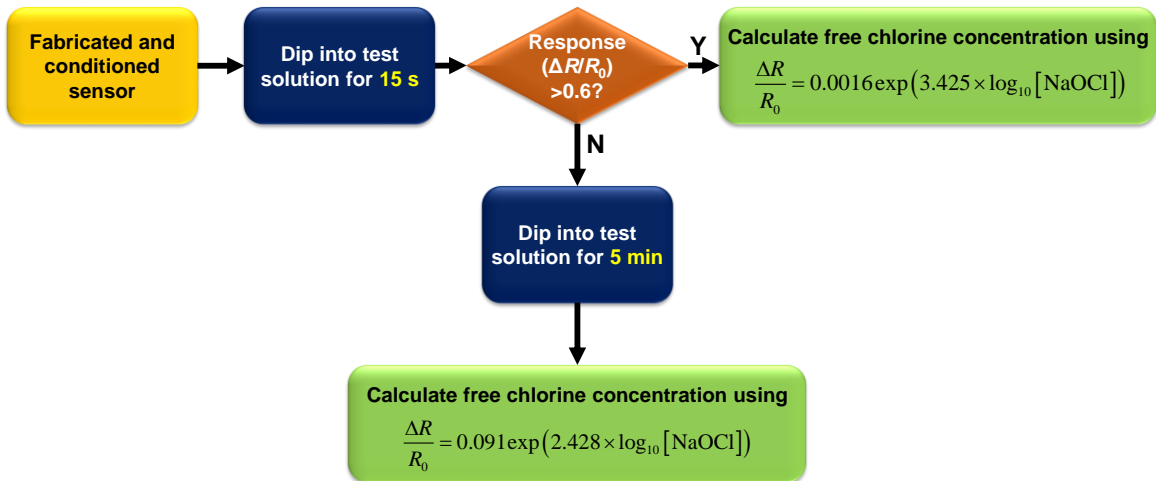


Figure 5-7. Flow chart of the procedures to use the drawn sensor for practical free chlorine measurement.

### 5.4.5. Stability

Because the free chlorine sensor developed in this study is reusable, its stability during the storage period between two tests should be studied. The sensor was stored in ambient air in dark at room temperature and tested every a few days. Figure 5-8 shows the variation of the sensor response is less than 15% in 30 days, indicating a high storage stability. Although the sensing material (PEDOT:PSS) may undergo degradation during storage [293], the expression of the sensor response using relative resistance change eliminates this effect.

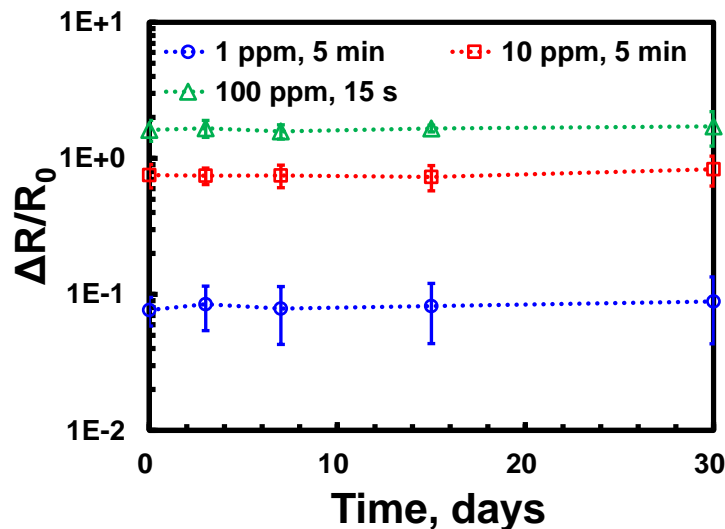
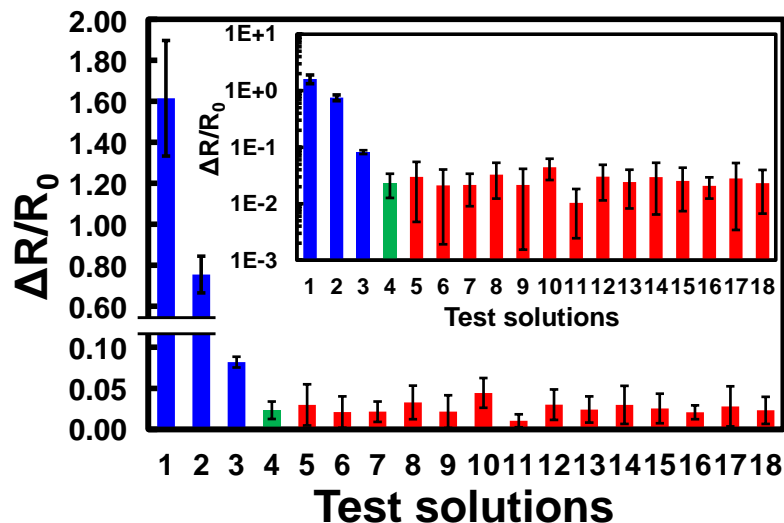


Figure 5-8. Storage stability of the drawn free chlorine sensor.

### 5.4.6. Selectivity

The selectivity of the drawn sensor should also be studied for practical considerations. Previous studies have shown that the resistivity of PEDOT:PSS films could be reduced by treating the films with acid, alkali, salt solutions or organic solvents [295]. However, high-concentration solutions ( $>10^4$  ppm for salt solutions) and high treatment temperatures ( $>100$  °C) were needed. These conditions are not common in practical drinking water quality monitoring applications. Here, interference solutions with a concentration of 1000 ppm (higher than the concentrations of common ions in natural water) were prepared (see list in Figure 5-9 caption). The sensor was tested in these solutions for 5 min at room temperature. The sensor responses were less than 0.025 (Figure 5-9), suggesting a high selectivity towards free chlorine due to the specific oxidation reaction. In real water samples, the concentrations of interference ions are less than 1000 ppm, so their effect on the sensor response will be less.



**Figure 5-9.** Sensor responses in free chlorine solutions and 1000 ppm interference solutions (1: 100 ppm NaOCl (15 s); 2: 10 ppm NaOCl; 3: 1 ppm NaOCl; 4: DIW; 5: NaCl; 6: CaCl<sub>2</sub>; 7: MgCl<sub>2</sub>; 8: ZnCl<sub>2</sub>; 9: K<sub>2</sub>SO<sub>4</sub>; 10: CuSO<sub>4</sub>; 11: (NH<sub>4</sub>)<sub>2</sub>SO<sub>4</sub>; 12: NaHCO<sub>3</sub>; 13: Na<sub>2</sub>CO<sub>3</sub>; 14: CH<sub>3</sub>COONa; 15: Na<sub>2</sub>HPO<sub>4</sub>; 16: KNO<sub>3</sub>; 17: Urea; 18: Ethylene glycol). Inset: sensor responses in logarithm scale.

### 5.4.7. Test of real water samples

To prove the practical usability of the drawn sensor, free chlorine concentrations in real water samples were measured. Table 5-2 lists the measurement results of free chlorine

concentrations in tap water and swimming pool water. The measured free chlorine concentrations using the drawn sensor were close to the reference values obtained from conventional colorimetric and amperometric sensors, with a difference less than 15%.

**Table 5-2.** Free chlorine measurement of real water samples (average results from n measurements).

Water sample	Measured by a drawn sensor, ppm	Measured by the reference method, ppm	Reference method
Tap water (McMaster)	$0.8 \pm 0.3$ (n = 20)	$0.7 \pm 0.2$ (n = 7)	DPD-based colorimetric sensor (CN-70, Hach)
Swimming pool water (McMaster)	$1.8 \pm 0.4$ (n = 20)	$2.00 \pm 0.00$ (continuous monitoring)	Amperometric sensor (PC DYNAMICS, Dinotec)

## 5.5. Advantages of the hand-drawn free chlorine sensor

The sensitivity of our sensor is based on their relative resistance change. In contrast, most previously reported electrochemical free chlorine sensors used current change to determine their sensitivities (Table A-2, Appendix B), thus making a direct comparison difficult. However, for other key sensor features such as substrate material, fabrication, detection range, response time, stability and reusability, the sensor developed in this study have the following advantages:

- **The fabrication is simple and cost-effective.** All steps are at room temperature, are compatible with low-cost paper substrates, require no instrumentation, allow simple layout design, and can be performed by untrained personnel. Multiple sensors can be fabricated on the same substrate, and their response can be averaged to reduce the inter-sensor variation.
- **The use of the sensor is straightforward.** A commercial multimeter is sufficient to provide quantitative results (in contrast to potentiostat in amperometric sensors and optical detectors in colorimetric sensors).
- **A wide sensing range (0.5-500 ppm) is obtained.** The wide sensing range allows the sensor to be used in different applications (low-concentration end for monitoring drinking and recreational water, and high-concentration end for food processing water).
- **The sensor is reusable (comparing to commercial colorimetric strips that are disposable).** The reusability further reduces the cost for each free chlorine test.

## **5.6. Conclusions**

We have developed a simple, cost-efficient, instrument-free, hand-drawing process to fabricate free chlorine sensors on paper substrates at room temperature. The sensing mechanism was based on the oxidation of PEDOT:PSS chemoresistor by free chlorine solutions. The final oxidation product had a higher electrical resistivity than PEDOT:PSS so that the relative resistance change of a chemoresistor could be used to express the sensor response. The sensor had a high mechanical stability, reusability, and wide sensing range. Also, the sensor was easy-to-use so that untrained personnel could accurately measure free chlorine concentrations in real water samples. The outcomes of this study was very important for the monitoring of drinking water quality in resource-limited areas.

# Chapter 6 FPGA-based, integrated drinking water quality monitoring system\*

This chapter describes an integrated sensing system with microfabricated pH, free chlorine and temperature sensors on a common glass substrate. Such a sensing system must be accurate, efficient, user friendly, and inexpensive in the monitoring of multiple drinking water quality parameters, which is critical for continued water safety in varied geographical locations including developed regions and resource-limited areas. The potentiometric pH sensor and the Wheatstone bridge temperature sensors are fabricated by inkjet printing of Pd/PdO and Ag. These sensors are highly sensitive, fast in response, and they do not require signal conditioning for data analysis. The free chlorine sensor is based on an electrochemically modified pencil lead, which is highly stable and reproducible. Such a free chlorine sensor is potentiostat-free and calibration-free, so it is easy-to-use. The three sensors are connected to a FPGA board for data analysis and display, with real-time pH and temperature compensation for free chlorine sensing. The developed sensing platform enables drinking water quality monitoring by nonprofessionals in a simple manner.

## 6.1. Background

The monitoring of water quality is extremely important for maintaining the safety of water resources used for various purposes such as drinking, recreation and food processing [11], [13], [166], [296]–[298]. Water quality is determined by interdependent chemical, microbial and physical factors including but are not limited to pH, free chlorine concentration, turbidity, dissolved oxygen, conductivity, organic carbon, microorganisms,

---

\* Part of this work will be submitted for consideration for publication as: Y. Qin, A. U. Alam, S. Pan, M. M. R. Howlader, R. Ghosh, N.-X. Hu, M. J. Deen, Portable water quality monitoring system with integrated pH, free chlorine and temperature sensors, April 2017.

and temperature [1]. Many conventional drinking water quality monitoring technologies lack integration, are labor-intensive, time-consuming, and expensive. Typically in many systems, only one parameter such as free chlorine [299] or pH [300] is measured at a time [42]. These technical limitations raise imminent challenges in maintaining high quality drinking water in heavily-populated cities (large water consumption and fast water quality degradation) and also in remote areas (resource-limited) [281]. Therefore, low-cost, highly sensitive, accurate, reliable, easy-to-use, and integrated sensing systems are needed for the on-demand/real-time monitoring of multiple water quality parameters in multiple locations to ensure continued drinking water safety.

Free chlorine is widely used for water disinfection, and the free chlorine concentration should be accurately monitored for the water safety, especially for drinking, recreational, and food processing water [12]. The WHO recommends the usage of 2 to 3 ppm free chlorine in the drinking water [13]. The free chlorine concentration in a swimming pool should be maintained between 1.5 to 2 ppm [16]. For food processing, the water should contain 50 to 200 ppm free chlorine [17]. The accurate measuring of free chlorine concentration is challenging because it is correlated with the temperature and pH of the water sample [25]. The dissociation constant of HOCl in water is a function of temperature. The pH of the water sample determines the concentration ratio between HOCl and OCl<sup>-</sup> at a certain temperature. In addition, the response of a pH sensor is usually affected by temperature [166]. Thus, pH and temperature sensors are required and should be integrated into a free chlorine sensing system.

The standard method to measure the free chlorine concentration is to use a DPD-based absorptiometry method [26]. However, this optical method is difficult to use, high-cost, difficult to perform continuous monitoring, and DPD free chlorine reagent contains chemicals that are harmful to humans, such as *N,N*-diethyl-*p*-phenyldiamine-compound and ethylenedinitrilotetraacetic acid disodium salt dihydrate. Amperometric electrodes are utilized for the online monitoring of free chlorine [163], [301]. One of the difficulties in

using the existing amperometric sensors is the requirement of frequent calibration due to the poor stability of the sensors. Chemoresistor-based free chlorine sensors are not suitable for continuous monitoring because the sensing materials need to be activated or dried after each/several measurement(s) [17], [302]. For both optical and electrochemical free chlorine sensing systems, pH sensors and temperature sensors are usually not integrated on a common platform (at most connecting a discrete pH/temperature sensor using a cable).

For pH sensing, conventional glass electrodes are bulky, fragile and costly. These electrodes are also difficult-to-use due to the need for frequent calibration and the requirement of complicated electronic circuits for signal conditioning (amplification, filtering, etc.) [166]. To improve conventional pH meters, many studies focused on developing microfabricated pH sensors with smaller dimensions, higher stability, simpler operation, and lower cost [11], [57], [81], [166], [303]. Besides, studies on micro-scale temperature sensors are extensive. One of the most commonly used temperature sensors is a thermistor made from metals [272], polymers [304], ceramics [305], carbon nanomaterials [306], or their composites [307]. However, the technologies to fabricate low-cost, integrated pH and temperature sensors that are compatible with other water quality sensors are still to be explored.

Recently developed integrated sensing systems have already shown advantages in human perspiration analysis [308], [309] and diabetes monitoring/therapy [306]. For example, the integrated sensor arrays in such systems had a high spatial and temporal sensing resolution. The integrated electronics could perform simultaneous on-site signal processing. Thus, the integrated systems were compatible with multiplexed analysis. For water quality monitoring, integrated sensors were developed for measuring dissolved oxygen, conductivity, temperature, pH, bacteria (*Escherichia coli*), and cell nutrients/metabolites [49], [310]–[312]. However, an integrated free chlorine monitoring system is not yet developed.

In this chapter, we report on an integrated sensing system which could simultaneously measure the pH, free chlorine concentration, and temperature of a water sample. The potentiometric pH sensor was fabricated by inkjet printing of Pd/PdO as the sensing electrode and Ag/AgCl/KCl as the reference electrode (developed in Chapter 3). Such a pH sensor had a high sensitivity and did not require signal conditioning for data analysis. A Wheatstone bridge temperature sensor was inkjet-printed together with the pH sensor using the same Pd and Ag ink. The temperature sensor showed a higher sensitivity compared with a thermistor. The free chlorine sensor is a potentiostat-free amperometric sensor, consisting of an electrochemically modified pencil lead and an inkjet-printed Ag electrode. Such a free chlorine sensor measured the HOCl concentration, and was calibration-free due to its high reproducibility and stability. The three microfabricated sensors were on a common glass substrate, and they were connected to a FPGA board for on-site monitoring of real water samples. A high measurement accuracy was obtained. This indicated that the integrated sensing system has the potential to be used as a rapid, user-friendly, cost-effective, and widely applicable method for drinking water quality monitoring.

## 6.2. Fabrication of integrated sensors

The integrated pH, free chlorine, and temperature sensors were fabricated on glass substrates (7525M, J. Melvin Freed Brand) cleaned by IPA and DI water (Figure 6-1(a)). The pH and temperature sensors were inkjet-printed onto the glass substrates while the free chlorine sensors were fabricated separately by the electrochemical modification of pencil leads. The layout designs of the inkjet-printed structures are shown in Appendix C.

The Pd ink was prepared by diluting the as-received Pd precursor solution using 20 wt% toluene. The inkjet printing process (Figure 6-1(b)) followed our previous report (reference [81] and Chapter 3) using a Dimatix DMP-2831 materials printer (Fujifilm) equipped with DMC-11610 Dimatix materials cartridges (Fujifilm). The thermolysis of the printed Pd ink was carried out on a hotplate in air at 200 °C for 4 min to form a smooth Pd film for the pH sensor (Figure 6-1(c)). Then, the Pd ink was printed again, and the thermolysis was

performed in a low-vacuum chamber (Isotemp 280A, Fisher Scientific) at 200 °C for 20 min to form rough Pd films (Figure 6-1(d-e)) ([305] and Chapter 4). The rough films are used as two thermistors with a negative TCR in the Wheatstone-bridge-based temperature sensor. The printed Pd films (both smooth and rough) were oxidized in air at 200 °C for 48 h to form PdO-rich films (Figure 6-1(f)).

Next, the SU-8 photoresist was diluted by 10 times using PGMEA and inkjet-printed onto the substrate (Figure 6-1(g)) to improve the adhesion between the substrate and the Ag films (printed in the next step). The SU-8 ink was cured in air at 200 °C for 1 h (Figure 6-1(h)). The as-received Ag NP ink was then inkjet-printed to form two thermistors with positive TCR values in the temperature sensor, the Ag layer of the reference electrode in the pH sensor, and the Ag electrode in the free chlorine sensor (Figure 6-1(i)). The sintering condition for the Ag NP ink was 120 °C for 10 min in air (Figure 6-1(j)). The AgCl layer in the Ag/AgCl reference electrode was obtained by drop casting 0.4 wt% NaOCl solution onto the printed Ag for 30 s before rinsing with DI water (Figure 6-1(k)). A solution of the solid electrolyte of the reference electrode was formulated by dissolving 2 wt% PVC in KCl- and AgCl-saturated cyclohexanone. The solution was drop casted on top of the Ag/AgCl film and heated at 140 °C for 5 min to form a solid electrolyte layer (Figure 6-1(l)).

The sensing electrode of the free chlorine sensor was fabricated by the electrochemical modification of the pencil lead surface [313]. A voltage of 1 V was applied between the pencil lead and a Ag/AgCl reference electrode (CHI111, CH Instruments). The electrolyte solution contained 0.1 M PBS (pH 7.0) and an appropriate amount of ammonium carbamate (0.1 M) to adjust the pH to 8.9. The middle part of the modified pencil lead was mounted onto the glass substrate by using a 2 wt% PVC solution in cyclohexanone as adhesive (Figure 6-1(m-n)). The PVC solution also covered the entire temperature sensor and the printed electrical connections of the pH and free chlorine sensors as a water-resistant layer (Figure 6-1(n)). After drying the PVC solution in air at 80 °C for 30 min, conductive copper tapes (Tapes Master) were used to make electrical contacts. The integrated sensor was

conditioned in 1 M KCl solution for 12 h before use. An image of the fabricated integrated sensor is shown in Figure 6-2(b).

The fabricated sensors were connected to a FPGA board (Basys 3, Artix-7, Digilent) for data analysis and display. The FPGA was programmed using the Verilog language with the Vivado Design Suite (2015.4, Xilinx). The Verilog code is shown in Appendix D.

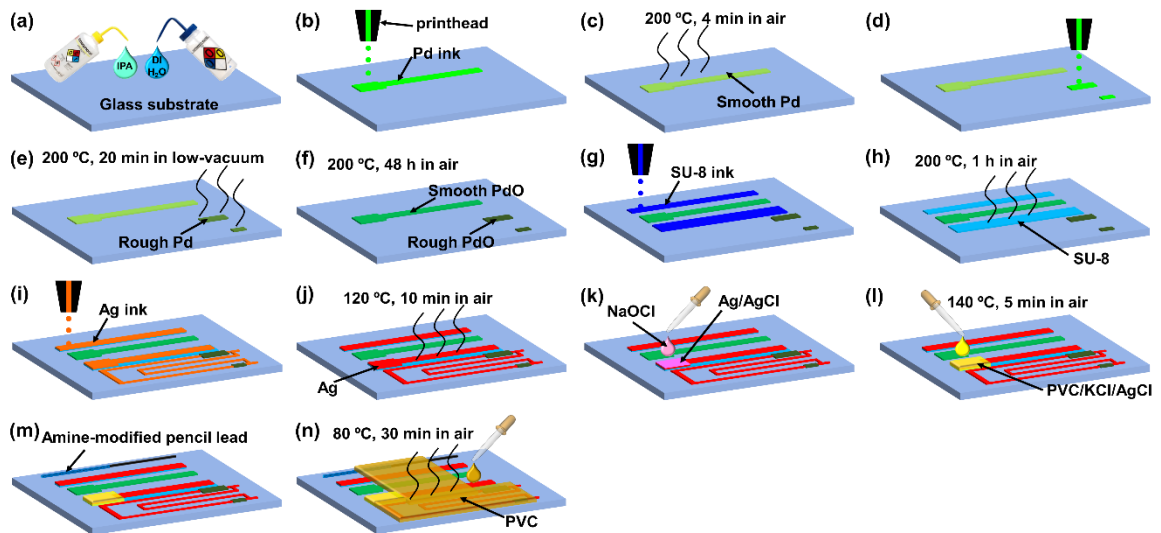


Figure 6-1. Fabrication process of an integrated pH, free chlorine and temperature sensor.

### 6.3. System design

Monitoring the drinking water quality using the developed integrated sensing system has the following advantages over using discrete sensors and conventional analytical method:

- As illustrated in Figure 6-2(a), the integrated sensing system includes an integrated sensor probe, a signal conditioning circuit board for free chlorine sensing, a FPGA board, and a portable power supply. The integrated system allows simultaneous on-site monitoring of three important water quality parameters: pH, free chlorine concentration, and temperature. The integrated system also allows the real-time compensation for the sensor readings for high measurement accuracy. For example, the pH reading is compensated using the measured temperature. The free chlorine concentration is compensated using both pH and temperature.

- By fabricating the pH, free chlorine and temperature sensors on a common substrate with a small footprint (Figure 6-2(b)), water quality monitoring with a high spatial resolution can be realized. In addition, the sensing signals can be accurately compensated due to the three sensors being closely located to each other.
- Since the main technology used to fabricate the sensors is inkjet printing, the integrated sensor is low-cost due to the small amount of consumed materials and the elimination of cleanroom environment, high-temperature equipment, and high-vacuum chambers.

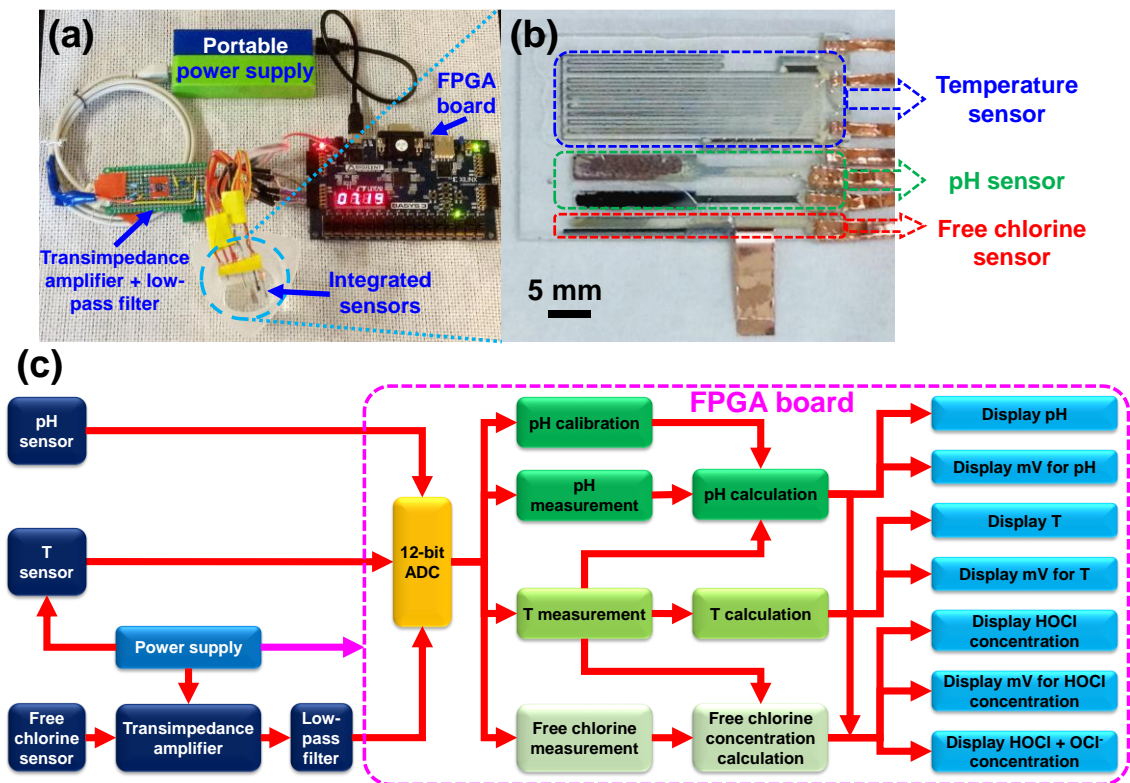


**Figure 6-2.** (a) A portable integrated water quality monitoring system measuring the pH value of tap water. (b) An integrated water quality sensing probe with pH, temperature and free chlorine sensors. (c) A schematic diagram of the water quality monitoring system including signal conditioning (amplification and filtering for free chlorine sensor), data analysis (on the FPGA board), and results display (on the FPGA board). “T” represents “temperature” in the schematic diagram.

The output signals of different sensors should be within the input range of the electronic system (FPGA board in this study) to realize an integrated system. Here, the sensor signal was digitized using a 12-bit analogue-to-digital converter (ADC, on the FPGA board), whose input voltage range was 0 - 1 V with a resolution of 0.305 mV. The data sampling frequency was set to be 1 Hz to realize real-time monitoring.

For the pH sensor, we have developed a Pd/PdO-based potentiometric pH sensor having an output voltage range of 0 - 500 mV (within the input range of the ADC) for the pH range between 4 and 10. The voltage resolution of 0.305 mV of the ADC results in a pH resolution of  $\sim 0.005$  (a pH sensitivity of 60 mV/pH is used here), which is better than the requirement of most water quality monitoring applications. In other words, the resolution of the pH output is not determined by the voltage resolution of the ADC, but the resolution of the pH sensor. Therefore, the pH sensor can be directly connected to the ADC without the need for data conditioning circuits.

For the free chlorine sensor, the paper-based, hand-drawn sensor developed in Chapter 5 is not suitable for real-time monitoring because of the drying step in using the sensor. Thus, an amperometric free chlorine sensor for measuring HOCl concentration developed in our group was employed in the integrated system [313]. The amperometric sensor consisted of a sensing electrode of an amine-modified pencil lead. The first challenge of integrating such a free chlorine sensor is the requirement of three electrodes and a potentiostat, which increases the system complexity. In our previous study [313], the reduction potential for HOCl was found to be 0.1 V, which is close to 0 V. Thus, we simplified the three-electrode configuration to a two-electrode configuration: the modified pencil lead as the working electrode and a Ag film as the reference/counter electrode. In the simplified configuration, 0 V was used as the reduction potential so that an external power supply (potentiostat) for activating the sensor can be eliminated [309]. The second challenge of implementing the free chlorine sensor is to convert its output current signals to voltage signals that are readable by the ADC on the FPGA board. To address this challenge, a transimpedance amplifier (Figure 6-3(a-b)) converted and amplified the output signal to 0 to 1 V for a free chlorine concentration of 0 to 8 ppm (common range for drinking and recreational water). Before the output voltage was read by the ADC, a low-pass filter circuit was applied to reduce the noise introduced by the transimpedance amplifier.

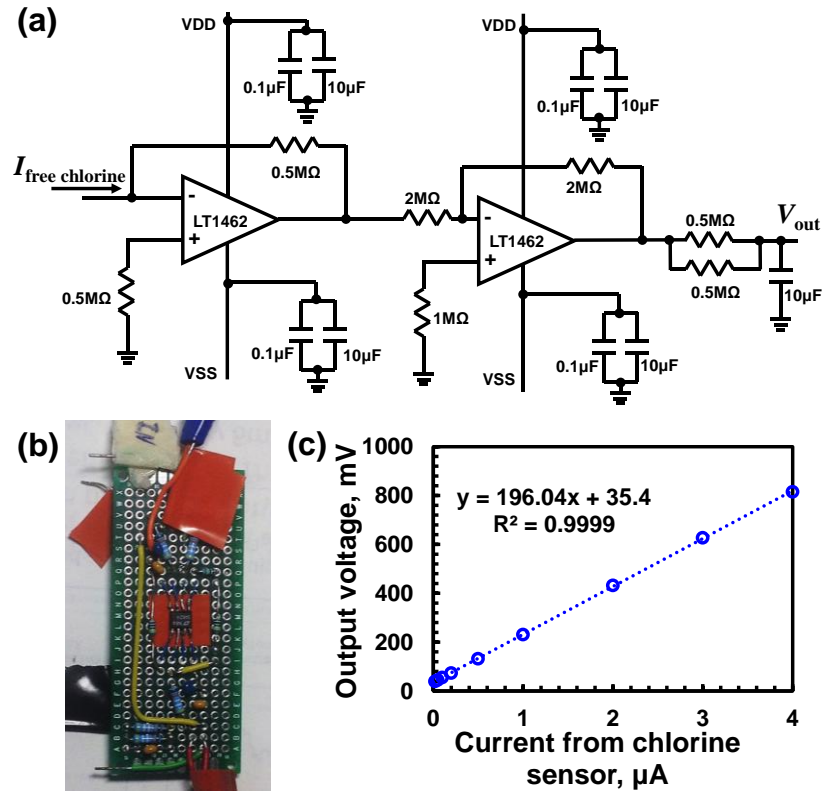


**Figure 6-3.** (a) Circuit diagram of a transimpedance amplifier with a low-pass filter for the signal conditioning for the free chlorine sensor. (b) Photo of the fabricated transimpedance amplifier with a low-pass filter. (c) Transfer characteristic curve of the transimpedance amplifier with a low-pass filter circuit.

For the temperature sensor, a Wheatstone bridge circuit (Figure 6-4) was used. In this circuit,  $R_{PdO1,2}$  were inkjet-printed Pd/PdO films with a bilayer morphology (see Chapter 4 for details) that have a negative TCR value.  $R_{Ag1,2}$  were inkjet-printed Ag films that have a positive TCR value. The resistance values of the four thermistors in the Wheatstone bridge circuit should be chosen to satisfy the following conditions:

- The output voltage is in the range of 0-1 V to be read by the ADC for a temperature between 0 °C and 50 °C (for most water quality monitoring applications).
- The sensitivity of the temperature sensor is maximized for a highly accurate measurement.
- The resistance between the power supply and ground should be large so that the self-heating of the resistors is kept low to reduce drift of the sensor output.
- The size of the sensor is kept small to obtain a high spatial resolution.

Taking the four considerations into account, we designed the Wheatstone bridge circuit with  $R_{Ag1} = 150 \Omega$ ,  $R_{Ag2} = 525 \Omega$ ,  $R_{PdO1} = 675 \Omega$ , and  $R_{PdO2} = 150 \Omega$  (Figure 6-4).

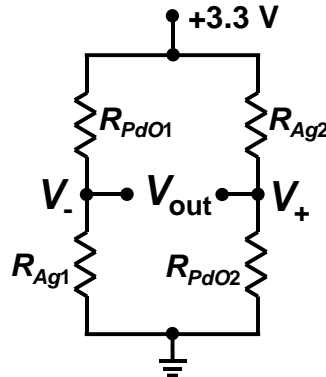


**Figure 6-4.** Wheatstone bridge circuit of an inkjet-printed temperature sensor with 4 thermistors.

For data analyses and results display, the three sensors (Figure 6-2(b)) and the conditioning circuit were connected to the FPGA board. The digitized signal was sent to the microprocessor programmed with the following functions (Figure 6-2(c)):

- **Temperature measurement.** The output voltage of the temperature sensor is recorded in real-time. The temperature is calculated using a built-in equation (see details in subsection 6.6).
- **pH calibration.** The stabilized output voltage of the pH sensor is stored as the calibration voltage when the sensor is immersed in a standard calibration solution of  $\text{pH} = 7$ .
- **pH measurement.** The output voltage of the pH sensor is recorded in real-time. The pH value is calculated using the sensitivity of the sensor and the calibration voltage. The pH sensitivity is compensated using the measured temperature (see details in section 6.4).
- **Free chlorine measurement.** The output voltage of the free chlorine sensor is recorded in real-time. The concentration of HOCl is calculated using an equation programmed in the FPGA. The free chlorine sensitivity is compensated using the measured temperature. Also, to calculate the free chlorine concentration (both HOCl and  $\text{OCl}^-$ ), another built-in equation is used based on the measured pH and temperature of the water sample (see details in subsection 6.5).

## 6.4. Characterization of pH sensor

The pH sensor used in the integrated system was identical to that developed in Chapter 3. Therefore, detailed characterization of the sensor performance is not presented here.

Briefly, when the pH of the water sample varied between 4 and 10, the sensor exhibited a large and low-noise output voltage in the range of 0 - 500 mV (Figure 3-17(a)). The output of such a sensor was within the ADC voltage range in the electronic system so that a power supply, amplifier or low-pass filter was not required for driving the sensor or signal conditioning. Also, the sensor showed a short response time of ~15 s (Figure 3-17(a)). This fast response allowed the implementation of the sensor for real-time monitoring.

The sensor-to-sensor variation of the pH sensitivity was as small as  $\pm 0.11$  mV/pH (~0.36% of the sensitivity of 60.6 mV/pH). However, the standard electrode potential ( $E^0$  in equation (2.22), or the output voltage for a certain pH value) of different sensors exhibited a difference of ~30 mV (Figure 6-5). This output voltage difference limited the accuracy of the sensors to be 0.5 pH. Thus, single-point calibration (normally at pH = 7 at 25 °C) should be carried out for each sensor to find its standard electrode potential ( $E^0$ ) for improved sensing accuracy. Moreover, in subsection 3.3.2.1, we showed that the pH sensitivity is a function of temperature. The pH sensitivity showed a linear temperature dependence of ~0.23 mV/pH/°C (Figure 3-18). Thus, temperature compensation for the pH sensitivity is required to improve the accuracy of a pH measurement. The equation for calculating the pH value can be written as:

$$\text{pH}=7+\frac{E_{cal}-E_{meas}}{60.6+(T_{meas}-25)\times 0.23}, \quad (6.1)$$

and this equation was programmed into the microprocessor on the FPGA board. In equation (6.1),  $E_{cal}$  (in mV) is the recorded voltage when the sensor is immersed into the calibration solution (pH = 7),  $E_{meas}$  (in mV) is voltage reading during pH monitoring,  $T_{meas}$  (in °C) is the measured temperature of the water sample.

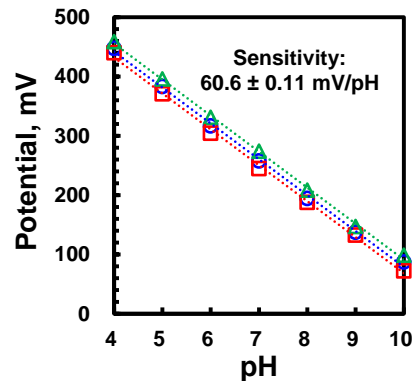


Figure 6-5. Calibration curves for three inkjet-printed pH sensors.

The hysteresis of the sensor ( $\sim 8.9$  mV, shown in Figure 3-17(a)) determined its resolution, which was  $\sim 0.15$  pH. The drift behavior of the sensor in 1 M KCl solution (to reduce the drift of the Ag/AgCl/KCl reference electrode) at room temperature in dark was  $\sim 1.6$  mV/h (Figure 3-17(e)), which was equivalent to 0.03 pH/h. The drift-induced inaccuracy was 5 times lower than the resolution of the sensor, so time compensation is not needed for most on-demand drinking water quality monitoring applications using this fast-response sensor.

In summary, the developed pH sensor has the following advantages comparing to conventional glass electrodes and other microfabricated pH sensors:

- An external power supply, amplifier, or filter is not needed, which simplifies the integration and signal processing.
- The sensor can be calibrated at a single pH value due to its reproducible sensitivity and linear response.
- The sensor fabricated by inkjet printing technology is low-cost.

## 6.5. Characterization of free chlorine sensor

The free chlorine concentration was monitored by a simplified amperometric configuration with an amine-modified pencil lead as the working electrode. The reference and counter electrodes in a conventional amperometric sensor were combined as an inkjet-printed Ag film. This 2-electrode system also did not require an external power supply to activate the

sensor [309]. This sensor measures the concentration of HOCl in the water sample [313], and the result can be used to calculate the free chlorine concentration (both HOCl and OCl<sup>-</sup>).

Free chlorine solutions with different concentrations were prepared by diluting the as-received NaOCl solution using a PBS solution (0.01 M, pH = 7.4). The free chlorine concentrations of the prepared solutions were calibrated using a DPD-based colorimetric test kit (CN-70, Hach). The current flowing through the working and the reference/counter electrodes was recorded using a semiconductor analyzer (4200-SCS, Keithley) every 2 s for 60 s when the electrodes were immersed in free chlorine solutions (without stirring). The electrodes were transferred into the next free chlorine solution without cleaning or drying. All free chlorine sensing tests were performed at  $27 \pm 2$  °C.

When the free chlorine concentration of the water sample varied between 0.2 and 8 ppm, the amplitude of the output current of the sensor was between 0 and 3000 nA (Figure 6-6(a)). A transimpedance amplifier with a gain of 196 k $\Omega$  was designed to convert the current signal to a voltage signal between 0 and 1 V (Figure 6-3(c)). To suppress the noise introduced by the transimpedance amplifier, a resistor-capacitor low-pass filter with a cutoff frequency of 0.06 Hz was used for signal conditioning.

### 6.5.1. Sensitivity and response time

The sensitivities of 5 free chlorine sensors (fabricated in the same batch) were measured (Figure 6-6(b)). The average sensitivity was  $\sim 342$  nA/ppm (10.36 nA/mm<sup>2</sup>/ppm for the sensors with an electrode area of  $\sim 33$  mm<sup>2</sup>) and the sensitivity variation was only  $\pm 12$  nA/ppm (0.36 nA/mm<sup>2</sup>/ppm,  $\sim 7\%$  of the sensitivity). Although the sensitivity was not as high as that of other reported free chlorine sensors [17], [166], our sensor had a high reproducibility with a negligible sensor-to-sensor variation of the output current at a certain free chlorine concentration. This high reproducibility was appealing for an easy-to-use sensor because calibration is not needed before each measurement once the calibration equation was stored in the electronic system.

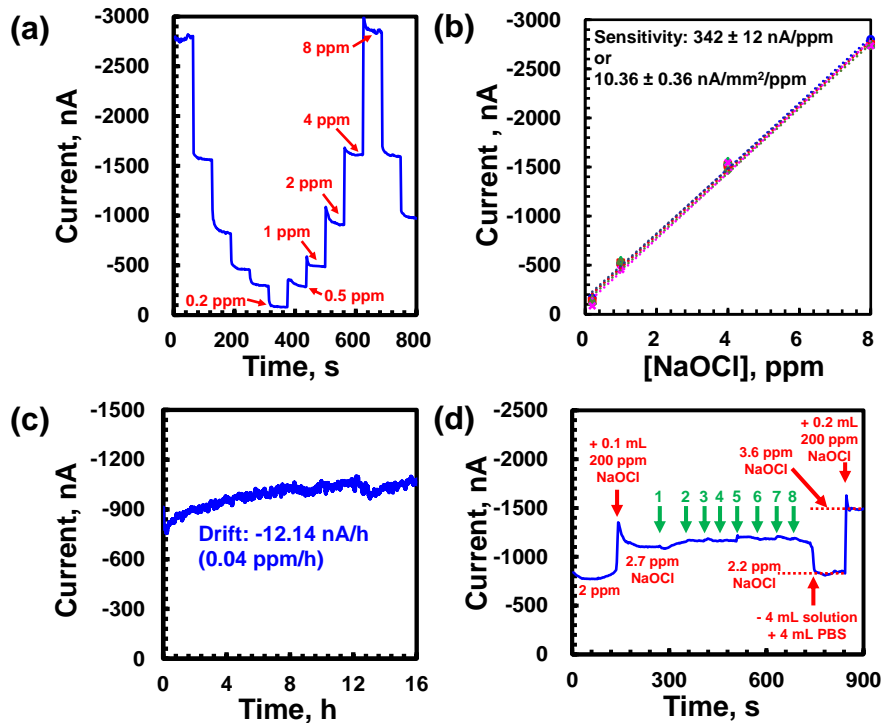


**Figure 6-6.** (a) Temporal response of a free chlorine sensor for free chlorine concentrations between 0.2 and 8 ppm. (b) Calibration curves for five free chlorine sensors. (c) Drift behavior of a free chlorine sensor in 2 ppm NaOCl solution in dark. (d) The response of a free chlorine sensor to NaOCl solutions and 400 ppm interfering solutions. Each green arrow indicates the addition of 0.2 mL of 5% interfering solution to 25 mL NaOCl solution (1, KNO<sub>3</sub>; 2, K<sub>2</sub>SO<sub>4</sub>; 3, Na<sub>2</sub>CO<sub>3</sub>; 4, NaHCO<sub>3</sub>; 5, NaCl; 6, (NH<sub>4</sub>)<sub>2</sub>SO<sub>4</sub>; 7, NaHPO<sub>4</sub>; 8, NaOAc).

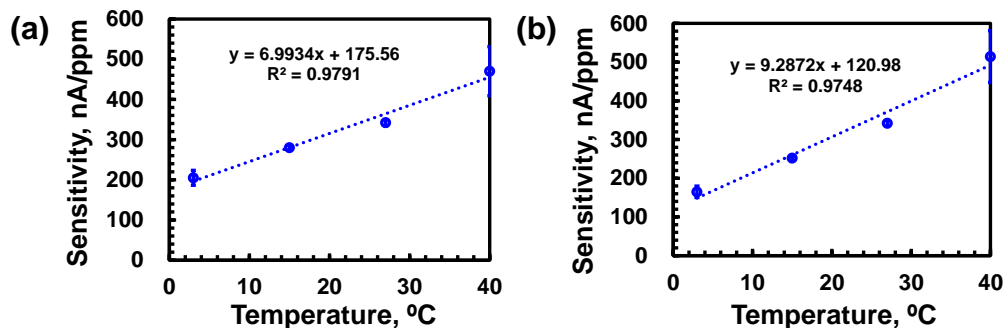


**Figure 6-7.** (a) The measured sensitivity of the free chlorine sensor as a function of temperature (without considering the temperature dependence of the dissociation constant of HOCl). (b) Corrected sensitivity of the free chlorine sensor as a function of temperature (considering the temperature dependence of the dissociation constant of HOCl).

To study the temperature dependence of the sensitivity, the sensitivity of the free chlorine sensor was measured at 3 °C, 15 °C, 27 °C and 40 °C. Measurement results showed that the temperature change of 1 °C would result in a sensitivity change of ~7 nA/ppm (Figure 6-7(a)). However, this temperature dependence should be corrected due to the temperature

dependence of the dissociation constant of HOCl. In other words, the amount of HOCl (which caused the sensor response) and the sensor response both change with temperature. The dissociation constant of HOCl as a function of temperature is [25]:

$$pK_a = \frac{3000}{T_{meas} + 273} - 10.0686 + 0.0253(T_{meas} + 273). \quad (6.2)$$

At pH = 7.4, the percentage of HOCl in a water sample is 70.77%, 63.15%, 56.92%, and 52.01% at 3 °C, 15 °C, 27 °C, and 40 °C, respectively. Therefore, the temperature dependence of the sensitivity of the free chlorine sensor can be corrected by equation (6.2) and the measured data shown in Figure 6-7(a). After correction, the sensitivity of the sensor showed a temperature dependence of ~9.3 nA/ppm/°C (Figure 6-7(c)). The calibration equation of the free chlorine sensor is:

$$I_{out} = [342 + (T_{meas} - 27) \times 9.3] C_{NaOCl} + 109.6, \quad (6.3)$$

where  $I_{out}$  (in nA) is the amplitude of the output current of the free chlorine sensor (input current of the signal conditioning circuit),  $T_{meas}$  (in °C) is the measured temperature of the water sample, and  $C_{NaOCl}$  (in ppm) is the concentration of NaOCl in the water sample for sensor characterization. The transfer function of the signal conditioning circuit (transimpedance amplifier and low-pass filter) can be described by (Figure 6-3(c)):

$$V = 0.196I_{out} + 35.4, \quad (6.4)$$

where  $V$  (in mV) is the output voltage of the signal conditioning circuit. Therefore, using equations (6.3) and (6.4), the NaOCl concentration can be calculated using:

$$C_{NaOCl} = \frac{\frac{V - 35.4}{0.196} - 109.6}{342 + (T_{meas} - 27) \times 9.3}. \quad (6.5)$$

Because the sensor response is caused by HOCl in the water sample [313] and ~57% of the free chlorine is HOCl at pH = 7.4 (condition for the sensor characterization) [166], the concentration of HOCl ( $C_{HOCl}$ ) at any solution pH value is:

$$C_{HOCl} = 0.57 \times \frac{\frac{V - 35.4}{0.196} - 109.6}{342 + (T_{meas} - 27) \times 9.3}. \quad (6.6)$$

In a solution, the percentage distribution of HOCl and OCl<sup>-</sup> is pH-dependent [166]:

$$\log \frac{C_{OCl^-}}{C_{HOCl}} = -pK_a + pH, \quad (6.7)$$

where  $C_{OCl^-}$  is the concentration of OCl<sup>-</sup> ion. Based on equations (6.2), (6.6) and (6.7), the concentration of the free chlorine ( $C_{free\ chlorine}$ ) can be calculated using:

$$\begin{aligned} C_{free\ chlorine} &= C_{HOCl} \left[ 1 + 10^{(pH-pK_a)} \right] \\ &= 0.57 \times \frac{\frac{V-35.4}{0.196} - 109.6}{342 + (T_{meas} - 27) \times 9.3} \left\{ 1 + 10^{\text{pH} - \left[ \frac{3000}{T_{meas} + 273} - 10.0686 + 0.0253(T_{meas} + 273) \right]} \right\}. \end{aligned} \quad (6.8)$$

Therefore, equation (6.8) was programmed into the microprocessor to calculate the free chlorine concentration based on the output voltage of the free chlorine sensor, the pH, and the temperature of the water sample. In Figure 6-6(a), we can find the response time of the free chlorine sensor was ~30 s, which is suitable for real-time monitoring.

### 6.5.2. Reversibility and drift

The resolution of the free chlorine sensor is determined by its hysteresis. When the free chlorine concentration was cycled between 0.2 and 8 ppm (Figure 6-6(a)), the average hysteresis of 53.5 nA resulted in a resolution of 0.16 ppm. The drift behavior was studied by keeping the free chlorine sensor in 2 ppm NaOCl solution at 4 °C (to reduce the decomposition of free chlorine) in dark for 16 h. The drift rate was ~12.14 nA/h (Figure 6-6(c)), which was equivalent to 0.04 ppm/h (4 times lower than the sensor resolution).

### 6.5.3. Selectivity

The selectivity was studied by recording the sensor response when 0.2 mL of 5% interfering solutions were added into 25 mL of 2 ppm NaOCl solution (Figure 6-6(d)). The added interfering solutions had an equivalent concentration of ~400 ppm. The sensor revealed negligible response to KNO<sub>3</sub>, K<sub>2</sub>SO<sub>4</sub>, Na<sub>2</sub>CO<sub>3</sub>, NaHCO<sub>3</sub>, NaCl, (NH<sub>4</sub>)<sub>2</sub>SO<sub>4</sub>, NaHPO<sub>4</sub> and

NaOAc. After the selectivity test, the sensor was still able to show a stable response to the change of free chlorine concentration.

#### 6.5.4. Stability

The free chlorine sensor was stored in 1 M KCl solution at room temperature for studying its stability. Figure 6-8 shows the change of the sensor sensitivity with storage time. The sensitivity right after sensor fabrication was  $342 \pm 12$  nA/ppm, and the sensitivity after storing for 7, 21, and 50 days was  $360 \pm 13$ ,  $343 \pm 18$ , and  $331 \pm 21$  nA/ppm, respectively (4 measurement cycles for each test). The sensitivity variation in the 50-day duration was 28 nA/ppm, which was only ~8% of the initial sensitivity. This small variation indicates a high stability of the pencil-lead-based free chlorine sensor.

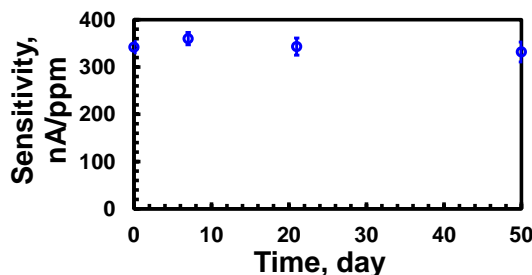


Figure 6-8. Stability of the pencil-lead-based free chlorine sensor.

In summary, the developed free chlorine sensor has the following advantages compared to conventional amperometric sensors and other microfabricated free chlorine sensors:

- A potentiostat is not needed for activating the sensor, which simplifies the integration.
- The sensor is highly reproducible, and calibration is only required for one sensor before the first use (calibration-free for other sensors fabricated in the same batch).
- The sensor is cost-effective due to the use of pencil lead and inkjet-printed Ag film.

#### 6.6. Characterization of temperature sensor

The performance the Wheatstone-bridge-based temperature sensors were characterized in a reliability test chamber (ESL-2CA, ESPEC) in water with the temperature varying

between 0 °C and 50 °C. The bias voltage for the sensors was 3.3 V and the output voltage was recorded using a semiconductor parameter analyzer (4200-SCS, Keithley).

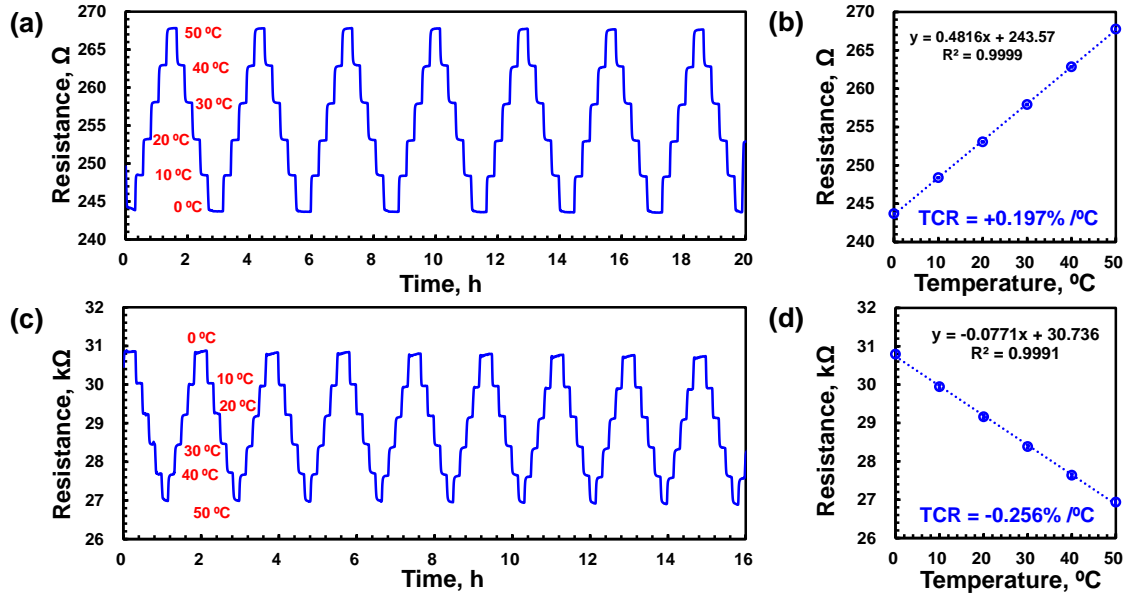


**Figure 6-9.** (a) Temporal response of a thermistor fabricated by an inkjet-printed Ag film when the temperature cycles between 0 °C and 50 °C. (b) Calibration curve of the inkjet-printed Ag thermistor. (c) Temporal response of a thermistor fabricated by an inkjet-printed Pd/PdO film when the temperature cycles between 0 °C and 50 °C. (d) Calibration curve of the inkjet-printed Pd/PdO thermistor.

In the Wheatstone bridge circuit (Figure 6-4), two thermistors were inkjet-printed Ag films with a positive TCR of 0.197% /°C (Figure 6-9(a-b)). The other two thermistors were inkjet-printed PdO films with a negative TCR of -0.256% /°C (Figure 6-9(c-d)). The selected thermistor materials of Ag and PdO were the same for the fabrication of the pH sensor. Hence, the temperature sensor could be simultaneously fabricated with the pH sensor, thus simplify the integration process.

### 6.6.1. Sensitivity

When the temperature increases, the resistance of  $R_{Ag1}$  in the Wheatstone bridge circuit increases and the resistance of  $R_{PdO1}$  decreases. Thus, the voltage of  $V_-$  (in Figure 6-4) increases. Similarly, the voltage of  $V_+$  decreases ( $V_{out} = V_+ - V_-$  also decreases) as the temperature increases. Using this differential sensing concept, the temperature sensitivity,  $dV_{out}/dT$ , of the Wheatstone bridge is increased compared with a single thermistor. In

addition, the output voltage showed a fast (almost immediate) and linear response with the temperature change (Figure 6-10(a)), so the sensor is capable for real-time compensation of the pH and free chlorine sensors.

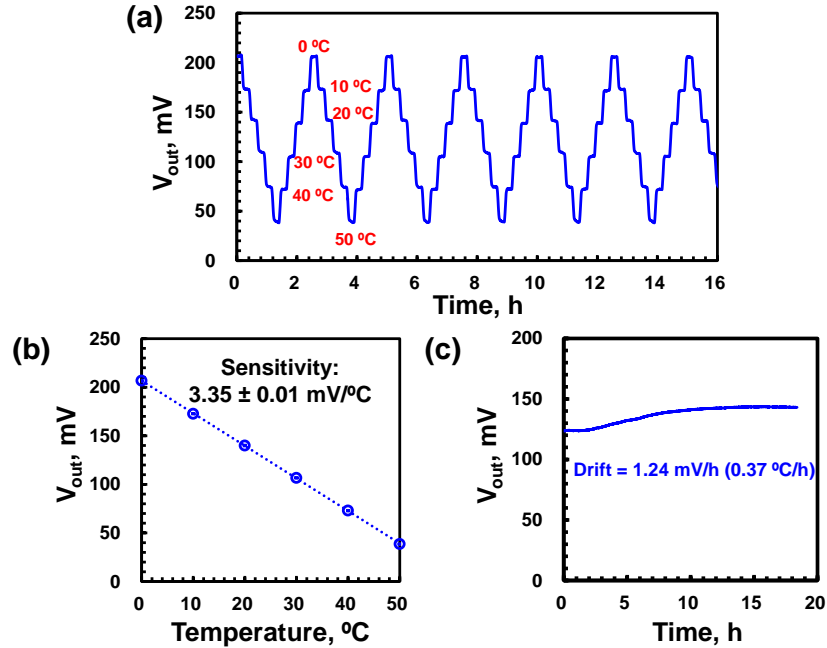


**Figure 6-10.** (a) Temporal response of the temperature sensor for temperatures between 0 and 50 °C. (b) Calibration curve of the temperature sensor. (c) Drift of the temperature sensor at 25 °C in water in dark.

From the temporal response, the sensitivity of the temperature sensor was calculated to be  $\sim 3.35$  mV/°C (Figure 6-10(b)), which was lower than the theoretical value ( $\sim 4.3$  mV/°C). This reduced sensitivity might be caused by the PVC coating on the 4 thermistors. Because PVC (52 ppm/°C) has a different thermal expansion coefficient than Ag (19 ppm/°C) and PdO (12 ppm/°C), the temperature variation induced stress could cause resistance increases of the 4 thermistors, resulted in a reduced sensitivity. The equation to be programmed into the microprocessor for temperature calculation can be written as:

$$T_{meas} = \frac{206.7 - V_{out}}{3.35}, \quad (6.9)$$

where  $T_{meas}$  (in °C) is the measured temperature of the water sample and  $V_{out}$  (in mV) is the output voltage of the temperature sensor.

### 6.6.2. Reversibility and drift

The temperature sensor exhibited a hysteresis of  $\sim 0.93$  mV (Figure 6-10(a)), so the resolution of the sensor was  $\sim 0.28$  °C. The drift behavior of the sensor was studied by storing the sensor at 25 °C in water in dark. Over the total test time of  $\sim 18$  h, the drift rate was 1.24 mV/h (0.37 °C/h). In Figure 6-10(c), the drift behavior can be divided into two segments. The drift rate of  $\sim 2.07$  mV/h ( $\sim 0.62$  °C/h) was relatively large for the first 10 hours, which might be due to the water absorption of the PVC film. The swelling of the PVC film resulted in stress on the underlying thermistors so that their resistance drifted. After 10 hours of the test, the drift rate decreased to  $\sim 0.23$  mV/h ( $\sim 0.09$  °C/h). This slow drift suggested that an equilibrium condition was reached for the swelling of PVC in water. To reduce the drift, the temperature sensor can be encapsulated by a polymer with a lower water absorption rate such as parylene-C or liquid crystal polymer [180].

In summary, the developed temperature sensor has the following advantages:

- The Wheatstone-bridge-based temperature sensor has a higher sensitivity than a thermistor.
- The sensor is fabricated by inkjet printing using the same materials as fabricating the pH sensor, so the sensor is inexpensive and easy-to-integrate.

## 6.7. Measurement of real water samples

The integrated sensors were connected to the programmed FPGA board for the monitoring of tap water, lake water, and swimming pool water. The pH, free chlorine, temperature readings from our developed system were compared with results from reference methods (Table 6-1). For pH sensing, a commercial pH meter (PHB-600R, OMEGA) with a glass electrode (PHE1311, OMEGA) was used as the reference. For free chlorine sensing, a DPD-based colorimetric test kit (CN-70, Hach) was used as the reference. For temperature sensing, a thermometer (HI98509 Checktemp 1, HANNA) was used as the reference. The results obtained using our system were close to those measured from reference methods,

with a difference less than 7%, 18%, and 15% for pH, free chlorine, and temperature, respectively.

**Table 6-1.** Monitoring of pH, free chlorine concentration and temperature of real water samples (average results from 5 measurements).

	Tap water (Toronto)		Lake water (Ontario lake)		Swimming pool water (McMaster University)	
	Our system	Reference	Our system	Reference	Our system	Reference
pH	$8.30 \pm 0.29$	$8.11 \pm 0.07$	$7.49 \pm 0.10$	$7.88 \pm 0.03$	$6.88 \pm 0.10$	$7.36 \pm 0.10$
Free chlorine, ppm	$0.95 \pm 0.13$	$0.86 \pm 0.13$	$0.01 \pm 0.01$	$0.00 \pm 0.00$	$2.62 \pm 0.32$	$2.22 \pm 0.22$
Temperature, °C	$14.70 \pm 0.52$	$15.04 \pm 0.11$	$0.20 \pm 0.08$	$0.24 \pm 0.05$	$26.34 \pm 0.53$	$27.72 \pm 0.08$

## 6.8. Conclusions

We have developed an integrated sensing system for the simultaneous monitoring of drinking water quality parameters including pH, free chlorine concentration, and temperature. The system consisted of an integrated sensing probe with inkjet-printed pH and temperature sensors, and an electrochemically modified free chlorine sensor. These sensors were compact in size (total size  $\sim 25 \text{ mm} \times 30 \text{ mm}$ ), highly sensitive, fast-in-response, user-friendly, and cost-effective. A high accuracy of  $\sim 85\%$  was obtained for the monitoring of real water samples using the sensing probe with a programmed FPGA board. This study signifies the practical application of the integrated sensing system as a simplification of the conventional laboratory-based analytical methods for on-site drinking water quality monitoring. The developed platform can also be exploited for the monitoring of other water quality parameters such as conductivity, heavy metal ions, and dissolved oxygen.

## Chapter 7

# Conclusions and recommendations

### 7.1. Conclusions

Existing laboratory-based analytical approaches to monitor drinking water quality parameters are highly accurate and reliable. However, these analytical techniques are time-consuming, labor-intensive, and costly, which are not suitable for realizing continued drinking water safety in resource limited and heavily populated areas. Although recent research activities demonstrated individual microfabricated sensors for affordable and efficient water quality monitoring, these microfabricated sensors were still expensive and difficult to be integrated into a functioning system. Therefore, the purpose of this research was to develop a compact, low-cost, easy-to-use, and accurate pH, temperature, and free chlorine sensing system for real-time, multi-parameter drinking water quality monitoring.

The research in this thesis focused on the design, fabrication, and characterization of microfabricated pH, temperature, and free chlorine sensors. An integrated demonstration system using the three sensors is also presented. For pH sensing, Pd/PdO thin films were used as the potentiometric sensing electrode due to the material's high pH sensitivity, short response time, and high stability. For temperature sensing, a Wheatstone bridge consisting of two Pd/PdO thermistors with negative TCR, and two Ag thermistors with positive TCR were employed to increase the sensitivity. The materials used for temperature sensing were the same as the pH sensing materials, which enabled a simple fabrication for the integrated sensors. For free chlorine measurement, two types of sensors were developed. One type was a PEDOT:PSS-based chemoresistor drawn on a paper. The relative resistance change of the chemoresistor was used to indicate the free chlorine concentration in water. Such a paper sensor was low-cost, easy-to-use, but not suitable for real-time monitoring. Thus,

another amperometric sensor was developed for continuous monitoring. The amperometric sensor had a simplified three-electrode configuration (using only 2 electrodes). The sensing was based on the redox reaction between the amine groups on a pencil lead and HOCl in water, which provided a repeatable and stable output current. The simplified amperometric sensor was potentiostat-free and calibration-free, which was very promising for an integrated system. The highly sensitive and efficient measurement was attributed to the abovementioned sensing materials and sensor configurations.

To improve the cost efficiency of the system, the sensors were fabricated on a common glass substrate using solution-based processes: inkjet printing and electrochemical modification. These fabrication techniques consumed a small amount of materials and did not require cleanroom environment, high-temperature/pressure conditions, or high-vacuum equipment.

The integrated sensor was connected to a signal conditioning circuit and a programmed FPGA board for signal processing and display. The integrated and portable water quality monitoring system was able to accurately measure the pH value, temperature, and free chlorine concentration in tap water and lake water. Next we present short summaries of each chapter in this thesis.

In Chapter 1, the background of drinking water quality (pH and free chlorine) monitoring was introduced, followed by a comprehensive review of microfabricated electrochemical pH and free chlorine sensors. By comparing different types of sensors and sensing materials, we choose to use metal/metal oxide-based potentiometric sensor for pH monitoring, and functionalized carbon materials for free chlorine sensing.

In Chapter 2, we studied the pH sensing mechanism and property of solution-processed Pd/PdO thin films. XPS, SEM, and AFM studies were used to determine the chemical composition and surface morphology of deposited Pd/PdO films. High sensitivity can be

realized by forming more PdO at the electrode surface and in the bulk. Dense and flat surface morphology of the electrode can lead to a fast response. The presence of both metallic Pd and surface nano-voids in the electrodes resulted in a decreased long-term sensitivity. pH sensing electrodes prepared by annealing Pd precursor solution at 200 °C for 48 h exhibited a linear super-Nernstian pH sensitivity of  $64.71 \pm 0.56$  mV/pH in the pH range of 2 to 12 with a short response time less than 18 s, small hysteresis less than 7.81 mV, and high reproducibility with a SD of 0.56 mV/pH of sensitivity. The super-Nernstian behavior may be related to the hydrous PdO<sub>x</sub> ( $x > 1$ ) produced from the solution-based process at low temperatures.

In Chapter 3, we developed a drop-on-demand inkjet printing process for a highly loaded Pd ink to deposit Pd/PdO thin films. The viscosity and surface tension of as-received Pd precursor solution were adjusted by toluene to form a printable ink. The printed ink was converted to continuous, homogenous, low-resistivity Pd films using a 2-step thermolysis. The printed Pd films exhibited good adhesion to air-plasma-treated PI substrates. After thermal oxidation at 200 °C, the film surface was PdO-rich and it served as a pH sensing layer. The underlying layer in the film was Pd-rich, and was the conductive path for electrons. The optimal sensitivity and response time were obtained with an electrode size of 10 mm<sup>2</sup> and a thickness of 100 nm. This pH sensing electrode was then integrated with a solid-state reference electrode to form a potentiometric sensor. The integrated sensors on glass and PI showed a fast and repeatable pH response with a sensitivity of  $60.6 \pm 0.1$  mV/pH and  $57 \pm 0.6$  mV/pH, respectively. Also, accurate pH values of real water samples were obtained with the printed sensors.

In Chapter 4, the thermolysis process of the inkjet-printed Pd ink was investigated. The morphology of the Pd/PdO films could be tuned by using different thermolysis atmospheres. The precursor was reductively decomposed into amine-stabilized Pd clusters at 200 °C. The O<sub>2</sub> in air facilitated the decomposition of the ligands for the Pd clusters and clean Pd NPs were formed. The fusion of the small NPs resulted in a smooth and dense film. In N<sub>2</sub>,

the generated NPs were larger and were embedded with organic species. Such NPs form sub-micron spherical aggregates. In low vacuum, a bilayer morphology was formed due to the competition between the film formation processes in air and in N<sub>2</sub>. The smooth film had a low resistivity since the electrical conduction was throughout the film. For the bilayer film, only the bottom layer participated in the conduction and a higher resistivity was observed. The TCR value of the films can be tuned from 0.067% /°C to -0.189% /°C due to the different amounts of PdO in the conduction paths. When the Pd/PdO films were studied in humid air, the adsorbed -OH groups raise the inter-grain barrier for the charge carrier transport and caused a positive resistance drift. This chapter showed that the inkjet-printed Pd/PdO films can be used for temperature sensing.

In Chapter 5, we developed a simple, cost-efficient, instrument-free, hand-drawing process to fabricate free chlorine sensors on paper substrates at room temperature. The sensing mechanism was based on the oxidation of PEDOT:PSS chemoresistor by free chlorine solutions. The final oxidation product had a higher electrical resistivity than PEDOT:PSS so that the relative resistance change of a chemoresistor could be used to express the sensor response. The sensor had a high mechanical stability, reusability, and wide sensing range. Also, the sensor was easy-to-use so that untrained personnel could accurately measure free chlorine concentrations in real water samples.

In Chapter 6, we developed an integrated sensing system for the simultaneous monitoring of drinking water quality parameters including pH, free chlorine concentration, and temperature. The system consisted of an integrated sensing probe with inkjet-printed pH and temperature sensors, and an electrochemically modified free chlorine sensor. These sensors were compact in sizes, highly sensitive, fast-in-response, user-friendly, and cost-effective. A high accuracy was obtained for the monitoring of real water samples using the sensing probe with a programmed FPGA board. This study signifies the practical application of the integrated sensing system as a simplification of the conventional laboratory-based analytical methods for on-site drinking water quality monitoring.

## 7.2. Recommendations

This research work resulted in several advances towards the development of an integrated, easy-to-use, accurate, and low-cost sensing system for drinking water quality monitoring. However, there are some features of the sensors and integrated sensing systems that need to be improved:

- The main difficulty in using the pH sensor is the requirement of the calibration step. Calibration is needed due to the variation in the sensor sensitivity, and/or the drift of the sensor output voltage. Thus, the stability of the Pd/PdO sensing electrode needs to be improved for a calibration-free sensor.
  - In Chapter 2, we observed that the Pd/PdO pH sensing electrode had a super-Nernstian sensitivity due to the presence of PdO<sub>x</sub> ( $x > 1$ ) in the film. Due to the slow decomposition of PdO<sub>2</sub>, the super-Nernstian sensitivity gradually decreased to a near-Nernstian sensitivity. Thus, a stable near-Nernstian sensitivity may be realized by converting PdO<sub>x</sub> ( $x > 1$ ) to PdO, by thermal treatment, high-vacuum treatment, or preconditioning in an aqueous environment such as in DI water.
  - In Chapter 3, we found that the sensitivity of the pH sensing electrode was affected by the electrode's surface area. A small surface area (<10 mm<sup>2</sup>) resulted in a sub-Nernstian sensitivity. When the sensing electrode was used in water for over 7 days, mechanical delamination of the Pd/PdO film on the glass substrate was observed. The delamination reduced the electrode's area, resulting in a lower sensitivity. Therefore, the mechanical adhesion between the Pd/PdO film and glass can be improved, for example, by applying a PI layer between them.
  - The drift and hysteresis of the pH sensor was due to the buried sites in the Pd/PdO film. These buried sites may be physical defects such as sub-surface grain boundaries, and/or chemical defects such as residual amines in the film. The buried sites had a slow reaction (adsorption/desorption of H<sub>3</sub>O<sup>+</sup>) rate than the surface active sites that caused the delayed sensor response or the so-called "memory

effect”. To eliminate the buried sites and improve the film quality, high temperature ( $>600\text{ }^{\circ}\text{C}$ ), high pressure, and/or vacuum-based post processing steps may be used. These post-processing steps use external energies to remove chemical contaminants, reconstruct the crystal structures, and reduce the amount of defects in the film.

- To make the sensor and sensing system easier to use, we can prepare a cap for the storage of the sensor (Figure 7-1). The cap will contain a gel saturated with the  $\text{pH} = 7$  buffer solution, and the pH sensor surface will be in contact with the gel during storage. Before using the sensor, we can calibrate the sensor with the cap on (similar to putting the sensor into a  $\text{pH} = 7$  buffer solution), and the calibration voltage is recorded. Then we can remove the cap and use the sensor with the calibration voltage already stored in the memory of the electronic system.

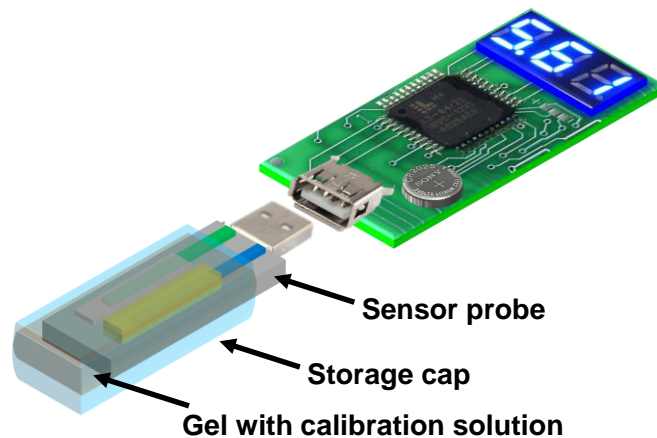


**Figure 7-1.** Proposed future water quality monitoring system.

- The stability of the pH sensor was also determined by the  $\text{Ag}/\text{AgCl}/\text{KCl}$  reference electrode, mainly by its drift. Therefore, the stability of the reference electrode needs to be improved. The potential drift of the reference electrode was caused by the leaching of  $\text{KCl}$  in the solid electrolyte layer when the electrode was immersed in water. Theoretically, a stable reference electrode potential is generated by a constant and very slow leaching of  $\text{KCl}$ . However, the practical realization of this  $\text{KCl}$  leaching condition is very challenging. Hence, alternative structures/materials of the reference electrode

should be employed. One promising configuration for future microscale solid-state reference electrodes consists of a nano-textured hydrophobic polymer matrix (e.g. PVC) with embedded ionic liquid (e.g.  $[\text{C}_8\text{min}^+][\text{C}_1\text{C}_1\text{N}^-]$ ) and redox couples (e.g.  $\text{Co}^{2+}$  and  $\text{Co}^{3+}$ ) on a conductive electrode. Such a reference electrode utilizes the environment-independent redox reaction (e.g. between  $\text{Co}^{2+}$  and  $\text{Co}^{3+}$ ) to provide a constant electrode potential. The huge double layer capacitance provided by the nano-textured hydrophobic polymer ensures a small potential variation with time. The ionic liquid is responsible for the efficient ion-to-electron transferring.

- The size of the pH sensor can be reduced by creating 3-dimensional nano structures at the electrode surface. As long as the effective sensing area is  $>10 \text{ mm}^2$ , a near-Nernstian response can be obtained. Three-dimensional nano structures provide surface areas in the vertical direction so the horizontal area of the electrode can be shrunk. The miniaturized pH sensor can be applied for measurements requiring high spatial resolution such as in implantable applications.
- If high temperature, high pressure, and/or vacuum processing is not preferred to improve the film quality, the pH sensor should be operated in a smart way to improve its stability. For example, the concept of differential sensing can be deployed. One sensor is kept in a standard solution, and the other identical sensor is used to monitor the water quality parameters. If the drift behaviors of the two sensors are the same, the output voltage difference of the two sensors should be a drift-free signal.
- The size of the temperature sensor needs to be reduced. In Chapter 6, the temperature had a size of  $\sim 10 \text{ mm} \times 20 \text{ mm}$ , which was limited by the size of the thermistors with large resistance values. The resistance of the thermistor, hence the sensor size, can be reduced by using a lower bias voltage, and/or by printing thinner Pd/PdO and Ag films.

- The fabrication of the free chlorine sensor based on amine modification of pencil leads needs to be improved. To make the integrated sensor more compact, the free chlorine sensor should be a planar configuration. One possible approach is to inkjet print amine-modified carbon-based materials (e.g. CNTs, graphene/graphene oxide, and carbon dots) on to the substrate. One expected challenge of this approach is the poor adhesion of the carbon materials on glass. Proper surface treatment and/or functionalization of the carbon materials has to be conducted to address this adhesion issue.
- The sensing range of the amine-modified free chlorine sensor needs to be increased. Although the free chlorine sensor was able to monitor low free chlorine concentrations (0-8 ppm) accurately, the sensing range was too narrow for the monitoring of food processing water (50-200 ppm). To obtain a wide sensing range, the amount of amine groups attached to the pencil lead should be increased.
- The developed Pd inkjet printing technology can be used as a low-cost fabrication approach for other applications. For example, Pd-based hydrogen gas sensor and ammonia sensor can be developed because Pd has a high affinity for these gases. Pd-based resistive stress/strain sensor can be fabricated for wearable applications. Inkjet-printed Pd can also be used as electrical interconnects for carbon nanomaterials due to the high work function of Pd.
- For the electronics part of the integrated drinking water quality monitoring system, a PCB board including conditioning circuits, data acquisition component, signal processing module, and result display unit needs to be developed in the future. Such a PCB board will replace the separated conditioning circuit and FPGA board for a lower cost and a smaller size.
- The monitoring of the amount of *Escherichia coli* in drinking water is also important for water safety. Other students in our group developed infrared sensors for the

identification of different types of bacteria [314], and a micro-flow cytometer for counting the amount of *Escherichia coli* in water [315]. In addition, a micro-Raman spectroscopy was developed for the monitoring of more types of chemical and biological species in water [316]–[318]. Regarding the electrochemical sensing of *Escherichia coli*, an *Escherichia coli*-sensitive electrode/device (e.g. FET-based biosensor) [93], [238] can be integrated into the platform developed in this study. Its output voltage/current can be readout using the same system developed in Chapter 6.

The work presented in this thesis was a pilot research and development project, targeting an integrated, easy-to-use, accurate, and low-cost sensing system for drinking water quality monitoring. It is demonstrated that solution-based processing could be a viable candidate to fabricate and integrate multiple types of micro-scale sensors with high performance features. This research demonstrated the feasibility, challenges, and potential solutions for developing drinking water quality monitoring systems for real-world applications.

## References

- [1] USEPA, “WaterSentinel online water quality monitoring as an indicator of drinking water contamination, EPA 817-D-05-002,” Washington, D.C., U.S. Environmental Protection Agency, Water Security Division, 2005.
- [2] W. F. Boron and E. L. Boulpaep, *Medical physiology: A cellular and molecular approach*. Philadelphia, PA, USA: Saunders/Elsevier, 2003.
- [3] WHO, “Guidelines for drinking-water quality, 2nd edition, Volume 2, Health criteria and other supporting information,” Geneva, Switzerland, 1996.
- [4] Health Canada, “Guidelines for Canadian drinking water quality: Chlorine,” Authority of the Minister of Health, Ottawa, Canada, 2009.
- [5] USEPA, “Nitrification,” Office of Water, Washington, D.C., USA, 2002.
- [6] L. M. Prescott, J. P. Harley, and D. A. Klein, *Microbiology (5th edition)*. New York, NY, USA: McGraw-Hill Companies, Inc., 2002.
- [7] WHO Working Group, “Health impact of acidic deposition,” *Sci. Total Environ.*, vol. 52, no. 3, pp. 157–187, Jul. 1986.
- [8] E. I. Gill, A. Arshak, K. Arshak, and O. Korostynska, “Investigation of thick-film polyaniline-based conductimetric pH sensors for medical applications,” *IEEE Sens. J.*, vol. 9, no. 5, pp. 555–562, May 2009.
- [9] R. Sadiq, S. Imran, and V. Kleiner, “Examining the impact of water quality on the integrity of distribution infrastructure,” in *American Water Works Association Research Foundation*, 2007.
- [10] P. Payment, M. Waite, and A. Durfour, “Assessing microbial safety of drinking water improving approaches and methods: Improving approaches and methods,” OECD Publishing, Organisation for Economic Cooperation and Development and World Health Organization, 2003.
- [11] M. H. Banna, S. Imran, A. Francisque, H. Najjaran, R. Sadiq, M. Rodriguez, and M. Hoorfar, “Online drinking water quality monitoring: Review on available and emerging technologies,” *Crit. Rev. Environ. Sci. Technol.*, vol. 44, no. 12, pp. 1370–1421, Jun. 2014.
- [12] G. Connell, *Water disinfection series: The chlorination/chloramination handbook*. Denver, CO, USA: American Water Works Association, 1996.
- [13] WHO, “Guidelines for drinking-water quality, 3rd edition,” Geneva, Switzerland, 2008.
- [14] USEPA, “National primary drinking water regulations,” Washington, D.C., USA, 2009.
- [15] USEPA, “Edition of the drinking water standards and health advisories,” Office of Water, Washington, D.C., USA, 2012.
- [16] K. Senthilkumar and J.-M. Zen, “Free chlorine detection based on EC’ mechanism at an electroactive polymelamine-modified electrode,” *Electrochem. commun.*, vol. 46, pp. 87–90, Sep. 2014.
- [17] Y. Qin, S. Pan, M. M. R. Howlader, R. Ghosh, N.-X. Hu, and M. J. Deen, “Paper-based, hand-drawn free chlorine sensor with poly(3,4-ethylenedioxythiophene):poly(styrenesulfonate),” *Anal. Chem.*, vol. 88, no. 21, pp. 10384–10389, Nov. 2016.
- [18] J. P. Guyer, *Engineering SoundBite: Water treatment*. Guyer Partners, 2010.
- [19] “Chlorine measurement by amperometric sensor, Application Data Sheet, ADS 43-6063/rev.B,” Emerson Process Management, 2009.
- [20] D. S. Tarbell and A. T. Tarbell, “The development of the pH meter,” *J. Chem. Educ.*, vol. 57, no. 2, p. 133, Feb. 1980.

- [21] F. Haber and Z. Klemensiewicz, "Über elektrische phasengrenzkräfte," *Z. phys. Chem*, vol. 67, pp. 385–431, 1909.
- [22] P. Kurzweil, "Metal oxides and ion-exchanging surfaces as pH sensors in liquids: State-of-the-art and outlook," *Sensors*, vol. 9, no. 6, pp. 4955–4985, Jun. 2009.
- [23] R. P. Buck, S. Rondinini, A. K. Covington, F. G. K. Baucke, C. M. A. Brett, M. F. Camoes, M. J. T. Milton, T. Mussini, R. Naumann, K. W. Pratt, P. Spitzer, and G. S. Wilson, "Measurement of pH. Definition, standards, and procedures (IUPAC Recommendations 2002)," *Pure Appl. Chem.*, vol. 74, no. 11, Jan. 2002.
- [24] J. C. Morris, "Health perspective in the oxidative treatment of water for potable supply. Part 2. Health assessment of current oxidant-disinfectants," National Institute for Water Supply, Leidschendam, the Netherlands, 1982.
- [25] J. C. Morris, "The acid ionization constant of HOCl from 5 to 35°," *J. Phys. Chem.*, vol. 70, no. 12, pp. 3798–3805, Dec. 1966.
- [26] G. Gordon, D. L. Sweetin, K. Smith, and G. E. Pacey, "Improvements in the N,N-diethyl-p-phenylenediamine method for the determination of free and combined residual chlorine through the use of FIA," *Talanta*, vol. 38, no. 2, pp. 145–149, Feb. 1991.
- [27] J. D. Johnson and R. Overby, "Stabilized neutral o-tolidine, SNORT, colorimetric method for chlorine," *Anal. Chem.*, vol. 41, no. 13, pp. 1744–1750, Nov. 1969.
- [28] M. Zenki, H. Komatsubara, and K. Tōei, "Determination of residual chlorine in tap water by flow-injection spectrophotometry," *Anal. Chim. Acta*, vol. 208, pp. 317–320, 1988.
- [29] K. K. Verma, A. Jain, and A. Townshend, "Determination of free and combined residual chlorine by flow-injection spectrophotometry," *Anal. Chim. Acta*, vol. 261, no. 1–2, pp. 233–240, May 1992.
- [30] S. G. Dmitrienko, O. A. Sviridova, L. N. Pyatkova, V. A. Zhukova, and Y. A. Zolotov, "Rapid determination of free active chlorine in water by diffuse reflectance spectroscopy after reaction with polyurethane foams," *Anal. Chim. Acta*, vol. 405, no. 1–2, pp. 231–237, Jan. 2000.
- [31] G. C. White, *Handbook of chlorination*. New York, NY, USA: Van Nostrand Reinhold Company, 1986.
- [32] J. Ellis and P. L. Brown, "Determination of residual chlorine by derivatisation with 2,6-dimethylphenol and gas chromatographic separation," *Anal. Chim. Acta*, vol. 124, no. 2, pp. 431–436, Mar. 1981.
- [33] T. Nakagama, M. Yamada, and T. Hobo, "Chemiluminescence sensor with uranine immobilized on an anion-exchange resin for monitoring free chlorine in tap water," *Anal. Chim. Acta*, vol. 231, pp. 7–12, 1990.
- [34] F. Kodera, M. Umeda, and A. Yamada, "Determination of free chlorine based on anodic voltammetry using platinum, gold, and glassy carbon electrodes," *Anal. Chim. Acta*, vol. 537, no. 1–2, pp. 293–298, Apr. 2005.
- [35] F. J. Del Campo, O. Ordeig, and F. J. Muñoz, "Improved free chlorine amperometric sensor chip for drinking water applications," *Anal. Chim. Acta*, vol. 554, no. 1–2, pp. 98–104, Dec. 2005.
- [36] V. B. Malkov, B. Zachman, and T. Scribner, "Comparison of online chlorine analysis methods and instrumentation built on amperometric and colorimetric technologies," in *Water Quality Technology Conference and Exposition*, 2009.
- [37] Y. Moser and M. A. M. Gijs, "Miniaturized flexible temperature sensor," *J. Microelectromechanical Syst.*, vol. 16, no. 6, pp. 1349–1354, Dec. 2007.
- [38] J. P. Bentley, "Temperature sensor characteristics and measurement system design," *J. Phys. E.*, vol. 17, no. 6, pp. 430–439, Jun. 1984.
- [39] A. W. Van Herwaarden and P. M. Sarro, "Thermal sensors based on the seebeck effect," *Sensor. Actuat.*, vol. 10, no. 3–4, pp. 321–346, Nov. 1986.
- [40] W. F. Roeser and S. T. Lonberger, *Methods of testing thermocouples and thermocouple materials*. US Department of Commerce, National Bureau of Standards, 1958.

- [41] M. Kimura and K. Toshima, "Thermistor-like pn junction temperature-sensor with variable sensitivity and its combination with a micro-air-bridge heater," *Sensors Actuators A Phys.*, vol. 108, no. 1–3, pp. 239–243, Nov. 2003.
- [42] M. Badihi-Mossberg, V. Buchner, and J. Rishpon, "Electrochemical biosensors for pollutants in the environment," *Electroanalysis*, vol. 19, no. 19–20, pp. 2015–2028, Oct. 2007.
- [43] G. Hanrahan, D. G. Patil, and J. Wang, "Electrochemical sensors for environmental monitoring: Design, development and applications," *J. Environ. Monit.*, vol. 6, no. 8, pp. 657–664, 2004.
- [44] N. Jaffrezic-Renault and S. V. Dzyadevych, "Conductometric microbiosensors for environmental monitoring," *Sensors*, vol. 8, no. 4, pp. 2569–2588, Apr. 2008.
- [45] M. Yuqing, C. Jianrong, and F. Keming, "New technology for the detection of pH," *J. Biochem. Biophys. Methods*, vol. 63, no. 1, pp. 1–9, Apr. 2005.
- [46] Y. Qin, M. M. R. Howlader, and M. Deen, "Low-temperature bonding for silicon-based micro-optical systems," *Photonics*, vol. 2, no. 4, pp. 1164–1201, Dec. 2015.
- [47] M. M. R. Howlader, M. J. Deen, and T. Suga, "Nanobonding: A key technology for emerging applications in health and environmental sciences," *Jpn. J. Appl. Phys.*, vol. 54, no. 3, p. 30201, Mar. 2015.
- [48] M. M. R. Howlader, P. R. Selvaganapathy, M. J. Deen, and T. Suga, "Nanobonding technology toward electronic, fluidic, and photonic systems integration," *IEEE J. Sel. Top. Quantum Electron.*, vol. 17, no. 3, pp. 689–703, May 2011.
- [49] M. H. Banna, H. Najjaran, R. Sadiq, S. A. Imran, M. J. Rodriguez, and M. Hoorfar, "Miniaturized water quality monitoring pH and conductivity sensors," *Sensor. Actuat. B Chem.*, vol. 193, pp. 434–441, Mar. 2014.
- [50] G. Gerlach, M. Guenther, J. Sorber, G. Suchaneck, K.-F. Arndt, and A. Richter, "Chemical and pH sensors based on the swelling behavior of hydrogels," *Sensor. Actuat. B Chem.*, vol. 111–112, pp. 555–561, Nov. 2005.
- [51] Q. Thong Trinh, G. Gerlach, J. Sorber, and K.-F. Arndt, "Hydrogel-based piezoresistive pH sensors: Design, simulation and output characteristics," *Sensor. Actuat. B Chem.*, vol. 117, no. 1, pp. 17–26, Sep. 2006.
- [52] Y. Zhang, H. Ji, D. Snow, R. Sterling, and G. M. Brown, "A pH sensor based on a microcantilever coated with intelligent hydrogel," *Instrum. Sci. Technol.*, vol. 32, no. 4, pp. 361–369, Dec. 2004.
- [53] Z. Cheng, M. J. Deen, and H. Peng, "A low-power gateable vernier ring oscillator time-to-digital converter for biomedical imaging applications," *IEEE Trans. Biomed. Circuits Syst.*, vol. 10, no. 2, pp. 445–454, Apr. 2016.
- [54] M. J. Deen and F. Pascal, "Electrical characterization of semiconductor materials and devices—review," *J. Mater. Sci. Mater. Electron.*, vol. 17, no. 8, pp. 549–575, Aug. 2006.
- [55] M. Jamal Deen, B. Iñiguez, O. Marinov, and F. Lime, "Electrical studies of semiconductor–dielectric interfaces," *J. Mater. Sci. Mater. Electron.*, vol. 17, no. 9, pp. 663–683, Sep. 2006.
- [56] M. J. Deen and P. K. Basu, *Silicon photonics: Fundamentals and devices*. Chichester, UK: John Wiley & Sons, 2012.
- [57] D. Wencel, T. Abel, and C. McDonagh, "Optical chemical pH sensors," *Anal. Chem.*, vol. 86, no. 1, pp. 15–29, Jan. 2014.
- [58] P. Gou, N. D. Kraut, I. M. Feigel, H. Bai, G. J. Morgan, Y. Chen, Y. Tang, K. Bocan, J. Stachel, L. Berger, M. Mickle, E. Sejdíć, and A. Star, "Carbon nanotube chemiresistor for wireless pH sensing," *Sci. Rep.*, vol. 4, p. 4468, Mar. 2014.
- [59] P. Bergveld, "Thirty years of ISFETOLOGY," *Sensor. Actuat. B Chem.*, vol. 88, no. 1, pp. 1–20, Jan. 2003.
- [60] A. Fog and R. P. Buck, "Electronic semiconducting oxides as pH sensors," *Sensor. Actuat.*, vol. 5, no. 2, pp. 137–146, Feb. 1984.

- [61] D. K. Kampouris, R. O. Kadara, N. Jenkinson, and C. E. Banks, "Screen printed electrochemical platforms for pH sensing," *Anal. Methods*, vol. 1, no. 1, pp. 25–28, 2009.
- [62] P. Gupta, S. K. Yadav, B. Agrawal, and R. N. Goyal, "A novel graphene and conductive polymer modified pyrolytic graphite sensor for determination of propranolol in biological fluids," *Sensor. Actuat. B Chem.*, vol. 204, pp. 791–798, Dec. 2014.
- [63] N. Mzoughi, A. Abdellah, Q. Gong, H. Grothe, P. Lugli, B. Wolf, and G. Scarpa, "Characterization of novel impedimetric pH-sensors based on solution-processable biocompatible thin-film semiconducting organic coatings," *Sensor. Actuat. B Chem.*, vol. 171–172, pp. 537–543, Aug. 2012.
- [64] L.-M. Kuo, K.-N. Chen, Y.-L. Chuang, and S. Chao, "A flexible pH-sensing structure using WO<sub>3</sub>/IrO<sub>2</sub> junction with Al<sub>2</sub>O<sub>3</sub> encapsulation layer," *ECS Solid State Lett.*, vol. 2, no. 3, pp. P28–P30, Dec. 2012.
- [65] S. Safari, P. R. Selvaganapathy, A. Derardja, and M. J. Deen, "Electrochemical growth of high-aspect ratio nanostructured silver chloride on silver and its application to miniaturized reference electrodes," *Nanotechnology*, vol. 22, no. 31, p. 315601, Aug. 2011.
- [66] S. Safari, P. R. Selvaganapathy, and M. J. Deen, "Microfluidic reference electrode with free-diffusion liquid junction," *J. Electrochem. Soc.*, vol. 160, no. 10, pp. B177–B183, Jul. 2013.
- [67] M. A. Rahman, P. Kumar, D.-S. Park, and Y.-B. Shim, "Electrochemical sensors based on organic conjugated polymers," *Sensors*, vol. 8, no. 1, pp. 118–141, Jan. 2008.
- [68] W.-D. Huang, H. Cao, S. Deb, M. Chiao, and J. C. Chiao, "A flexible pH sensor based on the iridium oxide sensing film," *Sensors Actuators A Phys.*, vol. 169, no. 1, pp. 1–11, Sep. 2011.
- [69] S. Yao, M. Wang, and M. Madou, "A pH electrode based on melt-oxidized iridium oxide," *J. Electrochem. Soc.*, vol. 148, no. 4, pp. H29–H36, 2001.
- [70] T. Y. Kim and S. Yang, "Fabrication method and characterization of electrodeposited and heat-treated iridium oxide films for pH sensing," *Sensor. Actuat. B Chem.*, vol. 196, pp. 31–38, Jun. 2014.
- [71] H.-J. Chung, M. S. Sulkin, J.-S. Kim, C. Goudeseune, H.-Y. Chao, J. W. Song, S. Y. Yang, Y.-Y. Hsu, R. Ghaffari, I. R. Efimov, and J. A. Rogers, "Stretchable, multiplexed pH sensors with demonstrations on rabbit and human hearts undergoing ischemia," *Adv. Healthc. Mater.*, vol. 3, no. 1, pp. 59–68, Jan. 2014.
- [72] C. M. Nguyen, S. Rao, Y.-S. Seo, K. Schadt, Y. Hao, and J.-C. Chiao, "Micro pH sensors based on iridium oxide nanotubes," *IEEE Trans. Nanotechnol.*, vol. 13, no. 5, pp. 945–953, Sep. 2014.
- [73] L.-M. Kuo, Y.-C. Chou, K.-N. Chen, C.-C. Lu, and S. Chao, "A precise pH microsensor using RF-sputtering IrO<sub>2</sub> and Ta<sub>2</sub>O<sub>5</sub> films on Pt-electrode," *Sensor. Actuat. B Chem.*, vol. 193, pp. 687–691, Mar. 2014.
- [74] J. Park, M. Kim, and S. Kim, "Surface renewable nano-iridium oxide polymeric composite pH electrodes," *Sensor. Actuat. B Chem.*, vol. 204, pp. 197–202, Dec. 2014.
- [75] S. Zaman, M. H. Asif, A. Zainelabdin, G. Amin, O. Nur, and M. Willander, "CuO nanoflowers as an electrochemical pH sensor and the effect of pH on the growth," *J. Electroanal. Chem.*, vol. 662, no. 2, pp. 421–425, Nov. 2011.
- [76] M. Hussain, Z. H. Ibupoto, M. A. Abbasi, O. Nur, and M. Willander, "Effect of anions on the morphology of Co<sub>3</sub>O<sub>4</sub> nanostructures grown by hydrothermal method and their pH sensing application," *J. Electroanal. Chem.*, vol. 717–718, pp. 78–82, Mar. 2014.
- [77] L. Santos, J. P. Neto, A. Crespo, D. Nunes, N. Costa, I. M. Fonseca, P. Barquinha, L. Pereira, J. Silva, R. Martins, and E. Fortunato, "WO<sub>3</sub> nanoparticle-based conformable pH sensor," *ACS Appl. Mater. Interfaces*, vol. 6, no. 15, pp. 12226–12234, Aug. 2014.
- [78] A. Sardarnejad, D. K. Maurya, and K. Alameh, "The effects of sensing electrode thickness on ruthenium oxide thin-film pH sensor," *Sensors Actuators A Phys.*, vol. 214, pp. 15–19, Aug. 2014.
- [79] H. Arida, "Novel pH microsensor based on a thin film gold electrode modified with lead dioxide nanoparticles," *Microchim. Acta*, vol. 182, no. 1–2, pp. 149–156, Jan. 2015.

- [80] Y. Qin, A. U. Alam, S. Pan, M. M. R. Howlader, R. Ghosh, P. R. Selvaganapathy, Y. Wu, and M. J. Deen, "Low-temperature solution processing of palladium/palladium oxide films and their pH sensing performance," *Talanta*, vol. 146, pp. 517–524, 2016.
- [81] Y. Qin, A. U. Alam, M. M. R. Howlader, N.-X. Hu, and M. J. Deen, "Inkjet printing of a highly loaded palladium ink for integrated, low-cost pH sensors," *Adv. Funct. Mater.*, vol. 26, no. 27, pp. 4923–4933, Jul. 2016.
- [82] U. Lange, N. V. Roznyatovskaya, and V. M. Mirsky, "Conducting polymers in chemical sensors and arrays," *Anal. Chim. Acta*, vol. 614, no. 1, pp. 1–26, Apr. 2008.
- [83] B. Lakard, O. Segut, S. Lakard, G. Herlem, and T. Gharbi, "Potentiometric miniaturized pH sensors based on polypyrrole films," *Sensor. Actuat. B Chem.*, vol. 122, no. 1, pp. 101–108, Mar. 2007.
- [84] T. Lindfors and A. Ivaska, "pH sensitivity of polyaniline and its substituted derivatives," *J. Electroanal. Chem.*, vol. 531, no. 1, pp. 43–52, Aug. 2002.
- [85] B. Lakard, G. Herlem, S. Lakard, R. Guyetant, and B. Fahys, "Potentiometric pH sensors based on electrodeposited polymers," *Polymer (Guildf.)*, vol. 46, no. 26, pp. 12233–12239, Dec. 2005.
- [86] T. Guinovart, G. Valdés-Ramírez, J. R. Windmiller, F. J. Andrade, and J. Wang, "Bandage-based wearable potentiometric sensor for monitoring wound pH," *Electroanalysis*, vol. 26, no. 6, pp. 1345–1353, Jun. 2014.
- [87] A. J. Bandodkar, V. W. S. Hung, W. Jia, G. Valdés-Ramírez, J. R. Windmiller, A. G. Martinez, J. Ramírez, G. Chan, K. Kerman, and J. Wang, "Tattoo-based potentiometric ion-selective sensors for epidermal pH monitoring," *Analyst*, vol. 138, no. 1, pp. 123–128, 2013.
- [88] W. Prissanaroon-Ouajai, P. J. Pigram, R. Jones, and A. Sirivat, "A novel pH sensor based on hydroquinone monosulfonate-doped conducting polypyrrole," *Sensor. Actuat. B Chem.*, vol. 135, no. 1, pp. 366–374, Dec. 2008.
- [89] T. Trantidou, D. J. Payne, V. Tsiligiridis, Y.-C. Chang, C. Toumazou, and T. Prodromakis, "The dual role of Parylene C in chemical sensing: Acting as an encapsulant and as a sensing membrane for pH monitoring applications," *Sensor. Actuat. B Chem.*, vol. 186, pp. 1–8, Sep. 2013.
- [90] C. A. Li, K. N. Han, X.-H. Pham, and G. H. Seong, "A single-walled carbon nanotube thin film-based pH-sensing microfluidic chip," *Analyst*, vol. 139, no. 8, pp. 2011–2015, 2014.
- [91] Y. Qin, H.-J. Kwon, A. Subrahmanyam, M. M. R. Howlader, P. R. Selvaganapathy, A. Adronov, and M. J. Deen, "Inkjet-printed bifunctional carbon nanotubes for pH sensing," *Mater. Lett.*, vol. 176, pp. 68–70, Apr. 2016.
- [92] C. Batic and G. Borghs, "Organic thin-film transistors as transducers for (bio) analytical applications," *Anal. Bioanal. Chem.*, vol. 384, no. 2, pp. 354–365, Dec. 2005.
- [93] M. W. Shinwari and M. J. Deen, "Impedance modelling of FET-based biosensors," *J. Electrochem. Soc.*, vol. 158, no. 6, pp. J189–J194, 2011.
- [94] M. Waleed Shinwari, M. Jamal Deen, and D. Landheer, "Study of the electrolyte-insulator-semiconductor field-effect transistor (EISFET) with applications in biosensor design," *Microelectron. Reliab.*, vol. 47, no. 12, pp. 2025–2057, Dec. 2007.
- [95] P. D. Batista and M. Mulato, "ZnO extended-gate field-effect transistors as pH sensors," *Appl. Phys. Lett.*, vol. 87, no. 14, p. 143508, 2005.
- [96] J.-C. Chou and L. P. Liao, "Study on pH at the point of zero charge of TiO<sub>2</sub> pH ion-sensitive field effect transistor made by the sputtering method," *Thin Solid Films*, vol. 476, no. 1, pp. 157–161, Apr. 2005.
- [97] J. C. Chou and L. P. Liao, "Study of TiO<sub>2</sub> thin films for ion sensitive field effect transistor application with RF sputtering deposition," *Jpn. J. Appl. Phys.*, vol. 43, no. 1, pp. 61–65, Jan. 2004.
- [98] P.-K. Shin, "The pH-sensing and light-induced drift properties of titanium dioxide thin films deposited by MOCVD," *Appl. Surf. Sci.*, vol. 214, no. 1–4, pp. 214–221, May 2003.
- [99] T. Mikolajick, R. Kühnhold, and H. Ryssel, "The pH-sensing properties of tantalum pentoxide films fabricated by metal organic low pressure chemical vapor deposition," *Sensor. Actuat. B Chem.*, vol. 44, no. 1–3, pp. 262–267, Oct. 1997.

- [100] M. Chen, Y. Jin, X. Qu, Q. Jin, and J. Zhao, "Electrochemical impedance spectroscopy study of Ta<sub>2</sub>O<sub>5</sub> based EIOS pH sensors in acid environment," *Sens. Actu. B Chem.*, vol. 192, pp. 399–405, Mar. 2014.
- [101] C. Haur Kao, H. Chen, M. Ling Lee, C. Chun Liu, H.-Y. Ueng, Y. Cheng Chu, Y. Jie Chen, and K. Ming Chang, "Multianalyte biosensor based on pH-sensitive ZnO electrolyte–insulator–semiconductor structures," *J. Appl. Phys.*, vol. 115, no. 18, p. 184701, May 2014.
- [102] C.-S. Lai, T.-F. Lu, C.-M. Yang, Y.-C. Lin, D. G. Pijanowska, and B. Jaroszewicz, "Body effect minimization using single layer structure for pH-ISFET applications," *Sens. Actu. B Chem.*, vol. 143, no. 2, pp. 494–499, Jan. 2010.
- [103] C.-M. Yang, C.-Y. Wang, and C.-S. Lai, "Characterization on pH sensing performance and structural properties of gadolinium oxide post-treated by nitrogen rapid thermal annealing," *J. Vac. Sci. Technol. B Microelectron. Nanom. Struct.*, vol. 32, no. 3, p. 03D113, May 2014.
- [104] T.-M. Pan, P.-Y. Liao, K.-Y. Chang, and L. Chi, "Structural and sensing characteristics of Gd<sub>2</sub>Ti<sub>2</sub>O<sub>7</sub>, Er<sub>2</sub>Ti<sub>2</sub>O<sub>7</sub> and Lu<sub>2</sub>Ti<sub>2</sub>O<sub>7</sub> sensing membrane electrolyte–insulator–semiconductor for bio-sensing applications," *Electrochim. Acta*, vol. 89, pp. 798–806, Feb. 2013.
- [105] K. Niigata, K. Narano, Y. Maeda, and J.-P. Ao, "Temperature dependence of sensing characteristics of a pH sensor fabricated on AlGa<sub>N</sub>/Ga<sub>N</sub> heterostructure," *Jpn. J. Appl. Phys.*, vol. 53, no. 11S, p. 11RD01, Nov. 2014.
- [106] S. Upadhyay, R. Frederiksen, N. Lloret, L. De Vico, P. Krogstrup, J. H. Jensen, K. L. Martinez, and J. Nygård, "Indium arsenide nanowire field-effect transistors for pH and biological sensing," *Appl. Phys. Lett.*, vol. 104, no. 20, p. 203504, May 2014.
- [107] K. Kim, T. Rim, C. Park, D. Kim, M. Meyyappan, and J.-S. Lee, "Suspended honeycomb nanowire ISFETs for improved stiction-free performance," *Nanotechnology*, vol. 25, no. 34, p. 345501, Aug. 2014.
- [108] T.-E. Bae, H. Kim, J. Jung, and W.-J. Cho, "Fabrication of high-performance graphene field-effect transistor with solution-processed Al<sub>2</sub>O<sub>3</sub> sensing membrane," *Appl. Phys. Lett.*, vol. 104, no. 15, p. 153506, Apr. 2014.
- [109] I. Fakih, S. Sabri, F. Mahvash, M. Nannini, M. Siaj, and T. Szkopek, "Large area graphene ion sensitive field effect transistors with tantalum pentoxide sensing layers for pH measurement at the Nernstian limit," *Appl. Phys. Lett.*, vol. 105, no. 8, p. 83101, Aug. 2014.
- [110] A. Loi, I. Manunza, and A. Bonfiglio, "Flexible, organic, ion-sensitive field-effect transistor," *Appl. Phys. Lett.*, vol. 86, no. 10, p. 103512, 2005.
- [111] J. Kofler, K. Schmoltner, A. Klug, and E. J. W. List-Kratochvil, "Hydrogen ion-selective electrolyte-gated organic field-effect transistor for pH sensing," *Appl. Phys. Lett.*, vol. 104, no. 19, p. 193305, May 2014.
- [112] S. Ritjareonwattu, Y. Yun, C. Pearson, and M. C. Petty, "Enhanced sensitivity of an organic field-effect transistor pH sensor using a fatty acid Langmuir–Blodgett film," *Org. Electron.*, vol. 11, no. 11, pp. 1792–1795, Nov. 2010.
- [113] S. Ritjareonwattu, Y. Yun, C. Pearson, and M. C. Petty, "An ion sensitive organic field-effect transistor incorporating the ionophore valinomycin," *IEEE Sens. J.*, vol. 12, no. 5, pp. 1181–1186, May 2012.
- [114] M.-J. Spijkman, J. J. Brondijk, T. C. T. Geuns, E. C. P. Smits, T. Cramer, F. Zerbetto, P. Stoliar, F. Biscarini, P. W. M. Blom, and D. M. de Leeuw, "Dual-gate organic field-effect transistors as potentiometric sensors in aqueous solution," *Adv. Funct. Mater.*, vol. 20, no. 6, pp. 898–905, Mar. 2010.
- [115] M. Yun, A. Sharma, C. Fuentes-Hernandez, D. K. Hwang, A. Dindar, S. Singh, S. Choi, and B. Kippelen, "Stable organic field-effect transistors for continuous and nondestructive sensing of chemical and biologically relevant molecules in aqueous environment," *ACS Appl. Mater. Interfaces*, vol. 6, no. 3, pp. 1616–1622, Feb. 2014.

- [116] J. van der Spiegel, I. Lauks, P. Chan, and D. Babic, "The extended gate chemically sensitive field effect transistor as multi-species microprobe," *Sensor. Actuat.*, vol. 4, pp. 291–298, Jan. 1983.
- [117] L. Maiolo, S. Mirabella, F. Maita, A. Alberti, A. Minotti, V. Strano, A. Pecora, Y. Shacham-Diamand, and G. Fortunato, "Flexible pH sensors based on polysilicon thin film transistors and ZnO nanowalls," *Appl. Phys. Lett.*, vol. 105, no. 9, p. 93501, Sep. 2014.
- [118] Jung-Chuan Chou and Cheng-Wei Chen, "Fabrication and application of ruthenium-doped titanium dioxide films as electrode material for ion-sensitive extended-gate FETs," *IEEE Sens. J.*, vol. 9, no. 3, pp. 277–284, Mar. 2009.
- [119] P.-C. Yao, J.-L. Chiang, and M.-C. Lee, "Application of sol-gel TiO<sub>2</sub> film for an extended-gate H<sup>+</sup> ion-sensitive field-effect transistor," *Solid State Sci.*, vol. 28, pp. 47–54, Feb. 2014.
- [120] Y.-H. Liao and J.-C. Chou, "Preparation and characterization of the titanium dioxide thin films used for pH electrode and procaine drug sensor by sol-gel method," *Mater. Chem. Phys.*, vol. 114, no. 2–3, pp. 542–548, Apr. 2009.
- [121] N. C. S. Vieira, A. Figueiredo, A. D. Faceto, A. A. A. de Queiroz, V. Zucolotto, and F. E. G. Guimarães, "Dendrimers/TiO<sub>2</sub> nanoparticles layer-by-layer films as extended gate FET for pH detection," *Sensor. Actuat. B Chem.*, vol. 169, pp. 397–400, Jul. 2012.
- [122] Y.-C. Huang, F.-S. Tsai, and S.-J. Wang, "Preparation of TiO<sub>2</sub> nanowire arrays through hydrothermal growth method and their pH sensing characteristics," *Jpn. J. Appl. Phys.*, vol. 53, no. 6S, p. 06JG02, Jun. 2014.
- [123] E. M. Guerra and M. Mulato, "Titanium oxide nanorods pH sensors: Comparison between voltammetry and extended gate field effect transistor measurements," *Mater. Sci. Appl.*, vol. 5, no. 7, p. 46458, 2014.
- [124] H.-H. Li, C.-E. Yang, C.-C. Kei, C.-Y. Su, W.-S. Dai, J.-K. Tseng, P.-Y. Yang, J.-C. Chou, and H.-C. Cheng, "Coaxial-structured ZnO/silicon nanowires extended-gate field-effect transistor as pH sensor," *Thin Solid Films*, vol. 529, pp. 173–176, Feb. 2013.
- [125] C.-H. Kao, H. Chen, L.-T. Kuo, J.-C. Wang, Y.-T. Chen, Y.-C. Chu, C.-Y. Chen, C.-S. Lai, S. W. Chang, and C. W. Chang, "Multi-analyte biosensors on a CF<sub>4</sub> plasma treated Nb<sub>2</sub>O<sub>5</sub>-based membrane with an extended gate field effect transistor structure," *Sensor. Actuat. B Chem.*, vol. 194, pp. 419–426, Apr. 2014.
- [126] A. Das, D. H. Ko, C.-H. Chen, L.-B. Chang, C.-S. Lai, F.-C. Chu, L. Chow, and R.-M. Lin, "Highly sensitive palladium oxide thin film extended gate FETs as pH sensor," *Sensor. Actuat. B Chem.*, vol. 205, pp. 199–205, Dec. 2014.
- [127] P. D. Batista and M. Mulato, "Polycrystalline fluorine-doped tin oxide as sensing thin film in EGFET pH sensor," *J. Mater. Sci.*, vol. 45, no. 20, pp. 5478–5481, Oct. 2010.
- [128] B.-R. Huang, S.-C. Hung, and Y.-P. Lo, "Effects of In<sub>2</sub>O<sub>3</sub> modification of sprayed multiwalled carbon nanotubes for pH-sensing applications," *Mater. Sci. Semicond. Process.*, vol. 26, pp. 710–715, Oct. 2014.
- [129] S.-C. Hung, N.-J. Cheng, C.-F. Yang, and Y.-P. Lo, "Investigation of extended-gate field-effect transistor pH sensors based on different-temperature-annealed bi-layer MWCNTs-In<sub>2</sub>O<sub>3</sub> films," *Nanoscale Res. Lett.*, vol. 9, no. 1, p. 502, 2014.
- [130] B.-R. Huang and T.-C. Lin, "Leaf-like carbon nanotube/nickel composite membrane extended-gate field-effect transistors as pH sensor," *Appl. Phys. Lett.*, vol. 99, no. 2, p. 23108, 2011.
- [131] T. Trantidou, M. Tariq, C. Terracciano, C. Toumazou, and T. Prodromakis, "Parylene C-based flexible electronics for pH monitoring applications," *Sensors*, vol. 14, no. 7, pp. 11629–11639, Jul. 2014.
- [132] N. Lei, P. Li, W. Xue, and J. Xu, "Simple graphene chemiresistors as pH sensors: fabrication and characterization," *Meas. Sci. Technol.*, vol. 22, no. 10, p. 107002, Oct. 2011.
- [133] W. S. Lee, Y.-S. Park, and Y.-K. Cho, "Hierarchically structured suspended TiO<sub>2</sub> nanofibers for use in UV and pH sensor devices," *ACS Appl. Mater. Interfaces*, vol. 6, no. 15, pp. 12189–12195, Aug. 2014.

- [134] Y. T. Lee, E. Lee, J. M. Lee, and W. Lee, "Micro-sized pH sensors based on patterned Pd structures using an electrolysis method," *Curr. Appl. Phys.*, vol. 9, no. 4, pp. e218–e221, Jul. 2009.
- [135] K. F. Lei, K.-F. Lee, and S.-I. Yang, "Fabrication of carbon nanotube-based pH sensor for paper-based microfluidics," *Microelectron. Eng.*, vol. 100, pp. 1–5, Dec. 2012.
- [136] P. Lin and F. Yan, "Organic thin-film transistors for chemical and biological sensing," *Adv. Mater.*, vol. 24, no. 1, pp. 34–51, Jan. 2012.
- [137] C. Liao and F. Yan, "Organic semiconductors in organic thin-film transistor-based chemical and biological sensors," *Polym. Rev.*, vol. 53, no. 3, pp. 352–406, Jul. 2013.
- [138] J. T. Mabeck and G. G. Malliaras, "Chemical and biological sensors based on organic thin-film transistors," *Anal. Bioanal. Chem.*, vol. 384, no. 2, pp. 343–353, Dec. 2005.
- [139] G. Tarabella, F. Mahvash Mohammadi, N. Coppedè, F. Barbero, S. Iannotta, C. Santato, and F. Cicoira, "New opportunities for organic electronics and bioelectronics: Ions in action," *Chem. Sci.*, vol. 4, no. 4, pp. 1395–1409, 2013.
- [140] G. Scarpa, A.-L. Idzko, A. Yadav, and S. Thalhammer, "Organic ISFET based on poly(3-hexylthiophene)," *Sensors*, vol. 10, no. 3, pp. 2262–2273, Mar. 2010.
- [141] P. Lin, F. Yan, and H. L. W. Chan, "Ion-sensitive properties of organic electrochemical transistors," *ACS Appl. Mater. Interfaces*, vol. 2, no. 6, pp. 1637–1641, Jun. 2010.
- [142] M. J. Panzer and C. D. Frisbie, "Exploiting ionic coupling in electronic devices: Electrolyte-gated organic field-effect transistors," *Adv. Mater.*, vol. 20, no. 16, pp. 3177–3180, Aug. 2008.
- [143] A. J. Bard and L. R. Faulkner, *Electrochemical methods: Fundamentals and applications, 2nd edition*. New York, NY, USA: John Wiley & Sons, 2001.
- [144] L. Kergoat, B. Piro, M. Berggren, G. Horowitz, and M.-C. Pham, "Advances in organic transistor-based biosensors: from organic electrochemical transistors to electrolyte-gated organic field-effect transistors," *Anal. Bioanal. Chem.*, vol. 402, no. 5, pp. 1813–1826, Feb. 2012.
- [145] V. Pachauri, K. Kern, and K. Balasubramanian, "Field-effect-based chemical sensing using nanowire-nanoparticle hybrids: The ion-sensitive metal-semiconductor field-effect transistor," *Appl. Phys. Lett.*, vol. 102, no. 2, p. 23501, 2013.
- [146] I.-Y. Sohn, D.-J. Kim, J.-H. Jung, O. J. Yoon, T. Nguyen Thanh, T. Tran Quang, and N.-E. Lee, "pH sensing characteristics and biosensing application of solution-gated reduced graphene oxide field-effect transistors," *Biosens. Bioelectron.*, vol. 45, pp. 70–76, Jul. 2013.
- [147] B. Mailly-Giacchetti, A. Hsu, H. Wang, V. Vinciguerra, F. Pappalardo, L. Occhipinti, E. Guidetti, S. Coffa, J. Kong, and T. Palacios, "pH sensing properties of graphene solution-gated field-effect transistors," *J. Appl. Phys.*, vol. 114, no. 8, p. 84505, 2013.
- [148] A. M. Münzer, K. Melzer, M. Heimgreiter, and G. Scarpa, "Random CNT network and regioregular poly(3-hexylthiophen) FETs for pH sensing applications: A comparison," *Biochim. Biophys. Acta*, vol. 1830, no. 9, pp. 4353–4358, Sep. 2013.
- [149] P. K. Ang, W. Chen, A. T. S. Wee, and K. P. Loh, "Solution-gated epitaxial graphene as pH sensor," *J. Am. Chem. Soc.*, vol. 130, no. 44, pp. 14392–14393, Nov. 2008.
- [150] F. Liao, C. Chen, and V. Subramanian, "Organic TFTs as gas sensors for electronic nose applications," *Sensor. Actuat. B Chem.*, vol. 107, no. 2, pp. 849–855, Jun. 2005.
- [151] L. Torsi and A. Dodabalapur, "Organic thin-film transistors as plastic analytical sensors," *Anal. Chem.*, vol. 77, no. 19, p. 380A–387A, Oct. 2005.
- [152] C. Feng, O. Marinov, M. J. Deen, P. R. Selvaganapathy, and Y. Wu, "Sensitivity of the threshold voltage of organic thin-film transistors to light and water," *J. Appl. Phys.*, vol. 117, no. 18, p. 185501, May 2015.
- [153] O. Knopfmacher, M. L. Hammock, A. L. Appleton, G. Schwartz, J. Mei, T. Lei, J. Pei, and Z. Bao, "Highly stable organic polymer field-effect transistor sensor for selective detection in the marine environment," *Nat. Commun.*, vol. 5, p. 2954, Jan. 2014.

- [154] S. J. Zilker, C. Detcheverry, E. Cantatore, and D. M. de Leeuw, "Bias stress in organic thin-film transistors and logic gates," *Appl. Phys. Lett.*, vol. 79, no. 8, p. 1124, 2001.
- [155] J.-H. Ahn, J.-Y. Kim, M.-L. Seol, D. J. Baek, Z. Guo, C.-H. Kim, S.-J. Choi, and Y.-K. Choi, "A pH sensor with a double-gate silicon nanowire field-effect transistor," *Appl. Phys. Lett.*, vol. 102, no. 8, p. 83701, 2013.
- [156] M. E. Roberts, S. C. B. Mannsfeld, N. Queralto, C. Reese, J. Locklin, W. Knoll, and Z. Bao, "Water-stable organic transistors and their application in chemical and biological sensors," *Proc. Natl. Acad. Sci.*, vol. 105, no. 34, pp. 12134–12139, Aug. 2008.
- [157] J. Jin, Y. Suzuki, N. Ishikawa, and T. Takeuchi, "A miniaturized FIA system for the determination of residual chlorine in environmental water samples," *Anal. Sci.*, vol. 20, no. 1, pp. 205–207, 2004.
- [158] A. Mehta, H. Shekhar, S. H. Hyun, S. Hong, and H. J. Cho, "A micromachined electrochemical sensor for free chlorine monitoring in drinking water," *Water Sci. Technol.*, vol. 53, no. 4–5, pp. 403–410, Feb. 2006.
- [159] R. Olivé-Monllau, J. Orozco, C. Fernández-Sánchez, M. Baeza, J. Bartrolí, C. Jimenez-Jorquera, and F. Céspedes, "Flow injection analysis system based on amperometric thin-film transducers for free chlorine detection in swimming pool waters," *Talanta*, vol. 77, no. 5, pp. 1739–1744, Mar. 2009.
- [160] A. Okumura, A. Hirabayashi, Y. Sasaki, and R. Miyake, "Simple miniaturized amperometric flow cell for monitoring residual chlorine in tap water," *Anal. Sci.*, vol. 17, no. 9, pp. 1113–1115, 2001.
- [161] F. Davis, S. D. Collyer, D. D. Gornall, K. A. Law, D. W. Mills, and S. P. J. Higson, "New techniques in monitoring water pollution - Development of sonochemically fabricated microarrays for the determination of pollutants," *Chim. Oggi-Chem. Today*, vol. 25, pp. 28–31, 2007.
- [162] M. Murata, T. A. Ivandini, M. Shibata, S. Nomura, A. Fujishima, and Y. Einaga, "Electrochemical detection of free chlorine at highly boron-doped diamond electrodes," *J. Electroanal. Chem.*, vol. 612, no. 1, pp. 29–36, Jan. 2008.
- [163] P. Salazar, M. Martín, F. J. García-García, J. L. González-Mora, and A. R. González-Elipe, "A novel and improved surfactant-modified Prussian Blue electrode for amperometric detection of free chlorine in water," *Sensor. Actuat. B Chem.*, vol. 213, pp. 116–123, Jul. 2015.
- [164] B. Wang and J. Anzai, "A facile electrochemical detection of hypochlorite ion based on ferrocene compounds," *Int. J. Electrochem. Sci.*, vol. 10, pp. 3260–3268, 2015.
- [165] J. Muñoz, F. Céspedes, and M. Baeza, "Modified multiwalled carbon nanotube/epoxy amperometric nanocomposite sensors with CuO nanoparticles for electrocatalytic detection of free chlorine," *Microchem. J.*, vol. 122, pp. 189–196, Sep. 2015.
- [166] Y. Qin, H.-J. Kwon, M. M. R. Howlader, and M. J. Deen, "Microfabricated electrochemical pH and free chlorine sensors for water quality monitoring: Recent advances and research challenges," *RSC Adv.*, vol. 5, no. 85, pp. 69086–69109, 2015.
- [167] A. Lale, A. Tsopela, A. Civélas, L. Salvagnac, J. Launay, and P. Temple-Boyer, "Integration of tungsten layers for the mass fabrication of WO<sub>3</sub>-based pH-sensitive potentiometric microsensors," *Sensor. Actuat. B Chem.*, vol. 206, pp. 152–158, Jan. 2015.
- [168] R. Zhao, M. Xu, J. Wang, and G. Chen, "A pH sensor based on the TiO<sub>2</sub> nanotube array modified Ti electrode," *Electrochim. Acta*, vol. 55, no. 20, pp. 5647–5651, Aug. 2010.
- [169] S. M. Al-Hilli, M. Willander, A. Öst, and P. Strålfors, "ZnO nanorods as an intracellular sensor for pH measurements," *J. Appl. Phys.*, vol. 102, no. 8, p. 84304, 2007.
- [170] C. Liu, D. Bocchicchio, P. Overmyer, and M. Neuman, "A Palladium-palladium oxide miniature pH electrode," *Science*, vol. 207, no. 4427, pp. 188–189, Jan. 1980.
- [171] W. T. Grubb and L. H. King, "Palladium-palladium oxide pH electrodes," *Anal. Chem.*, vol. 52, no. 2, pp. 270–273, Feb. 1980.
- [172] E. Kinoshita, F. Ingman, G. Edwall, S. Thulin, and S. Głąb, "Polycrystalline and monocrystalline antimony, iridium and palladium as electrode material for pH-sensing electrodes," *Talanta*, vol. 33, no. 2, pp. 125–134, Feb. 1986.

- [173] E. Kinoshita, F. Ingman, G. Edwall, and S. Glab, "An examination of the palladium/palladium oxide system and its utility for pH-sensing electrodes," *Electrochim. Acta*, vol. 31, no. 1, pp. 29–38, Jan. 1986.
- [174] V. A. Karagounis, C. C. Liu, M. R. Neuman, L. T. Romankiw, P. A. Leary, and J. J. Cuomo, "A Pd-PdO film potentiometric pH sensor," *IEEE Trans. Biomed. Eng.*, vol. BME-33, no. 2, pp. 113–116, Feb. 1986.
- [175] C. C. Liu and M. R. Neuman, "Fabrication of miniature PO<sub>2</sub> and pH sensors using microelectronic techniques," *Diabetes Care*, vol. 5, no. 3, pp. 275–277, May 1982.
- [176] L. J. Bloor and D. J. Malcolm-Lawes, "An electrochemical preparation of palladium oxide pH sensors," *J. Electroanal. Chem. Interfacial Electrochem.*, vol. 278, no. 1–2, pp. 161–173, Jan. 1990.
- [177] J. Y. Kim and Y. H. Lee, "Pd-PdO pH microprobe for local pH measurement," *Biotechnol. Bioeng.*, vol. 34, no. 1, pp. 131–136, Jun. 1989.
- [178] Y. Qin, D. H. Turkenburg, I. Barbu, W. T. T. Smaal, K. Myny, W.-Y. Lin, G. H. Gelinck, P. Heremans, J. Liu, and E. R. Meinders, "Organic thin-film transistors with anodized gate dielectric patterned by self-aligned embossing on flexible substrates," *Adv. Funct. Mater.*, vol. 22, no. 6, pp. 1209–1214, 2012.
- [179] J. Chu, Y. Zhao, S.-H. Li, H.-Q. Yu, G. Liu, and Y.-C. Tian, "An integrated solid-state pH microelectrode prepared using microfabrication," *Electrochim. Acta*, vol. 152, pp. 6–12, Jan. 2015.
- [180] Y. Qin, M. M. R. Howlader, M. J. Deen, Y. M. Haddara, and P. R. Selvaganapathy, "Polymer integration for packaging of implantable sensors," *Sensor. Actuat. B Chem.*, vol. 202, pp. 758–778, Oct. 2014.
- [181] A. Santos, M. J. Deen, and L. F. Marsal, "Low-cost fabrication technologies for nanostructures: State-of-the-art and potential," *Nanotechnology*, vol. 26, no. 4, p. 42001, Jan. 2015.
- [182] J. P. Metters, F. Tan, and C. E. Banks, "Screen-printed palladium electroanalytical sensors," *J. Solid State Electrochem.*, vol. 17, no. 6, pp. 1553–1562, Jun. 2013.
- [183] M. Ren, Y. Kang, W. He, Z. Zou, X. Xue, D. L. Akins, H. Yang, and S. Feng, "Origin of performance degradation of palladium-based direct formic acid fuel cells," *Appl. Catal. B Environ.*, vol. 104, no. 1–2, pp. 49–53, Apr. 2011.
- [184] D. Zemlyanov, B. Aszalos-Kiss, E. Kleimenov, D. Teschner, S. Zafeiratos, M. Hävecker, A. Knop-Gericke, R. Schlögl, H. Gabasch, W. Unterberger, K. Hayek, and B. Klötzer, "In situ XPS study of Pd(111) oxidation. Part 1: 2D oxide formation in 10–3mbar O<sub>2</sub>," *Surf. Sci.*, vol. 600, no. 5, pp. 983–994, Mar. 2006.
- [185] H. Wang, T. Sun, W. Xu, F. Xie, L. Ye, Y. Xiao, Y. Wang, J. Chen, and J. Xu, "Low-temperature facile solution-processed gate dielectric for combustion derived oxide thin film transistors," *RSC Adv.*, vol. 4, no. 97, pp. 54729–54739, Oct. 2014.
- [186] M. W. Lee, G. S. Ryu, Y. U. Lee, C. Pearson, M. C. Petty, and C. K. Song, "Control of droplet morphology for inkjet-printed TIPS-pentacene transistors," *Microelectron. Eng.*, vol. 95, pp. 1–4, Jul. 2012.
- [187] S. Glab, A. Hulanicki, G. Edwall, and F. Ingman, "Metal-metal oxide and metal oxide electrodes as pH sensors," *Crit. Rev. Anal. Chem.*, vol. 21, no. 1, pp. 29–47, Jan. 1989.
- [188] H. H. Kan, R. J. Colmyer, A. Asthagiri, and J. F. Weaver, "Adsorption of water on a PdO(101) thin film: Evidence of an adsorbed HO–H<sub>2</sub>O complex," *J. Phys. Chem. C*, vol. 113, no. 4, pp. 1495–1506, Jan. 2009.
- [189] J.-S. Filhol and M. Neurock, "Elucidation of the electrochemical activation of water over Pd by first principles," *Angew. Chemie Int. Ed.*, vol. 45, no. 3, pp. 402–406, Jan. 2006.
- [190] M. Grdeń, M. Łukaszewski, G. Jerkiewicz, and A. Czerwiński, "Electrochemical behaviour of palladium electrode: Oxidation, electrodisolution and ionic adsorption," *Electrochim. Acta*, vol. 53, no. 26, pp. 7583–7598, Nov. 2008.
- [191] J. Bobacka, A. Ivaska, and A. Lewenstam, "Potentiometric ion sensors," *Chem. Rev.*, vol. 108, no. 2, pp. 329–351, Feb. 2008.

- [192] E. Bakker, "The phase-boundary potential model," *Talanta*, vol. 63, no. 1, pp. 3–20, May 2004.
- [193] A. W. Adamson and A. P. Gast, *Physical chemistry of surfaces, 6th edition*. New York, NY, USA: John Wiley & Sons, 1997.
- [194] G. N. Lewis, "The atom and the molecule," *J. Am. Chem. Soc.*, vol. 38, no. 4, pp. 762–785, Apr. 1916.
- [195] R. P. Buck, "Theory of potential distribution and response of solid state membrane electrodes. I. Zero current," *Anal. Chem.*, vol. 40, no. 10, pp. 1432–1439, Aug. 1968.
- [196] L. M. Vracar, D. B. Sepa, and A. Damjanovic, "Palladium electrode in oxygen saturated solutions," *J. Electrochem. Soc.*, vol. 134, no. 7, pp. 1695–1697, 1987.
- [197] S. F. Parker, K. Refson, A. C. Hannon, and E. R. Barney, "Characterization of hydrous palladium oxide: Implications for low-temperature carbon monoxide oxidation," *J. Phys. Chem. C*, vol. 114, no. 33, pp. 14164–14172, 2010.
- [198] L. S. Kibis, A. I. Stadnichenko, S. V. Koscheev, V. I. Zaikovskii, and A. I. Boronin, "Highly oxidized palladium nanoparticles comprising Pd<sup>4+</sup> species: Spectroscopic and structural aspects, thermal stability, and reactivity," *J. Phys. Chem. C*, vol. 116, no. 36, pp. 19342–19348, Sep. 2012.
- [199] K. G. Kreider, M. J. Tarlov, and J. P. Cline, "Sputtered thin-film pH electrodes of platinum, palladium, ruthenium, and iridium oxides," *Sensor. Actuat. B Chem.*, vol. 28, no. 3, pp. 167–172, 1995.
- [200] L. Bousse, S. Mostarshed, B. van der Schoot, and N. F. de Rooij, "Comparison of the hysteresis of Ta<sub>2</sub>O<sub>5</sub> and Si<sub>3</sub>N<sub>4</sub> pH-sensing insulators," *Sensor. Actuat. B Chem.*, vol. 17, no. 2, pp. 157–164, Jan. 1994.
- [201] S. Chen, W. Huang, J. Zheng, and Z. Li, "Study on the electrodisolution and roughening of a palladium electrode in chloride containing solutions," *J. Electroanal. Chem.*, vol. 660, no. 1, pp. 80–84, 2011.
- [202] M. Singh, H. M. Haverinen, P. Dhagat, and G. E. Jabbour, "Inkjet printing-process and its applications," *Adv. Mater.*, vol. 22, no. 6, pp. 673–685, Feb. 2010.
- [203] M. Kuang, L. Wang, and Y. Song, "Controllable printing droplets for high-resolution patterns," *Adv. Mater.*, vol. 26, no. 40, pp. 6950–6958, Oct. 2014.
- [204] C. N. Hoth, S. A. Choulis, P. Schilinsky, and C. J. Brabec, "High photovoltaic performance of inkjet printed polymer: Fullerene blends," *Adv. Mater.*, vol. 19, no. 22, pp. 3973–3978, Nov. 2007.
- [205] E. Tekin, P. J. Smith, S. Hoepfener, A. M. J. van den Berg, A. S. Sussha, A. L. Rogach, J. Feldmann, and U. S. Schubert, "Inkjet printing of luminescent CdTe nanocrystal-polymer composites," *Adv. Funct. Mater.*, vol. 17, no. 1, pp. 23–28, Jan. 2007.
- [206] M. Medina-Sánchez, C. Martínez-Domingo, E. Ramon, and A. Merkoçi, "An inkjet-printed field-effect transistor for label-free biosensing," *Adv. Funct. Mater.*, vol. 24, no. 40, pp. 6291–6302, Oct. 2014.
- [207] B. Derby, "Printing and prototyping of tissues and scaffolds," *Science*, vol. 338, no. 6109, pp. 921–926, Nov. 2012.
- [208] A. Chen and C. Ostrom, "Palladium-based nanomaterials: Synthesis and electrochemical applications," *Chem. Rev.*, vol. 115, no. 21, pp. 11999–12044, Nov. 2015.
- [209] R. Westerström, M. E. Messing, S. Blomberg, A. Hellman, H. Grönbeck, J. Gustafson, N. M. Martin, O. Balmes, R. van Rijn, J. N. Andersen, K. Deppert, H. Bluhm, Z. Liu, M. E. Grass, M. Hävecker, and E. Lundgren, "Oxidation and reduction of Pd(100) and aerosol-deposited Pd nanoparticles," *Phys. Rev. B*, vol. 83, no. 11, p. 115440, Mar. 2011.
- [210] S. Busato, A. Belloli, and P. Ermanni, "Inkjet printing of palladium catalyst patterns on polyimide film for electroless copper plating," *Sensor. Actuat. B Chem.*, vol. 123, no. 2, pp. 840–846, May 2007.
- [211] M.-W. Wang, T.-Y. Liu, D.-C. Pang, J.-C. Hung, and C.-C. Tseng, "Inkjet printing of a pH sensitive palladium catalyst patterns of ITO glass for electroless copper," *Surf. Coatings Technol.*, vol. 259, pp. 340–345, Nov. 2014.

- [212] H. J. Gysling, "Nanoinks in inkjet metallization - Evolution of simple additive-type metal patterning," *Curr. Opin. Colloid Interface Sci.*, vol. 19, no. 2, pp. 155–162, Apr. 2014.
- [213] T. Bhuvana, W. Boley, B. Radha, B. D. Dolash, G. Chiu, D. Bergstrom, R. Reifenberger, T. S. Fisher, and G. U. Kulkarni, "Inkjet printing of palladium alkanethiolates for facile fabrication of metal interconnects and surface-enhanced Raman scattering substrates," *Micro Nano Lett.*, vol. 5, no. 5, pp. 296–299, 2010.
- [214] X. Fang, H. Li, R. Jackstell, and M. Beller, "Selective palladium-catalyzed aminocarbonylation of 1,3-dienes: Atom-efficient synthesis of  $\beta,\gamma$ -unsaturated amides," *J. Am. Chem. Soc.*, vol. 136, no. 45, pp. 16039–16043, Nov. 2014.
- [215] J. Borris, A. Dohse, A. Hinze, M. Thomas, C.-P. Klages, A. Möbius, D. Elbick, and E.-R. Weidlich, "Improvement of the adhesion of a galvanic metallization of polymers by surface functionalization using dielectric barrier discharges at atmospheric pressure," *Plasma Process. Polym.*, vol. 6, no. S1, pp. S258–S263, Jun. 2009.
- [216] M. Robin, W. Kuai, M. Amela-Cortes, S. Cordier, Y. Molard, T. Mohammed-Brahim, E. Jacques, and M. Harnois, "Epoxy based ink as versatile material for inkjet-printed devices," *ACS Appl. Mater. Interfaces*, vol. 7, no. 39, pp. 21975–21984, Oct. 2015.
- [217] Y. Chang, C. Yang, X.-Y. Zheng, D.-Y. Wang, and Z.-G. Yang, "Fabrication of copper patterns on flexible substrate by patterning–adsorption–plating process," *ACS Appl. Mater. Interfaces*, vol. 6, no. 2, pp. 768–772, Jan. 2014.
- [218] H. I. Rasool, C. Ophus, and A. Zettl, "Atomic defects in two dimensional materials," *Adv. Mater.*, vol. 27, no. 38, pp. 5771–5777, Oct. 2015.
- [219] A. Roshanghias, G. Khatibi, R. Pelzer, J. Steinbrenner, and J. Bernardi, "Cross-sectional nanoindentation (CSN) studies on the effect of thickness on adhesion strength of thin films," *J. Phys. D. Appl. Phys.*, vol. 48, no. 3, p. 35301, Jan. 2015.
- [220] X. Jin, J. Strueben, L. Heepe, A. Kovalev, Y. K. Mishra, R. Adelung, S. N. Gorb, and A. Staubitz, "Joining the un-joinable: adhesion between low surface energy polymers using tetrapodal ZnO linkers," *Adv. Mater.*, vol. 24, no. 42, pp. 5676–5680, Nov. 2012.
- [221] A. . Volinsky, N. . Moody, and W. . Gerberich, "Interfacial toughness measurements for thin films on substrates," *Acta Mater.*, vol. 50, no. 3, pp. 441–466, Feb. 2002.
- [222] M. D. Thouless, "Cracking and delamination of coatings," *J. Vac. Sci. Technol. A Vacuum, Surfaces, Film.*, vol. 9, no. 4, pp. 2510–2515, Jul. 1991.
- [223] D. Bernoulli, K. Häfliger, K. Thorwarth, G. Thorwarth, R. Hauert, and R. Spolenak, "Cohesive and adhesive failure of hard and brittle films on ductile metallic substrates: A film thickness size effect analysis of the model system hydrogenated diamond-like carbon (a-C:H) on Ti substrates," *Acta Mater.*, vol. 83, pp. 29–36, Jan. 2015.
- [224] Y.-T. Chen, "Optical, electrical, and adhesive properties of ZnO thin films," *J. Nanosci. Nanotechnol.*, vol. 16, no. 1, pp. 658–662, Jan. 2016.
- [225] N. Inagaki, S. Tasaka, and K. Hibi, "Surface modification of Kapton film by plasma treatments," *J. Polym. Sci. Part A Polym. Chem.*, vol. 30, no. 7, pp. 1425–1431, Jun. 1992.
- [226] J. H. Jung, J. A. Rim, S. J. Lee, and S. S. Lee, "Spatial organization and patterning of palladium nanoparticles on a self-assembled helical ribbon lipid," *Chem. Commun.*, no. 4, pp. 468–470, 2005.
- [227] G. Yu, X. Xie, L. Pan, Z. Bao, and Y. Cui, "Hybrid nanostructured materials for high-performance electrochemical capacitors," *Nano Energy*, vol. 2, no. 2, pp. 213–234, Mar. 2013.
- [228] J. Halme, M. Toivola, A. Tolvanen, and P. Lund, "Charge transfer resistance of spray deposited and compressed counter electrodes for dye-sensitized nanoparticle solar cells on plastic substrates," *Sol. Energy Mater. Sol. Cells*, vol. 90, no. 7–8, pp. 872–886, May 2006.
- [229] B. E. Conway, V. Birss, and J. Wojtowicz, "The role and utilization of pseudocapacitance for energy storage by supercapacitors," *J. Power Sources*, vol. 66, no. 1–2, pp. 1–14, May 1997.
- [230] J. C. Chou, K. Y. Huang, and J. S. Lin, "Simulation of time-dependent effects of pH-ISFETs," *Sensor. Actuat. B Chem.*, vol. 62, no. 2, pp. 88–91, Feb. 2000.

- [231] J. C. Chou, H. M. Tsai, C. N. Shiao, and J. S. Lin, "Study and simulation of the drift behaviour of hydrogenated amorphous silicon gate pH-ISFET," *Sensor. Actuat. B Chem.*, vol. 62, no. 2, pp. 97–101, Feb. 2000.
- [232] L. Bousse, D. Hafeman, and N. Tran, "Time-dependence of the chemical response of silicon nitride surfaces," *Sensor. Actuat. B Chem.*, vol. 1, no. 1–6, pp. 361–367, Jan. 1990.
- [233] S. Jamasb, S. D. Collins, and R. L. Smith, "A physical model for threshold voltage instability in Si<sub>3</sub>N<sub>4</sub>-gate H<sup>+</sup>-sensitive FET's (pH ISFET's)," *IEEE Trans. Electron Devices*, vol. 45, no. 6, pp. 1239–1245, Jun. 1998.
- [234] S. Jamasb, S. Collins, and R. L. Smith, "A physical model for drift in pH ISFETs," *Sensor. Actuat. B Chem.*, vol. 49, no. 1–2, pp. 146–155, Jun. 1998.
- [235] L. L. Zhang, R. Zhou, and X. S. Zhao, "Graphene-based materials as supercapacitor electrodes," *J. Mater. Chem.*, vol. 20, no. 29, p. 5983, 2010.
- [236] C.-W. Pan, J.-C. Chou, T.-P. Sun, and S.-K. Hsiung, "Development of the tin oxide pH electrode by the sputtering method," *Sensor. Actuat. B Chem.*, vol. 108, no. 1–2, pp. 863–869, Jul. 2005.
- [237] M. Berggren and A. Richter-Dahlfors, "Organic bioelectronics," *Adv. Mater.*, vol. 19, no. 20, pp. 3201–3213, Sep. 2007.
- [238] M. W. Shinwari, D. Zhitomirsky, I. A. Deen, P. R. Selvaganapathy, M. J. Deen, and D. Landheer, "Microfabricated reference electrodes and their biosensing applications," *Sensors*, vol. 10, no. 3, pp. 1679–1715, Mar. 2010.
- [239] J. Hu, A. Stein, and P. Bühlmann, "Rational design of all-solid-state ion-selective electrodes and reference electrodes," *TrAC Trends Anal. Chem.*, vol. 76, pp. 102–114, Feb. 2016.
- [240] F. Huang, Y. Jin, and L. Wen, "Investigations of the hydration effects on cyclic thermo-oxidized Ir/IrO<sub>x</sub> electrode," *J. Electrochem. Soc.*, vol. 162, no. 12, pp. B337–B343, Sep. 2015.
- [241] H. Suzuki, A. Hiratsuka, S. Sasaki, and I. Karube, "Problems associated with the thin-film Ag/AgCl reference electrode and a novel structure with improved durability," *Sensor. Actuat. B Chem.*, vol. 46, no. 2, pp. 104–113, Feb. 1998.
- [242] G. A. Rechnitz and S. B. Zamochnik, "Behaviour of silver(II) in phosphoric acid media and a general mechanism for solvent oxidation," *Talanta*, vol. 12, no. 5, pp. 479–483, May 1965.
- [243] P. Saini, "Tangential flow ultrafiltration as an antifouling strategy for water quality sensors," McMaster University, 2017.
- [244] Y. Qin, H.-J. Kwon, S. Pan, P. Saini, R. Ghosh, P. R. Selvaganapathy, and M. J. Deen, "Microfabricated pH sensors: Design, modeling and experiments," in *IC-IMPACTS Annual General Meeting*, 2015.
- [245] J. Henriksson, L. G. Villanueva, and J. Brugger, "Ultra-low power hydrogen sensing based on a palladium-coated nanomechanical beam resonator," *Nanoscale*, vol. 4, no. 16, pp. 5059–5064, 2012.
- [246] E. Rey, M. R. Kamal, R. B. Miles, and B. S. H. Royce, "The semiconductivity and stability of palladium oxide," *J. Mater. Sci.*, vol. 13, no. 4, pp. 812–816, Apr. 1978.
- [247] F. Xia, V. Perebeinos, Y. Lin, Y. Wu, and P. Avouris, "The origins and limits of metal–graphene junction resistance," *Nat. Nanotechnol.*, vol. 6, no. 3, pp. 179–184, Mar. 2011.
- [248] Y. Murakami, J. Li, D. Hirose, S. Kohara, and T. Shimoda, "Solution processing of highly conductive ruthenium and ruthenium oxide thin films from ruthenium–amine complexes," *J. Mater. Chem. C*, vol. 3, no. 17, pp. 4490–4499, 2015.
- [249] C.-J. Zhong, J. Luo, B. Fang, B. N. Wanjala, P. N. Njoki, R. Loukrakpam, and J. Yin, "Nanostructured catalysts in fuel cells," *Nanotechnology*, vol. 21, no. 6, p. 62001, Feb. 2010.
- [250] H.-J. Qiu, X. Li, H.-T. Xu, H.-J. Zhang, and Y. Wang, "Nanoporous metal as a platform for electrochemical and optical sensing," *J. Mater. Chem. C*, vol. 2, no. 46, pp. 9788–9799, Oct. 2014.
- [251] R. Griessen, N. Strohhfeldt, and H. Giessen, "Thermodynamics of the hybrid interaction of hydrogen with palladium nanoparticles," *Nat. Mater.*, vol. 15, no. 3, pp. 311–317, Nov. 2015.

- [252] Y. Pak, N. Lim, Y. Kumaresan, R. Lee, K. Kim, T. H. Kim, S.-M. Kim, J. T. Kim, H. Lee, M.-H. Ham, and G.-Y. Jung, "Palladium nanoribbon array for fast hydrogen gas sensing with ultrahigh sensitivity," *Adv. Mater.*, vol. 27, no. 43, pp. 6945–6952, Nov. 2015.
- [253] N. Ly, D. E. Xu, W. H. Song, and M. Mayer, "More uniform Pd distribution in free-air balls of Pd-coated Cu bonding wire using movable flame-off electrode," *Microelectron. Reliab.*, vol. 55, no. 1, pp. 201–206, Jan. 2015.
- [254] M. E. Franke, T. J. Koplín, and U. Simon, "Metal and metal oxide nanoparticles in chemiresistors: Does the nanoscale matter?," *Small*, vol. 2, no. 1, pp. 36–50, Jan. 2006.
- [255] J. F. Weaver, "Surface chemistry of late transition metal oxides," *Chem. Rev.*, vol. 113, no. 6, pp. 4164–4215, Jun. 2013.
- [256] Y. Cao and Z.-X. Chen, "Slab model studies of water adsorption and decomposition on clean and X- (X = C, N and O) contaminated Pd(111) surfaces," *Phys. Chem. Chem. Phys.*, vol. 9, no. 6, pp. 739–746, 2007.
- [257] Z. Jiang, L. Li, M. Li, R. Li, and T. Fang, "Density functional theory study on the adsorption and decomposition of H<sub>2</sub>O on clean and oxygen-modified Pd (100) surface," *Appl. Surf. Sci.*, vol. 301, pp. 468–474, May 2014.
- [258] Y.-J. Chiang, K.-C. Li, Y.-C. Lin, and F.-M. Pan, "A mechanistic study of hydrogen gas sensing by PdO nanoflake thin films at temperatures below 250 °C," *Phys. Chem. Chem. Phys.*, vol. 17, no. 5, pp. 3039–3049, 2015.
- [259] S. Choudhury, C. A. Betty, K. Bhattacharyya, V. Saxena, and D. Bhattacharya, "Nanostructured PdO thin film from Langmuir–Blodgett precursor for room temperature H<sub>2</sub> gas sensing," *ACS Appl. Mater. Interfaces*, vol. 8, no. 26, pp. 16997–17003, Jul. 2016.
- [260] A. Baylet, P. Marécot, D. Duprez, P. Castellazzi, G. Groppi, and P. Forzatti, "In situ Raman and in situ XRD analysis of PdO reduction and Pd<sup>0</sup> oxidation supported on  $\gamma$ -Al<sub>2</sub>O<sub>3</sub> catalyst under different atmospheres," *Phys. Chem. Chem. Phys.*, vol. 13, no. 10, pp. 4607–4613, 2011.
- [261] B. Jang, W. Kim, M.-J. Song, and W. Lee, "Thermal stability of the sensing properties in H<sub>2</sub> sensors composed of Pd nanogaps on an elastomeric substrate," *Sensor. Actuat. B Chem.*, vol. 240, pp. 186–192, Mar. 2017.
- [262] L. Fei, Y. Xu, X. Wu, Y. Li, P. Xie, S. Deng, S. Smirnov, and H. Luo, "SBA-15 confined synthesis of TiNb<sub>2</sub>O<sub>7</sub> nanoparticles for lithium-ion batteries," *Nanoscale*, vol. 5, no. 22, pp. 11102–11107, 2013.
- [263] G. Socrates, *Infrared and Raman characteristic group frequencies: Tables and charts*. New York, NY, USA: John Wiley & Sons, 2004.
- [264] Y. Zheng, Q. Qiao, J. Wang, X. Li, and J. Jian, "Gas sensing behavior of palladium oxide for carbon monoxide at low working temperature," *Sensor. Actuat. B Chem.*, vol. 212, pp. 256–263, Jun. 2015.
- [265] A. K. Datye, J. Bravo, T. R. Nelson, P. Atanasova, M. Lyubovsky, and L. Pfefferle, "Catalyst microstructure and methane oxidation reactivity during the Pd $\leftrightarrow$ PdO transformation on alumina supports," *Appl. Catal. A Gen.*, vol. 198, no. 1–2, pp. 179–196, May 2000.
- [266] S. Mishra and S. Daniele, "Metal–Organic Derivatives with Fluorinated Ligands as Precursors for Inorganic Nanomaterials," *Chem. Rev.*, vol. 115, no. 16, pp. 8379–8448, Aug. 2015.
- [267] E. Lundgren, G. Kresse, C. Klein, M. Borg, J. N. Andersen, M. De Santis, Y. Gauthier, C. Konvicka, M. Schmid, and P. Varga, "Two-dimensional oxide on Pd(111)," *Phys. Rev. Lett.*, vol. 88, no. 24, p. 246103, Jun. 2002.
- [268] A. McNally, B. Haffemayer, B. S. L. Collins, and M. J. Gaunt, "Palladium-catalysed C–H activation of aliphatic amines to give strained nitrogen heterocycles," *Nature*, vol. 510, no. 7503, pp. 129–133, May 2014.
- [269] E. Roduner, "Size matters: Why nanomaterials are different," *Chem. Soc. Rev.*, vol. 35, no. 7, pp. 583–592, 2006.

- [270] T. Teranishi and M. Miyake, "Size control of palladium nanoparticles and their crystal structures," *Chem. Mater.*, vol. 10, no. 2, pp. 594–600, Feb. 1998.
- [271] S. Polster, M. P. M. Jank, and L. Frey, "Correlation of film morphology and defect content with the charge-carrier transport in thin-film transistors based on ZnO nanoparticles," *J. Appl. Phys.*, vol. 119, no. 2, p. 24504, Jan. 2016.
- [272] D.-H. Kim, N. Lu, R. Ghaffari, Y.-S. Kim, S. P. Lee, L. Xu, J. Wu, R.-H. Kim, J. Song, Z. Liu, J. Viventi, B. de Graff, B. Elolampi, M. Mansour, M. J. Slepian, S. Hwang, J. D. Moss, S.-M. Won, Y. Huang, B. Litt, and J. A. Rogers, "Materials for multifunctional balloon catheters with capabilities in cardiac electrophysiological mapping and ablation therapy," *Nat. Mater.*, vol. 10, no. 4, pp. 316–323, Apr. 2011.
- [273] A. U. Alam, Y. Qin, M. M. R. Howlader, and M. J. Deen, "Direct bonding of liquid crystal polymer to glass," *RSC Adv.*, vol. 6, no. 109, pp. 107200–107207, 2016.
- [274] S. K. Mahadeva, K. Walus, and B. Stoeber, "Paper as a platform for sensing applications and other devices: A review," *ACS Appl. Mater. Interfaces*, vol. 7, no. 16, pp. 8345–8362, 2015.
- [275] J. Mettakoonpitak, K. Boehle, S. Nantaphol, P. Teengam, J. A. Adkins, M. Srisa-Art, and C. S. Henry, "Electrochemistry on paper-based analytical devices: A review," *Electroanalysis*, vol. 28, no. 7, pp. 1420–1436, Jul. 2016.
- [276] S. Ahmed, M.-P. N. Bui, and A. Abbas, "Paper-based chemical and biological sensors: Engineering aspects," *Biosens. Bioelectron.*, vol. 77, pp. 249–263, 2016.
- [277] M. Cuartero, G. A. Crespo, and E. Bakker, "Paper-based thin-layer coulometric sensor for halide determination," *Anal. Chem.*, vol. 87, no. 3, pp. 1981–1990, Feb. 2015.
- [278] W.-J. Lan, X. U. Zou, M. M. Hamed, J. Hu, C. Parolo, E. J. Maxwell, P. Bühlmann, and G. M. Whitesides, "Paper-based potentiometric ion sensing," *Anal. Chem.*, vol. 86, no. 19, pp. 9548–9553, Oct. 2014.
- [279] B. D. Grant, C. A. Smith, K. Karvonen, and R. Richards-Kortum, "Highly sensitive two-dimensional paper network incorporating biotin-streptavidin for the detection of malaria," *Anal. Chem.*, vol. 88, no. 5, pp. 2553–2557, Mar. 2016.
- [280] A. C. Glavan, J. Niu, Z. Chen, F. Güder, C.-M. Cheng, D. Liu, and G. M. Whitesides, "Analytical devices based on direct synthesis of DNA on paper," *Anal. Chem.*, vol. 88, no. 1, pp. 725–731, Jan. 2016.
- [281] Y. Xia, J. Si, and Z. Li, "Fabrication techniques for microfluidic paper-based analytical devices and their applications for biological testing: A review," *Biosens. Bioelectron.*, vol. 77, pp. 774–789, Mar. 2016.
- [282] W. Kim, J.-C. Lee, J.-H. Shin, K.-H. Jin, H.-K. Park, and S. Choi, "Instrument-free synthesizable fabrication of label-free optical biosensing paper strips for the early detection of infectious keratoconjunctivitis," *Anal. Chem.*, vol. 88, no. 10, pp. 5531–5537, May 2016.
- [283] J. Ho, M. K. Tan, D. B. Go, L. Y. Yeo, J. R. Friend, and H.-C. Chang, "Paper-based microfluidic surface acoustic wave sample delivery and ionization source for rapid and sensitive ambient mass spectrometry," *Anal. Chem.*, vol. 83, no. 9, pp. 3260–3266, 2011.
- [284] X. Li, K. Scida, and R. M. Crooks, "Detection of hepatitis B virus DNA with a paper electrochemical sensor," *Anal. Chem.*, vol. 87, no. 17, pp. 9009–9015, Sep. 2015.
- [285] J. Olkkonen, K. Lehtinen, and T. Erho, "Flexographically printed fluidic structures in paper," *Anal. Chem.*, vol. 82, no. 24, pp. 10246–10250, Dec. 2010.
- [286] B. Gao, H. Liu, and Z. Gu, "Patterned photonic nitrocellulose for pseudo-paper microfluidics," *Anal. Chem.*, vol. 88, no. 10, pp. 5424–5429, May 2016.
- [287] Z. Li, H. Liu, C. Ouyang, W. Hong Wee, X. Cui, T. Jian Lu, B. Pingguan-Murphy, F. Li, and F. Xu, "Recent advances in pen-based writing electronics and their emerging applications," *Adv. Funct. Mater.*, vol. 26, no. 2, pp. 165–180, Jan. 2016.
- [288] J. R. Choi, Z. Liu, J. Hu, R. Tang, Y. Gong, S. Feng, H. Ren, T. Wen, H. Yang, Z. Qu, B. Pingguan-Murphy, and F. Xu, "Polydimethylsiloxane-paper hybrid lateral flow assay for highly

- sensitive point-of-care nucleic acid testing,” *Anal. Chem.*, vol. 88, no. 12, pp. 6254–6264, Jun. 2016.
- [289] B. Kang, N. Park, H. Min, J. Lee, H. Jeong, S. Baek, K. Cho, and H. S. Lee, “Fully drawn all-organic flexible transistors prepared by capillary pen printing on flexible planar and curvilinear substrates,” *Adv. Electron. Mater.*, vol. 1, no. 12, p. 1500301, Dec. 2015.
- [290] Q. Hua, H. Liu, J. Zhao, D. Peng, X. Yang, L. Gu, and C. Pan, “Bioinspired electronic whisker arrays by pencil-drawn paper for adaptive tactile sensing,” *Adv. Electron. Mater.*, vol. 2, no. 7, p. 1600093, Jul. 2016.
- [291] A. J. Bandodkar, W. Jia, J. Ramírez, and J. Wang, “Biocompatible enzymatic roller pens for direct writing of biocatalytic materials: ‘Do-it-yourself’ electrochemical biosensors,” *Adv. Healthc. Mater.*, vol. 4, no. 8, pp. 1215–1224, 2015.
- [292] A. J. Oostra, K. H. W. van den Bos, P. W. M. Blom, and J. J. Michels, “Disruption of the electrical conductivity of highly conductive poly(3,4-ethylenedioxythiophene):poly(styrene sulfonate) by hypochlorite,” *J. Phys. Chem. B*, vol. 117, no. 37, pp. 10929–10935, Sep. 2013.
- [293] D. Alemu, H.-Y. Wei, K.-C. Ho, and C.-W. Chu, “Highly conductive PEDOT:PSS electrode by simple film treatment with methanol for ITO-free polymer solar cells,” *Energy Environ. Sci.*, vol. 5, no. 11, pp. 9662–9671, 2012.
- [294] G. Barbarella, L. Favaretto, M. Zambianchi, O. Pudova, C. Arbizzani, A. Bongini, and M. Mastragostino, “From easily oxidized to easily reduced thiophene-based materials,” *Adv. Mater.*, vol. 10, no. 7, pp. 551–554, 1998.
- [295] H. Shi, C. Liu, Q. Jiang, and J. Xu, “Effective approaches to improve the electrical conductivity of PEDOT:PSS: A review,” *Adv. Electron. Mater.*, vol. 1, no. 4, p. 1500017, 2015.
- [296] M. V. Storey, B. van der Gaag, and B. P. Burns, “Advances in on-line drinking water quality monitoring and early warning systems,” *Water Res.*, vol. 45, no. 2, pp. 741–747, Jan. 2011.
- [297] D. Chapman, “Water quality assessments: A guide to the use of biota, sediments, and water in environmental monitoring,” University Press, Cambridge, UK, 1996.
- [298] Y. Qin, S. Pan, Z. Cheng, A. U. Alam, M. M. R. Howlader, R. Ghosh, N.-X. Hu, and M. J. Deen, “Integrated water quality monitoring system with pH, free chlorine, and temperature sensors,” p. submitted to *Sensors and Actuators B: Chemical*, 2017.
- [299] Y. Feng, D. W. Smith, and J. R. Bolton, “Photolysis of aqueous free chlorine species (HOCl and OCl-) with 254 nm ultraviolet light,” *J. Environ. Eng. Sci.*, vol. 6, no. 3, pp. 277–284, May 2007.
- [300] S. Joo and R. B. Brown, “Chemical sensors with integrated electronics,” *Chem. Rev.*, vol. 108, no. 2, pp. 638–651, Jan. 2008.
- [301] P. Salazar, M. Martín, J. L. González-Mora, and A. R. González-Elipse, “Application of Prussian Blue electrodes for amperometric detection of free chlorine in water samples using flow injection analysis,” *Talanta*, vol. 146, pp. 410–416, Jan. 2016.
- [302] L. H. H. Hsu, E. Hoque, P. Kruse, and P. Ravi Selvaganapathy, “A carbon nanotube based resettable sensor for measuring free chlorine in drinking water,” *Appl. Phys. Lett.*, vol. 106, no. 6, p. 63102, Feb. 2015.
- [303] A. Richter, G. Paschew, S. Klatt, J. Lienig, K.-F. Arndt, and H.-J. P. Adler, “Review on hydrogel-based pH sensors and microsensors,” *Sensors*, vol. 8, no. 1, pp. 561–581, Jan. 2008.
- [304] M. Sezen, J. T. Register, Y. Yao, B. Glisic, and Y.-L. Loo, “Eliminating piezoresistivity in flexible conducting polymers for accurate temperature sensing under dynamic mechanical deformations,” *Small*, vol. 12, no. 21, pp. 2832–2838, Jun. 2016.
- [305] Y. Qin, A. U. Alam, M. M. R. Howlader, N.-X. Hu, and M. J. Deen, “Morphology and electrical properties of inkjet-printed palladium/palladium oxide,” *J. Mater. Chem. C*, vol. 5, no. 8, pp. 1893–1902, 2017.
- [306] H. Lee, T. K. Choi, Y. B. Lee, H. R. Cho, R. Ghaffari, L. Wang, H. J. Choi, T. D. Chung, N. Lu, T. Hyeon, S. H. Choi, and D.-H. Kim, “A graphene-based electrochemical device with

- thermoreponsive microneedles for diabetes monitoring and therapy,” *Nat. Nanotechnol.*, vol. 11, no. 6, pp. 566–572, Mar. 2016.
- [307] W. Honda, S. Harada, T. Arie, S. Akita, and K. Takei, “Wearable, human-interactive, health-monitoring, wireless devices fabricated by macroscale printing techniques,” *Adv. Funct. Mater.*, vol. 24, no. 22, pp. 3299–3304, Jun. 2014.
- [308] H. Y. Y. Nyein, W. Gao, Z. Shahpar, S. Emaminejad, S. Challa, K. Chen, H. M. Fahad, L.-C. Tai, H. Ota, R. W. Davis, and A. Javey, “A wearable electrochemical platform for noninvasive simultaneous monitoring of  $\text{Ca}^{2+}$  and pH,” *ACS Nano*, vol. 10, no. 7, pp. 7216–7224, Jul. 2016.
- [309] W. Gao, S. Emaminejad, H. Y. Y. Nyein, S. Challa, K. Chen, A. Peck, H. M. Fahad, H. Ota, H. Shiraki, D. Kiriya, D.-H. Lien, G. A. Brooks, R. W. Davis, and A. Javey, “Fully integrated wearable sensor arrays for multiplexed in situ perspiration analysis,” *Nature*, vol. 529, no. 7587, pp. 509–514, Jan. 2016.
- [310] Z. Xu, Q. Dong, B. Otieno, Y. Liu, I. Williams, D. Cai, Y. Li, Y. Lei, and B. Li, “Real-time in situ sensing of multiple water quality related parameters using micro-electrode array (MEA) fabricated by inkjet-printing technology (IPT),” *Sensor. Actuat. B Chem.*, vol. 237, pp. 1108–1119, Dec. 2016.
- [311] S. Mross, T. Zimmermann, N. Winkin, M. Kraft, and H. Vogt, “Integrated multi-sensor system for parallel in-situ monitoring of cell nutrients, metabolites, cell density and pH in biotechnological processes,” *Sensor. Actuat. B Chem.*, vol. 236, pp. 937–946, Nov. 2016.
- [312] D. Kirsanov, A. Korepanov, D. Dorovenko, E. Legin, and A. Legin, “Indirect monitoring of protein A biosynthesis in *E. coli* using potentiometric multisensor system,” *Sensor. Actuat. B Chem.*, vol. 238, pp. 1159–1164, Jan. 2017.
- [313] S. Pan, M. J. Deen, and R. Ghosh, “Low-cost graphite-based free chlorine sensor,” *Anal. Chem.*, vol. 87, no. 21, pp. 10734–10737, Nov. 2015.
- [314] T. Guo, “An optical system towards in-line monitoring of bacteria in drinking water,” McMaster University, 2016.
- [315] T. Guo, Y. Wei, C. Xu, B. R. Watts, Z. Zhang, Q. Fang, H. Zhang, P. R. Selvaganapathy, and M. J. Deen, “Counting of *Escherichia coli* by a microflow cytometer based on a photonic-microfluidic integrated device,” *Electrophoresis*, vol. 36, no. 2, pp. 298–304, Jan. 2015.
- [316] Z. Li, M. J. Deen, S. Kumar, and P. R. Selvaganapathy, “Raman spectroscopy for in-line water quality monitoring - instrumentation and potential,” *Sensors*, vol. 14, no. 9, pp. 17275–1730, Sep. 2014.
- [317] Z. Li and M. J. Deen, “Towards a portable Raman spectrometer using a concave grating and a time-gated CMOS SPAD,” *Opt. Express*, vol. 22, no. 15, p. 18736, Jul. 2014.
- [318] Z. Li, M. J. Deen, Q. Fang, and P. R. Selvaganapathy, “Design of a flat field concave-grating-based micro-Raman spectrometer for environmental applications,” *Appl. Opt.*, vol. 51, no. 28, p. 6855, Oct. 2012.
- [319] M. Khalil, S. Wang, J. Yu, R. L. Lee, and N. Liu, “Electrodeposition of iridium oxide nanoparticles for pH sensing electrodes,” *J. Electrochem. Soc.*, vol. 163, no. 9, pp. B485–B490, Jun. 2016.
- [320] J. Yang, T. J. Kwak, X. Zhang, R. McClain, W.-J. Chang, and S. Gunasekaran, “Digital pH test strips for in-field pH monitoring using iridium oxide-reduced graphene oxide hybrid thin films,” *ACS Sensors*, vol. 1, no. 10, pp. 1235–1243, Oct. 2016.
- [321] T. Alizadeh and F. Jamshidi, “Synthesis of nanosized sulfate-modified  $\alpha\text{-Fe}_2\text{O}_3$  and its use for the fabrication of all-solid-state carbon paste pH sensor,” *J. Solid State Electrochem.*, vol. 19, no. 4, pp. 1053–1062, Apr. 2015.
- [322] K. Xu, X. Zhang, K. Hou, M. Geng, and L. Zhao, “The effects of antimony thin film thickness on antimony pH electrode coated with Nafion membrane,” *J. Electrochem. Soc.*, vol. 163, no. 8, pp. B417–B421, May 2016.
- [323] T. Hashimoto, M. Miwa, H. Nasu, A. Ishihara, and Y. Nishio, “pH Sensors using 3D-block metal oxide-coated stainless steel electrodes,” *Electrochim. Acta*, vol. 220, pp. 699–704, Dec. 2016.

- [324] P. Salazar, F. J. Garcia-Garcia, F. Yubero, J. Gil-Rostra, and A. R. González-Elipe, "Characterization and application of a new pH sensor based on magnetron sputtered porous WO<sub>3</sub> thin films deposited at oblique angles," *Electrochim. Acta*, vol. 193, pp. 24–31, Mar. 2016.
- [325] N. C. S. Vieira, W. Avansi, A. Figueiredo, V. R. Mastelaro, and V. Zucolotto, "Potentiometric detection of chemical species by spin-assisted assembly of vanadium pentoxide nanorods," *Sensor. Actuat. B Chem.*, vol. 229, pp. 461–465, Jun. 2016.
- [326] W. Lonsdale, D. K. Maurya, M. Wajrak, and K. Alameh, "Effect of ordered mesoporous carbon contact layer on the sensing performance of sputtered RuO<sub>2</sub> thin film pH sensor," *Talanta*, vol. 164, pp. 52–56, Mar. 2017.
- [327] M. Liu, Y. Ma, L. Su, K.-C. Chou, and X. Hou, "A titanium nitride nanotube array for potentiometric sensing of pH," *Analyst*, vol. 141, no. 5, pp. 1693–1699, 2016.
- [328] D. Sharp, "Printed composite electrodes for in-situ wound pH monitoring," *Biosens. Bioelectron.*, vol. 50, pp. 399–405, Dec. 2013.
- [329] E. L. Silva, A. C. Bastos, M. A. Neto, R. F. Silva, M. G. S. Ferreira, M. L. Zheludkevich, and F. J. Oliveira, "Novel diamond microelectrode for pH sensing," *Electrochem. commun.*, vol. 40, pp. 31–34, Mar. 2014.
- [330] A. Määttänen, U. Vanamo, P. Ihalainen, P. Pulkkinen, H. Tenhu, J. Bobacka, and J. Peltonen, "A low-cost paper-based inkjet-printed platform for electrochemical analyses," *Sensor. Actuat. B Chem.*, vol. 177, pp. 153–162, Feb. 2013.
- [331] J. H. Yoon, S. B. Hong, S.-O. Yun, S. J. Lee, T. J. Lee, K. G. Lee, and B. G. Choi, "High performance flexible pH sensor based on polyaniline nanopillar array electrode," *J. Colloid Interface Sci.*, vol. 490, pp. 53–58, Mar. 2017.
- [332] M. Kaempgen and S. Roth, "Transparent and flexible carbon nanotube/polyaniline pH sensors," *J. Electroanal. Chem.*, vol. 586, no. 1, pp. 72–76, Jan. 2006.
- [333] P. C. Pandey and G. Singh, "Tetraphenylborate doped polyaniline based novel pH sensor and solid-state urea biosensor," *Talanta*, vol. 55, no. 4, pp. 773–782, Oct. 2001.
- [334] Q. Li, H. Li, J. Zhang, and Z. Xu, "A novel pH potentiometric sensor based on electrochemically synthesized polybisphenol A films at an ITO electrode," *Sensor. Actuat. B Chem.*, vol. 155, no. 2, pp. 730–736, Jul. 2011.
- [335] H. Xu, Y. Pan, Y. Wang, G. Li, Y. Chen, and Y. Ye, "An all-solid-state screen-printed carbon paste reference electrode based on poly(3,4-ethylenedioxythiophene) as solid contact transducer," *Meas. Sci. Technol.*, vol. 23, no. 12, p. 125101, Dec. 2012.
- [336] J. Hao, T. Xiao, F. Wu, P. Yu, and L. Mao, "High antifouling property of ion-selective membrane: Toward in vivo monitoring of pH change in live brain of rats with membrane-coated carbon fiber electrodes," *Anal. Chem.*, vol. 88, no. 22, pp. 11238–11243, Nov. 2016.
- [337] B. Shapira, E. Avraham, and D. Aurbach, "Proton-selective electrode for pH sensing," *Electrochem. commun.*, vol. 73, pp. 80–84, Dec. 2016.
- [338] M. Amiri, E. Amali, A. Nematollahzadeh, and H. Salehniya, "Poly-dopamine films: Voltammetric sensor for pH monitoring," *Sensor. Actuat. B Chem.*, vol. 228, pp. 53–58, Jun. 2016.
- [339] J. Zhou, L. Zhang, and Y. Tian, "Micro electrochemical pH sensor applicable for real-time ratiometric monitoring of pH values in rat brains," *Anal. Chem.*, vol. 88, no. 4, pp. 2113–2118, Feb. 2016.
- [340] F. Zhao, L. Zhang, A. Zhu, G. Shi, and Y. Tian, "In vivo monitoring of local pH values in a live rat brain based on the design of a specific electroactive molecule for H<sup>+</sup>," *Chem. Commun.*, vol. 52, no. 18, pp. 3717–3720, 2016.
- [341] M.-B. Gholivand and A. Akbari, "A novel voltammetric sensor for citalopram based on multiwall carbon nanotube/(poly(p-aminobenzene sulfonic acid)/β-cyclodextrin)," *Mater. Sci. Eng. C*, vol. 62, pp. 480–488, May 2016.
- [342] W. Su, J. Xu, and X. Ding, "An electrochemical pH sensor based on the amino-functionalized graphene and polyaniline composite film," *IEEE Trans. Nanobioscience*, pp. 1–1, 2016.

- [343] P. Kumar, S. Maikap, J.-T. Qiu, S. Jana, A. Roy, K. Singh, H.-M. Cheng, M.-T. Chang, R. Mahapatra, H.-C. Chiu, and J.-R. Yang, "Detection of pH and enzyme-free H<sub>2</sub>O<sub>2</sub> sensing mechanism by using GdOx membrane in electrolyte-insulator-semiconductor structure," *Nanoscale Res. Lett.*, vol. 11, no. 1, p. 434, Dec. 2016.
- [344] T.-M. Pan, C.-W. Wang, C.-Y. Chen, and J.-L. Her, "Impact of yttrium content and thermal annealing on the structural and sensing characteristics of YbY<sub>x</sub>O<sub>y</sub> sensing membranes," *J. Appl. Phys.*, vol. 119, no. 7, p. 74503, 2016.
- [345] T.-M. Pan and C.-Y. Tan, "Influence of praseodymium content and postdeposition annealing on the structural and sensing characteristics of PrTixOy sensing films using the sol-gel spin-coating method," *J. Mater. Chem. C*, vol. 4, pp. 7436–7442, 2016.
- [346] C.-M. Yang, T.-W. Chiang, Y.-T. Yeh, A. Das, Y.-T. Lin, and T.-C. Chen, "Sensing and pH-imaging properties of niobium oxide prepared by rapid thermal annealing for electrolyte-insulator-semiconductor structure and light-addressable potentiometric sensor," *Sensor. Actuat. B Chem.*, vol. 207, pp. 858–864, Feb. 2015.
- [347] N. Hong, C. Park, D. Kim, K.-S. Jeong, J.-S. Yoon, B. Jin, M. Meyyappan, and J.-S. Lee, "Buffer effects of two functional groups against pH variation at aminosilanized electrolyte-oxide-semiconductor (EOS) capacitor," *Sensor. Actuat. B Chem.*, vol. 242, pp. 324–331, Apr. 2017.
- [348] L. Wang, Y. Bu, and J.-P. Ao, "Effect of oxygen plasma treatment on the performance of AlGa<sub>N</sub>/Ga<sub>N</sub> ion-sensitive field-effect transistors," *Diam. Relat. Mater.*, vol. 73, pp. 1–6, Mar. 2017.
- [349] H.-Y. Liu, W.-C. Hsu, W.-F. Chen, C.-W. Lin, Y.-Y. Li, C.-S. Lee, W.-C. Sun, S.-Y. Wei, and S.-M. Yu, "Investigation of AlGa<sub>N</sub>/Ga<sub>N</sub> ion-sensitive heterostructure field-effect transistors-based pH sensors with Al<sub>2</sub>O<sub>3</sub> surface passivation and sensing membrane," *IEEE Sens. J.*, vol. 16, no. 10, pp. 3514–3522, May 2016.
- [350] T.-H. Yoo, B.-I. Sang, B.-Y. Wang, D.-S. Lim, H. W. Kang, W. K. Choi, Y. T. Lee, Y.-J. Oh, and D. K. Hwang, "Metal-oxide thin-film transistor-based pH sensor with a silver nanowire top gate electrode," *J. Korean Phys. Soc.*, vol. 68, no. 7, pp. 901–907, Apr. 2016.
- [351] C.-C. Chen, H.-I. Chen, H.-Y. Liu, P.-C. Chou, J.-K. Liou, and W.-C. Liu, "On a Ga<sub>N</sub>-based ion sensitive field-effect transistor (ISFET) with a hydrogen peroxide surface treatment," *Sensor. Actuat. B Chem.*, vol. 209, pp. 658–663, Mar. 2015.
- [352] S. Rigante, P. Scarbolo, M. Wipf, R. L. Stoop, K. Bedner, E. Buitrago, A. Bazigos, D. Bouvet, M. Calame, C. Schönenberger, and A. M. Ionescu, "Sensing with advanced computing technology: Fin field-effect transistors with high-k gate stack on bulk silicon," *ACS Nano*, vol. 9, no. 5, pp. 4872–4881, May 2015.
- [353] S. K. Ameri, P. K. Singh, and S. R. Sonkusale, "Three dimensional graphene transistor for ultra-sensitive pH sensing directly in biological media," *Anal. Chim. Acta*, vol. 934, pp. 212–217, Aug. 2016.
- [354] C.-H. Lu, T.-H. Hou, and T.-M. Pan, "Low-voltage InGaZnO ion-sensitive thin-film transistors fabricated by low-temperature process," *IEEE Trans. Electron Devices*, vol. 63, no. 12, pp. 5060–5063, Dec. 2016.
- [355] H. Yuan, J. Zhang, C. Cao, G. Zhang, and S. Zhang, "Novel H<sup>+</sup> ion sensor based on a gated lateral BJT pair," *Sensors*, vol. 16, no. 1, p. 14, Dec. 2015.
- [356] J.-K. Park, H.-J. Jang, J.-T. Park, and W.-J. Cho, "SOI dual-gate ISFET with variable oxide capacitance and channel thickness," *Solid. State. Electron.*, vol. 97, pp. 2–7, Jul. 2014.
- [357] N. Liu, Y. Hui Liu, P. Feng, L. Qiang Zhu, Y. Shi, and Q. Wan, "Enhancing the pH sensitivity by laterally synergic modulation in dual-gate electric-double-layer transistors," *Appl. Phys. Lett.*, vol. 106, no. 7, p. 73507, Feb. 2015.
- [358] E. Accastelli, P. Scarbolo, T. Ernst, P. Palestri, L. Selmi, and C. Guiducci, "Multi-wire tri-gate silicon nanowires reaching milli-pH unit resolution in one micron square footprint," *Biosensors*, vol. 6, no. 1, p. 9, 2016.

- [359] D. Rani, V. Pachauri, A. Mueller, X. T. Vu, T. C. Nguyen, and S. Ingebrandt, "On the use of scalable nanoISFET arrays of silicon with highly reproducible sensor performance for biosensor applications," *ACS Omega*, vol. 1, no. 1, pp. 84–92, Jul. 2016.
- [360] S. Kim, D. W. Kwon, R. Lee, D. H. Kim, and B.-G. Park, "Investigation of drift effect on silicon nanowire field effect transistor based pH sensor," *Jpn. J. Appl. Phys.*, vol. 55, no. 6S1, p. 06GG01, Jun. 2016.
- [361] T. N. Lee, H. J. H. Chen, and K. C. Hsieh, "Study on sensing properties of ion-sensitive field-effect-transistors fabricated with stack sensing membranes," *IEEE Electron Device Lett.*, vol. 37, no. 12, pp. 1642–1645, Dec. 2016.
- [362] K. Takechi, S. Iwamatsu, T. Yahagi, Y. Abe, S. Kobayashi, and H. Tanabe, "Bottom-gate amorphous InGaZnO<sub>4</sub> thin-film transistor pH sensors utilizing top-gate effects," *Jpn. J. Appl. Phys.*, vol. 53, no. 7, p. 76702, Jul. 2014.
- [363] T.-M. Pan, C.-H. Cheng, and C.-D. Lee, "Yb<sub>2</sub>O<sub>3</sub> thin films as a sensing membrane for pH-ISFET application," *J. Electrochem. Soc.*, vol. 156, no. 5, pp. J108–J111, 2009.
- [364] T. Ji, P. Rai, S. Jung, and V. K. Varadan, "In vitro evaluation of flexible pH and potassium ion-sensitive organic field effect transistor sensors," *Appl. Phys. Lett.*, vol. 92, no. 23, p. 233304, Jun. 2008.
- [365] I.-K. Lee, K. H. Lee, S. Lee, and W.-J. Cho, "Microwave annealing effect for highly reliable biosensor: Dual-gate ion-sensitive field-effect transistor using amorphous InGaZnO thin-film transistor," *ACS Appl. Mater. Interfaces*, vol. 6, no. 24, pp. 22680–22686, Dec. 2014.
- [366] N. Al-Hardan, M. Abdul Hamid, N. Ahmed, A. Jalar, R. Shamsudin, N. Othman, L. Kar Keng, W. Chiu, and H. Al-Rawi, "High sensitivity pH sensor based on porous silicon (PSi) extended gate field-effect transistor," *Sensors*, vol. 16, no. 6, p. 839, Jun. 2016.
- [367] F. A. Sabah, N. M. Ahmed, Z. Hassan, M. A. Almessiere, and N. H. Al-Hardan, "Sensitivity of CuS membrane pH sensor with and without MOSFET," *JOM*, Nov. 2016.
- [368] J.-L. Chiang, J.-F. Hsu, S.-F. Lee, L.-Y. Lee, and H.-Y. Liu, "Ion sensitivity of the flowerlike ZnO nanorods synthesized by the hydrothermal process," *J. Vac. Sci. Technol. B Microelectron. Nanom. Struct.*, vol. 27, no. 3, pp. 1462–1465, 2009.
- [369] Y.-R. Li, S. Chang, C.-T. Chang, W.-L. Tsai, Y.-K. Chiu, P.-Y. Yang, and H.-C. Cheng, "High-sensitivity extended-gate field-effect transistors as pH sensors with oxygen-modified reduced graphene oxide films coated on different reverse-pyramid silicon structures as sensing heads," *Jpn. J. Appl. Phys.*, vol. 55, no. 4S, p. 04EM08, Apr. 2016.
- [370] H. J. N. P. D. Mello and M. Mulato, "Well-established materials in microelectronic devices systems for differential-mode extended-gate field effect transistor chemical sensors," *Microelectron. Eng.*, vol. 160, pp. 73–80, Jul. 2016.
- [371] A. Caboni, E. Orgiu, E. Scavetta, M. Barbaro, and A. Bonfiglio, "Organic-based sensor for chemical detection in aqueous solution," *Appl. Phys. Lett.*, vol. 95, no. 12, p. 123304, Sep. 2009.
- [372] L. Liu, J. Shao, X. Li, Q. Zhao, B. Nie, C. Xu, and H. Ding, "High performance flexible pH sensor based on carboxyl-functionalized and DEP aligned SWNTs," *Appl. Surf. Sci.*, vol. 386, pp. 405–411, Nov. 2016.
- [373] D. Jung, M.-E. Han, and G. S. Lee, "pH-sensing characteristics of multi-walled carbon nanotube sheet," *Mater. Lett.*, vol. 116, pp. 57–60, Feb. 2014.
- [374] G. Scheiblin, R. Coppard, R. M. Owens, P. Mailley, and G. G. Malliaras, "Referenceless pH sensor using organic electrochemical transistors," *Adv. Mater. Technol.*, p. 1600141, Nov. 2016.
- [375] Y. Zhang, J. Clausmeyer, B. Babakinejad, A. López Córdoba, T. Ali, A. Shevchuk, Y. Takahashi, P. Novak, C. Edwards, M. Lab, S. Gopal, C. Chiappini, U. Anand, L. Magnani, R. C. Coombes, J. Gorelik, T. Matsue, W. Schuhmann, D. Klenerman, E. V. Sviderskaya, and Y. Korchev, "Spearhead nanometric field-effect transistor sensors for single-cell analysis," *ACS Nano*, vol. 10, no. 3, pp. 3214–3221, Mar. 2016.

- [376] T. Ikuta, T. Oe, Y. Ohno, K. Maehashi, K. Inoue, and K. Matsumoto, "Graphene device array using transfer-free patterned growth on insulator for an electrolyte-gated sensor," *Thin Solid Films*, vol. 612, pp. 87–90, Aug. 2016.
- [377] K. Melzer, V. D. Bhatt, E. Jaworska, R. Mittermeier, K. Maksymiuk, A. Michalska, and P. Lugli, "Enzyme assays using sensor arrays based on ion-selective carbon nanotube field-effect transistors," *Biosens. Bioelectron.*, vol. 84, pp. 7–14, Oct. 2016.
- [378] C. Reiner-Rozman, M. Larisika, C. Nowak, and W. Knoll, "Graphene-based liquid-gated field effect transistor for biosensing: Theory and experiments," *Biosens. Bioelectron.*, vol. 70, pp. 21–27, Aug. 2015.
- [379] Y. Shintani, S. Ibori, K. Igarashi, T. Naramura, M. Inaba, and H. Kawarada, "Polycrystalline boron-doped diamond with an oxygen-terminated surface channel as an electrolyte-solution-gate field-effect transistor for pH sensing," *Electrochim. Acta*, vol. 212, pp. 10–15, Sep. 2016.
- [380] E. Piccinini, C. Bliem, C. Reiner-Rozman, F. Battaglini, O. Azzaroni, and W. Knoll, "Enzyme-polyelectrolyte multilayer assemblies on reduced graphene oxide field-effect transistors for biosensing applications," *Biosens. Bioelectron.*, Oct. 2016.
- [381] F. Buth, D. Kumar, M. Stutzmann, and J. A. Garrido, "Electrolyte-gated organic field-effect transistors for sensing applications," *Appl. Phys. Lett.*, vol. 98, no. 15, p. 153302, Apr. 2011.
- [382] M. Hajmirzaheydarali, M. Sadeghipari, M. Akbari, A. Shahsafi, and S. Mohajerzadeh, "Nanotextured high sensitivity ion sensitive field effect transistors," *J. Appl. Phys.*, vol. 119, no. 5, p. 54303, Feb. 2016.
- [383] L.-C. Yen, T.-M. Pan, C.-H. Lee, and T.-S. Chao, "Label-free and real-time detection of ferritin using a horn-like polycrystalline-silicon nanowire field-effect transistor biosensor," *Sensor. Actuat. B Chem.*, vol. 230, pp. 398–404, Jul. 2016.
- [384] J. Seo, M. Song, J. Jeong, S. Nam, I. Heo, S.-Y. Park, I.-K. Kang, J.-H. Lee, H. Kim, and Y. Kim, "Broadband pH-sensing organic transistors with polymeric sensing layers featuring liquid crystal microdomains encapsulated by di-block copolymer chains," *ACS Appl. Mater. Interfaces*, vol. 8, no. 36, pp. 23862–23867, Sep. 2016.
- [385] H. Shekhar, V. Chathapuram, S. H. Hyun, S. Hong, and H. J. Cho, "A disposable microsensor for continuous monitoring of free chlorine in water," in *Sensors, 2003. Proceedings of IEEE, 2003*, vol. 1, pp. 67–70.
- [386] D. R. Kumar, S. Kesavan, T. T. Nguyen, J. Hwang, C. Lamiel, and J.-J. Shim, "Polydopamine@electrochemically reduced graphene oxide-modified electrode for electrochemical detection of free-chlorine," *Sensor. Actuat. B Chem.*, vol. 240, pp. 818–828, Mar. 2017.
- [387] M. Jović, F. Cortés-Salazar, A. Lesch, V. Amstutz, H. Bi, and H. H. Girault, "Electrochemical detection of free chlorine at inkjet printed silver electrodes," *J. Electroanal. Chem.*, vol. 756, pp. 171–178, Nov. 2015.

# Appendix A

## Comparison table of microfabricated electrochemical pH sensors

**Table A-1.** Summary of microfabricated electrochemical pH sensors.

Structure	Sensing material	Operation voltage, V	Detection range, pH	Sensitivity	Response time, s	Stability	Fabrication of sensing materials	Ref.
Potentiometric	CuO	-	2-11	28 mV/pH	25	Drift=150 mV/h	Hydrothermal deposition	[75]
	IrO <sub>x</sub>	-	2-10	74 mV/pH	<100	Sensitivity drops to 65 mV/pH in 14 days	Electrochemical deposition of IrO <sub>x</sub> in anodized Al <sub>2</sub> O <sub>3</sub>	[72]
	IrO <sub>x</sub>	-	2.38-11.61	69 mV/pH	<2	Potential variation<10 mV	Electrochemical deposition, annealing at >300 °C	[70]
	IrO <sub>x</sub>	-	4-9	70 mV/pH	-	-	Electrochemical deposition	[71]
	IrO <sub>x</sub>	-	2-12	73 mV/pH	-	-	Electrochemical deposition	[319]
	IrO <sub>2</sub>	-	1.56-12	74 mV/pH	-	Stable>7 days	Electrochemical deposition	[179]
	IrO <sub>2</sub>	-	1-13	59 mV/pH	<1	Drift<0.1 mV/day	Thermal oxidation at 870 °C	[69]
	IrO <sub>2</sub> +PMMA	-	3-11	60 mV/pH	<2	Stable>1 month	Hydrolysis of (NH <sub>4</sub> ) <sub>2</sub> IrCl <sub>6</sub> for IrO <sub>2</sub> , thermal molding with PMMA at 150 °C	[74]
	IrO <sub>2</sub> +reduced graphene oxide	-	2-12	62 mV/pH	<120	Hysteresis=8.2 mV, sensitivity drops to 52 mV/pH in 2 weeks	Electrochemical deposition of IrO <sub>2</sub> , electrochemical reduction/deposition of reduced graphene oxide	[320]
	Ta <sub>2</sub> O <sub>5</sub> -IrO <sub>2</sub> bilayer	-	2-13	60 mV/pH	15	Drift<0.1 mV/h	RF sputtering	[73]
	S-modified- $\alpha$ -Fe <sub>2</sub> O <sub>3</sub>	-	1.5-12.5	59 mV/pH	10	Stable<1 week	Hydrothermal synthesis, annealing at 600 °C	[321]
	Sb	-	4-9.2	63 mV/pH	<22	Voltage variation <2 mV in 10 min, stable for 28 days	Sputtering of Sb, drop casting of Nafion on Sb	[322]
	Co <sub>3</sub> O <sub>4</sub>	-	3-13	58 mV/pH	53	Stable for 3 days	Hydrothermal deposition, annealing at 450 °C	[76]
	Co <sub>3</sub> O <sub>4</sub>	-	4-9	59 mV/pH	9	-	Sol-gel dip coating, annealing at 500 °C	[323]
	WO <sub>3</sub>	-	5-9	57 mV/pH	25	11.6% sensitivity drop in 3 tests	Hydrothermal deposition	[77]
	WO <sub>3</sub>	-	2-12	55 mV/pH	-	Drift=6 mV/h; hysteresis=50 mV	RF sputtering and O <sub>2</sub> plasma oxidation	[167]
	WO <sub>3</sub>	-	1-12	59 mV/pH	100	Drift=2.5 mV/h; hysteresis<10.5 mV; stable>3 month	Reactive sputtering of WO <sub>3</sub> at oblique angles on Au	[324]
	V <sub>2</sub> O <sub>5</sub> + poly(allylamine hydrochloride)	-	2-12	61 mV/pH	-	Drift=13 mV/min; stable for 5 days	Hydrothermal synthesis of V <sub>2</sub> O <sub>5</sub> at 200 °C, spin coating of poly(allylamine hydrochloride) and V <sub>2</sub> O <sub>5</sub> solutions	[325]
	RuO <sub>2</sub>	-	4-10	69 mV/pH	10	Potential variation=9 mV	RF sputtering	[78]
RuO <sub>2</sub>	-	4-10	58 mV/pH	30	Drift=5 mV/h; hysteresis=1.1 mV	RF sputtering	[326]	

Structure	Sensing material	Operation voltage, V	Detection range, pH	Sensitivity	Response time, s	Stability	Fabrication of sensing materials	Ref.
	TiO <sub>2</sub>	-	2-12	59 mV/pH	<30	-	Anodization, annealing at 450 °C	[168]
	TiN	-	2-11	55 mV/pH	4.4	Stable for 200 s	Ti anodization, annealing at 450 °C, reduction and nitridation at 900 °C	[327]
	PdO	-	2-12	65 mV/pH	<18	Hysteresis=7.8 mV; stable>60 days	Spin coating, annealing at 200 °C	[80]
	PdO	-	4-10	57 mV/pH	6	Drift=0.6 mV/h; hysteresis=5.3 mV; stable>70 days	Inkjet printing, annealing at 200 °C	[81]
	ZnO	-	4-11	52 mV/pH	-	-	Hydrothermal deposition	[169]
	PbO <sub>x</sub>	-	0.25-13	84 mV/pH	-	-	Electrochemical deposition/oxidation	[79]
	Uric acid composite	-	4-10	73 mV/pH	-	-	Electrochemical deposition	[328]
	Diamond	-	2-12	51 mV/pH	<1	-	Hot filament CVD	[329]
	PANI	-	2-9	62 mV/pH	-	-	Electropolymerisation	[84]
	PANI	-	3-7	54 mV/pH	<25	Stable for 30 min	Electropolymerisation	[87]
	PANI	-	2.69-8.51	59 mV/pH	<20	Stable>35 days	Electropolymerisation	[86]
	PANI	-	2-10	71 mV/pH	-	Stable for 5 weeks	Electropolymerisation	[330]
	PANI	-	3-8	63 mV/pH	20	Drift=0.07 mV/h; hysteresis: 1% deviation in 2 tests	Electropolymerisation	[308]
	PANI	-	2-12	60 mV/pH	<1	Drift=0.49 mV/h; hysteresis=9.2 mV	Soft lithography, electropolymerisation	[331]
	PANI+CNT	-	1-13	58 mV/pH	<40	Drift=2-10 mV/h	Spray of CNT suspension, electrochemical deposition of PANI	[332]
	PANI doped with tetraphenylborate	-	3-9	86 mV/pH	-	-	Electropolymerisation	[333]
	Parylene C	-	4-10	16 mV/pH	-	Drift=3-20 mV/h	CVD + O <sub>2</sub> plasma etching	[89]
	PEI	-	2-11	46 mV/pH	15	Sensitivity drops at 0.65 mV/pH/day	Electropolymerisation	[85]
	Polybisphenol A	-	-1-15	57 mV/pH	<20	Stable>12 days	Electropolymerisation	[334]
	PEDOT:PSS	-	5.9-8.7	52 mV/pH	15	3.2 mV/pH sensitivity variation in 50 days	Electropolymerisation	[335]
	PPY	-	2-11	51 mV/pH	120	Stable for 30 days	Electropolymerisation	[83]
	PPY:hydroquinone monosulfonate	-	2-12	51 mV/pH	<100	Stable for 30 days	Electropolymerisation	[88]
	PVC:H <sup>+</sup> ionophore tridodecylamine, on carbon fiber	-	6-8	58 mV/pH	<1	-	Dip coating	[336]
	CNT	-	3-11	60 mV/pH	<30	-	CNT deposited from solution	[90]
	SWCNT-COOH	-	3-11	48 mV/pH	7	Hysteresis=7.8 mV; stable>14 days	Inkjet printing, annealing at 160 °C	[91]
	Porous carbon	-	1.68-10	57 mV/pH	-	-	Pyrolysis of filter paper at 600 °C, chemical activation in 70% nitric acid	[337]
Voltammetric	Polydopamine	1.2	1-12	58 mV/pH	-	-	Electropolymerisation	[338]
	1,2-naphthoquinone	1	5.8-8	58 mV/pH	-	Stable for 1000 voltage cycles	Self-assembly	[339]
	N-(6-aminopyridin-2-yl)ferrocene	0.6	5.9-8	50 mV/pH	-	Stable for 7 days	Electrochemical deposition of Au, surface modification	[340]
	MWCNT/poly(p-aminobenzene sulfonic acid)/β-cyclodextrin	1.1	7.4-11	68 mV/pH	-	-	Drop casting of MWCNT, electrochemical polymer deposition	[341]

Structure	Sensing material	Operation voltage, V	Detection range, pH	Sensitivity	Response time, s	Stability	Fabrication of sensing materials	Ref.
	NH <sub>2</sub> -graphene/PANI	1.5	1-11	51 mV/pH	-	Sensitivity drops to 80% in 2 weeks	Electropolymerisation	[342]
EIS	Er <sub>2</sub> TiO <sub>5</sub>	3	2-12	57 mV/pH	-	Drift=0.29 mV/h	Reactive sputtering, RTA at 900 °C	[104]
	Gd <sub>2</sub> O <sub>3</sub>	2	2-10	55 mV/pH	-	Sensitivity drops by 0.65 mV/pH in 12 h	Reactive sputtering, RTA at 800 °C	[103]
	Gd <sub>2</sub> O <sub>3</sub>	2	2-10	54 mV/pH	-	Drift=2.12 mV/h	E-beam evaporation	[343]
	Gd <sub>2</sub> Ti <sub>2</sub> O <sub>7</sub>	3	2-12	58 mV/pH	-	Drift=0.38 mV/h	Reactive sputtering, RTA at 900 °C	[104]
	Lu <sub>2</sub> Ti <sub>2</sub> O <sub>7</sub>	3	2-12	59 mV/pH	-	Drift=0.55 mV/h	Reactive sputtering, RTA at 900 °C	[104]
	YbY <sub>x</sub> O <sub>y</sub>	1.5	2-12	63 mV/pH	-	Drift=0.14 mV/h; hysteresis=1 mV	Co-sputtering in O <sub>2</sub> , RTA at 800 °C	[344]
	PrTi <sub>x</sub> O <sub>y</sub>	2	2-12	68 mV/pH	-	Drift=0.25 mV/h; hysteresis=1 mV	Sol-gel spin coating, RTA at 800 °C	[345]
	Ta <sub>2</sub> O <sub>5</sub>	-	1-10	56 mV/pH	60	Drift=5 mV/h	Thermal oxidation at 525 °C	[100]
	Ta <sub>2</sub> O <sub>5</sub>	1.6	3-12	53 mV/pH	-	-	ALD	[311]
	TiO <sub>2</sub>	-	3-11	62 mV/pH	-	Drift=0.9 mV/day	MOCVD, annealing at 700 to 900 °C	[98]
	Nb <sub>2</sub> O <sub>5</sub>	2.5	2-12	60 mV/pH	-	Drift=3 mV/h	RF sputtering, RTA at 700 °C	[346]
	3-APTES on SiO <sub>2</sub>	1.15	2-11	56 mV/pH	-	-	Thermally grown of SiO <sub>2</sub> , surface treatment using APTES and O <sub>2</sub> plasma	[347]
	ISFET	InAs	0.9	4.7-7.8	48 mV/pH	-	-	Molecular beam epitaxy
AlGaN		4	4-9	56 mV/pH	-	-	CVD, annealing at 850 °C, O <sub>2</sub> plasma treatment	[348]
AlGaN/GaN		10	4-9	52 mV/pH	-	-	Dry etching, annealing at 850 °C	[105]
Al <sub>2</sub> O <sub>3</sub>		4	2-12	56 mV/pH	3-7	Drift=1.25 mV/h; hysteresis=4.3 mV; sensitivity drops at 0.12 mV/pH/day	Ultrasonic spray pyrolysis deposition	[349]
Al <sub>2</sub> O <sub>3</sub>		2	3-11	69 mV/pH	20	-	ALD	[350]
Ga <sub>x</sub> O <sub>y</sub>		1.5	2-12	55 mV/pH	-	Drift=1.41 μA/h; hysteresis=0.4 mV; sensitivity drops at 0.14 mV/pH/day	MOCVD, RTA at 900 °C, H <sub>2</sub> O <sub>2</sub> surface treatment	[351]
HfO <sub>2</sub>		8	3-10	57 mV/pH	120	Drift=0.1 mV/h; hysteresis=8 mV	E-beam lithography, thermal SiO <sub>2</sub> growth, ALD of HfO <sub>2</sub>	[352]
HfO <sub>2</sub>		1	3-9	71 mV/pH	-	-	ALD	[353]
HfO <sub>2</sub>		1	3-11	61 mV/pH	60	Drift=2.5 mV/h; hysteresis=8 mV	ALD	[354]
Si <sub>3</sub> N <sub>4</sub>		8	4-10	175 nA/pH	-	-	Standard CMOS process	[355]
SiO <sub>2</sub>		6	3-12	363 mV/pH	-	Drift=3 mV/h; hysteresis=13 mV	RF sputtering, RTA at 450 °C	[356]
SiO <sub>2</sub>		3	4-10	168 mV/pH	-	-	PECVD	[357]
SiO <sub>2</sub>		1.5	3-8	30 mV/pH	40	-	Standard CMOS process	[358]
SiO <sub>2</sub>		1	5-9	43 mV/pH	-	-	Nanoimprinting, dry etching, ion implantation, annealing at 810 °C, gas-phase silanization	[359]
3-APTES on SiO <sub>2</sub>		2	5-9	54 mV/pH	250	-	Standard CMOS process	[360]
3-APTES on SiO <sub>2</sub>		3	4-10	51 mV/pH	60	Drift=1.83 mV/h; hysteresis=4 mV	Thermal oxidation of Si at 925 °C, O <sub>2</sub> plasma treatment, RTA at 1000 °C, self-assembly of APTES	[361]

Structure	Sensing material	Operation voltage, V	Detection range, pH	Sensitivity	Response time, s	Stability	Fabrication of sensing materials	Ref.
	TiO <sub>2</sub>	4	1-13	57 mV/pH	-	-	RF sputtering, annealing at 500 °C	[97]
	Ta <sub>2</sub> O <sub>5</sub>	1.2	3-8	55 mV/pH	-	Drift=1 mV/week	ALD	[109]
	Ta <sub>2</sub> O <sub>5</sub>	12	3-8	120 mV/pH	-	-	RF sputtering, annealing at 300 °C	[362]
	Yb <sub>2</sub> O <sub>3</sub>	2	2-12	56 mV/pH	60	Drift=1.54 mV/h	Reactive sputtering, RTA at 800 °C	[363]
	ZnO	3	2-12	42mV/pH	-	Drift=1.78 mV/h	RF sputtering, annealing at >600 °C	[125]
	Graphene+Al <sub>2</sub> O <sub>3</sub>	60	3-10	37 mV/pH	200	Drift=6.34 mV/h	Rapid thermal CVD of graphene at 950 °C, low temperature transferring; spin coating of Al <sub>2</sub> O <sub>3</sub> , annealing at 250 °C	[108]
	P3HT+valinomycin membrane	1	3.4-5.6	3 nA/pH	360	-	P3HT spin coating, valinomycin membrane deposited by Langmuir-Blodgett technique	[113]
	P3HT+Ta <sub>2</sub> O <sub>5</sub> +valinomycin membrane	5	6.6-9.5	71 nA/pH	-	-	RF sputtering of Ta <sub>2</sub> O <sub>5</sub> , drop casting of valinomycin membrane, P3HT spin coating	[364]
	P3HT+arachidic acid	1	3.3-5.5	4 nA/pH	100	-	Spin coating of P3HT, arachidic acid deposited by Langmuir-Blodgett technique	[112]
	P3HT+hydrogen ionophore	0.6	3-12	25-52 mV/pH	-	Stable for 30 s	Drop casting	[111]
	Pentacene	100	4-10	30 nA/pH	>2000	-	Vacuum sublimation.	[110]
	Pentacene/PTAA+Al <sub>2</sub> O <sub>3</sub>	4	2-12	5 nA/pH	30	Stable>5000 cycles	Pentacene spin coating, ALD of Al <sub>2</sub> O <sub>3</sub>	[115]
	PTAA+poly(isobutyl methacrylate)+Teflon	40	2-10	60 mV/pH	-	-	PTAA spin coating, Teflon spin coating	[114]
ExGFET	Nb <sub>2</sub> O <sub>5</sub>	6	2-12	52 mV/pH	75	Drift=3.34 mV/h	RF sputtering, CF <sub>4</sub> plasma treatment, RTA at 600 °C	[125]
	TiO <sub>2</sub> :Ru	6	1-13	55 mV/pH	-	Drift=0.745 mV/h	RF sputtering of TiO <sub>2</sub> , sputtering of Ru, annealing at 600 °C	[118]
	TiO <sub>2</sub>	6	1-11	59 mV/pH	40	Drift=1.97 mV/h	Sol-gel spin coating, annealing at 600 °C	[120]
	TiO <sub>2</sub>	5	2-12	50 mV/pH	-	-	Hydrothermal deposition	[123]
	TiO <sub>2</sub>	5	2-12	62 mV/pH	-	-	Hydrothermal deposition	[122]
	TiO <sub>2</sub>	10	1-11	61 mV/pH	-	Drift=9-60 mV/h	Sol-gel spin coating, annealing < 500 °C	[119]
	TiO <sub>2</sub> -PPI bilayer	-	4-10	57 mV/pH	-	-	Layer-by-layer deposition of PPI and TiO <sub>2</sub> from solution	[121]
	In <sub>2</sub> O <sub>3</sub> -CNT bilayer	3	2-12	36 mV/pH	-	-	Sputtering of indium, spray coating of CNTs, annealing at 400 °C	[129]
	SnO <sub>2</sub>	40	3-10	287 mV/pH	-	Drift=48.77 mV/h	RF sputtering, microwave annealing at 1000 W (~87 °C)	[365]
	SnO <sub>2</sub> :F	5	2-12	50 mV/pH	-	-	Vacuum deposition	[127]
	Si	3	2-12	66 mV/pH	-	Hysteresis<11 mV	Si anodization	[366]
	CuS	3	2-12	24 mV/pH	<10	Hysteresis<13 mV	Spray pyrolysis	[367]
	PdO	2	2-12	63 mV/pH	-	Drift=2.3 mV/h; hysteresis=7.9 mV; stable for 6 tests	Reactive e-beam evaporation, annealing at 700 °C	[126]
	ZnO	6	2-12	38 mV/pH	-	-	Sol-gel brushing, annealing at 150 °C	[95]

Structure	Sensing material	Operation voltage, V	Detection range, pH	Sensitivity	Response time, s	Stability	Fabrication of sensing materials	Ref.
	ZnO	10	1-9	59 mV/pH	-	-	Hydrothermal deposition	[117]
	ZnO	6	5-9	18 mV/pH	-	-	Hydrothermal deposition	[368]
	ZnO	4	1-13	46 mV/pH	300	-	ALD	[124]
	CNT+Ni	3	2-10	59 mV/pH	9	-	Electrodeposition	[130]
	Reduced graphene oxide	4	1-13	58 mV/pH	<5	Drift=10.5 mV/min	Spray coating, annealing in N <sub>2</sub> at 300 °C, O <sub>2</sub> plasma treatment	[369]
	PANI	-	2-8	37 mV/pH	20	Drift=40 mV/h; hysteresis=5.3 mV	Electrodeposition	[370]
	Pentacene	100	2.5-7	5 V/pH	-	-	Vacuum sublimation	[371]
	Parylene C	1.5	4-10	23 mV/pH	<5	Drift=18 mV/h	CVD, O <sub>2</sub> plasma treatment	[131]
Chemoresistor	Pd	2	4-10	5% /pH	100	-	DC sputtering	[134]
	TiO <sub>2</sub>	1	2-12	6 nS/pH	-	Stable>60 s	Electrospinning and hydrothermal deposition	[133]
	Graphene	3	4-10	2000 Ω/pH	20	-	Mechanical exfoliation of bulk graphite, annealing at 200 °C	[132]
	CNT	-	5-9	65 Ω/pH	-	-	Vacuum filtration of aqueous solution	[135]
	SWCNT-COOH	0.2	5-9	28.5% /pH	<23	-	Drop casting, dielectrophoresis	[372]
	CNT+Ni	-	2-10	1% / pH	-	Stable>1 day	CNT: LPCVD at 780 °C; Ni: electrodeposition	[373]
ECT	IrO <sub>2</sub>	1	5-7.3	21 mV/pH	-	-	Electrochemical deposition	[374]
	P3HT	2	4-10	10 nA/pH	-	Stable for 12 h	Spin coating	[140]
	PPY	0.6	2.4-7.5	51 mV/pH	-	-	Laser pulling with nanopipettes, electropolymerisation	[375]
	PEDOT:PSS	0.4	-	64 mV/pH	10	-	Spin coating, annealing at 200 °C	[141]
	Graphene	0.15	4-8.6	20 mV/pH	-	Large drift	E-beam evaporation, annealing at 850 °C in Ar	[376]
	CNT+PAA	1	2-12	73 mS/pH	-	Stable>120 days	Electropolymerisation	[58]
EGFET	ZnO+Pd/Au	2	7-9	-	-	-	Hydrothermal deposition	[145]
	CNT	0.6	3-8	27 mV/pH	40	-	Spin coating	[148]
	CNT with PVC membrane	0.8	4.5-10.5	83 mV/pH	-	-	Spray coating of CNT, drop casting of PVC	[377]
	Graphene	2	2-12	100 mV/pH	-	-	High temperature growth (1100 °C)	[149]
	Graphene	0.4	4.3-9.4	22 mV/pH	-	-	CVD at 1000 °C, low temperature transferring, anneal at 500 °C	[147]
	Reduced graphene oxide	0.7	4-8	34 mV/pH	-	-	Graphene oxide prepared from Hummers method, spin coating, reducing with hydrazine at 70 °C	[378]
	Reduced graphene oxide	1.6	6-9	29 mV/pH	-	-	Self-assembly and reduction of graphene oxide, annealing at 200 °C	[146]
	Boron-doped diamond	0.6	2-12	31 mV/pH	-	10% sensitivity variation in 10 months	CVD at 850 °C, annealing at 450 °C, UV treatment	[379]
	P3HT	0.6	3-8	28 mV/pH	20	-	Spin coating	[148]
	Polyethylenimine	0.5	5-10	23 mV/pH	150	-	Layer-by-layer assembly	[380]
	α6T	0.8	2-7	-	-	Drift by 10% in 3 h	Thermal evaporation	[381]
FET	Si	0.8	4-10	68 mV/pH	-	Drift=27 mV/h	Deep-UV lithography, chemical-mechanical polishing, annealing at 1000 °C, wet etching	[155]
	Poly Si (native oxide)	5	4-10	410 mV/pH	-	-	LPCVD of poly Si, phosphorous diffusion at 850 °C, DRIE	[382]

Structure	Sensing material	Operation voltage, V	Detection range, pH	Sensitivity	Response time, s	Stability	Fabrication of sensing materials	Ref.
	TEOS-Si <sub>3</sub> N <sub>4</sub> -TEOS	15	4-10	113 mV/pH	-	-	LPCVD	[383]
	4-cyano-4'-pentyl-biphenyl/[poly(4-cyano-biphenyl-4-oxyundecylacrylate)-PAA	0.5	2-7	40 nA/pH	-	-	Spin coating	[384]
	DDFTTF	2	3-11	50 nA/pH	90	Stable>10 <sup>4</sup> tests	Thermal evaporation	[156]

# Appendix B

## Comparison table of microfabricated electrochemical free chlorine sensors

**Table A-2.** Summary of microfabricated electrochemical free chlorine sensors.

Sensor configuration	Sensor material	Sensing range, ppm	Sensitivity	Response time, s	Stability	Reusability	Fabrication	Ref.
Amperometric	Au	0.08-0.4	13.7 $\mu\text{A}/\text{cm}^2$ /ppm	-	>7 days	-	Photolithography, evaporation, lift-off	[35]
	Au	1.5-8	69.2 $\mu\text{A}/\text{cm}^2$ /ppm	20	-	-	Photolithography, evaporation, electrochemical deposition, etching	[385]
	Au	0.2-5	14.2 $\mu\text{A}/\text{cm}^2$ /ppm	120	>10 days	>6 times	Photolithography, evaporation, lift-off	[159]
	Pt	0.1-1.5	8.0 $\mu\text{A}$ /ppm <sup>a</sup>	-	>5 h	-	Photolithography, sputtering, lift-off	[160]
	Pt	4-400	-	-	-	-	Mechanical polishing, electrochemical activation	[34]
	Potassium iodide	0-20	2.1 $\mu\text{A}/\text{cm}^2$ /ppm	30	-	-	Screen printing, solution dispensing	[161]
	Polymelamine	0.4-521	4.0 $\mu\text{A}/\text{cm}^2$ /ppm	-	>7 days	-	Electro-polymerization	[16]
	Boron-doped diamond	0.1-100	0.74 $\mu\text{A}/\text{cm}^2$ /ppm	-	>90 days	>20 times	Microwave plasma-assisted CVD, anodization	[162]
	Benzethonium chloride modified Prussian Blue	0.009-10	12.3 $\mu\text{A}/\text{cm}^2$ /ppm	< 5	>3 weeks	>15 times	Electrochemical deposition	[163], [301]
	CuO NP /MWCNT	0.0006-0.008	16.1 $\mu\text{A}/\text{cm}^2$ /ppm	30	>7 days	-	Drop casting, mechanical polishing	[165]
	Ammonium carbamate modified graphite	1-6	0.3 $\mu\text{A}/\text{cm}^2$ /ppm	<3	>7 weeks	-	Electrochemical deposition	[313]
	Ammonium carbamate modified graphite	1-8	1.04 $\mu\text{A}/\text{cm}^2$ /ppm	30	>50 days	-	Electrochemical deposition	[298]
Linear sweep voltammetry	Polydopamine on reduced graphene oxide	0.52-11.3	1.91 $\mu\text{A}/\text{cm}^2$ /ppm	30	-	28 times	Electrochemical reduction, electropolymerization	[386]
	Ag	1-100	125 $\mu\text{A}/\text{cm}^2$ /ppm	200	-	3 times	Inkjet printing, sintering	[387]
Chemoresistor	Phenyl capped aniline tetramer modified SWCNT	0.06-60	91.5 nA/decade	<300	>30 h	>3 times	Photolithography, evaporation, etching, drop casting, chemical modification	[302]
	PEDOT:PSS	0.5-50 50-500	1.05/decade <sup>b</sup> 1.49/decade <sup>b</sup>	300 15	>30 days	>9 times >5 times	Hand drawing	[17]

<sup>a</sup> Data for electrode surface area was not given.

<sup>b</sup> The common logarithm of relative resistance changes.

## Appendix C

# Digital masks for integrated pH, free chlorine, and temperature sensors



**Figure A-1.** Digital mask for the inkjet printing pattern of rough Pd/PdO films for temperature sensors (2 cm in figure = 1 cm in real device).



**Figure A-2.** Digital mask for the inkjet printing pattern of smooth Pd/PdO films for pH sensors (2 cm in figure = 1 cm in real device).



**Figure A-3.** Digital mask for the inkjet printing pattern of SU-8 films (2 cm in figure = 1 cm in real device).

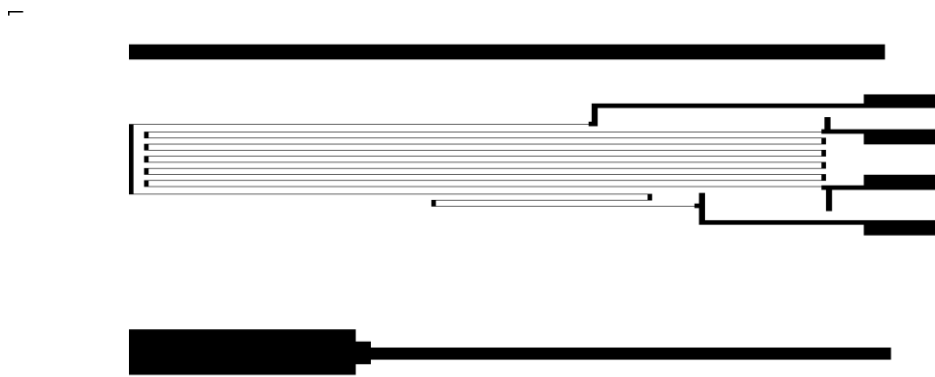


**Figure A-4.** Digital mask for the inkjet printing pattern of Ag films (2 cm in figure = 1 cm in real device).

# Appendix D

## Verilog/VHDL code for FPGA programming

### Hardware constrains

```

## To use it in a project:
## - uncomment the lines corresponding to used pins
## - rename the used ports (in each line, after get_ports) according to the top level signal names in the project

# Clock signal
set_property PACKAGE_PIN W5 [get_ports CLK100MHZ]
    set_property IOSTANDARD LVCMOS33 [get_ports CLK100MHZ]
        create_clock -add -name sys_clk_pin -period 10.00 -waveform {0 5} [get_ports CLK100MHZ]

# Switches
set_property PACKAGE_PIN V17 [get_ports {reset}]
    set_property IOSTANDARD LVCMOS33 [get_ports {reset}]
set_property PACKAGE_PIN V16 [get_ports {test_cal}]
    set_property IOSTANDARD LVCMOS33 [get_ports {test_cal}]
set_property PACKAGE_PIN W16 [get_ports {ph}]
    set_property IOSTANDARD LVCMOS33 [get_ports {ph}]
set_property PACKAGE_PIN W17 [get_ports {temperature}]
    set_property IOSTANDARD LVCMOS33 [get_ports {temperature}]
set_property PACKAGE_PIN W15 [get_ports {chlorine}]
    set_property IOSTANDARD LVCMOS33 [get_ports {chlorine}]
set_property PACKAGE_PIN V15 [get_ports {total_cl}]
    set_property IOSTANDARD LVCMOS33 [get_ports {total_cl}]
#set_property PACKAGE_PIN W14 [get_ports {sw[6]}]
    #set_property IOSTANDARD LVCMOS33 [get_ports {sw[6]}]
#set_property PACKAGE_PIN W13 [get_ports {ph7}]
    #set_property IOSTANDARD LVCMOS33 [get_ports {ph7}]
#set_property PACKAGE_PIN V2 [get_ports {sw[8]}]
    #set_property IOSTANDARD LVCMOS33 [get_ports {sw[8]}]
#set_property PACKAGE_PIN T3 [get_ports {sw[9]}]
    #set_property IOSTANDARD LVCMOS33 [get_ports {sw[9]}]
#set_property PACKAGE_PIN T2 [get_ports {sw[10]}]
    #set_property IOSTANDARD LVCMOS33 [get_ports {sw[10]}]
#set_property PACKAGE_PIN R3 [get_ports {sw[11]}]
    #set_property IOSTANDARD LVCMOS33 [get_ports {sw[11]}]
#set_property PACKAGE_PIN W2 [get_ports {sw[12]}]
    #set_property IOSTANDARD LVCMOS33 [get_ports {sw[12]}]
#set_property PACKAGE_PIN U1 [get_ports {sw[13]}]
    #set_property IOSTANDARD LVCMOS33 [get_ports {sw[13]}]
#set_property PACKAGE_PIN T1 [get_ports {sw[14]}]
    #set_property IOSTANDARD LVCMOS33 [get_ports {sw[14]}]
set_property PACKAGE_PIN R2 [get_ports {v_signal}]
    set_property IOSTANDARD LVCMOS33 [get_ports {v_signal}]

# LEDs
set_property PACKAGE_PIN U16 [get_ports {LED[0]}]
    set_property IOSTANDARD LVCMOS33 [get_ports {LED[0]}]
set_property PACKAGE_PIN E19 [get_ports {LED[1]}]
    set_property IOSTANDARD LVCMOS33 [get_ports {LED[1]}]
set_property PACKAGE_PIN U19 [get_ports {LED[2]}]
    set_property IOSTANDARD LVCMOS33 [get_ports {LED[2]}]
set_property PACKAGE_PIN V19 [get_ports {LED[3]}]
    set_property IOSTANDARD LVCMOS33 [get_ports {LED[3]}]

```

```

set_property PACKAGE_PIN W18 [get_ports {LED[4]]
    set_property IOSTANDARD LVCMOS33 [get_ports {LED[4]]}
set_property PACKAGE_PIN U15 [get_ports {LED[5]]}
    set_property IOSTANDARD LVCMOS33 [get_ports {LED[5]]}
set_property PACKAGE_PIN U14 [get_ports {LED[6]]}
    set_property IOSTANDARD LVCMOS33 [get_ports {LED[6]]}
set_property PACKAGE_PIN V14 [get_ports {LED[7]]}
    set_property IOSTANDARD LVCMOS33 [get_ports {LED[7]]}
set_property PACKAGE_PIN V13 [get_ports {LED[8]]}
    set_property IOSTANDARD LVCMOS33 [get_ports {LED[8]]}
set_property PACKAGE_PIN V3 [get_ports {LED[9]]}
    set_property IOSTANDARD LVCMOS33 [get_ports {LED[9]]}
set_property PACKAGE_PIN W3 [get_ports {LED[10]]}
    set_property IOSTANDARD LVCMOS33 [get_ports {LED[10]]}
set_property PACKAGE_PIN U3 [get_ports {LED[11]]}
    set_property IOSTANDARD LVCMOS33 [get_ports {LED[11]]}
set_property PACKAGE_PIN P3 [get_ports {LED[12]]}
    set_property IOSTANDARD LVCMOS33 [get_ports {LED[12]]}
set_property PACKAGE_PIN N3 [get_ports {LED[13]]}
    set_property IOSTANDARD LVCMOS33 [get_ports {LED[13]]}
set_property PACKAGE_PIN P1 [get_ports {LED[14]]}
    set_property IOSTANDARD LVCMOS33 [get_ports {LED[14]]}
set_property PACKAGE_PIN L1 [get_ports {LED[15]]}
    set_property IOSTANDARD LVCMOS33 [get_ports {LED[15]]}

#7 segment display
set_property PACKAGE_PIN W7 [get_ports {seg[0]]}
    set_property IOSTANDARD LVCMOS33 [get_ports {seg[0]]}
set_property PACKAGE_PIN W6 [get_ports {seg[1]]}
    set_property IOSTANDARD LVCMOS33 [get_ports {seg[1]]}
set_property PACKAGE_PIN U8 [get_ports {seg[2]]}
    set_property IOSTANDARD LVCMOS33 [get_ports {seg[2]]}
set_property PACKAGE_PIN V8 [get_ports {seg[3]]}
    set_property IOSTANDARD LVCMOS33 [get_ports {seg[3]]}
set_property PACKAGE_PIN U5 [get_ports {seg[4]]}
    set_property IOSTANDARD LVCMOS33 [get_ports {seg[4]]}
set_property PACKAGE_PIN V5 [get_ports {seg[5]]}
    set_property IOSTANDARD LVCMOS33 [get_ports {seg[5]]}
set_property PACKAGE_PIN U7 [get_ports {seg[6]]}
    set_property IOSTANDARD LVCMOS33 [get_ports {seg[6]]}
set_property PACKAGE_PIN V7 [get_ports dp]
    set_property IOSTANDARD LVCMOS33 [get_ports dp]
set_property PACKAGE_PIN U2 [get_ports {an[0]]}
    set_property IOSTANDARD LVCMOS33 [get_ports {an[0]]}
set_property PACKAGE_PIN U4 [get_ports {an[1]]}
    set_property IOSTANDARD LVCMOS33 [get_ports {an[1]]}
set_property PACKAGE_PIN V4 [get_ports {an[2]]}
    set_property IOSTANDARD LVCMOS33 [get_ports {an[2]]}
set_property PACKAGE_PIN W4 [get_ports {an[3]]}
    set_property IOSTANDARD LVCMOS33 [get_ports {an[3]]}

##Buttons
#set_property PACKAGE_PIN U18 [get_ports btnC]
    #set_property IOSTANDARD LVCMOS33 [get_ports btnC]
#set_property PACKAGE_PIN T18 [get_ports btnU]
    #set_property IOSTANDARD LVCMOS33 [get_ports btnU]
#set_property PACKAGE_PIN W19 [get_ports btnL]
    #set_property IOSTANDARD LVCMOS33 [get_ports btnL]
#set_property PACKAGE_PIN T17 [get_ports btnR]
    #set_property IOSTANDARD LVCMOS33 [get_ports btnR]
#set_property PACKAGE_PIN U17 [get_ports btnD]
    #set_property IOSTANDARD LVCMOS33 [get_ports btnD]

##Pmod Header JA
##Sch name = JA1
#set_property PACKAGE_PIN J1 [get_ports {JA[0]]}

```

```

    #set_property IOSTANDARD LVCMOS33 [get_ports {JA[0]}]
##Sch name = JA2
#set_property PACKAGE_PIN L2 [get_ports {JA[1]}]
    #set_property IOSTANDARD LVCMOS33 [get_ports {JA[1]}]
##Sch name = JA3
#set_property PACKAGE_PIN J2 [get_ports {JA[2]}]
    #set_property IOSTANDARD LVCMOS33 [get_ports {JA[2]}]
##Sch name = JA4
#set_property PACKAGE_PIN G2 [get_ports {JA[3]}]
    #set_property IOSTANDARD LVCMOS33 [get_ports {JA[3]}]
##Sch name = JA7
#set_property PACKAGE_PIN H1 [get_ports {JA[4]}]
    #set_property IOSTANDARD LVCMOS33 [get_ports {JA[4]}]
##Sch name = JA8
#set_property PACKAGE_PIN K2 [get_ports {JA[5]}]
    #set_property IOSTANDARD LVCMOS33 [get_ports {JA[5]}]
##Sch name = JA9
#set_property PACKAGE_PIN H2 [get_ports {JA[6]}]
    #set_property IOSTANDARD LVCMOS33 [get_ports {JA[6]}]
##Sch name = JA10
#set_property PACKAGE_PIN G3 [get_ports {JA[7]}]
    #set_property IOSTANDARD LVCMOS33 [get_ports {JA[7]}]

##Pmod Header JB
##Sch name = JB1
#set_property PACKAGE_PIN A14 [get_ports {JB[0]}]
    #set_property IOSTANDARD LVCMOS33 [get_ports {JB[0]}]
##Sch name = JB2
#set_property PACKAGE_PIN A16 [get_ports {JB[1]}]
    #set_property IOSTANDARD LVCMOS33 [get_ports {JB[1]}]
##Sch name = JB3
#set_property PACKAGE_PIN B15 [get_ports {JB[2]}]
    #set_property IOSTANDARD LVCMOS33 [get_ports {JB[2]}]
##Sch name = JB4
#set_property PACKAGE_PIN B16 [get_ports {JB[3]}]
    #set_property IOSTANDARD LVCMOS33 [get_ports {JB[3]}]
##Sch name = JB7
#set_property PACKAGE_PIN A15 [get_ports {JB[4]}]
    #set_property IOSTANDARD LVCMOS33 [get_ports {JB[4]}]
##Sch name = JB8
#set_property PACKAGE_PIN A17 [get_ports {JB[5]}]
    #set_property IOSTANDARD LVCMOS33 [get_ports {JB[5]}]
##Sch name = JB9
#set_property PACKAGE_PIN C15 [get_ports {JB[6]}]
    #set_property IOSTANDARD LVCMOS33 [get_ports {JB[6]}]
##Sch name = JB10
#set_property PACKAGE_PIN C16 [get_ports {JB[7]}]
    #set_property IOSTANDARD LVCMOS33 [get_ports {JB[7]}]

##Pmod Header JC
##Sch name = JC1
#set_property PACKAGE_PIN K17 [get_ports {JC[0]}]
    #set_property IOSTANDARD LVCMOS33 [get_ports {JC[0]}]
##Sch name = JC2
#set_property PACKAGE_PIN M18 [get_ports {JC[1]}]
    #set_property IOSTANDARD LVCMOS33 [get_ports {JC[1]}]
##Sch name = JC3
#set_property PACKAGE_PIN N17 [get_ports {JC[2]}]
    #set_property IOSTANDARD LVCMOS33 [get_ports {JC[2]}]
##Sch name = JC4
#set_property PACKAGE_PIN P18 [get_ports {JC[3]}]
    #set_property IOSTANDARD LVCMOS33 [get_ports {JC[3]}]
##Sch name = JC7
#set_property PACKAGE_PIN L17 [get_ports {JC[4]}]
    #set_property IOSTANDARD LVCMOS33 [get_ports {JC[4]}]
##Sch name = JC8

```

```

#set_property PACKAGE_PIN M19 [get_ports {JC[5]}]
#set_property IOSTANDARD LVCMOS33 [get_ports {JC[5]}]
##Sch name = JC9
#set_property PACKAGE_PIN P17 [get_ports {JC[6]}]
#set_property IOSTANDARD LVCMOS33 [get_ports {JC[6]}]
##Sch name = JC10
#set_property PACKAGE_PIN R18 [get_ports {JC[7]}]
#set_property IOSTANDARD LVCMOS33 [get_ports {JC[7]}]

#Pmod Header JXADC
#Sch name = XA1_P
set_property PACKAGE_PIN J3 [get_ports {vauxp6}]
set_property IOSTANDARD LVCMOS33 [get_ports {vauxp6}]
#Sch name = XA2_P
set_property PACKAGE_PIN L3 [get_ports {vauxp14}]
set_property IOSTANDARD LVCMOS33 [get_ports {vauxp14}]
#Sch name = XA3_P
set_property PACKAGE_PIN M2 [get_ports {vauxp7}]
set_property IOSTANDARD LVCMOS33 [get_ports {vauxp7}]
#Sch name = XA4_P
set_property PACKAGE_PIN N2 [get_ports {vauxp15}]
set_property IOSTANDARD LVCMOS33 [get_ports {vauxp15}]
#Sch name = XA1_N
set_property PACKAGE_PIN K3 [get_ports {vauxn6}]
set_property IOSTANDARD LVCMOS33 [get_ports {vauxn6}]
#Sch name = XA2_N
set_property PACKAGE_PIN M3 [get_ports {vauxn14}]
set_property IOSTANDARD LVCMOS33 [get_ports {vauxn14}]
#Sch name = XA3_N
set_property PACKAGE_PIN M1 [get_ports {vauxn7}]
set_property IOSTANDARD LVCMOS33 [get_ports {vauxn7}]
#Sch name = XA4_N
set_property PACKAGE_PIN N1 [get_ports {vauxn15}]
set_property IOSTANDARD LVCMOS33 [get_ports {vauxn15}]

##VGA Connector
#set_property PACKAGE_PIN G19 [get_ports {vgaRed[0]}]
#set_property IOSTANDARD LVCMOS33 [get_ports {vgaRed[0]}]
#set_property PACKAGE_PIN H19 [get_ports {vgaRed[1]}]
#set_property IOSTANDARD LVCMOS33 [get_ports {vgaRed[1]}]
#set_property PACKAGE_PIN J19 [get_ports {vgaRed[2]}]
#set_property IOSTANDARD LVCMOS33 [get_ports {vgaRed[2]}]
#set_property PACKAGE_PIN N19 [get_ports {vgaRed[3]}]
#set_property IOSTANDARD LVCMOS33 [get_ports {vgaRed[3]}]
#set_property PACKAGE_PIN N18 [get_ports {vgaBlue[0]}]
#set_property IOSTANDARD LVCMOS33 [get_ports {vgaBlue[0]}]
#set_property PACKAGE_PIN L18 [get_ports {vgaBlue[1]}]
#set_property IOSTANDARD LVCMOS33 [get_ports {vgaBlue[1]}]
#set_property PACKAGE_PIN K18 [get_ports {vgaBlue[2]}]
#set_property IOSTANDARD LVCMOS33 [get_ports {vgaBlue[2]}]
#set_property PACKAGE_PIN J18 [get_ports {vgaBlue[3]}]
#set_property IOSTANDARD LVCMOS33 [get_ports {vgaBlue[3]}]
#set_property PACKAGE_PIN J17 [get_ports {vgaGreen[0]}]
#set_property IOSTANDARD LVCMOS33 [get_ports {vgaGreen[0]}]
#set_property PACKAGE_PIN H17 [get_ports {vgaGreen[1]}]
#set_property IOSTANDARD LVCMOS33 [get_ports {vgaGreen[1]}]
#set_property PACKAGE_PIN G17 [get_ports {vgaGreen[2]}]
#set_property IOSTANDARD LVCMOS33 [get_ports {vgaGreen[2]}]
#set_property PACKAGE_PIN D17 [get_ports {vgaGreen[3]}]
#set_property IOSTANDARD LVCMOS33 [get_ports {vgaGreen[3]}]
#set_property PACKAGE_PIN P19 [get_ports Hsync]
#set_property IOSTANDARD LVCMOS33 [get_ports Hsync]
#set_property PACKAGE_PIN R19 [get_ports Vsync]
#set_property IOSTANDARD LVCMOS33 [get_ports Vsync]

##USB-RS232 Interface

```

```

#set_property PACKAGE_PIN B18 [get_ports RsRx]
#set_property IOSTANDARD LVCMOS33 [get_ports RsRx]
#set_property PACKAGE_PIN A18 [get_ports RsTx]
#set_property IOSTANDARD LVCMOS33 [get_ports RsTx]

##USB HID (PS/2)
#set_property PACKAGE_PIN C17 [get_ports PS2Clk]
#set_property IOSTANDARD LVCMOS33 [get_ports PS2Clk]
#set_property PULLUP true [get_ports PS2Clk]
#set_property PACKAGE_PIN B17 [get_ports PS2Data]
#set_property IOSTANDARD LVCMOS33 [get_ports PS2Data]
#set_property PULLUP true [get_ports PS2Data]

##Quad SPI Flash
##Note that CCLK_0 cannot be placed in 7 series devices. You can access it using the
##STARTUPE2 primitive.
#set_property PACKAGE_PIN D18 [get_ports {QspiDB[0]}]
#set_property IOSTANDARD LVCMOS33 [get_ports {QspiDB[0]}]
#set_property PACKAGE_PIN D19 [get_ports {QspiDB[1]}]
#set_property IOSTANDARD LVCMOS33 [get_ports {QspiDB[1]}]
#set_property PACKAGE_PIN G18 [get_ports {QspiDB[2]}]
#set_property IOSTANDARD LVCMOS33 [get_ports {QspiDB[2]}]
#set_property PACKAGE_PIN F18 [get_ports {QspiDB[3]}]
#set_property IOSTANDARD LVCMOS33 [get_ports {QspiDB[3]}]
#set_property PACKAGE_PIN K19 [get_ports QspiCSn]
#set_property IOSTANDARD LVCMOS33 [get_ports QspiCSn]

```

## XADC configuration

```

library ieee;
use ieee.std_logic_1164.all;
use ieee.numeric_std.all;
Library UNISIM;
use UNISIM.VCOMPONENTS.ALL;

```

```
entity xadc_wiz_0 is
```

```

    port
    (
        daddr_in : in  STD_LOGIC_VECTOR (6 downto 0);    -- Address bus for the dynamic reconfiguration port
        den_in   : in  STD_LOGIC;                        -- Enable Signal for the dynamic reconfiguration port
        di_in    : in  STD_LOGIC_VECTOR (15 downto 0);   -- Input data bus for the dynamic reconfiguration port
        dwe_in   : in  STD_LOGIC;                        -- Write Enable for the dynamic reconfiguration port
        do_out   : out STD_LOGIC_VECTOR (15 downto 0);   -- Output data bus for dynamic reconfiguration port
        drdy_out : out STD_LOGIC;                        -- Data ready signal for the dynamic reconfiguration port
        dclk_in  : in  STD_LOGIC;                        -- Clock input for the dynamic reconfiguration port
        vauxp6   : in  STD_LOGIC;                        -- Auxiliary Channel 6
        vauxn6   : in  STD_LOGIC;
        vauxp7   : in  STD_LOGIC;                        -- Auxiliary Channel 7
        vauxn7   : in  STD_LOGIC;
        vauxp14  : in  STD_LOGIC;                        -- Auxiliary Channel 14
        vauxn14  : in  STD_LOGIC;
        vauxp15  : in  STD_LOGIC;                        -- Auxiliary Channel 15
        vauxn15  : in  STD_LOGIC;
        busy_out : out STD_LOGIC;                        -- ADC Busy signal
        channel_out : out STD_LOGIC_VECTOR (4 downto 0); -- Channel Selection Outputs
        eoc_out  : out STD_LOGIC;                        -- End of Conversion Signal
        eos_out  : out STD_LOGIC;                        -- End of Sequence Signal
        alarm_out : out STD_LOGIC;                       -- OR'ed output of all the Alarms
        vp_in   : in  STD_LOGIC;                        -- Dedicated Analog Input Pair
        vn_in   : in  STD_LOGIC;
    );
end xadc_wiz_0;

```

```

architecture xilinx of xadc_wiz_0 is
    attribute CORE_GENERATION_INFO : string;

```

```

attribute CORE_GENERATION_INFO of xilinx : architecture is
"xadc_wiz_0,xadc_wiz_v3_0,{component_name=xadc_wiz_0,enable_axi=false,enable_axi4stream=false,dclk_frequency=100,enable_
_busy=true,enable_convst=false,enable_convstclk=false,enable_dclk=true,enable_drp=true,enable_eoc=true,enable_eos=true,enable_v
bram_alarms=false,enable_vccddro_alarms=false,enable_Vccint_Alarm=false,enable_Vccaux_alarms=false,enable_vccpaux_alarms
=false,enable_vccpint_alarms=false,ot_alarms=false,user_temp_alarms=false,timing_mode=continuous,channel_averaging=None,seq
uencer_mode=on,startup_channel_selection=contineous_sequence}";

```

```

signal FLOAT_VCCAUX_ALARM : std_logic;
signal FLOAT_VCCINT_ALARM : std_logic;
signal FLOAT_USER_TEMP_ALARM : std_logic;
signal FLOAT_VBRAM_ALARM : std_logic;
signal FLOAT_MUXADDR : std_logic_vector (4 downto 0);
signal aux_channel_p : std_logic_vector (15 downto 0);
signal aux_channel_n : std_logic_vector (15 downto 0);
signal alm_int : std_logic_vector (7 downto 0);

```

```
begin
```

```

alarm_out <= alm_int(7);
aux_channel_p(0) <= '0';      aux_channel_n(0) <= '0';      aux_channel_p(1) <= '0';
aux_channel_n(1) <= '0';      aux_channel_p(2) <= '0';      aux_channel_n(2) <= '0';
aux_channel_p(3) <= '0';      aux_channel_n(3) <= '0';      aux_channel_p(4) <= '0';
aux_channel_n(4) <= '0';      aux_channel_p(5) <= '0';      aux_channel_n(5) <= '0';
aux_channel_p(6) <= vauxp6;    aux_channel_n(6) <= vauxn6;
aux_channel_p(7) <= vauxp7;    aux_channel_n(7) <= vauxn7;
aux_channel_p(8) <= '0';      aux_channel_n(8) <= '0';      aux_channel_p(9) <= '0';
aux_channel_n(9) <= '0';      aux_channel_p(10) <= '0';     aux_channel_n(10) <= '0';
aux_channel_p(11) <= '0';     aux_channel_n(11) <= '0';     aux_channel_p(12) <= '0';
aux_channel_n(12) <= '0';     aux_channel_p(13) <= '0';     aux_channel_n(13) <= '0';
aux_channel_p(14) <= vauxp14;  aux_channel_n(14) <= vauxn14;
aux_channel_p(15) <= vauxp15;  aux_channel_n(15) <= vauxn15;

```

```
U0 : XADC
```

```
generic map(
```

```

INIT_40 => X"3000", -- config reg 0
INIT_41 => X"210F", -- config reg 1
INIT_42 => X"0400", -- config reg 2
INIT_48 => X"0000", -- Sequencer channel selection
INIT_49 => X"C0C0", -- Sequencer channel selection
INIT_4A => X"3000", -- Sequencer Average selection
INIT_4B => X"3000", -- Sequencer Average selection
INIT_4C => X"0000", -- Sequencer Bipolar selection
INIT_4D => X"0000", -- Sequencer Bipolar selection
INIT_4E => X"0000", -- Sequencer Acq time selection
INIT_4F => X"0000", -- Sequencer Acq time selection
INIT_50 => X"B5ED", -- Temp alarm trigger
INIT_51 => X"57E4", -- Vccint upper alarm limit
INIT_52 => X"A147", -- Vccaux upper alarm limit
INIT_53 => X"CA33", -- Temp alarm OT upper
INIT_54 => X"A93A", -- Temp alarm reset
INIT_55 => X"52C6", -- Vccint lower alarm limit
INIT_56 => X"9555", -- Vccaux lower alarm limit
INIT_57 => X"AE4E", -- Temp alarm OT reset
INIT_58 => X"5999", -- Vccbram upper alarm limit
INIT_5C => X"5111", -- Vccbram lower alarm limit
SIM_DEVICE => "7SERIES",
SIM_MONITOR_FILE

```

```
=>
```

```

"c:/Users/Nate/Desktop/work/GitProject/Demos/DemoTest/Basys3/Projects/Basys3_XADC_Demo/src/ip/xadc_wiz_0_1/xadc_wiz_0/
simulation/functional/design.txt"
)

```

```
port map (
```

```

CONVST          => '0',
CONVSTCLK       => '0',
DADDR(6 downto 0) => daddr_in(6 downto 0),
DCLK           => dclk_in,
DEN            => den_in,

```

```

DI(15 downto 0)      => di_in(15 downto 0),
DWE                 => dwe_in,
RESET               => '0',
VAUXN(15 downto 0)  => aux_channel_n(15 downto 0),
VAUXP(15 downto 0)  => aux_channel_p(15 downto 0),
ALM                 => alm_int,
BUSY                => busy_out,
CHANNEL(4 downto 0) => channel_out(4 downto 0),
DO(15 downto 0)     => do_out(15 downto 0),
DRDY                => drdy_out,
EOC                 => eoc_out,
EOS                 => eos_out,
JTAGBUSY            => open,
JTAGLOCKED          => open,
JTAGMODIFIED        => open,
OT                  => open,
MUXADDR             => FLOAT_MUXADDR,
VN                  => vn_in,
VP                  => vp_in
);
end xilinx;

```

### 3-bit counter

```

module counter3bit (input clk,      input rst,      output reg [2:0] Q);
always @ (posedge(clk)) // When will Always Block Be Triggered
begin
    if (rst == 3'b111) // How Output reacts when Reset Is Asserted
        Q <= 3'b0;
    else // How Output reacts when Rising Edge of Clock Arrives?
        Q <= Q + 1'b1;
    end
end
endmodule

```

### 3-8 decoder

```

module decoder_3_8 (input [2:0] I,      input v_signal,      output [3:0] an,      output dp);
assign an[0] = ~(~I[2] & ~I[1] & ~I[0]);
assign an[1] = ~(~I[2] & ~I[1] & I[0]);
assign an[2] = ~(~I[2] & I[1] & ~I[0]);
assign an[3] = ~(~I[2] & I[1] & I[0]);
//assign an[4] = ~(I[2] & ~I[1] & ~I[0]);
//assign an[5] = ~(I[2] & ~I[1] & I[0]);
//assign an[6] = ~(I[2] & I[1] & ~I[0]);
//assign an[7] = ~(I[2] & I[1] & I[0]);
//decimal place
assign dp = (v_signal ? ~(~I[2] & ~I[1] & I[0]): ~(~I[2] & I[1] & ~I[0]));//v_signal=1, dp@ 3rd bit; v_signal=0, dp@ 2nd bit
endmodule

```

### 7-segment display

```

module DigitToSeg(in1, in2, in3, in4, in5, in6, in7, in8, mclk, an, dp, seg, v_signal);
input [3:0] in1;      input [3:0] in2;      input [3:0] in3;      input [3:0] in4;
input [3:0] in5;      input [3:0] in6;      input [3:0] in7;      input [3:0] in8;
input mclk;           output [3:0] an;      output [6:0] seg;      output dp;      input v_signal;
//wire swt7;
wire XLXN_94;      wire [3:0] XLXN_102;      wire [2:0] XLXN_109;
sevensegdecoder XLXI_6 (.nIn(XLXN_102[3:0]), .ssOut(seg[6:0]));
mux4_4bus XLXI_45 (.I0(in1[3:0]), .I1(in2[3:0]), .I2(in3[3:0]), .I3(in4[3:0]),
.I4(in5[3:0]), .I5(in6[3:0]), .I6(in7[3:0]), .I7(in8[3:0]),
.Sel(XLXN_109[2:0]), .Y(XLXN_102[3:0]));
segClkDivider XLXI_47 (.clk(mclk), .rst(), .clk_div(XLXN_94));

```

```
//GND XLXI_48 (.G(swt7));
counter3bit XLXI_49 (.clk(XLXN_94), .rst(), .Q(XLXN_109[2:0]));
decoder_3_8 XLXI_50 (.I(XLXN_109[2:0]), .dp(dp), .v_signal(v_signal), .an(an[3:0]));
endmodule
```

## 7-segment decoder

```
module sevensegdecoder(input [3:0] nIn, output reg [6:0] ssOut);
always @(nIn)
  case (nIn)
    4'h0: ssOut = 7'b1000000;    4'h1: ssOut = 7'b1111001;    4'h2: ssOut = 7'b0100100;
    4'h3: ssOut = 7'b0110000;    4'h4: ssOut = 7'b0011001;    4'h5: ssOut = 7'b0010010;
    4'h6: ssOut = 7'b0000010;    4'h7: ssOut = 7'b1111000;    4'h8: ssOut = 7'b0000000;
    4'h9: ssOut = 7'b0011000;    4'hA: ssOut = 7'b0001000;    4'hB: ssOut = 7'b0000011;
    4'hC: ssOut = 7'b1000110;    4'hD: ssOut = 7'b0100001;    4'hE: ssOut = 7'b0000110;
    4'hF: ssOut = 7'b0001110;    default: ssOut = 7'b1001001;
  endcase
endmodule
```

## MUX4

```
module mux4_4bus(input [3:0] I0, input [3:0] I1, input [3:0] I2, input [3:0] I3, input [3:0] I4,
input [3:0] I5, input [3:0] I6, input [3:0] I7, input [2:0] Sel, output [3:0] Y);
assign Y = ( Sel == 0 )? I0 : ( Sel == 1 )? I1 : ( Sel == 2 )? I2 : ( Sel == 3 )? I3 : ( Sel == 4 )? I4 : ( Sel == 5 )? I5 : ( Sel == 6 )? I6 : I7;
endmodule
```

## Clock

```
module segClkDevider(input clk, input rst, output reg clk_div );
localparam constantNumber = 100000;
reg [31:0] count;
always @ (posedge(clk), posedge(rst))
begin
  if (rst == 1'b1) count <= 32'b0;
  else if (count == constantNumber - 1) count <= 32'b0;
  else count <= count + 1;
end

always @ (posedge(clk), posedge(rst))
begin
  if (rst == 1'b1) clk_div <= 1'b0;
  else if (count == constantNumber - 1) clk_div <= ~clk_div;
  else clk_div <= clk_div;
end
endmodule
```

## Main (top-level) program

```
module XADCdemo(
input CLK100MHZ,input vauxp6,input vauxn6,input vauxp7,input vauxn7, input vauxp15,input vauxn15,input vauxp14,input
vauxn14,
input reset, input test_cal, input v_signal, input ph, input temperature, input chlorine, input total_cl,
//sw0_reset1; sw1_test0/calbration1; sw2_ph; sw15_v/signal ; sw3_T; sw4_Cl; sw5_total free chlorine
output reg [15:0] LED, output [3:0] an, output dp, output [6:0] seg);
wire enable; wire ready; wire [15:0] data;
reg [15:0] data_test, data_test_t, data_test_cl, data_current, data_previous; reg [32:0] count; reg [6:0] Address_in;
reg [32:0] decimal_cal, decimal_cal_ph, decimal_test, decimal_v, decimal_ph, decimal_vt, decimal_cal_vt, decimal_t,
decimal_cal_t, decimal_cl, decimal_vcl, decimal_ph_now, delta_ph, int_exp_cal, decimal_exp_cal, cl_ratio_cal, pka;
reg [3:0] dig0, dig1, dig2, dig3, dig4, dig5, dig6, digv0, digv1, digv2, digv3, digv4, digv5, digv6, digph0, digph1, digph2, digph3,
digph4, digph5, digph6;
```



```

        decimal_ph = decimal_ph / 10; digph6 = decimal_ph % 10; decimal_ph = decimal_ph / 10;
        dig0 = 0; dig1 = 0; dig2 = 0; dig3 <= digph3; dig4 <= digph4; dig5 <= digph5; dig6 <= digph6;
    end
end
else begin count <= count + 1; LED <= 16'b0000_0000_0000_0000; end //sampling interval
end
end

//////////////////////temperature//////////////////////////////////////
else if (temperature == 1'b1) //read T
begin
if(count == 1) //set sampling frequency, here (1/2)x1Hz
begin LED <= 16'b0000_0000_0000_1000; //read data
data_test_t <= data; decimal_vt = data_test_t >> 4; count = 0;
//test data for processing, display; looks nicer if our max value is 1V instead of .999755
decimal_vt = decimal_vt * 250000; decimal_vt = decimal_vt >> 10; decimal_cal_t <= decimal_vt;
if (v_signal == 1'b1) //display mV, in mV xxx.x mV
begin digv0 = decimal_vt % 10; decimal_vt = decimal_vt / 10; digv1 = decimal_vt % 10;
decimal_vt=decimal_vt/10; digv2=decimal_vt%10; decimal_vt=decimal_vt/10; digv3=decimal_vt%10;
decimal_vt=decimal_vt/10; digv4=decimal_vt%10; decimal_vt=decimal_vt/10; digv5= decimal_vt%10;
decimal_vt = decimal_vt / 10; digv6 = decimal_vt % 10; decimal_vt = decimal_vt / 10;
dig0<=digv0; dig1<= digv0; dig2 <= digv1; dig3 <= digv2; dig4 <= digv3; dig5 <= digv4; dig6 <= digv5;
end
else //display T, use uV, xx.xx deg
begin decimal_t = 1000*(v_t_27 + 27 * t_s - decimal_vt)/t_s; digph2 = decimal_t % 10;
decimal_t=decimal_t/10; digph3=decimal_t%10; decimal_t=decimal_t/10; digph4 = decimal_t % 10;
decimal_t=decimal_t/10; digph5=decimal_t % 10; decimal_t=decimal_t/10; digph6 = decimal_t % 10;
decimal_t = decimal_t / 10;
dig0 = 0; dig1 = 0; dig2 = 0; dig3 <= digph3; dig4 <= digph4; dig5 <= digph5; dig6 <= digph6;
end
end
end
else begin count <= count + 1; LED <= 16'b0000_0000_0000_0000; end //sampling interval
end

//////////////////////HOCL only//////////////////////////////////////
else if (chlorine == 1'b1) // read Cl
begin
if(count == 1) //set sampling frequency, here (1/2)x1Hz
begin LED <= 16'b0000_0000_0001_0000; //read data
data_test_cl <= data; decimal_vcl = data_test_cl >> 4; count = 0;
//test data for processing, display; looks nicer if our max value is 1V instead of .999755
decimal_vcl = decimal_vcl * 250000; decimal_vcl = decimal_vcl >> 10;
if (v_signal == 1'b1) //display mV, in mV xxx.x mV
begin digv0 = decimal_vcl % 10; decimal_vcl = decimal_vcl / 10; digv1 = decimal_vcl % 10;
decimal_vcl=decimal_vcl/10; digv2=decimal_vcl%10; decimal_vcl=decimal_vcl/10;
digv3= decimal_vcl%10; decimal_vcl = decimal_vcl / 10; digv4 = decimal_vcl % 10;
decimal_vcl = decimal_vcl / 10; digv5 = decimal_vcl % 10; decimal_vcl = decimal_vcl / 10;
digv6 = decimal_vcl % 10; decimal_vcl = decimal_vcl / 10;
dig0 <= digv0; dig1 <= digv0; dig2 <= digv1; dig3 <= digv2; dig4 <= digv3; dig5 <= digv4; dig6 <= digv5;
end
else //display Cl, use uV, xx.xx ppm ///use _ph to represent _Cl
begin decimal_cl = 1000*(decimal_vcl - cl_intecept)/(cl_s+(v_t_27-decimal_cal_t)*cl_t_coeff/t_s);
digph2 = decimal_cl % 10; // [HOCl]=(V-21482uV)/sensitivity ppm
decimal_cl = decimal_cl / 10; digph3 = decimal_cl % 10; decimal_cl = decimal_cl / 10;
digph4 = decimal_cl % 10; decimal_cl = decimal_cl / 10; digph5 = decimal_cl % 10;
decimal_cl = decimal_cl / 10; digph6 = decimal_cl % 10; decimal_cl = decimal_cl / 10;
dig0 = 0; dig1 = 0; dig2 = 0; dig3 <= digph3; dig4 <= digph4; dig5 <= digph5; dig6 <= digph6;
end
end
end
else begin count <= count + 1; LED <= 16'b0000_0000_0000_0000; end //sampling interval
end

//////////////////////total free chlorine//////////////////////////////////////
else if (total_cl == 1'b1) // read Cl
begin
if(count == 1) //set sampling frequency, here (1/2)x1Hz

```



# Appendix E

## Copyright permissions

### ELSEVIER LICENSE TERMS AND CONDITIONS

Apr 04, 2017

---

This Agreement between Yiheng Qin ("You") and Elsevier ("Elsevier") consists of your license details and the terms and conditions provided by Elsevier and Copyright Clearance Center.

License Number	4082031382214
License date	
Licensed Content Publisher	Elsevier
Licensed Content Publication	Talanta
Licensed Content Title	Low-temperature solution processing of palladium/palladium oxide films and their pH sensing performance
Licensed Content Author	Yiheng Qin, Arif U. Alam, Si Pan, Matiar M.R. Howlader, Raja Ghosh, P. Ravi Selvaganapathy, Yiliang Wu, M. Jamal Deen
Licensed Content Date	1 January 2016
Licensed Content Volume	146
Licensed Content Issue	n/a
Licensed Content Pages	8
Start Page	517
End Page	524
Type of Use	reuse in a thesis/dissertation
Portion	full article
Format	both print and electronic
Are you the author of this Elsevier article?	Yes
Will you be translating?	No
Order reference number	
Title of your thesis/dissertation	Microfabricated pH, temperature, and free chlorine sensors for integrated drinking water quality monitoring systems

Expected completion date	May 2017
Estimated size (number of pages)	230
Elsevier VAT number	GB 494 6272 12
Requestor Location	Yiheng Qin ITB-A301 McMaster University 1280 Main Street West Hamilton, ON L8S 4K1 Canada Attn: Yiheng Qin
Total	0.00 CAD
Terms and Conditions	

### INTRODUCTION

1. The publisher for this copyrighted material is Elsevier. By clicking "accept" in connection with completing this licensing transaction, you agree that the following terms and conditions apply to this transaction (along with the Billing and Payment terms and conditions established by Copyright Clearance Center, Inc. ("CCC"), at the time that you opened your Rightslink account and that are available at any time at <http://myaccount.copyright.com>).

### GENERAL TERMS

2. Elsevier hereby grants you permission to reproduce the aforementioned material subject to the terms and conditions indicated.
3. Acknowledgement: If any part of the material to be used (for example, figures) has appeared in our publication with credit or acknowledgement to another source, permission must also be sought from that source. If such permission is not obtained then that material may not be included in your publication/copies. Suitable acknowledgement to the source must be made, either as a footnote or in a reference list at the end of your publication, as follows:  
"Reprinted from Publication title, Vol /edition number, Author(s), Title of article / title of chapter, Pages No., Copyright (Year), with permission from Elsevier [OR APPLICABLE SOCIETY COPYRIGHT OWNER]." Also Lancet special credit - "Reprinted from The Lancet, Vol. number, Author(s), Title of article, Pages No., Copyright (Year), with permission from Elsevier."
4. Reproduction of this material is confined to the purpose and/or media for which permission is hereby given.
5. Altering/Modifying Material: Not Permitted. However figures and illustrations may be altered/adapted minimally to serve your work. Any other abbreviations, additions, deletions and/or any other alterations shall be made only with prior written authorization of Elsevier Ltd. (Please contact Elsevier at [permissions@elsevier.com](mailto:permissions@elsevier.com)). No modifications can be made to any Lancet figures/tables and they must be reproduced in full.
6. If the permission fee for the requested use of our material is waived in this instance, please be advised that your future requests for Elsevier materials may attract a fee.
7. Reservation of Rights: Publisher reserves all rights not specifically granted in the combination of (i) the license details provided by you and accepted in the course of this licensing transaction, (ii) these terms and conditions and (iii) CCC's Billing and Payment terms and conditions.
8. License Contingent Upon Payment: While you may exercise the rights licensed immediately upon issuance of the license at the end of the licensing process for the transaction, provided that you have disclosed complete and accurate details of your proposed use, no license is finally effective unless and until full payment is received from you (either by publisher or by CCC) as provided in CCC's Billing and Payment terms and conditions. If full payment is not received on a timely basis, then any license preliminarily granted shall be deemed automatically revoked and shall be void as if never granted. Further, in the event that you breach any of these terms and conditions or any of CCC's Billing

and Payment terms and conditions, the license is automatically revoked and shall be void as if never granted. Use of materials as described in a revoked license, as well as any use of the materials beyond the scope of an unrevoked license, may constitute copyright infringement and publisher reserves the right to take any and all action to protect its copyright in the materials.

9. Warranties: Publisher makes no representations or warranties with respect to the licensed material.

10. Indemnity: You hereby indemnify and agree to hold harmless publisher and CCC, and their respective officers, directors, employees and agents, from and against any and all claims arising out of your use of the licensed material other than as specifically authorized pursuant to this license.

11. No Transfer of License: This license is personal to you and may not be sublicensed, assigned, or transferred by you to any other person without publisher's written permission.

12. No Amendment Except in Writing: This license may not be amended except in a writing signed by both parties (or, in the case of publisher, by CCC on publisher's behalf).

13. Objection to Contrary Terms: Publisher hereby objects to any terms contained in any purchase order, acknowledgment, check endorsement or other writing prepared by you, which terms are inconsistent with these terms and conditions or CCC's Billing and Payment terms and conditions. These terms and conditions, together with CCC's Billing and Payment terms and conditions (which are incorporated herein), comprise the entire agreement between you and publisher (and CCC) concerning this licensing transaction. In the event of any conflict between your obligations established by these terms and conditions and those established by CCC's Billing and Payment terms and conditions, these terms and conditions shall control.

14. Revocation: Elsevier or Copyright Clearance Center may deny the permissions described in this License at their sole discretion, for any reason or no reason, with a full refund payable to you. Notice of such denial will be made using the contact information provided by you. Failure to receive such notice will not alter or invalidate the denial. In no event will Elsevier or Copyright Clearance Center be responsible or liable for any costs, expenses or damage incurred by you as a result of a denial of your permission request, other than a refund of the amount(s) paid by you to Elsevier and/or Copyright Clearance Center for denied permissions.

#### LIMITED LICENSE

The following terms and conditions apply only to specific license types:

15. **Translation:** This permission is granted for non-exclusive world **English** rights only unless your license was granted for translation rights. If you licensed translation rights you may only translate this content into the languages you requested. A professional translator must perform all translations and reproduce the content word for word preserving the integrity of the article.

16. **Posting licensed content on any Website:** The following terms and conditions apply as follows:

Licensing material from an Elsevier journal: All content posted to the web site must maintain the copyright information line on the bottom of each image; A hyper-text must be included to the Homepage of the journal from which you are licensing

at <http://www.sciencedirect.com/science/journal/xxxxx> or the Elsevier homepage for books

at <http://www.elsevier.com>; Central Storage: This license does not include permission for a scanned version of the material to be stored in a central repository such as that provided by Heron/XanEdu.

Licensing material from an Elsevier book: A hyper-text link must be included to the Elsevier homepage at <http://www.elsevier.com>. All content posted to the web site must maintain the copyright information line on the bottom of each image.

**Posting licensed content on Electronic reserve:** In addition to the above the following clauses are applicable: The web site must be password-protected and made available only to bona fide students registered on a relevant course. This permission is granted for 1 year only. You may obtain a new license for future website posting.

17. **For journal authors:** the following clauses are applicable in addition to the above:

**Preprints:**

A preprint is an author's own write-up of research results and analysis, it has not been peer-reviewed, nor has it had any other value added to it by a publisher (such as formatting, copyright, technical enhancement etc.).

Authors can share their preprints anywhere at any time. Preprints should not be added to or enhanced in any way in order to appear more like, or to substitute for, the final versions of articles however authors can update their preprints on arXiv or RePEc with their Accepted Author Manuscript (see below).

If accepted for publication, we encourage authors to link from the preprint to their formal publication via its DOI. Millions of researchers have access to the formal publications on ScienceDirect, and so links will help users to find, access, cite and use the best available version. Please note that Cell Press, The Lancet and some society-owned have different preprint policies. Information on these policies is available on the journal homepage.

**Accepted Author Manuscripts:** An accepted author manuscript is the manuscript of an article that has been accepted for publication and which typically includes author-incorporated changes suggested during submission, peer review and editor-author communications.

Authors can share their accepted author manuscript:

- immediately
  - via their non-commercial person homepage or blog
  - by updating a preprint in arXiv or RePEc with the accepted manuscript
  - via their research institute or institutional repository for internal institutional uses or as part of an invitation-only research collaboration work-group
  - directly by providing copies to their students or to research collaborators for their personal use
  - for private scholarly sharing as part of an invitation-only work group on commercial sites with which Elsevier has an agreement
- After the embargo period
  - via non-commercial hosting platforms such as their institutional repository
  - via commercial sites with which Elsevier has an agreement

In all cases accepted manuscripts should:

- link to the formal publication via its DOI
- bear a CC-BY-NC-ND license - this is easy to do
- if aggregated with other manuscripts, for example in a repository or other site, be shared in alignment with our hosting policy not be added to or enhanced in any way to appear more like, or to substitute for, the published journal article.

**Published journal article (JPA):** A published journal article (PJA) is the definitive final record of published research that appears or will appear in the journal and embodies all value-adding publishing activities including peer review co-ordination, copy-editing, formatting, (if relevant) pagination and online enrichment.

Policies for sharing publishing journal articles differ for subscription and gold open access articles:

**Subscription Articles:** If you are an author, please share a link to your article rather than the full-text. Millions of researchers have access to the formal publications on ScienceDirect, and so links will help your users to find, access, cite, and use the best available version.

Theses and dissertations which contain embedded PJAs as part of the formal submission can be posted publicly by the awarding institution with DOI links back to the formal publications on ScienceDirect. If you are affiliated with a library that subscribes to ScienceDirect you have additional private sharing rights for others' research accessed under that agreement. This includes use for classroom teaching and internal training at the institution (including use in course packs and courseware programs), and inclusion of the article for grant funding purposes.

**Gold Open Access Articles:** May be shared according to the author-selected end-user license and should contain a [CrossMark logo](#), the end user license, and a DOI link to the formal publication on ScienceDirect.

Please refer to Elsevier's [posting policy](#) for further information.

18. **For book authors** the following clauses are applicable in addition to the above: Authors are permitted to place a brief summary of their work online only. You are not allowed to download and post the published electronic version of your chapter, nor may you scan the printed edition to create an electronic version. **Posting to a repository:** Authors are permitted to post a summary of their chapter only in their institution's repository.

19. **Thesis/Dissertation:** If your license is for use in a thesis/dissertation your thesis may be submitted to your institution in either print or electronic form. Should your thesis be published commercially, please reapply for permission. These requirements include permission for the Library and Archives of Canada to supply single copies, on demand, of the complete thesis and include permission for Proquest/UMI to supply single copies, on demand, of the complete thesis. Should your thesis be published commercially, please reapply for permission. Theses and dissertations which contain embedded PJAs as part of the formal submission can be posted publicly by the awarding institution with DOI links back to the formal publications on ScienceDirect.

#### **Elsevier Open Access Terms and Conditions**

You can publish open access with Elsevier in hundreds of open access journals or in nearly 2000 established subscription journals that support open access publishing. Permitted third party re-use of these open access articles is defined by the author's choice of Creative Commons user license. See our [open access license policy](#) for more information.

#### **Terms & Conditions applicable to all Open Access articles published with Elsevier:**

Any reuse of the article must not represent the author as endorsing the adaptation of the article nor should the article be modified in such a way as to damage the author's honour or reputation. If any changes have been made, such changes must be clearly indicated.

The author(s) must be appropriately credited and we ask that you include the end user license and a DOI link to the formal publication on ScienceDirect.

If any part of the material to be used (for example, figures) has appeared in our publication with credit or acknowledgement to another source it is the responsibility of the user to ensure their reuse complies with the terms and conditions determined by the rights holder.

#### **Additional Terms & Conditions applicable to each Creative Commons user license:**

**CC BY:** The CC-BY license allows users to copy, to create extracts, abstracts and new works from the Article, to alter and revise the Article and to make commercial use of the Article (including reuse and/or resale of the Article by commercial entities), provided the user gives appropriate credit (with a link to the formal publication through the relevant DOI), provides a link to the license, indicates if changes were made and the licensor is not represented as endorsing the use made of the work. The full details of the license are available at <http://creativecommons.org/licenses/by/4.0>.

**CC BY NC SA:** The CC BY-NC-SA license allows users to copy, to create extracts, abstracts and new works from the Article, to alter and revise the Article, provided this is not done for commercial purposes, and that the user gives appropriate credit (with a link to the formal publication through the relevant DOI), provides a link to the license, indicates if changes were made and the licensor is not represented as endorsing the use made of the work. Further, any new works must be made available on the same conditions. The full details of the license are available at <http://creativecommons.org/licenses/by-nc-sa/4.0>.

**CC BY NC ND:** The CC BY-NC-ND license allows users to copy and distribute the Article, provided this is not done for commercial purposes and further does not permit distribution of the Article if it is changed or edited in any way, and provided the user gives appropriate credit (with a link to the formal publication through the relevant DOI), provides a link to the license, and that the licensor is not represented as endorsing the use made of the work. The full details of the license are available at <http://creativecommons.org/licenses/by-nc-nd/4.0>. Any commercial reuse of Open Access articles

published with a CC BY NC SA or CC BY NC ND license requires permission from Elsevier and will be subject to a fee.

Commercial reuse includes:

- Associating advertising with the full text of the Article
- Charging fees for document delivery or access
- Article aggregation
- Systematic distribution via e-mail lists or share buttons

Posting or linking by commercial companies for use by customers of those companies.

#### 20. Other Conditions:

v1.9

**Questions? [customercare@copyright.com](mailto:customercare@copyright.com) or +1-855-239-3415 (toll free in the US) or +1-978-646-2777.**

### JOHN WILEY AND SONS LICENSE TERMS AND CONDITIONS

Apr 04, 2017

This Agreement between Yiheng Qin ("You") and John Wiley and Sons ("John Wiley and Sons") consists of your license details and the terms and conditions provided by John Wiley and Sons and Copyright Clearance Center.

License Number	4082040324262
License date	
Licensed Content Publisher	John Wiley and Sons
Licensed Content Publication	Advanced Functional Materials
Licensed Content Title	Inkjet Printing of a Highly Loaded Palladium Ink for Integrated, Low-Cost pH Sensors
Licensed Content Author	Yiheng Qin, Arif U. Alam, Matiar M. R. Howlader, Nan-Xing Hu, M. Jamal Deen
Licensed Content Date	May 24, 2016
Licensed Content Pages	11
Type of use	Dissertation/Thesis
Requestor type	Author of this Wiley article
Format	Print and electronic

Portion	Full article
Will you be translating?	No
Title of your thesis / dissertation	Microfabricated pH, temperature, and free chlorine sensors for integrated drinking water quality monitoring systems
Expected completion date	May 2017
Expected size (number of pages)	230
Requestor Location	Yiheng Qin ITB-A301 McMaster University 1280 Main Street West Hamilton, ON L8S 4K1 Canada Attn: Yiheng Qin
Publisher Tax ID	EU826007151
Billing Type	Invoice
Billing Address	Yiheng Qin ITB-A301 McMaster University 1280 Main Street West Hamilton, ON L8S 4K1 Canada Attn: Yiheng Qin
Total	0.00 CAD
Terms and Conditions	

#### TERMS AND CONDITIONS

This copyrighted material is owned by or exclusively licensed to John Wiley & Sons, Inc. or one of its group companies (each a "Wiley Company") or handled on behalf of a society with which a Wiley Company has exclusive publishing rights in relation to a particular work (collectively "WILEY"). By clicking "accept" in connection with completing this licensing transaction, you agree that the following terms and conditions apply to this transaction (along with the billing and payment terms and conditions established by the Copyright Clearance Center Inc., ("CCC's Billing and Payment terms and conditions"), at the time that you opened your RightsLink account (these are available at any time at <http://myaccount.copyright.com>).

#### Terms and Conditions

- The materials you have requested permission to reproduce or reuse (the "Wiley Materials") are protected by copyright.
- You are hereby granted a personal, non-exclusive, non-sub licensable (on a stand-alone basis), non-transferable, worldwide, limited license to reproduce the Wiley Materials for the purpose specified in the licensing process. This license, **and any CONTENT (PDF or image file) purchased as part of your order**, is for a one-time use only and limited to any maximum distribution number specified in the license. The first instance of republication or reuse granted by this license must be completed within two years of the date of the grant of this license (although copies prepared before the end date may be distributed thereafter). The Wiley

Materials shall not be used in any other manner or for any other purpose, beyond what is granted in the license. Permission is granted subject to an appropriate acknowledgement given to the author, title of the material/book/journal and the publisher. You shall also duplicate the copyright notice that appears in the Wiley publication in your use of the Wiley Material. Permission is also granted on the understanding that nowhere in the text is a previously published source acknowledged for all or part of this Wiley Material. Any third party content is expressly excluded from this permission.

- With respect to the Wiley Materials, all rights are reserved. Except as expressly granted by the terms of the license, no part of the Wiley Materials may be copied, modified, adapted (except for minor reformatting required by the new Publication), translated, reproduced, transferred or distributed, in any form or by any means, and no derivative works may be made based on the Wiley Materials without the prior permission of the respective copyright owner. **For STM Signatory Publishers clearing permission under the terms of the STM Permissions Guidelines only, the terms of the license are extended to include subsequent editions and for editions in other languages, provided such editions are for the work as a whole in situ and does not involve the separate exploitation of the permitted figures or extracts,** You may not alter, remove or suppress in any manner any copyright, trademark or other notices displayed by the Wiley Materials. You may not license, rent, sell, loan, lease, pledge, offer as security, transfer or assign the Wiley Materials on a stand-alone basis, or any of the rights granted to you hereunder to any other person.
- The Wiley Materials and all of the intellectual property rights therein shall at all times remain the exclusive property of John Wiley & Sons Inc, the Wiley Companies, or their respective licensors, and your interest therein is only that of having possession of and the right to reproduce the Wiley Materials pursuant to Section 2 herein during the continuance of this Agreement. You agree that you own no right, title or interest in or to the Wiley Materials or any of the intellectual property rights therein. You shall have no rights hereunder other than the license as provided for above in Section 2. No right, license or interest to any trademark, trade name, service mark or other branding ("Marks") of WILEY or its licensors is granted hereunder, and you agree that you shall not assert any such right, license or interest with respect thereto
- NEITHER WILEY NOR ITS LICENSORS MAKES ANY WARRANTY OR REPRESENTATION OF ANY KIND TO YOU OR ANY THIRD PARTY, EXPRESS, IMPLIED OR STATUTORY, WITH RESPECT TO THE MATERIALS OR THE ACCURACY OF ANY INFORMATION CONTAINED IN THE MATERIALS, INCLUDING, WITHOUT LIMITATION, ANY IMPLIED WARRANTY OF MERCHANTABILITY, ACCURACY, SATISFACTORY QUALITY, FITNESS FOR A PARTICULAR PURPOSE, USABILITY, INTEGRATION OR NON-INFRINGEMENT AND ALL SUCH WARRANTIES ARE HEREBY EXCLUDED BY WILEY AND ITS LICENSORS AND WAIVED BY YOU.
- WILEY shall have the right to terminate this Agreement immediately upon breach of this Agreement by you.
- You shall indemnify, defend and hold harmless WILEY, its Licensors and their respective directors, officers, agents and employees, from and against any actual or threatened claims, demands, causes of action or proceedings arising from any breach of this Agreement by you.
- IN NO EVENT SHALL WILEY OR ITS LICENSORS BE LIABLE TO YOU OR ANY OTHER PARTY OR ANY OTHER PERSON OR ENTITY FOR ANY SPECIAL,

CONSEQUENTIAL, INCIDENTAL, INDIRECT, EXEMPLARY OR PUNITIVE DAMAGES, HOWEVER CAUSED, ARISING OUT OF OR IN CONNECTION WITH THE DOWNLOADING, PROVISIONING, VIEWING OR USE OF THE MATERIALS REGARDLESS OF THE FORM OF ACTION, WHETHER FOR BREACH OF CONTRACT, BREACH OF WARRANTY, TORT, NEGLIGENCE, INFRINGEMENT OR OTHERWISE (INCLUDING, WITHOUT LIMITATION, DAMAGES BASED ON LOSS OF PROFITS, DATA, FILES, USE, BUSINESS OPPORTUNITY OR CLAIMS OF THIRD PARTIES), AND WHETHER OR NOT THE PARTY HAS BEEN ADVISED OF THE POSSIBILITY OF SUCH DAMAGES. THIS LIMITATION SHALL APPLY NOTWITHSTANDING ANY FAILURE OF ESSENTIAL PURPOSE OF ANY LIMITED REMEDY PROVIDED HEREIN.

- Should any provision of this Agreement be held by a court of competent jurisdiction to be illegal, invalid, or unenforceable, that provision shall be deemed amended to achieve as nearly as possible the same economic effect as the original provision, and the legality, validity and enforceability of the remaining provisions of this Agreement shall not be affected or impaired thereby.
- The failure of either party to enforce any term or condition of this Agreement shall not constitute a waiver of either party's right to enforce each and every term and condition of this Agreement. No breach under this agreement shall be deemed waived or excused by either party unless such waiver or consent is in writing signed by the party granting such waiver or consent. The waiver by or consent of a party to a breach of any provision of this Agreement shall not operate or be construed as a waiver of or consent to any other or subsequent breach by such other party.
- This Agreement may not be assigned (including by operation of law or otherwise) by you without WILEY's prior written consent.
- Any fee required for this permission shall be non-refundable after thirty (30) days from receipt by the CCC.
- These terms and conditions together with CCC's Billing and Payment terms and conditions (which are incorporated herein) form the entire agreement between you and WILEY concerning this licensing transaction and (in the absence of fraud) supersedes all prior agreements and representations of the parties, oral or written. This Agreement may not be amended except in writing signed by both parties. This Agreement shall be binding upon and inure to the benefit of the parties' successors, legal representatives, and authorized assigns.
- In the event of any conflict between your obligations established by these terms and conditions and those established by CCC's Billing and Payment terms and conditions, these terms and conditions shall prevail.
- WILEY expressly reserves all rights not specifically granted in the combination of (i) the license details provided by you and accepted in the course of this licensing transaction, (ii) these terms and conditions and (iii) CCC's Billing and Payment terms and conditions.
- This Agreement will be void if the Type of Use, Format, Circulation, or Requestor Type was misrepresented during the licensing process.

- This Agreement shall be governed by and construed in accordance with the laws of the State of New York, USA, without regards to such state's conflict of law rules. Any legal action, suit or proceeding arising out of or relating to these Terms and Conditions or the breach thereof shall be instituted in a court of competent jurisdiction in New York County in the State of New York in the United States of America and each party hereby consents and submits to the personal jurisdiction of such court, waives any objection to venue in such court and consents to service of process by registered or certified mail, return receipt requested, at the last known address of such party.

#### **WILEY OPEN ACCESS TERMS AND CONDITIONS**

Wiley Publishes Open Access Articles in fully Open Access Journals and in Subscription journals offering Online Open. Although most of the fully Open Access journals publish open access articles under the terms of the Creative Commons Attribution (CC BY) License only, the subscription journals and a few of the Open Access Journals offer a choice of Creative Commons Licenses. The license type is clearly identified on the article.

##### **The Creative Commons Attribution License**

The Creative Commons Attribution License (CC-BY) allows users to copy, distribute and transmit an article, adapt the article and make commercial use of the article. The CC-BY license permits commercial and non-

##### **Creative Commons Attribution Non-Commercial License**

The Creative Commons Attribution Non-Commercial (CC-BY-NC) License permits use, distribution and reproduction in any medium, provided the original work is properly cited and is not used for commercial purposes.(see below)

##### **Creative Commons Attribution-Non-Commercial-NoDerivs License**

The Creative Commons Attribution Non-Commercial-NoDerivs License (CC-BY-NC-ND) permits use, distribution and reproduction in any medium, provided the original work is properly cited, is not used for commercial purposes and no modifications or adaptations are made. (see below)

##### **Use by commercial "for-profit" organizations**

Use of Wiley Open Access articles for commercial, promotional, or marketing purposes requires further explicit permission from Wiley and will be subject to a fee.

Further details can be found on Wiley Online Library <http://olabout.wiley.com/WileyCDA/Section/id-410895.html>

#### **Other Terms and Conditions:**

**v1.10 Last updated September 2015**

**Questions? [customercare@copyright.com](mailto:customercare@copyright.com) or +1-855-239-3415 (toll free in the US) or +1-978-646-2777.**

---

---

**Title:** Paper-Based, Hand-Drawn Free Chlorine Sensor with Poly(3,4-ethylenedioxythiophene):Poly(styrenesulfonate)

**Author:** Yiheng Qin, Si Pan, Matiar M. R. Howlader, et al

**Publication:** Analytical Chemistry

**Publisher:** American Chemical Society

**Date:** Nov 1, 2016

Copyright © 2016, American Chemical Society

**PERMISSION/LICENSE IS GRANTED FOR YOUR ORDER AT NO CHARGE**

This type of permission/license, instead of the standard Terms & Conditions, is sent to you because no fee is being charged for your order. Please note the following:

- Permission is granted for your request in both print and electronic formats, and translations.
- If figures and/or tables were requested, they may be adapted or used in part.
- Please print this page for your records and send a copy of it to your publisher/graduate school.
- Appropriate credit for the requested material should be given as follows: "Reprinted (adapted) with permission from (COMPLETE REFERENCE CITATION). Copyright (YEAR) American Chemical Society." Insert appropriate information in place of the capitalized words.
- One-time permission is granted only for the use specified in your request. No additional uses are granted (such as derivative works or other editions). For any other uses, please submit a new request.

Copyright © 2017 [Copyright Clearance Center, Inc.](#) All Rights Reserved. [Privacy statement.](#) [Terms and Conditions.](#)

Comments? We would like to hear from you. E-mail us at [customercare@copyright.com](mailto:customercare@copyright.com)